# Cathodic corrosion

Hersbach, T.J.P.

Cover Page

# Universiteit Leiden

**Author**: Hersbach, T.J.P.
**Title**: Cathodic corrosion
**Issue Date**: 2018-12-19

# Cathodic Corrosion

## Thomas Johannes Petrus Hersbach
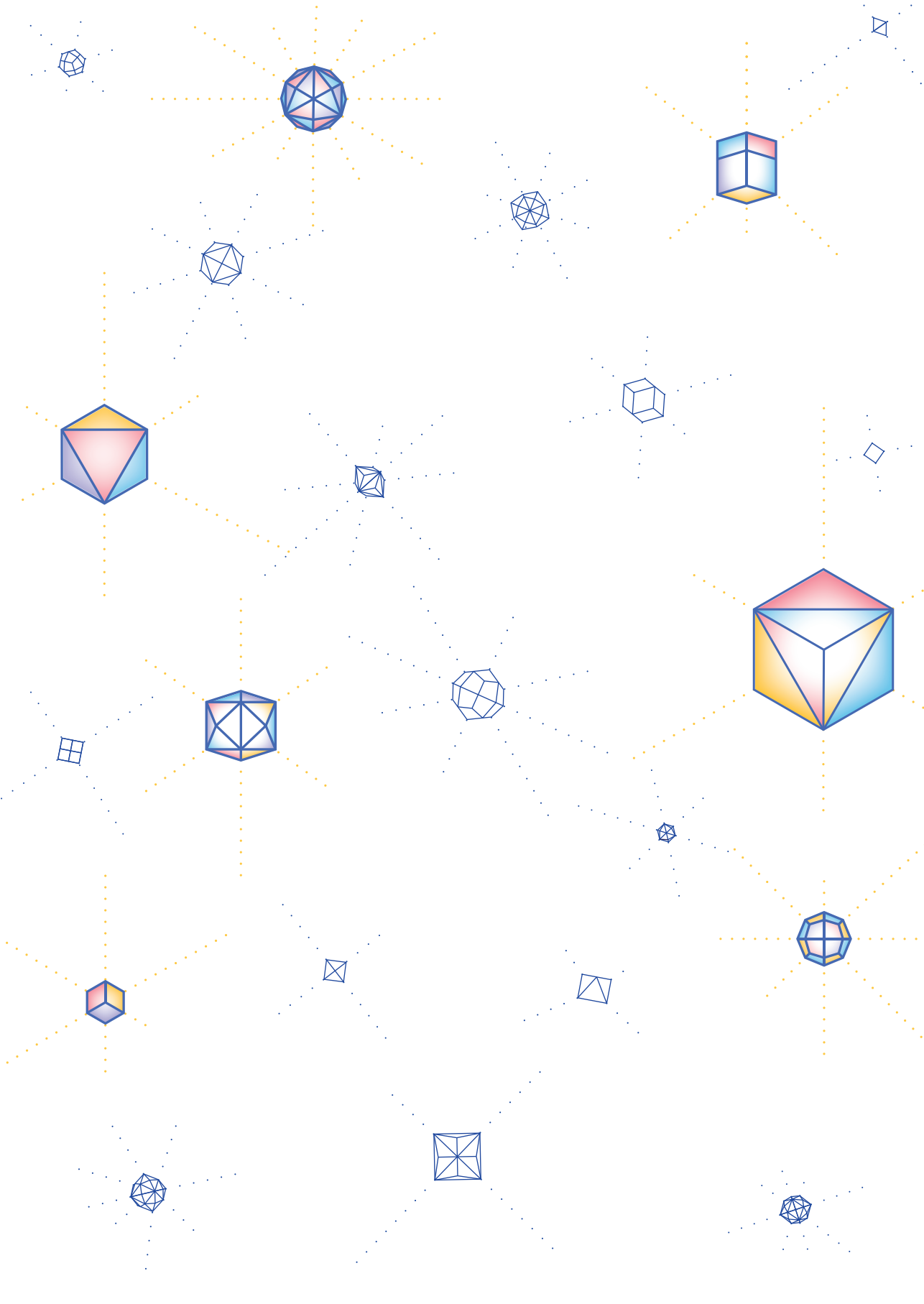
# Cathodic Corrosion

—

*Proefschrift*

ter verkrijging van
de graad van Doctor aan de Universiteit Leiden,
op gezag van Rector Magnificus Prof. mr. C.J.J.M. Stolker,
volgens besluit van het College voor Promoties,
te verdedigen op 19 december, 2018
klokke 12:30 uur

—

*door*

## Thomas Johannes Petrus Hersbach

geboren te Purmerend in 1991

# PROMOTIECOMISSIE

## PROMOTOR / SUPERVISOR

Prof. Dr. Marc T. M. Koper (Universiteit Leiden)

## CO-PROMOTORS / CO-SUPERVISORS

Dr. Amanda C. Garcia (TNO)
Dr. Federico Calle-Vallejo (Universitat de Barcelona)

## OVERIGE LEDEN / OTHER MEMBERS

Prof. Dr. H. S. Overkleeft (Universiteit Leiden)
Prof. Dr. E. Bouwman (Universiteit Leiden)
Prof. Dr. R. M. Crooks (University of Texas at Austin)
Prof. Dr. P. E. de Jongh (Universiteit Utrecht)

Si tu m'apprivoises, nous aurons besoin l'un de l'autre. Tu seras pour moi unique au monde. Je serai pour toi unique au monde.
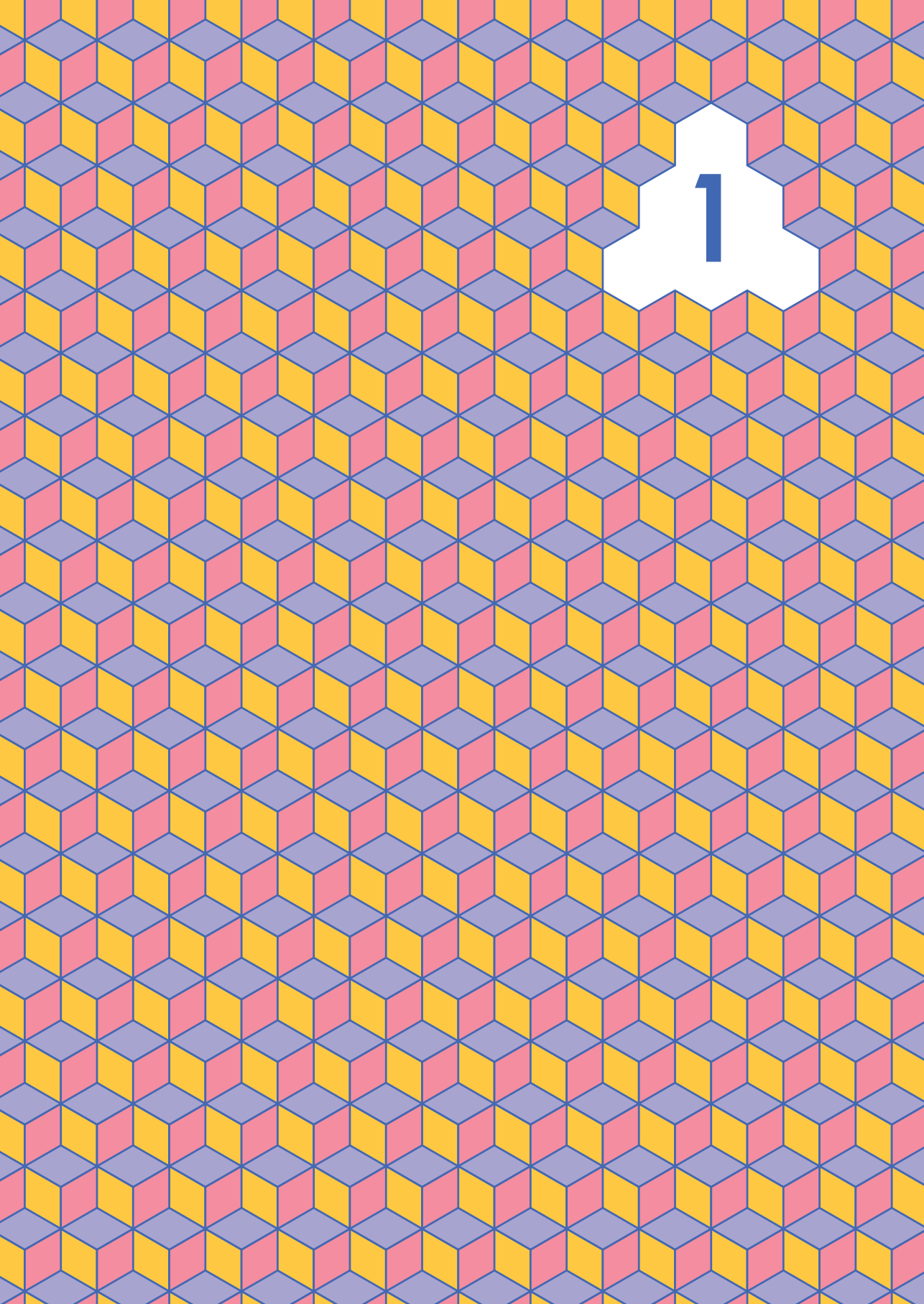
~ Antoine de Saint-Exupéry, *Le Petit Prince*

# TABLE OF CONTENTS

1

# Introduction

## 1.1 Electrochemistry

Electrochemistry is the scientific discipline that studies the intimate connection between electricity and chemistry.[1] It is the field that enables ever-improving energy storage and conversion by supercapacitors, batteries and fuel cells. It is also the chemical domain that will aid in solving pressing global challenges, like finding $CO_2$-neutral ways to produce the ammonia that sustains half the world population.[2] As such, electrochemistry is vital in the current transition from fossil fuels to renewable energy sources.

Electrochemistry uses "electrodes" for conducting experiments. This term either refers to the combination of an electrical conductor and an ionic conductor, or simply to the electrical conductor itself.[3] Given the crucial importance of conductors, it can be no surprise that electrochemistry has always made use of metals: the most well-known and ubiquitous electrical conductors. The electrochemical behavior of metals has therefore been studied extensively throughout the past two centuries. A large fraction of these studies has focused on corrosion.

## 1.2 Corrosion

Corrosion is the electrochemical degradation of a metal that interacts with its environment.[3] Most corrosion occurs when metals react with moisture in air. This causes the metal to oxidize (lose electrons) and convert into compounds like metal oxides. Probably the most well-known example of oxidation through corrosion is rusting, in which iron converts to iron oxide. Rusting and related corrosion phenomena can manifest in various ways: rust can form undesired but rather harmless spots on shiny bicycles, but can also cause catastrophic failure of infrastructure like bridges and oil pipelines.

Undesired corrosion has been a problem for centuries. Accordingly, efforts to combat corrosion have been documented since the industrial revolution.[4] These efforts have generated various methods of corrosion prevention. Some of these methods require chemical modification of either the bulk or the surface of the protected metal; examples include the development of stainless steel and protective coatings. Other methods do not require chemical modification, but instead aim to prevent corrosion through a 'more electrochemical' approach. These methods are collectively known as cathodic protection.
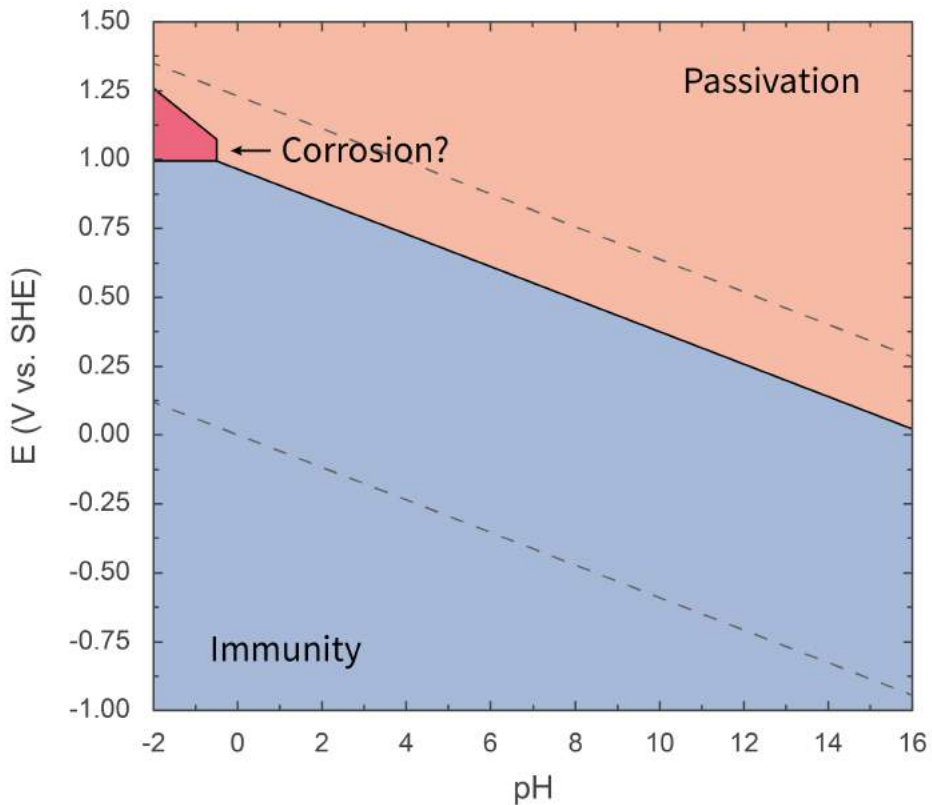
**Fig. 1.1 |** Simplified Pourbaix diagram for platinum, which indicates whether Pt is expected to corrode at a given combination of electrode potential and solution pH. The dashed grey lines mark the stability window of water; water is thermodynamically stable between the grey lines. This figure is only valid in absence of additional species with which Pt can form compounds. Figure is reproduced from literature.[5]

## 1.3   Cathodic protection

The invention of cathodic protection is frequently credited to Humphry Davy, a British chemist. Davy studied the corrosion of copper, because, in his words:[6] *"The rapid decay of the copper sheeting of His Majesty's ships of war (...) have long attracted the attention of those persons most concerned in the naval interests of the country."* Through his studies of copper corrosion, Davy discovered that corrosion could be prevented by attaching a small block of zinc to a piece of copper: as long as the 'noble' copper and the 'less noble'

zinc were in electrical contact, the zinc would corrode and protect the copper.

This protective effect of zinc can be perhaps be rationalized most visually with a tool that was invented approximately 150 years after Davy's discovery: the Pourbaix diagram.[5] Pourbaix diagrams predict the most stable state of an element as a function of its electrochemical potential and the pH of its surrounding electrolyte. An illustrative Pourbaix diagram is shown for platinum in Fig. 1.1. This diagram is simplified and simply illustrates whether platinum is expected to corrode.

The diagram is divided into a red/orange region at higher potentials and a blue region at lower potentials. In the red/orange region, platinum oxidizes. For platinum, such oxidation generally leads to a protective platinum oxide layer on the electrode. This layer significantly slows down corrosion and the platinum is considered 'passivated'. If this passivating layer does not form, the platinum corrodes, as is shown in red in Fig. 1.1. Similar diagrams can be drawn for other metals. Many of those, like iron and copper, contain large areas where the metal corrodes.

Corrosion can be prevented by moving the electrochemical potential of the protected metal into the blue region of the diagram. This was achieved by Davy's block of zinc, which gives up electrons rather easily and therefore has a low electrochemical potential. Alternatively, one can lower a metal's electrochemical potential by connecting it to an electrical power source. Though this approach differs from Davy's original method, it similarly immunizes a metal to corrosion by moving it into the blue region in the Pourbaix diagram.

One might interpret the Pourbaix diagram to mean that metallic platinum is stable at any potential marked in blue. After all, these potentials are too negative to oxidize platinum. However, the absence of oxidation only implies immunity to conventional *anodic* corrosion. Platinum can still corrode at low potentials, through an enigmatic process known as *cathodic* corrosion. Cathodic corrosion is the focus of this thesis.

## 1.4   Cathodic corrosion

Cathodic corrosion was first described around 1900 by Fritz Haber,[7,8][*] who observed the formation of large clouds of dust from cathodically (negatively) polarized metals. Haber

---

[*]   Though cathodic corrosion is generally not included in Pourbaix diagrams, Pourbaix was likely aware of Haber's work; Haber's article on the cathodic decomposition of platinum is briefly mentioned in Pourbaix' 1974 *Atlas of Electrochemical Equilibria*.
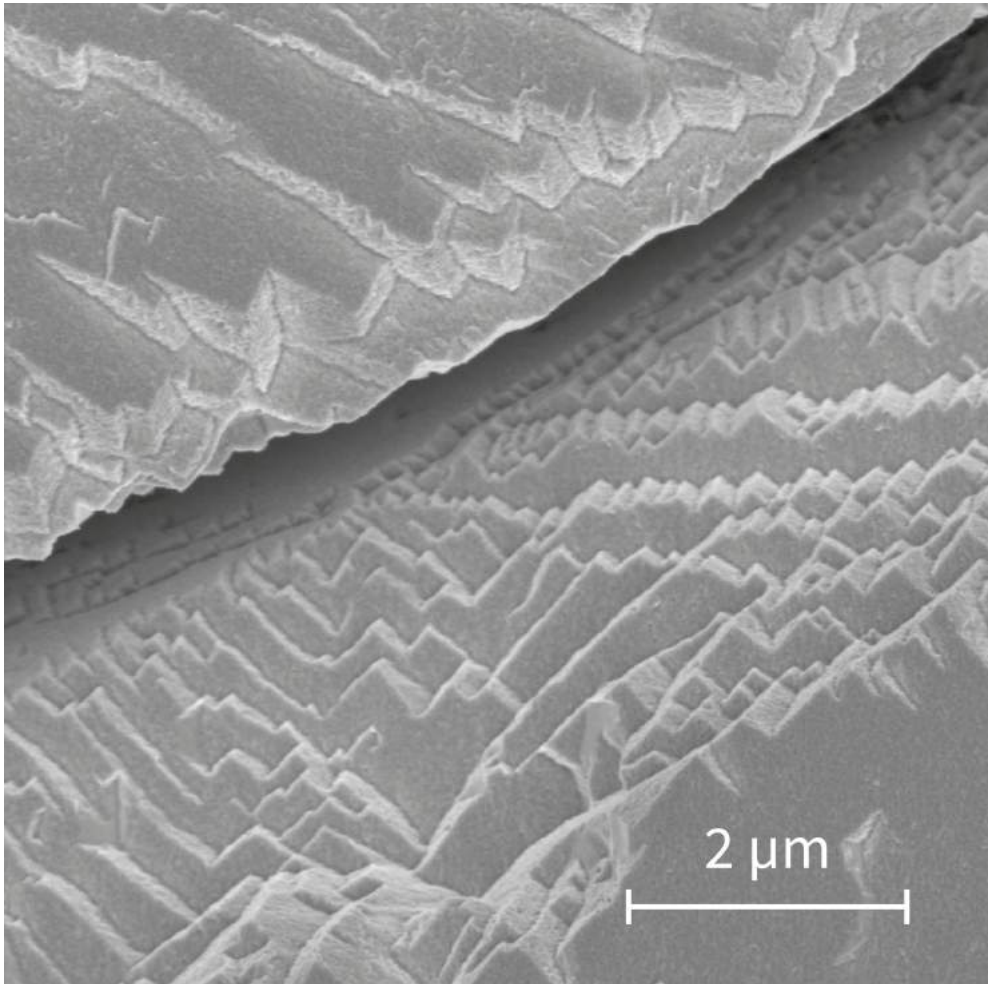
**Fig. 1.2 |** Scanning electron micrograph of a cathodically corroded platinum electrode. The image features a boundary between two crystal grains, on which etching produced large geometrical patterns. Etching was performed in $5\ M$ NaOH, by applying a $0.5\ Hz$ square wave with potential limits of $-1.0\ V$ and $2.0\ V$ *versus* the reversible hydrogen electrode for 2 minutes.

ascribed these metallic dust clouds to the formation and subsequent destruction of alloys of the corroded metal and cations like Na$^+$ and K$^+$ in the working solution. This appeared to explain cathodic corrosion and interest in the phenomenon vanished as quickly as it appeared; cathodic corrosion was briefly studied in the 1960s and 1970s,[9] but remained generally un-explored in the $20^{th}$ century.

Cathodic corrosion re-emerged as a topic of interest around 2009, when it was used

to create metallic nanoparticles.[10–12] This nanoparticle production method involves both cathodic and anodic corrosion, which are combined by applying an alternating current (AC) potential to a metallic electrode. This AC profile rapidly switches between positive (anodic) and negative (cathodic) potentials, which quickly produce a cloud of nanoparticles. These nanoparticles leave behind a dramatically etched metallic electrode, as is illustrated in Fig. 1.2.

Though these results re-ignited the interest in cathodic corrosion, they either invoked anodic corrosion as the cause of nanoparticle formation,[10,11] or referenced Haber's hypothesis of cation alloying.[12] Both explanations were disproven by work from Yanson *et al.* in 2011.[13] This work conclusively established cathodic corrosion as driving the nanoparticle formation and ruled out the creation and destruction of alkali metal alloys. Instead, an entirely new reaction mechanism was proposed.[13]

This hypothetical mechanism is illustrated in Fig. 1.3.[†] It takes into account that cathodic corrosion occurs at potentials where hydrogen evolution occurs. Due to this vigorous hydrogen production, the working solution near the platinum surface is presumably depleted from 'free water'. This means that all water is either solvating the working electrolyte (NaOH in this example), or is converted into $H_2$ and $OH^-$ upon contact with the platinum electrode. The electrode itself is covered in adsorbed hydrogen and cations like $Na^+$ (Panel 1).

Under these conditions, atoms from the electrode surface are then thought to convert into "metallic anions" (Panel 2). The exact nature of these anions is unknown, but there is strong evidence that they are stabilized by non-reducible cations: without the presence of cations like $Na^+$, cathodic corrosion does not take place.[13] After corrosion forms the cation-stabilized anionic species, this species dissolves into the working solution and moves away from the electrode.

The anion rapidly encounters free water (Panel 3). Upon contact, the ion is oxidized back to its metallic form by the water, which in turn decomposes into $H_2$ and $OH^-$. This metallic platinum then diffuses around the working solution. It either finds the original platinum surface and re-deposits or it finds other platinum atoms and nucleates to form a nanoparticle (Panel 4).

At the time of writing this thesis, this is the only reaction mechanism that is consis-

---

[†]  Though this figure illustrates the initial hypothesized reaction mechanism, it contains several elements that reflect the improved understanding gained in this thesis.
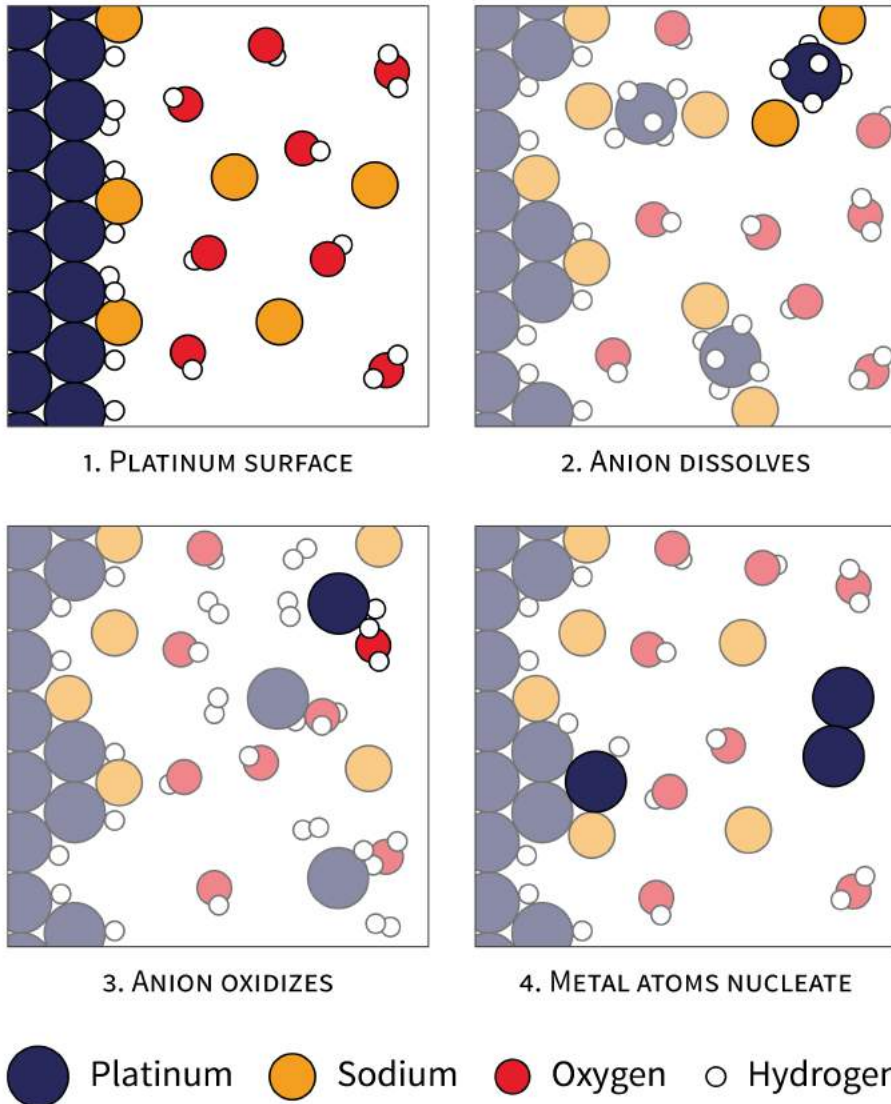
**Fig. 1.3 |** Illustration of the hypothesized cathodic corrosion mechanism, using Pt as an example. This corrosion occurs at potentials where the platinum is covered by adsorbed hydrogen and cations like Na$^+$ (Panel 1). At these potentials, hydrogen evolution occurs as well. Under these conditions, some Pt converts into an unknown cation-stabilized anion (Panel 2), which dissolves. (The anion might consist of more than one platinum atom.) Eventually, the anion encounters water and is oxidized back to atomic platinum (Panel 3). This platinum can then redeposit on the electrode or nucleate into nanoparticles (Panel 4).

tent with all experimental observations. However, this hypothesized mechanism presents several crucial questions. Perhaps most importantly, what is the exact nature of the mysterious anion? Is it, like originally suggested, a metallic anion or is it a compound containing other atoms? Furthermore, what causes the large, well-defined geometric patterns like those in Fig. 1.2? How do different metals and their alloys behave during cathodic corrosion? And could cathodic corrosion be used for more than just nanoparticle production?

## 1.5   Outline of this thesis

This thesis aims to answer the abovementioned questions regarding cathodic corrosion. In doing so, emphasis will be placed on well-defined systems. Most chapters will therefore use reference electrodes and exclude the occurrence of anodic corrosion. These two factors restrict the production of practical amounts of nanoparticles. Most of the work will therefore not focus on nanoparticles, but will instead mainly study the surfaces that are affected by cathodic corrosion. These surfaces will consist of Pt, Rh and Au, which can conveniently be characterized electrochemically.

Taking into account these considerations, this thesis contains six experimental chapters. These chapters can loosely be divided into four 'fundamental' chapters (Chapter 2–5) and two 'applied' chapters (Chapter 6–7).

As the first fundamental chapter, Chapter 2 establishes the experimental protocol that will be followed in the following four chapters. This protocol combines cyclic voltammetry and scanning electron microscopy to study corroded Pt electrodes. These techniques are used to establish the onset of cathodic corrosion in 10 $M$ NaOH. In addition, these methods reveal a strong preference for forming (100)-type sites on the surface, which correspond to the formation of geometric etch pits. This preference is hypothesized to be caused by $Na^+$ adsorption during cathodic corrosion.

Chapter 3 expands on these observations by studying the corrosion onset potential and etching preference for both Rh and Au. These metals are more challenging to handle, because of their constraints in electrode preparation. Nonetheless, Chapter 3 identifies both onset potentials and etching preferences for Rh and Au. Au differs from Pt and Rh, because it prefers forming (111) sites. This difference is tentatively explained by a difference in $Na^+$ adsorption on these metals, as will be supported by density functional theory (DFT) calculations of sodium adsorption.

Then, Chapter 4 closely examines the role of cations in determining both the onset potential and etching preference of cathodic corrosion. This examination relies on systematically studying the etching behavior of Pt, Rh and Au in solutions of LiOH, NaOH and KOH. These experiments reveal that cations indeed play a strong role in controlling cathodic corrosion. The experiments are supported by DFT calculations of cation adsorption, including the effects of solvation. Though the DFT calculations cannot quantify the exact role of cations, they do indicate that cations are adsorbed during cathodic corrosion. An equally important role is suggested for adsorbed hydrogen by additional theoretical calculations. Based on the importance of both adsorbed cations and hydrogen, Chapter 4 will suggest that the anionic cathodic corrosion intermediate is a ternary metal hydride.

The formation of ternary metal hydrides will be explored in Chapter 5. In this chapter, Pt is studied during corrosion with X-ray absorption spectroscopy (XAS). Through XAS, small changes in the chemical state of Pt are observed during cathodic corrosion. These changes are quantified through peak fitting and creating difference X-ray absorption spectra. This analysis is supported by using first-principles calculations to simulate spectra for ternary metal hydrides. One hydride, $Na_2PtH_6$, generates simulated spectra that closely match the experimental spectra. $Na_2PtH_6$ is therefore the most likely species underlying the cathodic corrosion of platinum.

Following these fundamental insights, the last two chapters will focus on applying cathodic corrosion. The first of these chapters is Chapter 6. This chapter uses the insights from Chapter 2 and 4 to optimize a Pt(111) single crystal for catalyzing the oxygen reduction reaction (ORR). Specifically, the Pt(111) electrode is mildly corroded cathodically, which creates optimal sites for ORR catalysis.

Finally, Chapter 7 concerns the creation of Pt, $Pt_{55}Rh_{45}$, $Pt_{12}Rh_{88}$ and Rh nanoparticles through combining cathodic and anodic corrosion. Pure and alloyed nanoparticles are created for various cathodic and anodic potential limits in the applied AC protocol. These variations generate insights into the relative roles of cathodic and anodic corrosion in nanoparticle production. The produced nanoparticles are then subjected to structural and compositional analysis by X-ray diffraction, X-ray absorption spectroscopy and transmission electron microscopy. This multifaceted analysis reveals small degrees of elemental segregation in the nanoparticles.

Combined, these chapters generate an improved understanding of cathodic corrosion. They provide a detailed impression of the etching behavior of Pt, Rh and Au during

purely cathodic corrosion. Perhaps most importantly, this understanding provides concrete indications for the existence of $Na_2PtH_6$ during cathodic corrosion. If correct, this would be the first reported case of ternary metal hydrides in aqueous media.

The chapters also facilitate the application of cathodic corrosion. Chapter 4 provides concrete guidelines for structuring metallic electrodes through cathodic corrosion. The implications of such structuring on catalysis are then illustrated in Chapter 6. Adding Chapter 7, the thesis ends with additional recommendations on nanoparticle production through cathodic corrosion.

As such, the present thesis marks a significant improvement in both the knowledge of cathodic corrosion and the prospects for using this unique phenomenon to tackle the electrochemical challenges of the $21^{st}$ century.

## References

1. Bard, A. J. & Faulkner, L. R. *Electrochemical Methods: Fundamentals and Applications* 2nd ed. (Wiley, New York, 2001).

2. Erisman, J. W., Sutton, M. A., Galloway, J., Klimont, Z. & Winiwarter, W. How a century of ammonia synthesis changed the world. *Nature Geoscience* **1,** 636–639 (2008).

3. Bard, A. J., Inzelt, G. & Scholz, F. *Electrochemical Dictionary* 2nd ed. (eds Bard, A. J., Inzelt, G. & Scholz, F.) (Springer Berlin, Heidelberg, 2012).

4. Sato, N. in *Green Corrosion Chemistry and Engineering* (ed Sharma, S. K.) 1–32 (Wiley-VCH Verlag GmbH & Co. KGaA, Weinheim, Germany, 2011).

5. Pourbaix, M. *Atlas of electrochemical equilibria in aqueous solutions* 2nd ed., 644 (National Association of Corrosion Engineers, 1974).

6. Davy, H. On the Corrosion of Copper Sheeting by Sea Water, and on Methods of Preventing This Effect; And on Their Application to Ships of War and Other Ships. *Philosophical Transactions of the Royal Society of London* **114,** 151–158 (1824).

7. Haber, F. Über Elektrolyse der Salzsäure nebst Mitteilungen über kathodische Formation von Blei. III. Mitteilung. *Zeitschrift für anorganische Chemie* **16,** 438–449 (1898).

8. Haber, F. The Phenomenon of the Formation of Metallic Dust from Cathodes. *Transactions of the American Electrochemical Society* **2,** 189–196 (1902).

9. Kabanov, B. N., Astakhov, I. I. & Kiseleva, I. G. Formation of crystalline intermetallic compounds and solid solutions in electrochemical incorporation of metals into cathodes. *Electrochimica Acta* **24,** 167–171 (1979).

10. Huang, W., Chen, S., Zheng, J. & Li, Z. Facile preparation of Pt hydrosols by dispersing bulk Pt with potential perturbations. *Electrochemistry Communications* **11,** 469–472 (2009).

11. Liu, J., Huang, W., Chen, S. & Hu, S. Facile electrochemical dispersion of bulk Rh into hydrosols. *Int. J. Electrochem. Sci.* **4,** 1302–1308 (2009).

12. Leontyev, I., Kuriganova, A., Kudryavtsev, Y., Dkhil, B. & Smirnova, N. New life of a forgotten method: Electrochemical route toward highly efficient Pt/C catalysts for low-temperature fuel cells. *Applied Catalysis A: General* **431-432,** 120–125 (2012).

13. Yanson, A. I. *et al.* Cathodic Corrosion: A Quick, Clean, and Versatile Method for the Synthesis of Metallic Nanoparticles. *Angewandte Chemie International Edition* **50,** 6346–6350 (2011).
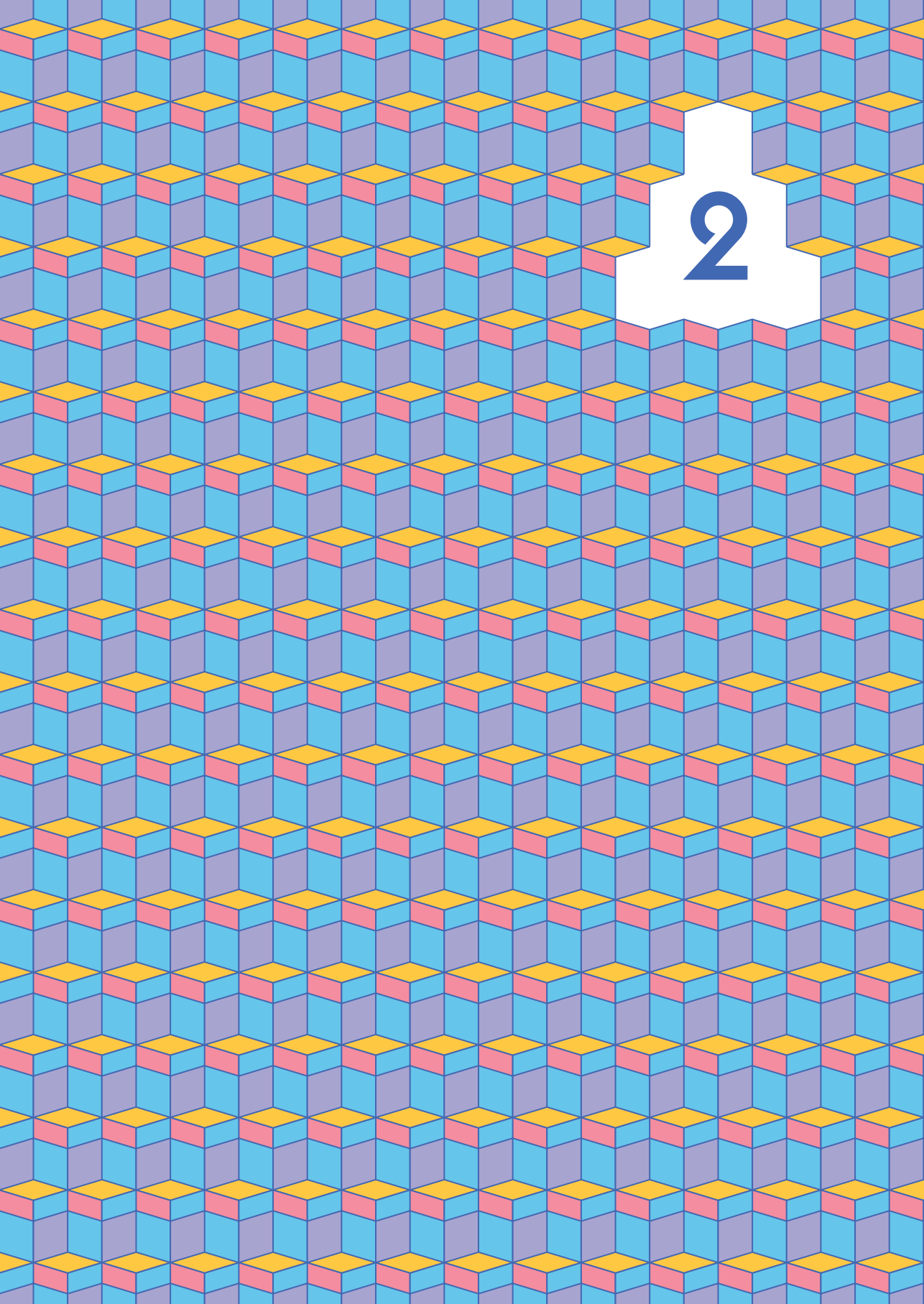
2

# Anisotropic Etching of Platinum Electrodes at the Onset of Cathodic Corrosion

*Cathodic corrosion is presumed to occur through anionic metallic reaction intermediates, but the exact nature of these intermediates and the onset potential of their formation is unknown. Here we determine the onset potential of cathodic corrosion on platinum electrodes. Electrodes are characterized electrochemically before and after cathodic polarization in* 10 *M sodium hydroxide, revealing that changes in the electrode surface start at an electrode potential of* −1.3 *V versus the normal hydrogen electrode. The value of this onset potential rules out previous hypotheses regarding the nature of cathodic corrosion. Scanning electron microscopy shows the formation of well-defined etch pits with a specific orientation, which match the voltammetric data and indicate a remarkable anisotropy in the cathodic etching process, favoring the creation of (100) sites. Such anisotropy is hypothesized to be due to surface charge-induced adsorption of electrolyte cations.*

## 2.1   Introduction

Cathodic corrosion is a phenomenon in which metal electrodes undergo degradation under cathodic conditions. This process has puzzled scientists since its discovery by Haber around 1900 because of the unexpected changes that are induced on the electrode surface at negative potentials.[1] Besides leading to extensive roughening of the surface, cathodic corrosion also generates nanoparticles as a corrosion by-product at strong cathodic polarization. This nanoparticle production can be enhanced by introducing an alternating anodic potential. These observations have led researchers to hypothesize incorporation and subsequent leaching of electrolyte protons or alkali metals as an explanation for cathodic corrosion.[1–3] This process would weaken the structure of the metal

---

This chapter is based on Hersbach, T. J. P., Yanson, A. I. & Koper, M. T. M., *Nature Communications* **7**, 12653 (2016).

lattice, leading to degradation of the surface and formation of nanoparticles. Another possible mechanism suggested for the formation of these particles was 'contact glow discharge', a phenomenon induced by high currents, which has the potential to rapidly degrade electrodes.[4]

However, we demonstrated that cathodic corrosion even takes place if the electrolyte cations are organic instead of alkali metals, if anodic potentials are not applied, and if the measured currents are far below those required for contact glow discharge.[5] Another important observation from our previous work was that cathodic corrosion does not take place if protons are the only cations in solution. These observations rule out the afore-mentioned hypotheses and instead point exclusively to cathodic chemical reactions be-ing the main reason for corrosion. On the basis of these observations, we suggested cathodic corrosion to occur via metastable metallic anions, which are stabilized by non-reducible electrolyte cations. The exact nature of these corrosion intermediates and the exact cathodic corrosion onset potential are, however, still unknown; most recent studies on cathodic corrosion have employed a practical approach towards nanoparticle synthe-sis,[6–11] rather than a fundamental approach towards understanding cathodic corrosion. Additionally, these studies often did not employ reference electrodes and generally ap-plied high-amplitude AC voltages, thereby impairing the ability to draw clear conclusions on the exclusive role of cathodic potentials.

In pursuit of elucidating the processes underlying cathodic corrosion, this work fo-cuses on studying the onset of cathodic corrosion at platinum electrodes by detailed electrochemical and structural characterization. The electrodes are subjected to various constant cathodic potentials in a 10 molar sodium hydroxide solution and are subse-quently characterized by cyclic voltammetry (CV). This CV analysis reveals a remarkable anisotropic etching with an onset potential only a few hundreds of millivolts negative of the onset of hydrogen evolution. These findings of anisotropic etching are supported by scanning electron microscopy (SEM), which reveals the formation of well-oriented etch pits. Our results match well with the previously observed preferred orientation of nanoparticles prepared by cathodic corrosion. This matching preferred orientation is hypothesized to be caused by the specific interaction of electrolyte cations, which are known to be crucial actors in the cathodic corrosion process.[5] Furthermore, the strategy employed in this work seems suitable for studying cathodic corrosion on other metals.

## 2.2 Materials and methods

### 2.2.1 Electrochemistry

Electrochemical experiments were performed with an Autolab PGSTAT12, which is equipped with a linear scan generator. All water used for rinsing and preparing electrolyte solutions was demineralized and ultrafiltered by a Millipore MilliQ system (resistivity > $18.2\ M\Omega \cdot cm^{-1}, TOC\ < 5\ ppb$). All electrolyte solutions were deoxygenated before experiments by purging with argon (Linde, 6.0 purity). Argon was kept flowing over the solution during experiments.

Platinum wires (Mateck, 99.99%; $\varnothing = 0.1\ mm$) were used as working electrodes. Before experiments, the electrode was carefully rinsed with water and subsequently flame-annealed for $60\ s$ and cooled down in air. Next, it was inserted into a standard three-electrode cell containing $0.5\ M$ $H_2SO_4$ (Merck, Ultrapur), using a platinum wire as the counter electrode and a reversible hydrogen electrode (RHE) as a reference electrode. The immersion depth of the working electrode was carefully controlled, using a micrometer screw. After immersion, the electrode was characterized using CV.

After CV characterization, the working electrode was rinsed and transferred to a home-made fluorinated ethylene propylene cell containing a $10\ M$ NaOH (Fluka, Traceselect) solution, which was outfitted with a titanium counter electrode and a HydroFlex RHE (Gaskatel). Following electrode immersion, a constant cathodic potential was applied for $60\ s$, after which the electrode was removed under potential control. Next, the electrode was rinsed, transferred back to the $H_2SO_4$ cell and characterized again using CV. After electrochemical characterization, electrodes were removed from the cell, rinsed and stored for later examination using SEM.

### 2.2.2 Scanning Electron Microscopy

Micrographs were obtained on a FEI NOVA NanoSEM 200 SEM, using an acceleration voltage of $5\ kV$ and a beam current of $0.9\ nA$. Storage time before SEM imaging did not affect the electrode, as similar images could be obtained after both several days and several months of storage.

## 2.3    Results and discussion

### 2.3.1    Surface changes observed by cyclic voltammetry

To determine the onset potential of cathodic corrosion, we followed the following proto-col. Platinum work electrodes were polarized cathodically at a given constant potential for $60$ *s* in a $10$ *M* NaOH solution. These cathodic potentials were applied *versus* an in-ternal reversible hydrogen electrode (RHE). Before and after polarization, the electrodes were characterized by CV in the hydrogen adsorption/desorption region to determine whether the electrode surface had changed. CV is a quick and versatile technique for characterizing platinum electrodes, since potential-induced adsorption and desorption of hydrogen on platinum in sulfuric acid are extremely sensitive to the orientation of the atoms on the electrode surface. Therefore, different surface sites produce different peaks in the voltammogram. Specifically, (100) sites near terrace borders produce a relatively sharp peak at $0.27$ *V vs.* RHE, whereas (100) terrace sites are responsible for a broad signal between $0.3$ and $0.4$ *V vs.* RHE.[12] In addition, (111) sites give a broad featureless signal between $0.06$ and $0.3$ *V vs.* RHE due to hydrogen desorption, along with another broad feature between $0.4$ and $0.55$ *V vs.* RHE due to sulfate desorption. Finally, (110) sites generate a peak at $0.13$ *V vs.* RHE. These peaks will be visible and distinguishable in the voltammogram if their corresponding surface sites are present on the electrode. Voltammograms for several studied platinum electrodes are displayed in Fig. 2.1.

As can be seen in Fig. 2.1 **a**, treating platinum at a potential of $-0.3$ *V vs.* RHE leads to voltammograms that overlap almost perfectly before and after polarization. Only a small increase in the (110) peak at $0.13$ *V vs.* RHE and a minor decrease in the (100) peak at $0.27$ *V vs.* RHE are observed after treatment, but these changes are minimal and occur consistently for all tested potentials above and including $-0.3$ *V vs.* RHE.

Equally subtle, yet reproducible changes in the voltammogram occur when the elec-trode is treated at $-0.4$ *V vs.* RHE. These changes are observable in Fig. 2.1 **b** and are marked by a small decrease in the (110) peak, accompanied by a small increase in the (100) peak. Moreover, a marginally higher current is observed between $0.3$ and $0.4$ *V vs.* RHE. These changes in the voltammogram imply an increase in the number of (100)-type sites.

This surface modification towards (100) sites is much more apparent after the elec-trode has been polarized at $-0.5$ *V vs.* RHE, as visualized in Fig. 2.1 **c**. The number of (100)-type sites has increased dramatically and (110) sites have almost completely disap-
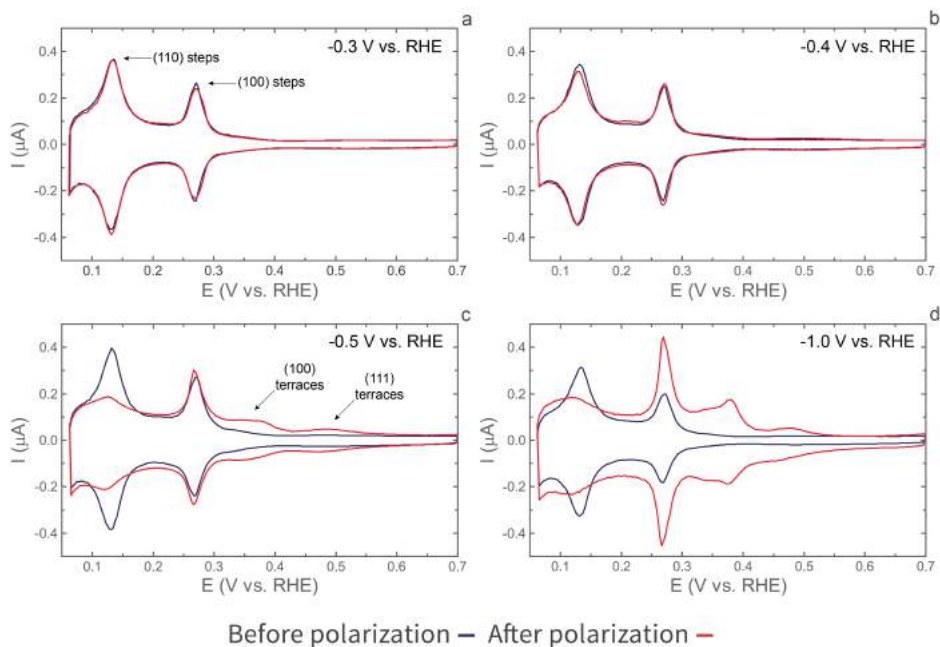
**Fig. 2.1 |** Cyclic voltammograms of platinum electrodes before (blue trace) and after (red trace) cathodic polarization in 10 *M* NaOH at −0.3 *V vs.* RHE **(a)**, −0.4 *V vs.* RHE **(b)**, −0.5 *V vs.* RHE **(c)** and −1.0 *V vs.* RHE **(d)**. Voltammograms were recorded in 0.5 *M* H$_2$SO$_4$, at a scan rate of 50 *mV · s$^{-1}$*.

peared; virtually all current at 0.13 *V vs.* RHE originates from the broad feature between 0.06 and 0.3 *V vs.* RHE, which corresponds to atoms arranged in a (111)-type fashion. The abundance of these (111)-type sites has increased slightly, as can be derived from the clearly increased (bi)sulfate adsorption feature between 0.4 and 0.55 *V vs.* RHE.

All changes described for −0.5 *V vs.* RHE polarization are even further enhanced if platinum is polarized at −1.0 *V vs.* RHE (Fig. 2.1 **d**). Most notably, the (100) peak at 0.27 *V vs.* RHE has grown strongly and a peak corresponding to wide (100)-type terraces has developed at 0.38 *V vs.* RHE. In addition, the amount of (111)-type sites has increased, as is indicated by an increase in the broad current features corresponding to these sites. Finally, the total charge corresponding to both the cathodic and anodic CV signals has increased by a factor of 1.6. This correlates with a factor 1.6 surface area increase,[13] which indicates significant roughening of the electrode surface.

## 2.3.2 Scanning Electron Microscopy

Since the CV data indicate changes in the arrangement of atoms on the surface and rough-
ening of the electrode, one would expect to observe a change in surface morphology
from inspection of the surface. The surface can be imaged by, for example, *in-situ* scan-
ning tunnelling microscopy (STM) or by *ex-situ* SEM. Although STM is capable of achiev-
ing atomic resolution on well-defined surfaces in electrochemical systems,[14,15] obtain-
ing such resolution during cathodic corrosion is prohibited by a variety of factors. Most
notably, vigorous evolution of hydrogen during corrosion prevents imaging of the elec-
trode.[16] In addition, a wide range of challenges is posed by the switching between $0.5\ M$
$H_2SO_4$ and $10\ M$ NaOH electrolyte that would be required to characterize the electrode
before and after cathodic treatment. To our best knowledge, resolving these challenges
is currently beyond the state-of-the-art.

Therefore, *ex-situ* SEM is a more easily accessible technique, which provides valu-
able information in addition to CV characterization. Typical SEM images are shown in
Fig. 2.2, which displays micrographs of electrodes treated at various potentials between
$-0.2$ and $-0.8\ V$ *vs.* RHE. It is vital to realize that these micrographs have a lower res-
olution than STM and cannot visualize the smallest conceivable electrode roughness.
Though nanoscale corrugation is present on even the most well-defined single crystals,[17]
observing such height differences is beyond the practical resolution of the employed mi-
croscope. Still, the images in Fig. 2.2 show excellent consistency with the conclusions
from the CV measurements, as will be discussed in the next paragraphs.

The SEM image in Fig. 2.2 **a** shows a platinum surface polarized at $-0.2\ V$ *vs.* RHE,
displaying only barely visible degrees of roughness in the bottom right quadrant. Apart
from the three intersecting crystal grain boundaries, the depicted area can therefore be
considered to be mostly flat from an SEM point of view. This matches with the observa-
tions made in CV, in which electrodes look identical when freshly annealed and polarized
at or above $-0.3\ V$ *vs.* RHE. Similarly, no observable roughening of the electrode can be
seen after polarizing it at $-0.4\ V$ *vs.* RHE (Fig. 2.2 **b**). Even when decreasing the poten-
tial to $-0.5\ V$ *vs.* RHE (Fig. 2.2 **c**), where voltammetry detects a clear change in surface
morphology, only a barely distinguishable roughening can be observed.

Significantly more roughening is observed after polarization at potentials of $-0.6\ V$
*vs.* RHE or lower; the micrograph in Fig. 2.2 **d** clearly depicts increased corrugation, both
at the crystal grains and their boundaries. Such corrugation is present on most parts of
the electrode, which agrees well with an electrochemically determined roughness factor
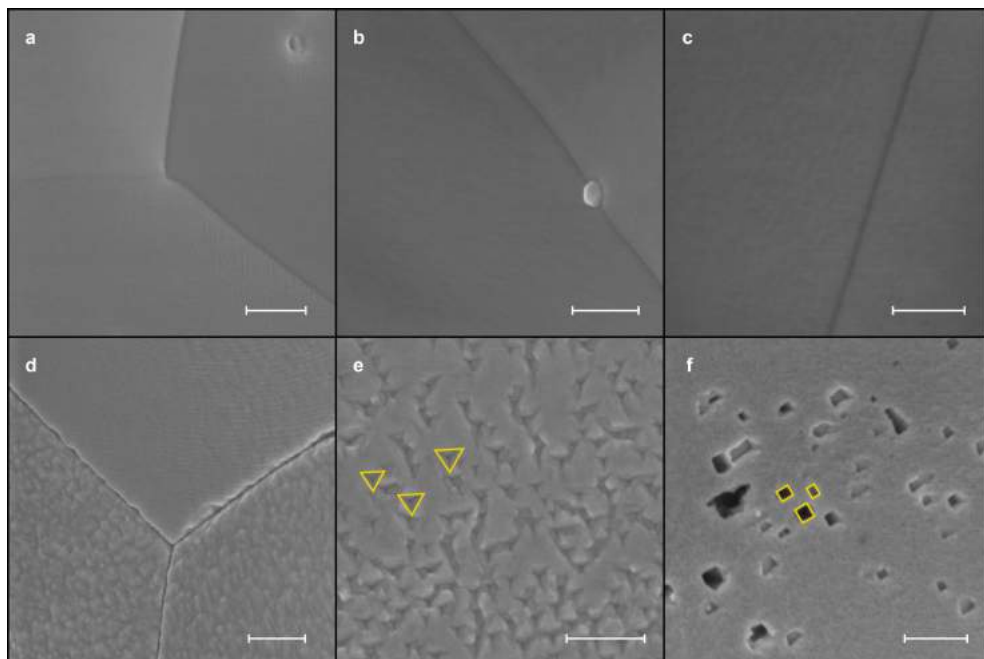
**Fig. 2.2 |** Scanning electron micrographs of platinum electrodes treated at $-0.2$ *V* vs. RHE **(a)**, $-0.4$ *V* vs. RHE **(b)**; $-0.5$ *V* vs. RHE **(c)**; $-0.6$ *V* vs. RHE **(d, e)** and $-0.8$ *V* vs. RHE **(f)**. In **e, f**, three etch pits have been outlined in yellow to illustrate shape and orientation similarities. Scale bars are 300 *nm* **(a, b, d–f)**. Scale bar is 100 *nm* in Panel **c**.

of 1.1 for the electrode in Fig. 2.2 **d, e** and 1.2 for the electrode in Fig. 2.2 **f**.

Interestingly, this general increase in corrugation is accompanied by the formation of well-defined etch pits on parts of the electrode. One type of etch pit is triangular, as shown in Fig. 2.2 **e**. Three of these pits have been outlined in yellow. Notably, all pits are oriented identically if they are on the same crystal grain.

The second type of pit is depicted in Fig.2.2 **f** and exclusively possesses 90° angles. Because of their shape, the pits can be seen as quasi-rectangular; similar pits have been observed previously in AC corrosion.[18] These pits are also oriented identically when they are formed on the same grain, as can readily be seen by comparing the three highlighted pits. The pits and corrugation described here are likely the only cause of the electrochemically observed surface area increase, since no cathodically formed nanoparticles were observed.

### 2.3.3 Discussion

The CV data presented in Fig. 2.1 show that the electrode surface structure remains unchanged when platinum wires are polarized at potentials of $-0.3$ *V vs.* RHE or higher in a 10 *M* NaOH solution. However, the surface structure is modified when the electrode is polarized at potentials of $-0.4$ *V vs.* RHE and below. We can therefore conclude that the onset potential of cathodic corrosion of platinum lies between $-0.3$ and $-0.4$ *V vs.* RHE. Since determining the exact onset potential requires an even greater accuracy than the current experimental setup provides, we suggest a tentative cathodic corrosion onset potential of $-0.4$ *V vs.* RHE for platinum in a 10 *M* NaOH solution. This corresponds to approximately $-1.3$ *V versus* the normal hydrogen electrode (NHE).

This experimentally determined onset potential presumably has a thermodynamic character because it is determined by the stability of the elusive metastable corrosion intermediate. However, this onset potential is not a standard equilibrium potential, such as those listed in the electrochemical series;[19] in order to define an equilibrium potential, one would require accurate knowledge of the concentration and nature of the involved reactants. Since this knowledge is currently unavailable due to the elusive nature of the cathodic corrosion reaction intermediates, the reported onset potential is simply the least negative potential at which cathodic corrosion can be detected. We can therefore not exclude that longer corrosion times would slightly shift the determined onset potential to less negative values, leading to the conclusion that this potential is also partly kinetic in nature.

Still, the value of the onset potential can be compared with tabulated equilibrium potentials. For example, the onset potential lies only 0.4 *V* below the thermodynamic onset of hydrogen evolution in alkaline media, which is surprisingly mild. This potential of $-1.3$ *V vs.* NHE definitively rules out the incorporation of sodium ions as the reason for cathodic corrosion; the $Na^+/Na$ couple has a standard equilibrium potential of $-2.71$ *V vs.* NHE.[19]

The CV data also indicate that cathodic corrosion is accompanied by the preferential formation of (100)-type sites. This implies that etching by cathodic corrosion is highly anisotropic. These observations are confirmed by the shape and orientation of the etch pits created by cathodic corrosion, displayed in the micrographs in Fig. 2.2 **e, f**. These shapes and orientations can be rationalized by the simple models shown in Fig. 2.3, which will be used to illustrate how the SEM data support the (100) etching preference observed in electrochemistry.
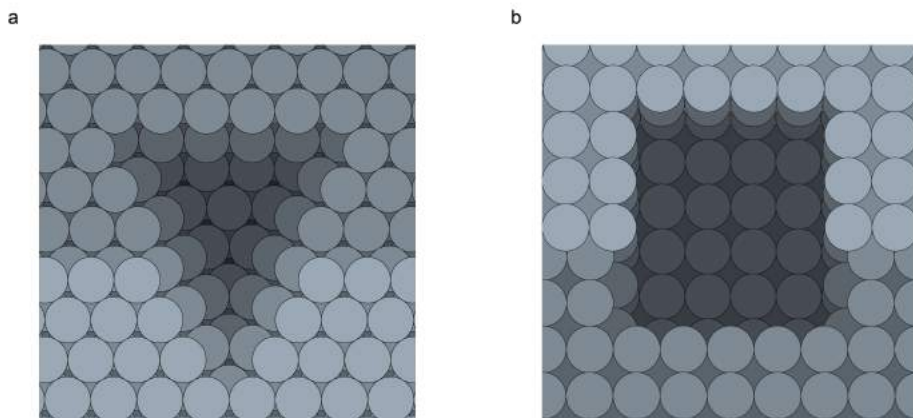
**Fig. 2.3** | A triangular etch pit with (100)-type sides in a (111)-type surface with a (110)-type step **(a)** and a rectangular etch pit with (100)-type sides in a (100)-type surface with a (111)-type step **(b)**.

Figure 2.3 **a** displays a (111)-type surface with a (110)-type step. Etching a hole in this surface that exposes (100) sites requires the hole to be triangular. This model etch pit shape matches the shape of the etch pits in Fig. 2.2 **e**. Moreover, Fig. 2.3 **a** indicates that all etch pits should have the same orientation, as dictated by the orientation of the underlying crystal grain. This is indeed apparent from the identically oriented outlines in Fig. 2.2 **e**. Finally, the model in Fig. 2.3 **a** matches the electrochemically observed decrease in (110) sites: if an etch pit is created in a surface section with a (110)-step, part of this step will be removed. Thus, the model in Fig. 2.3 **a** is able to unify the electrochemical and microscopic observations.

A similar analysis can be performed on (100)-type surfaces, displayed in Fig. 2.3 **b**. When exposing (100) sites in this surface, one is required to create holes with a rectangular shape of which the orientation is again dictated by the crystal grain. Furthermore, all angles within the hole must be 90°. These identically aligned rectangles match well with those in Fig. 2.2 **f**, as is emphasized by the orientation of the highlighted rectangles. Any deviation from the model rectangular shape has to add new rectangles to the existing pit in order to exclusively create (100) sites, thus creating quasi-rectangles such as the bottom left pit in Fig. 2.2 **f**. In addition, any (110) sites will be removed from the surface in which an etch pit is grown. Thus, the rectangular model pits are also in good agreement with both the electrochemical and microscopic data.

One should bear in mind that the presented model pit shapes are only meant to illustrate how pit shape and voltammetry are consistent, and that the actual etching process through which the pits are generated most likely occurs through an interplay of complex mechanisms, much alike surface growth by atom deposition.[20] For example, one could imagine hole initiation by corrosion of a (110)-step site, from which the hole grows over the surface. The complexity of the corrosion kinetics is explicitly suggested by the occurrence of corrugation that does not resemble the model pit shapes presented in Fig. 2.3, such as the type depicted in Fig. 2.2 **d**. This type of roughness on grains and grain boundaries is abundant on the electrode, as is the occurrence of complex etching grooves. These features are to be expected, since metallic surfaces possess elaborate reconstructions that are typically invisible to SEM, such as step bunching. Such reconstructions are much more complex than the idealized (111)- and (100)-type surfaces employed in our model. Explaining corrugation on these non-ideal areas of the electrode will thus require more complex kinetic models, which will be the focus of future studies of cathodic corrosion. Nonetheless, the presented model etch pits are able to unify the electrochemical and SEM data and emphasize the strong (100) etching preference of platinum.

This preference for (100) sites is remarkable, since (100)-type surfaces typically have higher surface energies than (111)-type surfaces and even (100) steps have a higher free energy than (111) steps on a (111) surface.[21,22] In addition, the preference for (100) sites is present for both the observed etch pits and the orientation of nanoparticles created by cathodic corrosion.[7,8] Any consistent explanation for this preference will therefore have to address both the anisotropy in cathodic etching and the preferential nanoparticle orientation. The preferential selection of a certain facet can be surface charge-driven (global) or adsorbate-driven (local).

A global explanation involving surface charge-induced reconstruction is less likely,[23] since such a hypothesis would only explain the etching anisotropy. This hypothesis does not take into account the anisotropic particle growth, which necessarily occurs through coalescence of uncharged intermediates. Any anionic intermediates will have to be oxidized before coalescence, since coulombic repulsion should prevent charged particles from colliding. Similarly, global hypotheses based on the potential-dependence of the free energy of different step types will only explain the etching anisotropy,[24] because nanoparticle growth is thought to occur in solution and should be largely unaffected by the electrochemical potential of the electrode.

Since global explanations typically only seem to explain the etching anisotropy, a

local hypothesis involving stabilization by adsorbing electrolyte cations seems more appropriate.[25] These positively charged ions are expected to interact strongly with the electrode surface at the negative potentials and surface charges relevant for cathodic corrosion. Therefore, these cations are likely able to restructure the platinum surface; it is well known that adsorbates can affect the structure of metallic surfaces by lowering the surface free energy of facets that would not be preferred under adsorbate-free conditions.[26–28] Furthermore, it is known that these cations are essential to cathodic corrosion, since they are required to stabilize the anionic corrosion intermediates.[29] This importance of cations parallels the role of adsorbates in traditional nanoparticle synthesis, in which cationic, anionic and molecular adsorbates are able to both restructure existing nanoparticles and control particle shape during formation by preferentially adsorbing to specific crystal facets.[30–32]

The above mechanism would imply a strong dependence of the anisotropy in cathodic corrosion on both the concentration and nature of the electrolyte cations, which has indeed been observed in previous studies: the (100) nanoparticle orientation preference decreases with decreasing cation concentration[8,18,25] and is less pronounced in potassium hydroxide than in sodium hydroxide.[8] On the basis of these experimental observations and the general tendency of adsorbates to restructure nanoparticles and bulk electrodes, we hypothesize that the specific interaction of cations is the most likely cause of both the preferential orientation of cathodically prepared nanoparticles and the anisotropic etching observed in the current work.

Finally, it is interesting to compare the surface modifications observed in cathodic corrosion to other electrochemical surface modifications. For example, Díaz *et al.* observed striking changes in the voltammetric profile of platinum after cathodic polarization in sulfuric acid solutions, which they attributed to the formation of 'superactive' platinum states.[33,34] Although experiments in ultraclean sulfuric acid demonstrated that these observations are not caused by cathodic corrosion,[5] these changes further illustrate the pronounced modifications that can occur at metallic electrodes after cathodic polarization.

The significance of the changes caused by cathodic corrosion is emphasized by comparing them to modifications caused by repeatedly cycling at predominantly anodic potentials.[35–37] These latter cycling procedures can modify electrode surfaces by repeatedly oxidizing and reducing platinum in experiments that typically last 5–10 min. These oxidation/reduction cycles are a strict requirement for modification in these experiments,

because platinum is quite stable under constant anodic polarization due to protection by a thin oxide layer.[38] By contrast, cathodic corrosion is able to induce similar or even more dramatic changes by polarizing the electrode just 0.5 V below the thermodynamic onset of hydrogen evolution for only a minute. This leads to the surprising and counterintuitive conclusion that cathodic corrosion can, in some electrolytes, be much more detrimental to platinum electrodes than anodic corrosion, suggesting that the concept of cathodic protection is relative.

## 2.4 Conclusions

Summarizing, we have determined the onset potential of cathodic corrosion of platinum in 10 *M* NaOH at $-1.3$ *V* *vs.* NHE. In addition, cathodic corrosion was shown to involve highly anisotropic etching, favoring the creation of (100) terraces and steps and the removal of (110) sites. Accordingly, SEM revealed well-oriented etch pits, confirming the anisotropic etching that was determined electrochemically. Our current understanding of the phenomenon suggests that this anisotropy is likely induced by strong interaction of electrolyte cations with the highly negative surface charge of the electrode. The fact that cathodic corrosion starts only 0.4 *V* below the thermodynamic onset of hydrogen evolution in alkaline media also leads to the surprising conclusion that cathodic protection is a relative concept, and that cathodic corrosion can be more detrimental to platinum surfaces (and noble metals in general) than anodic corrosion.
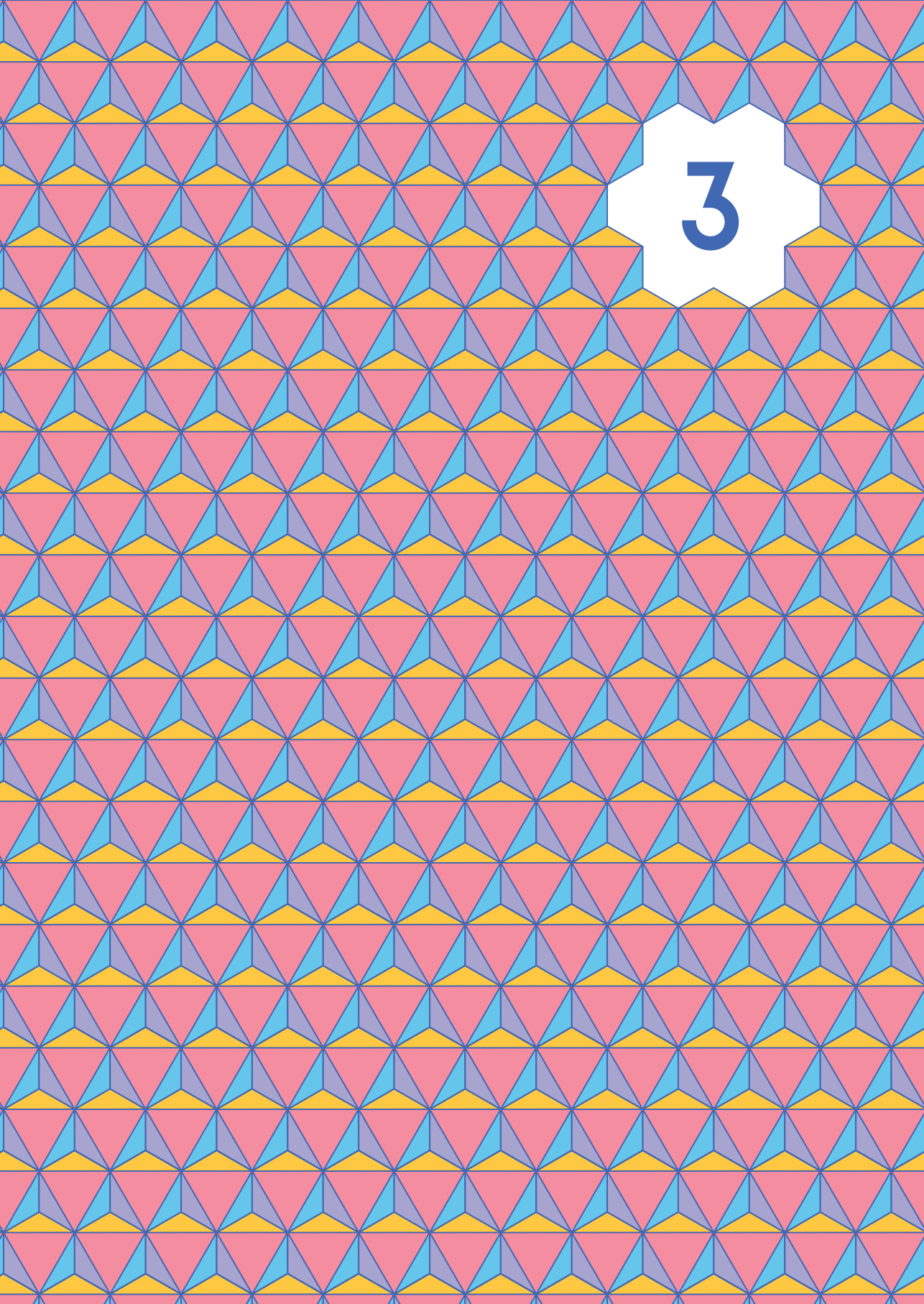
## References

1. Haber, F. The Phenomenon of the Formation of Metallic Dust from Cathodes. *Transactions of the American Electrochemical Society* **2,** 189–196 (1902).

2. Kabanov, B. N., Astakhov, I. I. & Kiseleva, I. G. Formation of crystalline intermetallic compounds and solid solutions in electrochemical incorporation of metals into cathodes. *Electrochimica Acta* **24,** 167–171 (1979).

3. Leontyev, I., Kuriganova, A., Kudryavtsev, Y., Dkhil, B. & Smirnova, N. New life of a forgotten method: Electrochemical route toward highly efficient Pt/C catalysts for low-temperature fuel cells. *Applied Catalysis A: General* **431-432,** 120–125 (2012).

4. Gangal, U., Srivastava, M. & Sen Gupta, S. K. Mechanism of the Breakdown of Normal Electrolysis and the Transition to Contact Glow Discharge Electrolysis. *Journal of The Electrochemical Society* **156,** F131–F136 (2009).

5. Yanson, A. I. *et al.* Cathodic Corrosion: A Quick, Clean, and Versatile Method for the Synthesis of Metallic Nanoparticles. *Angewandte Chemie International Edition* **50,** 6346–6350 (2011).

6. Rodriguez, P., Tichelaar, F. D., Koper, M. T. M. & Yanson, A. I. Cathodic Corrosion as a Facile and Effective Method To Prepare Clean Metal Alloy Nanoparticles. *Journal of the American Chemical Society* **133,** 17626–17629 (2011).

7. Yanson, A., Antonov, P., Yanson, Y. & Koper, M. Controlling the size of platinum nanoparticles prepared by cathodic corrosion. *Electrochimica Acta* **110,** 796–800 (2013).

8. Duca, M., Rodriguez, P., Yanson, A. I. & Koper, M. T. M. Selective Electrocatalysis on Platinum Nanoparticles with Preferential (100) Orientation Prepared by Cathodic Corrosion. *Topics in Catalysis* **57,** 255–264 (2014).

9. Lu, F., Ji, X., Yang, Y., Deng, W. & Banks, C. E. Room temperature ionic liquid assisted well-dispersed core-shell tin nanoparticles through cathodic corrosion. *RSC Advances* **3,** 18791–18793 (2013).

10. Najdovski, I., Selvakannan, P. & O'Mullane, A. P. Cathodic Corrosion of Cu Substrates as a Route to Nanostructured Cu/M (M=Ag, Au, Pd) Surfaces. *ChemElectroChem* **2,** 106–111 (2015).

11. Bennett, E. *et al.* A Synthetic Route for the Effective Preparation of Metal Alloy Nanoparticles and Their Use as Active Electrocatalysts. *ACS Catalysis* **6,** 1533–1539 (2016).

12. Solla-Gullón, J., Rodríguez, P., Herrero, E., Aldaz, A. & Feliu, J. M. Surface characterization of platinum electrodes. *Phys. Chem. Chem. Phys.* **10,** 1359–1373 (2008).

13. Vidal-Iglesias, F. J., Arán-Ais, R. M., Solla-Gullón, J., Herrero, E. & Feliu, J. M. Electrochemical Characterization of Shape-Controlled Pt Nanoparticles in Different Supporting Electrolytes. *ACS Catalysis* **2,** 901–910 (2012).

14. Pobelov, I. V., Li, Z. & Wandlowski, T. Electrolyte Gating in Redox-Active Tunneling Junctions—An Electrochemical STM Approach. *Journal of the American Chemical Society* **130,** 16045–16054 (2008).

15. Yanson, Y. I. & Rost, M. J. Structural Accelerating Effect of Chloride on Copper Electrodeposition. *Angewandte Chemie International Edition* **52,** 2454–2458 (2013).

16. Kim, Y.-G., Baricuatro, J. H., Javier, A., Gregoire, J. M. & Soriaga, M. P. The Evolution of the Polycrystalline Copper Surface, First to Cu(111) and Then to Cu(100), at a Fixed CO2RR Potential: A Study by Operando EC-STM. *Langmuir* **30,** 15053–15056 (2014).

17. Kibler, L., Cuesta, A., Kleinert, M. & Kolb, D. In-situ STM characterisation of the surface morphology of platinum single crystal electrodes as a function of their preparation. *Journal of Electroanalytical Chemistry* **484,** 73–82 (2000).

18. Yanson, A., Antonov, P., Rodriguez, P. & Koper, M. Influence of the electrolyte concentration on the size and shape of platinum nanoparticles synthesized by cathodic corrosion. *Electrochimica Acta* **112,** 913–918 (2013).

19. Vanýsek, P. in *CRC Handbook of Chemistry and Physics* (ed Haynes, W. M.) 96th ed., 5–80 – 5–89 (CRC Press, Boca Raton, FL, 2015).

20. Meakin, P. *Fractals, scaling and growth far from equilibrium* (Cambridge University Press, 1998).

21. Vitos, L., Ruban, A. V., Skriver, H. L. & Kollár, J. The surface energy of metals. *Surface Science* **411,** 186–202 (1998).

22. Ikonomov, J., Starbova, K., Ibach, H. & Giesen, M. Measurement of step and kink energies and of the step-edge stiffness from island studies on Pt(111). *Physical Review B* **75,** 245411–1 – 245411–8 (2007).

23. Lozovoi, A. Y. & Alavi, A. Reconstruction of charged surfaces: General trends and a case study of Pt(110) and Au(110). *Physical Review B* **68,** 245416–1 – 245416–18 (2003).

24. Dieluweit, S. & Giesen, M. Determination of step and kink energies on Au(100) electrodes in sulfuric acid solutions by island studies with electrochemical STM. *Journal of Electroanalytical Chemistry* **524-525,** 194–200 (2002).

25. Yanson, A. I. & Yanson, Y. I. Cathodic corrosion. II. Properties of nanoparticles synthesized by cathodic corrosion. *Low Temperature Physics* **39,** 312–317 (2013).

26. Kolb, D. Reconstruction phenomena at metal-electrolyte interfaces. *Progress in Surface Science* **51,** 109–173 (1996).

27. Somorjai, G. A. & McCrea, K. Roadmap for catalysis science in the 21st century: A personal view of building the future on past and present accomplishments. *Applied Catalysis A: General* **222,** 3–18 (2001).

28. Chen, Q. & Richardson, N. V. Surface facetting induced by adsorbates. *Progress in Surface Science* **73,** 59–77 (2003).

29. Yanson, Y. I. & Yanson, A. Cathodic corrosion. I. Mechanism of corrosion via formation of metal anions in aqueous medium. *Low Temperature Physics* **39,** 304–311 (2013).

30. Somorjai, G. A. & Borodko, Y. G. Research in nanosciences - Great opportunity for catalysis science. *Catalysis Letters* **76,** 1–5 (2001).

31. Peng, Z. & Yang, H. Designer platinum nanoparticles: Control of shape, composition in alloy, nanostructure and electrocatalytic property. *Nano Today* **4,** 143–164 (2009).

32. Liao, H.-G. *et al.* Facet development during platinum nanocube growth. *Science (New York, N.Y.)* **345,** 916–919 (2014).

33. Díaz, V. & Zinola, C. F. Catalytic effects on methanol oxidation produced by cathodization of platinum electrodes. *Journal of Colloid and Interface Science* **313,** 232–247 (2007).

34. Díaz, V., Real, S., Téliz, E., Zinola, C. & Martins, M. New experimental evidence on the formation of platinum super-active sites in an electrochemical environment. *International Journal of Hydrogen Energy* **34,** 3519–3530 (2009).

35. Visintin, A., Triaca, W. & Arvia, A. Changes in the surface morphology of platinum electrodes produced by the application of periodic potential treatments in alkaline solution. *Journal of Electroanalytical Chemistry and Interfacial Electrochemistry* **284,** 465–480 (1990).

36. Teliz, E., Díaz, V., Faccio, R., Mombrú, A. W. & Zinola, C. F. The Electrochemical Development of Pt(111) Stepped Surfaces and Its Influence on Methanol Electrooxidation. *International Journal of Electrochemistry* **2011,** 1–9 (2011).

37. Gómez-Marín, A. M. & Feliu, J. M. Pt(111) surface disorder kinetics in perchloric acid solutions and the influence of specific anion adsorption. *Electrochimica Acta* **82,** 558–569 (2012).

38. Cherevko, S. *et al.* Dissolution of Noble Metals during Oxygen Evolution in Acidic Media. *ChemCatChem* **6,** 2219–2223 (2014).

3

# Anisotropic Etching of Rhodium and Gold as the Onset of Nanoparticle Formation by Cathodic Corrosion

*Cathodic corrosion alters metallic electrodes under cathodic polarization. Though these alterations can be dramatic, the exact mechanisms underlying cathodic corrosion are still unclear. This work aims to improve the understanding of cathodic corrosion by studying its onset on rhodium and gold electrodes in* $10 \, M$ *NaOH. The electrodes are studied before and after cathodic polarization, using cyclic voltammetry and scanning electron microscopy. This allows to define a corrosion onset potential of* $-1.3 \, V$ *vs. NHE for rhodium and* $-1.6 \, V$ *vs. NHE for gold. Furthermore, well-defined rectangular etch pits are observed on rhodium. Combined with rhodium cyclic voltammetry, this indicates a preference for forming (100) sites during corrosion. In contrast, a (111) preference is indicated on gold by voltammetry and the presence of well-oriented quasi-octahedral nanoparticles. We suggest this differing etching behavior to be caused by adsorption of sodium ions to surface defects, as is corroborated by density functional theory calculations.*

## 3.1   Introduction

All metals undergo oxidation under sufficiently anodic (positive) polarization, as can readily be deduced from the electrochemical series.[1] This oxidation lies at the basis of a variety of processes, such as formation of catalytically active metal oxides,[2] reorganization of the metallic surface[3] and corrosion and dissolution of material.[4] In contrast, metals are generally considered to be chemically stable under cathodic (negative) polarization; reduction of metals is not listed in the electrochemical series, Pourbaix diagrams generally consider uncharged metallic species to be most stable at low potentials,[5] and metals are commonly polarized cathodically to prevent anodic corrosion.[6]

However, cathodic potentials are able to induce remarkable changes that are similar to those observed anodically, such as the generation of catalytically active undercoordinated sites[7] and reorganization of the surface.[8,9] In fact, it is even possible to degrade metallic electrodes in a process called cathodic corrosion.[10–12] This process etches metallic electrodes and is capable of forming nanoparticles by applying cathodic potentials, possibly by generating anionic metal intermediates. Though this process has typically been studied using strongly negative potentials,[13] Chapter 2 has demonstrated that the cathodic corrosion of platinum starts at the relatively mild potential of $-0.4$ *V versus* the reversible hydrogen electrode (RHE) in 10 $M$ NaOH. Furthermore, this chapter showed a strong preference for the creation of (100) sites during corrosion. In order to gain more insight into cathodic corrosion, it is important to explore the onset potential and etching preference of other metals. However, a key factor in determining these properties for platinum was the ability to create a reproducible electrode surface by flame annealing using a standard butane-oxygen burner,[14] which is not possible for all metals. Two of these metals are rhodium and gold: rhodium is rapidly covered by its oxide during annealing,[15] whereas gold electrodes of the required size melt almost immediately after reaching their glowing temperature.

In this study, we circumvent this problem by replacing the annealing step by a chemical cleaning step in which organic contaminants are removed from the electrodes using a 3:1 mixture of sulfuric acid and hydrogen peroxide. This procedure yields a highly polycrystalline, yet clean and reproducible electrochemical response for rhodium. A reproducible gold surface can also be created if repeated cyclic voltammograms (CVs) are performed in dilute sulfuric acid after chemical cleaning. After this preparation procedure, both rhodium and gold can be studied using the protocol from Chapter 2: electrodes are characterized using cyclic voltammetry in 0.1 $M$ $H_2SO_4$, after which they are treated cathodically in 10 $M$ NaOH. Subsequent cyclic voltammetry in $H_2SO_4$ will then reveal any changes in the electrode surface, allowing to pinpoint tentative cathodic corrosion onset potentials and detecting anisotropic etching preferences for both metals. Further study using scanning electron microscopy (SEM) reveals well-defined etch pits on rhodium and crystallites on gold, which are in excellent agreement with the electrochemically observed etching anisotropy. This etching anisotropy is explored further using density functional theory (DFT), which suggests the etching preference to arise from the specific adsorption of sodium ions to surface defects.

These results demonstrate that cathodic corrosion can occur as readily as anodic

corrosion, since both rhodium and gold etch anisotropically at mild cathodic potentials. Furthermore, this study provides a protocol for investigating cathodic corrosion on other metals that cannot be flame annealed, which is a crucial step in expanding cathodic corrosion studies.

## 3.2 Materials and methods

### 3.2.1 Electrochemistry

Electrochemical experiments were performed with an Autolab PGSTAT12. All water used in this study was demineralized and ultrafiltered by a Millipore MilliQ system (resistivity $> 18.2\ M\Omega \cdot cm$, $TOC < 5\ ppb$) before use. Working electrolytes were deoxygenated by purging argon (Linde, 6.0 purity) for at least 30 minutes prior to starting experiments. Deoxygenation was maintained by flowing argon over the solution during experiments.

Short lengths of Au (Materials Research Corporation, März Purity; $\varnothing = 0.125\ mm$) and Rh (Mateck, 99.9%; $\varnothing = 0.125\ mm$) wire were used as working electrodes. Each working electrode was rinsed with water, dipped in a 3:1 mixture of $H_2SO_4$ and $H_2O_2$ to remove organic contaminations and rinsed again before transfer into a standard 3-electrode cell filled with $0.1\ M$ $H_2SO_4$ (Merck, Ultrapur). This cell contained an Au or Pt spiral counter electrode for Au and Rh experiments, respectively. A reversible hydrogen electrode (RHE) was used as reference electrode and connected to an Au or Pt wire using a $4.7\ \mu F$ capacitor in order to filter noise during voltammetry. After careful immersion of the working electrode, which was controlled using a micrometer screw, gold electrodes were treated electrochemically by running 200 cyclic voltammetry cycles between 0 and 1.75 V *vs.* RHE at a scan rate of $1\ V \cdot s^{-1}$, in order to obtain a stable cyclic voltammogram (CV).[16] Such a cycling procedure was not necessary for rhodium. Next, the working electrodes were characterized by measuring four CVs at a scan rate of $50\ mV \cdot s^{-1}$.

Following characterization, the working electrodes were transferred to a home-made fluorinated ethylene propylene cell containing $10\ M$ NaOH (Fluka, Traceselect), a Ti counter electrode and a HydroFlex RHE (Gaskatel). After immersion of the working electrodes, a constant cathodic potential was applied for $60\ s$. This cathodic potential was not IR corrected, but ohmic drop estimates will be included in the text when relevant. Following polarization, working electrodes were removed from the electrolyte under potential control, rinsed and transferred back to the $H_2SO_4$ cell. In this cell, the electrodes were recharacterized using cyclic voltammetry. Finally, the working electrodes were taken out

of the cell, rinsed and stored for later analysis using scanning electron microscopy.

### 3.2.2   Scanning Electron Microscopy

Scanning electron micrographs were measured with a FEI NOVA NanoSEM 200 microscope, using an acceleration voltage of $5\ kV$ and a beam current of $0.9\ nA$.

### 3.2.3   Density Functional Theory

Density Functional Theory (DFT) calculations were performed using VASP,[17] the PBE exchange-correlation functional[18] and the projector augmented-wave (PAW) method.[19] The (111), (100), (211) and (553) surfaces contained four metal layers: the two topmost ones and the adsorbates were free to relax in all directions, while the two bottommost layers were fixed at the optimized bulk interatomic distances. The relaxations were performed with the conjugate-gradient scheme and a cut-off of $450\ eV$ for the plane-wave basis set, until the maximum force on any relaxed atom was below $0.01\ eV \cdot Å^{-1}$. $6 \times 6 \times 1$ k-point meshes were used for the $2 \times 2$ (111) surfaces; $6 \times 8 \times 1$ k-point meshes were used for the $3 \times 2$ (100) surfaces; $6 \times 4 \times 1$ k-point meshes were used for the 2-atom-wide (211) surface; and $5 \times 3 \times 1$ k-point meshes were used for the 2-atom-wide (553) surfaces. The distance between periodically repeated slabs was larger than $14\ Å$ in all cases and dipole corrections were applied. For the calculations, $k_B T = 0.2\ eV$ was used, and the energies were extrapolated to $T = 0\ K$. Na was calculated in cubic boxes of $15\ Å \times 15\ Å \times 15\ Å$, using a gamma point distribution and an electronic temperature of $0.001\ eV$. The following reaction was used to assess the adsorption energies of Na:

$$^{*} + Na_{(g)} \rightarrow {}^{*}Na \tag{3.1}$$

where $*$ is a free adsorption site. Thus, the adsorption energies were calculated as:

$$\Delta E_{Na} = E_{^{*}Na} - E_{^{*}} - E_{Na} \tag{3.2}$$

## 3.3   Results and discussion

In an attempt to formulate coherent corrosion models for rhodium and gold, each metal will be discussed separately. First, we will discuss the electrochemical characterization of rhodium, which is followed by the corresponding scanning electron microscopy. These

observations will then be combined into a consistent corrosion model. Gold will be discussed in the same manner. Finally, we will draw parallels and highlight important differences between the corrosion characteristics of both materials, while also comparing them to the results for platinum from Chapter 2. The most notable difference, which is the different etching preference of these metals, will be explained with the aid of density functional theory calculations.

### 3.3.1 Rhodium

**Electrochemical characterization**

Rhodium electrodes were characterized using cyclic voltammetry. By measuring cyclic voltammograms in $H_2SO_4$ before and after the application of a constant cathodic potential in NaOH, we are able to detect changes in the electrode surface. Rhodium voltammograms feature two regions of particular interest. The first region lies above approximately $0.4\ V$ vs. RHE and corresponds to the formation and reduction of surface rhodium oxide.[20] Though the shape of this region depends on the presence of various surface facets, the lack of sharp peaks impairs assessment of the relative distribution of surface sites.

This distribution can be assessed more reliably using the second CV region of interest, which lies below $0.3\ V$ vs. RHE. Cathodic peaks in this region are attributed to a combination of hydrogen adsorption and (bi)sulfate desorption, whereas anodic peaks correspond to hydrogen desorption and (bi)sulfate adsorption. The location of these peaks relates directly to the distribution of surface sites. For this study, we will focus on the anodic peak, which is located respectively at $0.122\ V$, $0.157\ V$ and $0.120\ V$ vs. RHE for (111), (100) and (110) surfaces.[20]

Cyclic voltammograms of rhodium before and after cathodic polarization are displayed in Fig. 3.1. As can be seen in Panel **a**, several small changes are visible after cathodic polarization at $-0.3\ V$ vs. RHE. Firstly, a small shoulder develops on the anodic and cathodic peaks between $0.15$ and $0.19\ V$ vs. RHE. Secondly, the main cathodic and anodic peaks are slightly more well-defined after cathodic treatment. Though the exact reason for these changes is unclear, they appear consistently after polarization at and above $-0.3\ V$ vs. RHE. Finally, it is important to note that polarization at these potentials does not shift the location of the anodic peak by more than $1\ mV$ (Fig. 3.2 **b**): it lies at approximately $0.121\ V$ vs. RHE before and after treatment in NaOH. This position indicates a high abundance of (111) and (110) sites.

More prominent changes are visible after polarization at $-0.4\ V$ vs. RHE (Fig. 3.1 **b**):
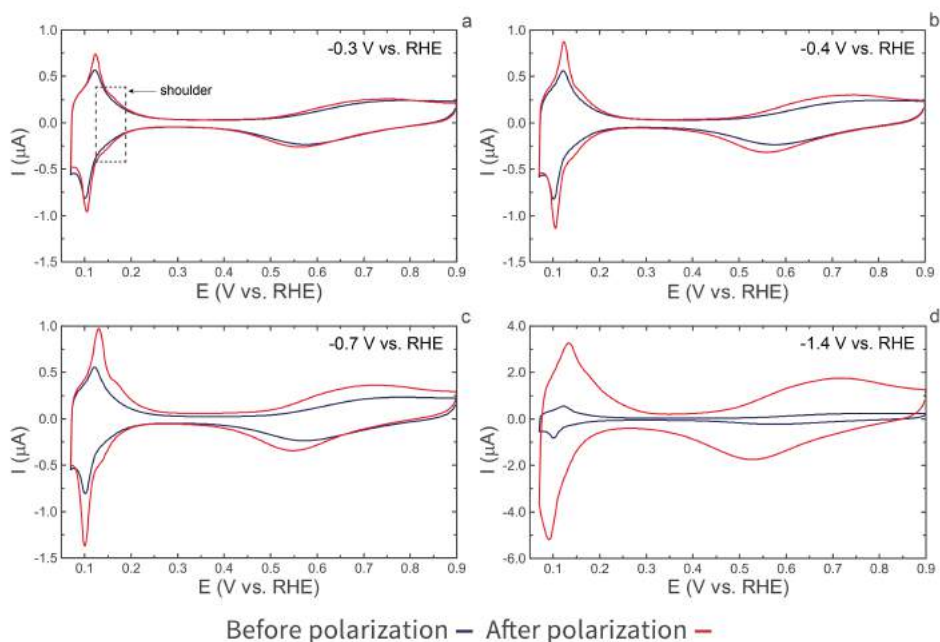
**Fig. 3.1 |** Cyclic voltammograms of rhodium electrodes before (blue trace) and after (red trace) cathodic polarization in 10 $M$ NaOH at $-0.3$ $V$ vs. RHE **(a)**, $-0.4$ $V$ vs. RHE **(b)**, $-0.7$ $V$ vs. RHE **(c)** and $-1.4$ $V$ vs. RHE **(d)**. Voltammograms were recorded in 0.1 $M$ $H_2SO_4$, at a scan rate of 50 $mV \cdot s^{-1}$.

the shoulder between 0.15 and 0.19 $V$ vs. RHE is more pronounced and the charges corresponding to all oxidative and reductive surface reactions have increased. These changes, which become more prominent if the cathodic potential is lowered to $-0.5$ and $-0.6$ $V$ vs. RHE, indicate an increase in the electrode area. This area increase is displayed as function of the polarization potential in Fig. 3.2 **a**. Furthermore, the hydrogen desorption peak shifts positively by approximately 2 $mV$. This shift increases slightly as the cathodic potential is decreased to $-0.5$ and $-0.6$ $V$ vs. RHE (Fig. 3.2 **b**), which points towards a small increase in the relative abundance of (100) sites. Thus, cyclic voltammetry suggests that, after polarization at $-0.4$ $V$ vs. RHE, the electrode is roughened by a process that favors the creation of (100) sites.

While the relative increase of (100) sites seems to develop only slightly until $-0.6$ $V$ vs. RHE, a bigger increase in the amount of these sites is visible after treatment at $-0.7$ $V$ vs. RHE (Fig. 3.1 **d**).[*] This is apparent from the position of the hydrogen desorption peak,
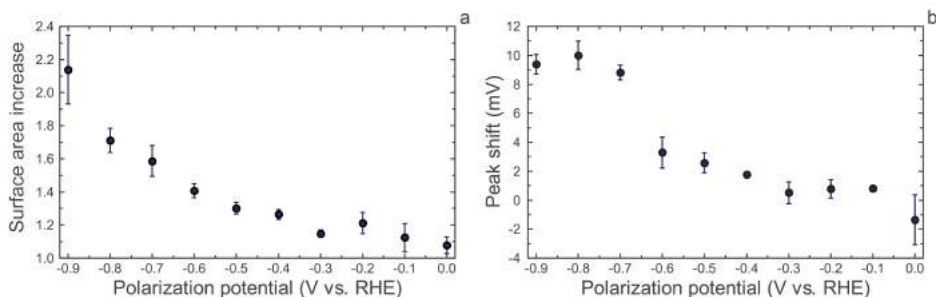
**Fig. 3.2 |** Relative rhodium surface area increase after cathodic polarization *vs.* polarization potential, as determined from the charge increase of the hydrogen desorption region **(a)**. Shift of the hydrogen desorption peak position after cathodic polarization *vs.* polarization potential **(b)**. Each data point is the average of 3 measurements and error bars represent one standard deviation. If no error bar is visible, it overlaps with its corresponding data point.

which shifts positively by roughly $9\ mV$, as is also visible in Fig. 3.2 **b**. This shift remains reasonably constant upon further lowering of the cathodic polarization potential. In contrast, the electrode area after polarization continues to increase monotonically (Fig. 3.2 **a**).

Though no other remarkable changes can be detected electrochemically, an important and surprising observation can be made visually: a black streak slowly extends from the electrode when a potential of $-0.9\ V$ *vs.* RHE[†] or lower is applied, which indicates detachment of nanoparticles from the electrode. This leads to severe roughening of the electrode, which is readily apparent from the voltammogram after treatment at $-1.4\ V$ *vs.* RHE:[‡] the increase in hydrogen desorption charge suggests that the electrode has 7.6 times more surface area, while the broadening of this peak is likely caused by the formation of nanoparticles.

---

[*] It should be noted that $-0.7\ V$ *vs.* RHE is the least negative applied potential for rhodium where ohmic drop effects start approaching the magnitude of the $0.1\ V$ potential steps: an ohmic drop of approximately $0.05\ V$ is present here.

[†] Ohmic drop causes the 'real' electrode potential to be $-0.8\ V$ *vs.* RHE.

[‡] Fully correcting for an estimated $240\ mV$ ohmic drop and rounding to the nearest $100\ mV$ leads to a 'real' electrode potential of $-1.2\ V$ *vs.* RHE.
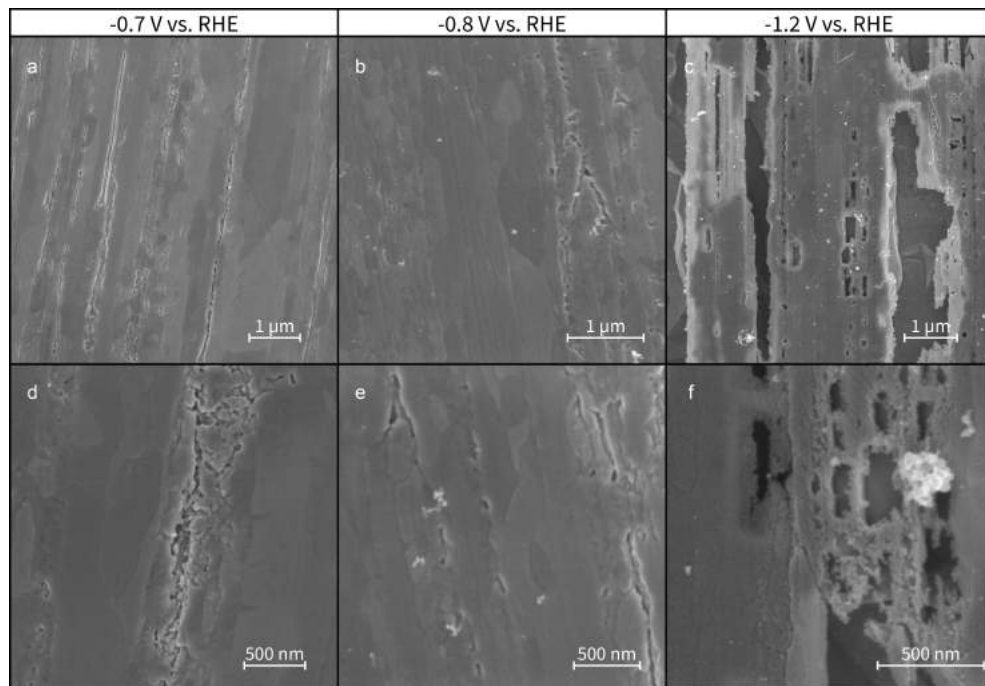
**Fig. 3.3 |** Scanning electron micrographs of rhodium electrodes treated at −0.7 *V vs.* RHE **(a, d)**, −0.8 *V vs.* RHE **(b, e)** and −1.2 *V vs.* RHE **(c, f)**.

**Scanning electron microscopy**

More information regarding the cathodic corrosion of rhodium can be gained by studying the polarized electrodes using scanning electron microscopy (SEM). Scanning electron micrographs of electrodes treated at −0.7, −0.8 and −1.2 *V vs.* RHE are presented in Fig. 3.3. These wire electrodes were mounted such that they are aligned vertically in the micrograph within a 5-degree error.

Several features stand out in micrographs of electrodes treated at or above −0.7 *V vs.* RHE (Fig. 3.3 **a, d**). Firstly, electrodes exhibit a high degree of polycrystallinity, since grain boundaries are visible at high magnifications. This polycrystallinity is also clearly visible in Fig. 3.3 as a variety of spots that appear to be darker than others, since grains with a significantly different orientation have a different contrast in SEM.[21,22] The degree of polycrystallinity is higher than that observed on platinum in Chapter 2, which is likely due to the platinum wires being flame-annealed before treatment. Such an annealing step should allow for merging of smaller grains. Secondly, electrodes typically exhibit

pits and ridges, such as those presented in Fig. 3.3 **d**. These ridges are not related to cathodic corrosion, because they are visible after polarization at all potentials above $-0.7\ V$ *vs.* RHE and on wires that were imaged without prior cathodic polarization. Thus, they are likely defects that were created during electrode preparation and not removed by an annealing step. Therefore, they do not seem to be related to cathodic corrosion, indicating that no signs of corrosion are detectable by SEM on wires that were treated at potentials of $-0.7\ V$ *vs.* RHE and higher.

In contrast, the effects of cathodic corrosion are ubiquitous on electrodes polarized at $-0.8\ V$ *vs.* RHE[§] or lower. As can be seen in Fig. 3.3 **b, e**, nanoparticle clusters of varying lengths are visible after cathodic treatment. These are the earliest sign of cathodic corrosion on rhodium. Upon decreasing the polarization potential to $-0.9\ V$ *vs.* RHE, rectangular etch pits such as those in Fig. 3.3 **c, f** start to develop. Though the borders of these pits are generally decorated with nanoparticles, their sides are offset by 90 degrees and the pit walls descend straight down. These etch pits can therefore be considered rectangles in terms of their outline and side-wall orientation, though their floor does not necessarily conform to this rectangular shape. Finally, it is interesting to note that these rectangles are always oriented such that their long sides are parallel to the wire direction.

**Model**

By combining the electrochemical and microscopic data, it is possible to formulate a preliminary model for the cathodic corrosion of rhodium. This process seems to start at approximately $-0.4\ V$ *vs.* RHE, since cyclic voltammetry indicates roughening of the electrode and the formation of (100) sites after polarization at this potential. However, more severe corrosion takes place below $-0.7\ V$ *vs.* RHE, as is indicated by a $9\ mV$ shift of the hydrogen desorption peak in voltammetry. Though any changes in the surface are too small to be detected by SEM after polarization at or above $-0.7\ V$ *vs.* RHE, nanoparticles can be seen after treatment at $-0.8\ V$ *vs.* RHE. These particles are accompanied by rectangular etch pits that are oriented along the wire if the potential is decreased to $-0.9\ V$ *vs.* RHE or lower. At this potential, dispersion of nanoparticles into the working solution is visible.

Though voltammetry before corrosion suggests that these etch pits are created in

---

[§] The electrode potential is $-0.7\ V$ *vs.* RHE after full ohmic drop correction.
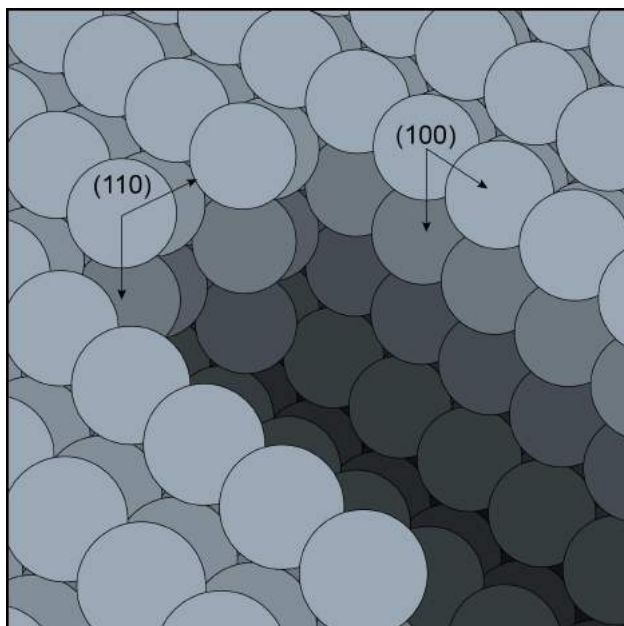
**Fig. 3.4 |** Model (110) surface with a rectangular etch pit. The bottom left and top right walls of the etch pit have a (100) orientation, whereas the top left side and bottom have a (110) configuration.

(111) or (110) surfaces, the shape of these pits rules out (111) surfaces; creating a (100)-type hole in a (111)-type surface will create triangular etch pits (Chapter 2). In contrast, creating a (100)-type hole in a (110)-type surface will form a rectangular hole with walls that are parallel to the [110] direction. These walls have a (100) surface orientation, as is visualized in the model etch pit in Fig. 3.4. Though the real cathodic corrosion etching kinetics are likely more complex than the formation of simple rectangles in an ideal (110) surface, the first-order approximation presented in Fig. 3.4 is able to explain important corrosion features by assuming the preferential formation of (100) sites in a (110)-type surface.

We will highlight two of these features. First of all, the model clarifies why the etch pits are rectangular and not square, since electrochemistry indicates that (100) sites are formed preferentially. Such preferential (100) site formation implies that the corresponding (100) pit walls should elongate at a higher rate than the (110) walls. This leads to the formation of a rectangular etch pit. Secondly, the model explains the orientation of the etch pits along the electrode direction, since it is likely that the grains in which they are formed are not oriented randomly due to the electrode production process.[23] Instead, it
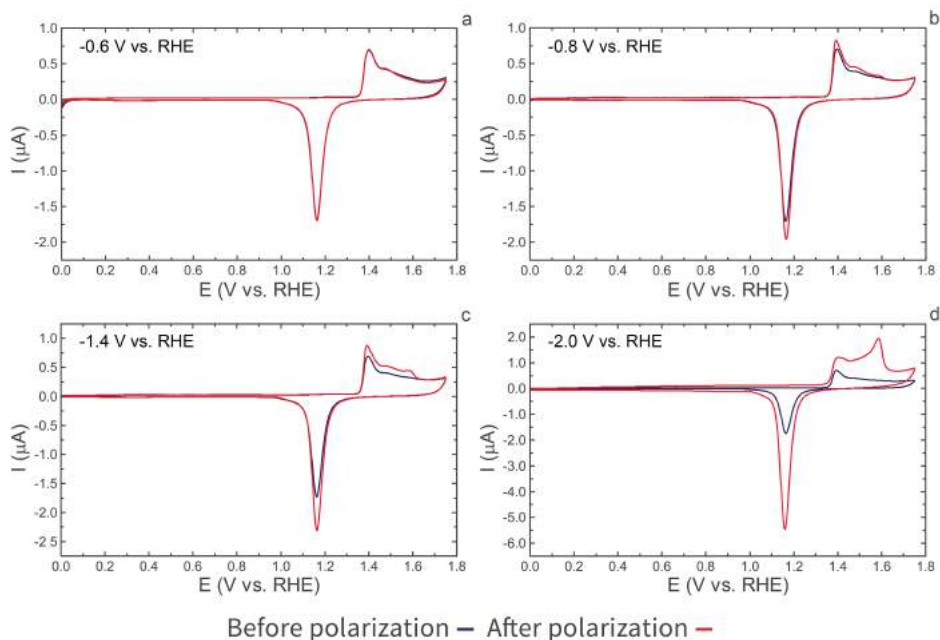
**Fig. 3.5 |** Cyclic voltammograms of gold electrodes before (blue trace) and after (red trace) cathodic polarization in 10 *M* NaOH at −0.6 *V vs.* RHE **(a)**, −0.8 *V vs.* RHE **(b)**, −1.4 *V vs.* RHE **(c)** and −2.0 *V vs.* RHE **(d)**. Voltammograms were recorded in 0.1 *M* H$_2$SO$_4$, at a scan rate of 50 *mV·s$^{-1}$*.

is reasonable to assume that the [110] crystal axes are aligned with the wire direction: the voltammetry displayed in Fig. 3.1 suggests a (110) surface preference, while the shape of grains on non-corroded electrodes in Fig. 3.3 indicates a non-random grain orientation. Based on the surface mainly consisting of (110) grains with a fiber-like orientation along the wire, the model in Fig. 3.4 would then dictate that the etch pits should be aligned such that their long (100) walls lie along the wire direction.

### 3.3.2 Gold

**Electrochemical characterization**

In contrast with rhodium, gold does not exhibit any appreciable hydrogen adsorption in its voltammogram. Instead, its oxide formation region shows sensitivity towards the orientation of the surface.[24] CVs of gold electrodes before and after polarization at various potentials are shown in Fig. 3.5.

Fig. 3.5 **a** shows the typical behavior of gold electrodes when polarized at −0.6 *V vs.*

RHE or higher. No significant changes are induced by these cathodic potentials; the peak and shoulder in the voltammogram around 1.4 and 1.5 *V vs.* RHE indicate that the electrodes exhibit features corresponding to (110) and (100) surfaces,[24] whereas a sharp feature corresponding to (111) sites around 1.59 *V vs.* RHE is absent before and after cathodic treatment. In addition, the electrode surface area remains reasonably constant after cathodic polarization.

In contrast, a minor increase in surface area is indicated by a small increase in the charges associated with oxide formation and reduction after polarization at $-0.8$ *V vs.* RHE. However, this increase in area is not as reliable for defining the corrosion onset potential as it is for rhodium, since it is relatively small and is sometimes even observed for electrodes that were polarized above $-0.6$ *V vs.* RHE. A more reliable descriptor is the development of a distinct shoulder at 1.59 *V vs.* RHE, corresponding to the formation of (111) sites. This development is subtle yet reproducible, so that closer inspection of the oxide formation region allows us to reveal the start of the formation of this (111) feature.

Such an analysis is performed in Fig. 3.6, which displays voltammograms of the oxide formation region of electrodes treated between $-0.5$ and $-0.8$ *V vs.* RHE. These voltammograms have been normalized by using the charge of the oxide reduction peak to determine the electrode surface area, assuming a specific charge of 390 $\mu A \cdot cm^{-2}$.[25] This normalization approach emphasizes relative changes in the orientation of the electrode surface. Fig. 3.6 does not show a (111) peak for electrodes treated at $-0.5$ and $-0.6$ *V vs.* RHE; both voltammograms run parallel at 1.59 *V vs.* RHE. However, a (111) shoulder develops in this region after polarization at $-0.7$ and $-0.8$ *V vs.* RHE. This indicates an increase in the relative amount of (111) sites after treatment at these potentials.

The amount of (111) sites steadily increases upon lowering the cathodic treatment potential, as is visible in Fig. 3.5 **c**.[¶] Though the current in all regions of the oxide formation region has increased, the (111) peak at 1.59 *V vs.* RHE is clearly visible. This peak continues developing as the treatment potential is lowered, which is visible in Fig. 3.5 **d**; a well-defined (111) peak is visible after corrosion and the increase in charge of the oxide reduction peak indicates a factor of 2.7 area increase.

---

[¶] For the gold experiments, the ohmic drop becomes significant at $-1.0$ *V vs.* RHE, where it shifts the potential by approximately 0.06 *V*. This causes the 'real' electrode potentials to be $-1.2$ and $-1.5$ *V vs.* RHE in Panel **c** and **d** of Fig. 3.5, respectively.
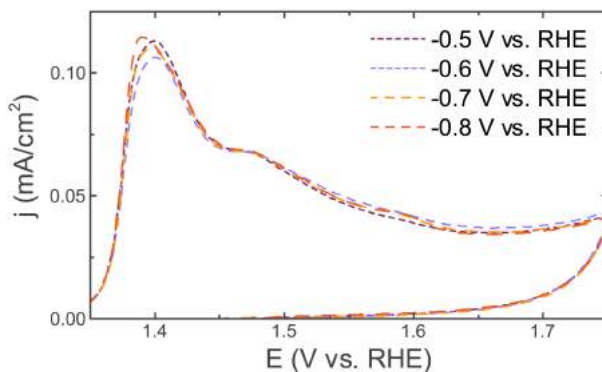
**Fig. 3.6** | Voltammograms of the gold oxide formation region after polarization at $-0.5\,V$, $-0.6\,V$, $-0.7\,V$ and $-0.8\,V$ vs. RHE. Voltammograms were recorded in 0.1 $M$ H$_2$SO$_4$, at a scan rate of $50\,mV \cdot s^{-1}$.

**Scanning electron microscopy**

Scanning electron microscopy (Fig. 3.7) allows for further analysis of the corrosion of gold. After polarization at $-0.9\,V$ vs. RHE or above (Fig. 3.7 **a, d**), the presence of many small crystal grains indicates a similar degree of polycrystallinity as rhodium. Another similarity with rhodium is the orientation of the grains, which show a fiber-like arrangement along the direction of the electrode. Finally, ridges are visible between some grain boundaries. As was the case for rhodium, the presence of these features can be attributed to the inability to flame anneal electrodes before experiments. No other remarkable features are present on the electrodes, indicating that no signs of corrosion are observable by SEM after polarization at and above $-0.9\,V$ vs. RHE.

When lowering the treatment potential to $-1.0\,V$ vs. RHE, no signs of corrosion can be seen at lower magnifications (Fig. 3.7 **b**). However, such signs are visible upon closer inspection of the crystal grains and ridges between them (Fig. 3.7 **e**). Along these ridges and on these grains, bright spots appear in the micrograph. These spots can be attributed to material budding out of the electrode. This budding becomes more pronounced as the cathodic potential is lowered. Furthermore, etch lines develop in the direction of the electrode, as is partly visible in Fig. 3.7 **c**. These lines indicate etching of gold, whereas the bright spots indicate redeposition of gold.

Along with etch lines, Fig. 3.7 **c** displays the formation of crystallites which are several hundreds of nanometers in size. These particles are first observable after polarization
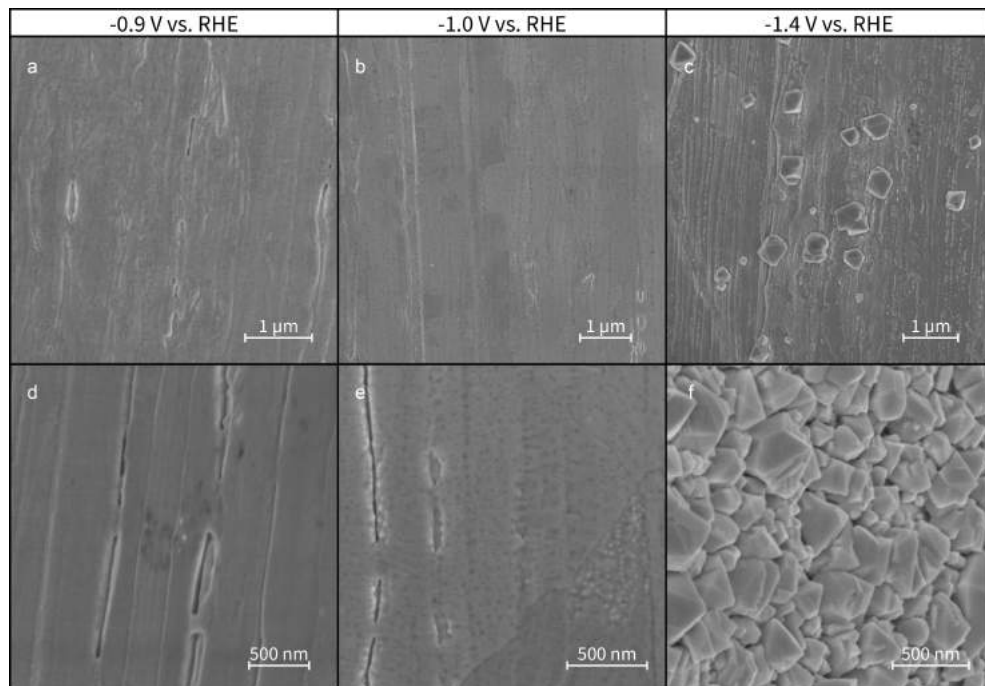
**Fig. 3.7 |** Scanning electron micrographs of gold electrodes treated at −0.9 *V* vs. RHE **(a, d)**, −1.0 *V* vs. RHE **(b, e)** and −1.4 *V* vs. RHE **(c, f)**.

at −1.3 *V* vs. RHE[‖] and predominantly contain 60° and 120° angles. The amount of observable particles increases as the cathodic potential is lowered. Their prevalence also increases towards the tip of the electrode, which is the furthest immersed point during polarization. This is readily visible when comparing Panel **c** and **f** in Fig. 3.7, since both micrographs were taken at different locations on the same electrode.

**Model**

These SEM and electrochemical observations lead to the following model of cathodic gold corrosion, which electrochemistry indicates to start at −0.7 *V* vs. RHE. This process favors the creation of (111) sites and initially leads to a minor increase in electrode surface area. Because this increase is small, no signs of corrosion are detectable by SEM until electrodes are polarized at or below −1.0 *V* vs. RHE. After polarization at these potentials, corrosion is initially visible as budding of material from the electrode surface.

---

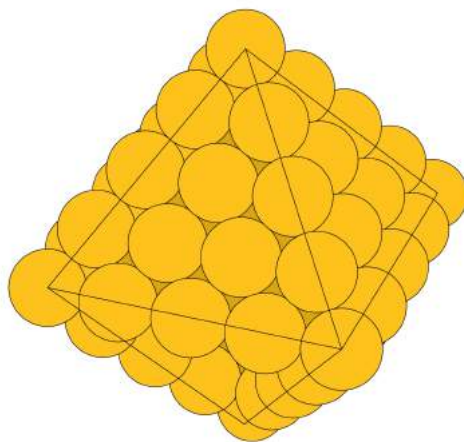[‖] −1.1 *V* vs. RHE after 100% IR correction.

**Fig. 3.8 |** Model octahedral (111) nanoparticle.

Corrosion becomes more pronounced as the potential is lowered to $-1.3$ *V vs.* RHE, after which particles are visible.

The shape of these particles strongly suggests their surface to have the (111) orientation, as can be visualized using the model in Fig. 3.8. This model displays an octahedral gold nanoparticle, which exclusively exposes (111) surface sites. Though this is an ideal, high-symmetry model particle, it allows for the rationalization of the shape of the observed particles; the angles that should arise from the formation of (111) sites are immediately visible, since the model exclusively contains 60° angles. 120° angles can also be obtained, by simply merging two model particles through a shared surface. In fact, merging model particles of various sizes or selectively extending one of the sides of a model particle allows for a relatively satisfactory description of the particles in Fig. 3.7.

### 3.3.3 Comparison

After formulating models for the corrosion of rhodium and gold, comparing corrosion on these metals yields further insights.

Firstly, it is vital to notice the similar corrosion onset potentials for both rhodium and gold. Upon conversion to the normal hydrogen electrode (NHE) scale, these corrosion onset potentials respectively are $-1.3$ and $-1.6$ *V vs.* NHE for rhodium and gold, which is similar to the $-1.3$ *V vs.* NHE found for platinum in Chapter 2. Such potentials are relatively mild, especially in alkaline media; indeed, they are not too different from the potentials applied in reactions such as $CO_2$ reduction.[26] This supports the line of rea-
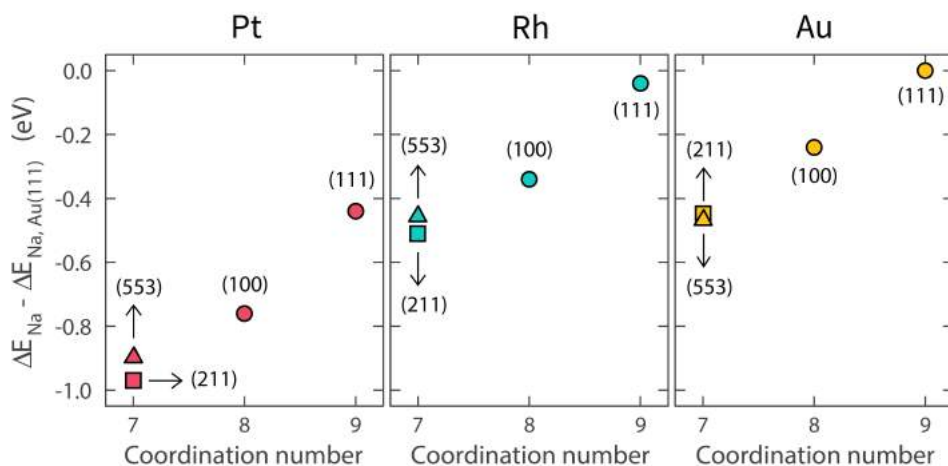
**Fig. 3.9 |** Adsorption energies of Na on various flat and stepped surfaces of Pt, Rh and Au, as a function of the coordination number of the adsorption sites. Energies are reported with respect to the adsorption of Na on Au(111).

soning that cathodic corrosion might, in fact, be just as detrimental to metal electrodes as the much better known phenomenon of anodic corrosion.

An important difference between both metals is their surface orientation preference. Gold favors the creation of (111) sites, whereas rhodium shows a preference for (100) sites. A similar (100) preference was observed for platinum in Chapter 2 and suggested to be caused by specific adsorption of sodium cations during cathodic polarization. This hypothesis is explored further in Fig. 3.9, which displays the DFT-calculated adsorption energy of sodium on the (111), (100), (211) and (553) facets of Rh, Pt and Au. The (211) and (553) surfaces both contain (111) terraces, but possess different step sites: (211) contains 3-atom-long (111) terraces and (100) steps (denoted [3(111)×(100)]), while (553) contains 5-atom-long (111) terraces and (111) steps (denoted [5(111)×(111)]). The adsorption on (211) and (533) surfaces was evaluated at these different steps. From Fig. 3.9, it is visible that sodium adsorbs strongest to platinum, followed respectively by rhodium and gold. This order is in agreement with the trends observed in scaling relations.[27,28] More importantly, Fig. 3.9 demonstrates that, for a given metal, sodium prefers to adsorb on open sites with lower coordination numbers; similar behavior has previously been observed for oxygen- and hydrogen-containing adsorbates.[29,30] Such an adsorption preference for steps indicates that adsorbate-induced anisotropies in cathodic corrosion should be caused by
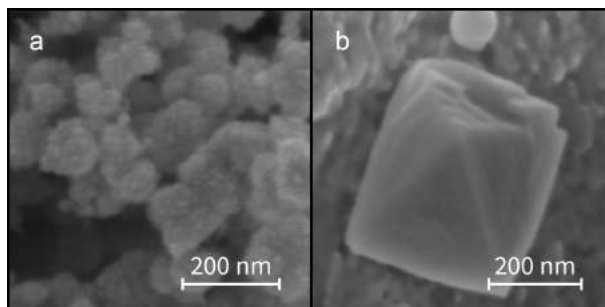
**Fig. 3.10 |** Scanning electrode micrographs of nanoparticles on a rhodium electrode treated at −1.3 *V* *vs.* RHE **(a)** and a gold electrode treated at −1.4 *V* *vs.* RHE **(b)**.

preferential sodium adsorption on steps or defect sites. Importantly, sodium adsorption is more favorable on (100)-type sites on rhodium and platinum, while it shows a small preference for (111)-type sites on gold. Thus, the DFT-calculated sodium adsorption energies are able to explain why platinum and rhodium preferentially expose (100) facets, while gold favors (111) facets: these sites are selectively stabilized by sodium adsorption. The minuteness of this stabilization on gold also indicates why the anisotropy at the onset of corrosion is less pronounced than for the other metals.

A second distinction between rhodium and gold is the size of their etch features and formed nanoparticles: a comparison of Fig. 3.3 & 3.7 demonstrates that rhodium displays much larger anisotropic etch features than gold, whereas the comparison of rhodium and gold nanoparticles in Fig. 3.10 demonstrates that gold forms larger anisotropic nanoparticles. This can tentatively be explained by the different mobility of surface atoms of the two metals. Since gold has a lower melting point and sublimation energy,[31] it is presumably more mobile than rhodium. This would allow gold to reconstruct more easily in order to minimize its surface energy, thereby counteracting the formation of etching features. In contrast, etching features in rhodium are lifted less easily by long-range reordering, causing the formation of large anisotropic etch pits. Similarly, the lower mobility of rhodium would lead to the formation of smaller nanoparticles with a high surface area such as those in Fig. 3.10 **a**, whereas gold particles can merge and reconstruct more easily to form larger particles with less exposed surface (Fig. 3.10 **b**). Thus, this difference in mobility does not only explain the differences observed in SEM, but also the electrochemically observed higher surface area increase for rhodium, as compared to gold.

## 3.4   Conclusions

In this work, we have studied the onset of cathodic corrosion on rhodium and gold. In doing so, we found tentative corrosion onset potentials of $-1.3$ *V vs.* NHE for rhodium and $-1.6$ *V vs.* NHE for gold in $10$ *M* NaOH. The mildness of these potentials suggests that cathodic corrosion can be at least as effective as anodic corrosion in inducing surface changes in metal electrodes.

Additionally, we were able to observe different crystallographic corrosion preferences for both metals: rhodium favors the formation of (100) sites, whereas gold preferentially forms (111) sites. This anisotropy is expressed in the formation of well-oriented rectangular etch pits on rhodium and quasi-octahedral nanoparticles on gold. The difference in anisotropy is attributed to the different adsorption of electrolyte cations on both metals, whereas the qualitative size differences in corrosion features are likely related to their different surface atom mobility.

Not only are these conclusions essential towards understanding cathodic corrosion, but the experimental procedure leading to these conclusions also provides a useful framework for studying cathodic corrosion on metals that cannot be flame-annealed.

## 3.5   Acknowledgements

## References

1.  Vanýsek, P. in *CRC Handbook of Chemistry and Physics* (ed Haynes, W. M.) 96th ed., 5–80 – 5–89 (CRC Press, Boca Raton, FL, 2015).

2.  Su, H.-Y. *et al.* Identifying active surface phases for metal oxide electrocatalysts: a study of manganese oxide bifunctional catalysts for oxygen reduction and water oxidation catalysis. *Physical Chemistry Chemical Physics* **14,** 14010 (2012).

3.  Gómez-Marín, A. M. & Feliu, J. M. Pt(111) surface disorder kinetics in perchloric acid solutions and the influence of specific anion adsorption. *Electrochimica Acta* **82,** 558–569 (2012).

4.  Cherevko, S. *et al.* Dissolution of Noble Metals during Oxygen Evolution in Acidic Media. *ChemCatChem* **6,** 2219–2223 (2014).

5.  Pourbaix, M. *Atlas of electrochemical equilibria in aqueous solutions* 2nd ed., 644 (National Association of Corrosion Engineers, 1974).

6.  V. Baeckmann, W., Schwenk, W. & Prinz, W. *Handbook of Cathodic Corrosion Protection* 3rd, 568 (Elsevier, 1997).

7.  Declan Burke, L. & O'Mullane, A. P. Generation of active surface states of gold and the role of such states in electrocatalysis. *Journal of Solid State Electrochemistry* **4,** 285–297 (2000).

8. Kolb, D. Reconstruction phenomena at metal-electrolyte interfaces. *Progress in Surface Science* **51,** 109–173 (1996).

9. Kim, Y.-G., Baricuatro, J. H., Javier, A., Gregoire, J. M. & Soriaga, M. P. The Evolution of the Polycrystalline Copper Surface, First to Cu(111) and Then to Cu(100), at a Fixed CO2RR Potential: A Study by Operando EC-STM. *Langmuir* **30,** 15053–15056 (2014).

10. Haber, F. The Phenomenon of the Formation of Metallic Dust from Cathodes. *Transactions of the American Electrochemical Society* **2,** 189–196 (1902).

11. Kabanov, B. N., Astakhov, I. I. & Kiseleva, I. G. Formation of crystalline intermetallic compounds and solid solutions in electrochemical incorporation of metals into cathodes. *Electrochimica Acta* **24,** 167–171 (1979).

12. Yanson, A. I. *et al.* Cathodic Corrosion: A Quick, Clean, and Versatile Method for the Synthesis of Metallic Nanoparticles. *Angewandte Chemie International Edition* **50,** 6346–6350 (2011).

13. Yanson, Y. I. & Yanson, A. Cathodic corrosion. I. Mechanism of corrosion via formation of metal anions in aqueous medium. *Low Temperature Physics* **39,** 304–311 (2013).

14. Clavilier, J. & Chauvineau, J. P. Chemical characterization by Auger electron spectroscopy and voltammetry of platinum electrode surfaces prepared in the gas phase. *Journal of Electroanalytical Chemistry and Interfacial Electrochemistry* **100,** 461–472 (1979).

15. Carol, L. A. & Mann, G. S. High-temperature oxidation of rhodium. *Oxidation of Metals* **34,** 1–12 (1990).

16. Jeyabharathi, C., Ahrens, P., Hasse, U. & Scholz, F. Identification of low-index crystal planes of polycrystalline gold on the basis of electrochemical oxide layer formation. *Journal of Solid State Electrochemistry* **20,** 3025–3031 (2016).

17. Kresse, G. & Furthmüller, J. Efficient iterative schemes for ab initio total-energy calculations using a plane-wave basis set. *Physical Review B* **54,** 11169–11186 (1996).

18. Perdew, J. P., Burke, K. & Ernzerhof, M. Generalized Gradient Approximation Made Simple. *Physical Review Letters* **77,** 3865–3868 (1996).

19. Kresse, G. & Joubert, D. From ultrasoft pseudopotentials to the projector augmented-wave method. *Physical Review B* **59,** 1758–1775 (1999).

20. Xu, Q., Linke, U., Bujak, R. & Wandlowski, T. Preparation and electrochemical characterization of low-index rhodium single crystal electrodes in sulfuric acid. *Electrochimica Acta* **54,** 5509–5521 (2009).

21. Zauter, R. *et al.* Electron channelling contrast as a supplementary method for microstructural investigations in deformed metals. *Philosophical Magazine A* **66,** 425–436 (1992).

22. Canovic, S., Jonsson, T. & Halvarsson, M. Grain contrast imaging in FIB and SEM. *Journal of Physics: Conference Series* **126,** 012054 (2008).

23. Dillamore, I. L. & Roberts, W. T. Preferred Orientation in Wrought in Annealed Metals. *Metallurgical Reviews* **10,** 271–380 (1965).

24. Hamelin, A. Cyclic voltammetry at gold single-crystal surfaces. Part 1. Behaviour at low-index faces. *Journal of Electroanalytical Chemistry* **407,** 1–11 (1996).

25. Trasatti, S. & Petrii, O. Real surface area measurements in electrochemistry. *Pure and applied chemistry* **63,** 711–734 (1991).

26. Hori, Y. in *Modern Aspects of Electrochemistry* (eds Vayenas, C. G., White, R. E. & Gamboa-Aldeco, M. E.) 42nd ed., 89–189 (Springer New York, 2008).

27. Calle-Vallejo, F., Martínez, J. I., García-Lastra, J. M., Rossmeisl, J. & Koper, M. T. M. Physical and Chemical Nature of the Scaling Relations between Adsorption Energies of Atoms on Metal Surfaces. *Physical Review Letters* **108,** 116103 (2012).

28. Calle-Vallejo, F., Loffreda, D., Koper, M. T. M. & Sautet, P. Introducing structural sensitivity into adsorption–energy scaling relations by means of coordination numbers. *Nature Chemistry* **7,** 403–410 (2015).

29. Calle-Vallejo, F. *et al.* Finding optimal surface sites on heterogeneous catalysts by counting nearest neighbors. *Science* **350,** 185–189 (2015).

30. Tymoczko, J., Calle-Vallejo, F., Schuhmann, W. & Bandarenka, A. S. Making the hydrogen evolution reaction in polymer electrolyte membrane electrolysers even faster. *Nature Communications* **7,** 10990 (2016).

31. Haynes, W. M. *CRC Handbook of Chemistry and Physics* 96th ed. (ed Haynes, W. M.) 2677 (CRC Press, Boca Raton, FL, 2015).
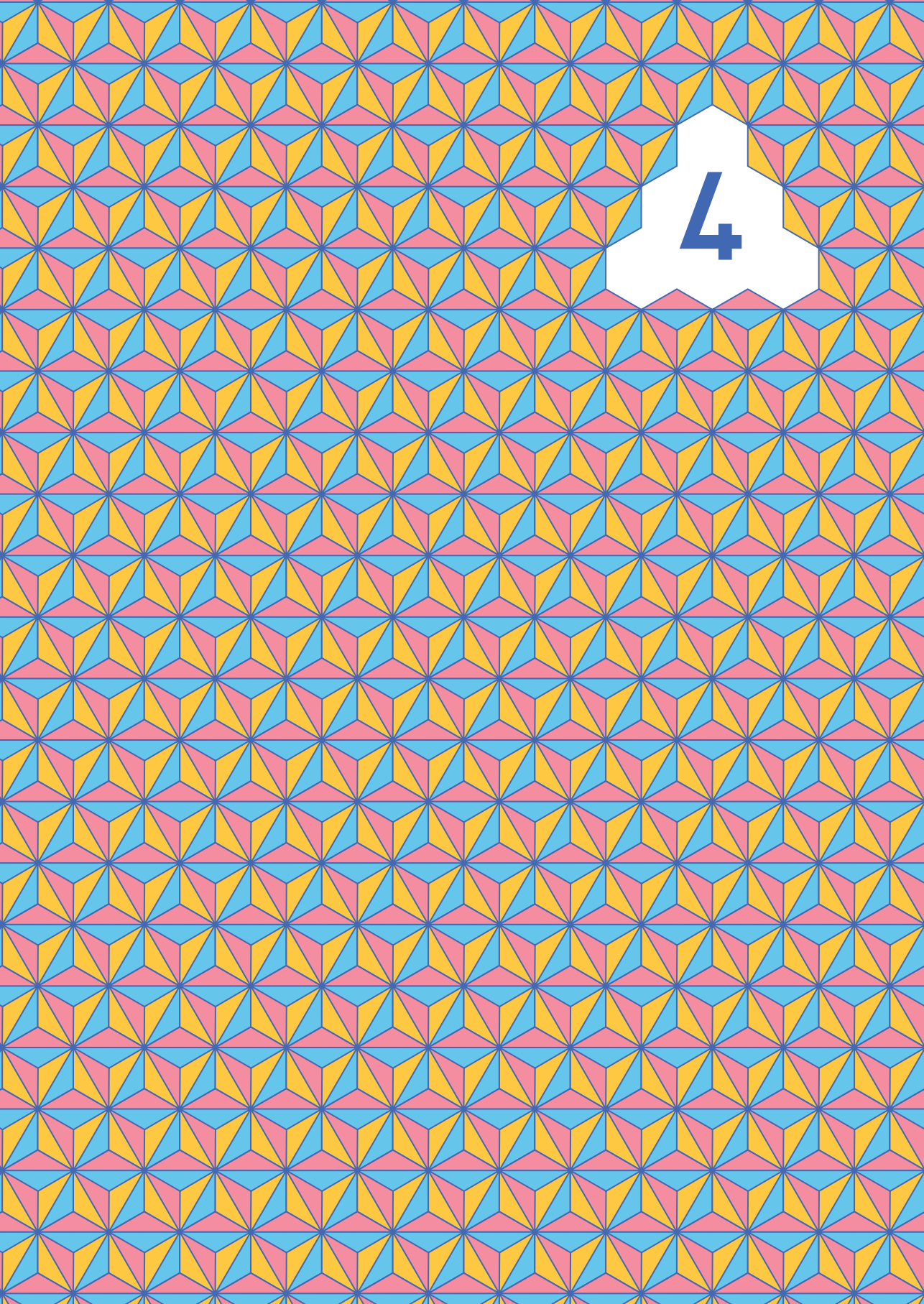
4

# Alkali Metal Cation Effects in Structuring Pt, Rh and Au Surfaces through Cathodic Corrosion

*Cathodic corrosion is an electrochemical etching process which alters metallic surfaces by creating nanoparticles and a variety of etching features. Because these features typically have a preferential orientation, cathodic corrosion can be applied to modify and nano-structure electrode surfaces. However, this application of cathodic corrosion is currently limited by an insufficient chemical understanding of its underlying mechanism. This includes the role of alkali metal cations, which are thought to be crucial in both enabling cathodic corrosion and controlling its final facet preference. This work addresses this knowledge gap by exploring the cathodic corrosion of Pt, Rh and Au in LiOH, NaOH and KOH through both experimental and theoretical methods. These methods demonstrate that cations are adsorbed during cathodic corrosion and play a major role in controlling the onset potential and final surface morphology in cathodic corrosion. Interestingly, an equally significant role appears to be played by adsorbed hydrogen, based on calculations using literature density functional theory data. Considering the significance of both hydrogen and electrolyte cations, it is hypothesized that cathodic corrosion might proceed via an intermediate ternary metal hydride. This fundamental insight leads to both metal-specific recommendations and more general guidelines for applying cathodic corrosion to structure metallic surfaces.*

## 4.1 Introduction

Cathodic corrosion is an enigmatic etching process that decomposes metallic cathodes at potentials where they are typically assumed to be cathodically protected. This decomposition leads to striking changes in the electrode surface, including the formation

of nanoparticles and geometric etch pits. Though these remarkable changes were already observed in the early 20th century[1] and briefly studied in the 1970s,[2] most fundamental studies of cathodic corrosion have been conducted relatively recently.[3–5] From these studies, it has been hypothesized that cathodic corrosion proceeds by forming an unknown metastable metal-containing anion,[6] instead of being caused by physical processes like contact glow discharge.[7] However, the exact nature of this (anionic) cathodic corrosion intermediate remains unclear. This limits fundamentally guided approaches towards applying cathodic corrosion to alter metallic surfaces and produce shape-controlled nanoparticles that exhibit favorable catalytic properties.[8] Such approaches would require more knowledge on the underlying mechanism and the different species involved in cathodic corrosion.

Perhaps the most crucial species in enabling cathodic corrosion is the electrolyte cation: without the presence of cations like Na$^+$, cathodic corrosion does not take place.[6] This key role of cations was underscored by several follow-up studies on nanoparticle production through cathodic corrosion, which reported effects of both the concentration and identity of the electrolyte cation on the corrosion rate,[9] particle size[9–11] and particle shape.[9,12,13] In terms of particle shape, these experiments found the (100)-to-(110) facet ratio to increase with increasing cation concentration,[9,12,13] and being higher for particles produced in 10 $M$ NaOH compared to 10 $M$ KOH.[12] These observations were tentatively ascribed to selective stabilization of (100) surface facets by Na$^+$ adsorption;[13] Na$^+$ would mimic the structure-influencing effect that other adsorbates exhibit in traditional nanoparticle synthesis methods.[14] In spite of the pronounced effect of Na$^+$, these observations were made for alternating current (AC) corrosion experiments, which accelerate the effects of cathodic corrosion by introducing periodic anodic corrosion steps. Though this approach is ideal for nanoparticle production, the convoluted presence of anodic and cathodic corrosion processes hinders explicit conclusions on the role of Na$^+$.

This ambiguity was alleviated by two subsequent studies on electrodes that were corroded under constant polarization (Chapter 2 & 3). These studies found that cathodic corrosion in 10 $M$ NaOH preferentially forms (100) sites on Pt and Rh and (111) sites on Au. By exploring this difference between Au on the one hand and Pt and Rh on the other hand with density functional theory (DFT) calculations (Chapter 3), sodium was shown to adsorb most favorably on the type of step that matches the type of site formed: (100) for Pt & Rh, and (111) for Au. These results therefore align with the results for AC corrosion by suggesting a crucial role of the electrolyte cation in determining the facet preference

for cathodic corrosion. However, a systematic study of the extent of this cation effect on various metals has previously not been conducted. Such a study would not only provide fundamental insights on cathodic corrosion, but would also provide concrete guidelines for using cathodic corrosion as a tool to structurally alter metallic electrodes.

Therefore, this chapter provides such a study by mapping the corrosion behavior of Pt, Rh and Au in various concentrations of LiOH, NaOH and KOH. The experiments indicate a key role of the electrolyte cations in controlling the corrosion onset potential, as well as the final surface area and facet distribution of the corroded electrodes. Though these results do not allow us to determine a single reaction mechanism with certainty, the calculations do provide strong indications for the presence of adsorbed cations during cathodic corrosion. Additional calculations based on literature DFT data indicate an additional role of adsorbed hydrogen in determining the onset potential of cathodic corrosion. Given the suggested role of both adsorbed hydrogen and adsorbed cations, we will argue that the elusive cathodic corrosion reaction intermediate might be a ternary metal hydride.

These results are relevant from both fundamental and applied perspectives. On the one hand, the suggested existence of ternary metal hydrides provides a concrete starting point for future fundamental studies and is therefore an important clue towards understanding the chemical nature of cathodic corrosion. On the other hand, the exploration of cathodic corrosion as a function of the corroded metal and the identity and concentration of electrolyte cations provides valuable guidelines for applying cathodic corrosion to systematically modify electrode surfaces and create shape-controlled nanoparticles.

## 4.2 Materials and methods

### 4.2.1 Experimental methods

All water used in this study was demineralized and filtered by a MilliQ water system to reach a final total organic carbon (TOC) content below $5\ ppb$ and a resistivity above $18.2\ M\Omega \cdot cm$. To further ensure cleanliness, both organic and inorganic contaminations were removed from the glassware before each experiment. Organic contaminations were decomposed by storing glassware overnight in an aqueous solution of $1\ g \cdot L^{-1}$ KMnO$_4$ (Fluka, ACS reagent) and $0.5\ M$ H$_2$SO$_4$ (Fluka, ACS reagent). After storage, the solution was drained from the glassware and any remaining KMnO$_4$ was removed with dilute H$_2$O$_2$ (Merck, Emprove exp). Finally, the glassware was boiled 5 times in water before

being filled with electrolyte solution. All electrolytes were purged from oxygen before experiments by bubbling argon (Linde, 6.0 purity) through the solution for 30 minutes. Deoxygenation was maintained during experiments by flowing Ar over the solution. Electrochemical experiments were performed using a Bio-Logic SP-300 potentiostat.

In this study, two types of electrochemical cells were used: a glass cell for electrode characterization in acidic solution and a fluorinated ethylene propylene (FEP) cell for cathodic corrosion in alkaline solution. The glass cell contained an internal reversible hydrogen electrode (RHE) as reference electrode. The counter electrode was either a Pt spiral for Pt and Rh characterization or an Au spiral for Au characterization. In addition, a Pt or Au wire was connected to the reference electrode with a $4.7\ \mu F$ capacitor to filter high-frequency noise during voltammetry.[15] Working electrolytes consisted of $H_2SO_4$ (Merck, Ultrapur) in concentrations of $0.5\ mol \cdot L^{-1}$ for Pt or $0.1\ mol \cdot L^{-1}$ for Rh and Au characterization. The FEP cell contained a commercial HydroFlex RHE electrode (Gaskatel), a Ti spiral counter electrode (Mateck, 99.99%) and aqueous electrolytes of either dissolved $LiOH \cdot H_2O$ (Alfa Aesar, 99.995%), NaOH (Merck, Suprapur) or $KOH \cdot H_2O$ (Fluka, TraceSelect).

The Ti counter electrode provides the important benefit of not being any of the studied working electrode materials. As such, the results presented in this work cannot be attributed to redeposition of dissolved Pt, Rh or Au from the anodically polarized counter electrode. However, the use of a Ti counter electrode caused a noteworthy complication for cathodic corrosion, which we found to be very sensitive to the presence of unintended contaminations: for unknown reasons, the Ti counter electrode would occasionally shift the onset potential of cathodic corrosion of platinum to less negative potentials by as much as $0.3\ V$ from the value reported in Chapter 2. This issue could generally be solved by performing ten minutes of pre-electrolysis at $-1\ V$ *vs.* RHE with a Pt electrode (Mateck, 99.99%; $\varnothing = 0.1\ mm$), which was removed under potential control and discarded. Though this protocol adequately resolved the issue of early and significant cathodic corrosion, results of Pt corrosion were reproduced with a Pt counter electrode where necessary to confirm the validity of the presented onset potentials and the proper functioning of the working setup.

After preparing the working setup, Pt electrodes were prepared by cutting a short length of wire (Mateck, 99.99%; $\varnothing = 0.1\ mm$) from a spool with clean wire cutters and flame annealing the electrode. Rh (Mateck, 99.9%; $\varnothing = 0.125\ mm$) and Au (Materials Research Corporation, März Purity; $\varnothing = 0.125\ mm$) wires could not be annealed before

experiments and were cleaned chemically by immersion in a 1:3 volumetric mixture of 35% $H_2O_2$ (Merck, Emprove exp) and 95–97% $H_2SO_4$ (Fluka, ACS reagent) for 30 seconds instead, as was done in Chapter 3. Au wires were then also polished electrochemically by running 200 cyclic voltammograms (CVs) between 0 and 1.75 $V$ vs. RHE at a scan rate of $1\ V \cdot s^{-1}$ in the characterization cell.[16]

After preparation, each electrode was immersed in the characterization cell at a depth that was carefully controlled by using a micrometer screw. In the characterization cell, the electrode surface was characterized by running 4 cyclic voltammograms. Following characterization, the electrode was rinsed and moved into the FEP cell. Here, an 85% ohmic drop-corrected constant cathodic voltage was applied for 60 seconds, after which the electrode was removed under potential control. After an additional rinse, the electrode was moved back into the characterization cell, immersed at the same depth as during the initial characterization and re-characterized by running 4 CVs. Finally, the electrode was stored for later characterization using scanning electron microscopy.

Scanning electron microscopy was carried out on a FEI NOVA NanoSEM 200 microscope, using an acceleration voltage of 5 $kV$ and an electron beam current of 0.9 $nA$. All samples were mounted to be aligned vertically in the presented micrographs, to within an error of several degrees.

### 4.2.2   Theoretical methods

We used density functional theory to examine the specific adsorption of alkali metal cations (Li, Na, and K) onto the (111), (100), (211), and (553) surfaces of Rh, Pt, and Au in the presence of near-surface solvation. The Vienna Ab Initio Simulation Package (VASP) was used to perform the electronic structure calculations,[17–19] with a plane-wave basis set and the Perdew-Burke-Ernzerhof (PBE) exchange-correlation functional.[20,21] Ion-core potentials were modeled using the projector augmented wave (PAW) approach.[22,23] The basis set cutoff energy was 450 $eV$. Structural optimization was performed until the forces on the atoms were below 0.02 $eV \cdot Å^{-1}$. Adsorption was modeled at only one coverage. The (111) surface was modeled with a $3 \times 3$ unit cell (with 3 alkali metal cation adsorbates giving a 1/3 monolayer (ML) coverage), the (100) surface with a $2 \times 2$ unit cell (with 1 alkali metal cation adsorbate, 1/4 ML coverage), and the (211) and (553) surfaces in a $2 \times 1$ unit cell (containing a two-atom-wide step edge, with one alkali metal cation adsorbate). K-space sampling was performed with a $5 \times 5 \times 1$ Monkhorst-Pack mesh grid for the (111) surfaces of Rh and Pt and a $7 \times 7 \times 1$ grid for all of the other surfaces

of Rh and Pt.[24] The Au surfaces were sampled with a denser grid, $7 \times 7 \times 1$ for Au(111), $11 \times 11 \times 1$ for Au(100), $15 \times 11 \times 1$ for Au(553), and $11 \times 15 \times 1$ for Au(211). Adsorption energies on each surface were converged to within $0.03 \ eV$ with respect to the k-space sampling. Each of the surfaces was modeled with a four-layer slab, with the bottom two layers frozen at the DFT-calculated lattice constant. Dipole corrections were included in the surface normal direction.[25]

Cation adsorption potentials were calculated following methods described previously, including the effect of near-surface water solvation.[26,27] For the (111) surface, six explicit water molecules were included in a bilayer structure; for the (100), (211), and (553) surfaces, four explicit water molecules were added in a hydrogen-bonded monolayer adsorbed on the surface (or step edge, in the case of the stepped surfaces). Only one water structure was considered on each surface, which was relaxed in the absence and presence of the alkali metal cation. The initial water structures have been found previously (on Pt) to be low or minimum energy structures: on the (111) surfaces, a hexagonal bilayer water structure was used;[28,29] on the (100) surfaces, a square-like arrangement of water molecules was used;[30] and on the stepped surfaces, a double-stranded structure was used.[31] Images of these structures, in the absence and presence of an alkali metal cation, are given in Fig. A.1–A.3. Images of the adsorbate structures were rendered using VESTA.[32]

This method approximates effects of solvation, since we can only identify water structures near the surface and the adsorbed cation that are at a local (but not necessarily global) minimum in energy, and we neglect translational and rotational entropy of the near-surface water (considering only vibrational energy and entropy). Our intent is therefore to only approximate the effects of near-surface solvation on the alkali metal cation adsorption energy. In our prior work, we found this energy to reach a plateau after solvating the adsorbed cation with four to six water molecules:[26] approximately the number of water molecules in the solvation shell of bulk, solution-phase alkali atoms, as found previously using *ab-initio* molecular dynamics.[33] We found previously that the addition of more water molecules causes the absolute alkali metal adsorption energy to fluctuate by $\pm0.5 \ eV$ per water molecule. We therefore expect our absolute adsorption energy accuracy to not be better than $\pm0.5 \ eV$. The error in the relative adsorption energy trend between cations is smaller.

Adsorption energies were also calculated in the absence of near-surface solvation and relative to gas phase, neutral alkali metal atoms, following the method described in

Chapter 3. These calculations neglect the stabilizing effect of solvent on both the reactant and adsorbed product states. This alters both the absolute adsorption energetics and the trend between the cations, because the degree of lost solvation upon adsorption is cation-dependent. These adsorption energies are given in the Fig. A.30–A.31, and allow for separate examination of the contribution of the solvation effects on adsorption. Fig. A.30–A.31 can be compared with the adsorption energetics in this chapter, which are all calculated using an aqueous solution-phase ion as the initial state.

Cation effects have been explained as being caused by the behavior of cations in the double-layer or outer Helmholtz plane, near the electrode surface.[34] However, we here examine the conditions under which some of these cations approach the electrode surface more closely and lose part of their solvation shell. This allows them to be considered "specifically adsorbed". Our current and previous calculations therefore support that such adsorption is favorable at low potentials and high pH,[26,35] where alkali cation adsorption becomes increasingly favorable compared to hydrogen adsorption.

We have also examined the stability of the (111) and (100) surfaces of Rh, Pt, and Au in the presence of high coverages of adsorbed hydrogen, using bare surface energies calculated using DFT by Tran *et al.*,[36] as well as hydrogen adsorption energies calculated using DFT at low coverage ($0.25\ ML$) by Ferrin *et al.*[37] To estimate the adsorption energy of hydrogen at high coverages, we assumed a simple mean-field model using a constant, repulsive, coverage dependence of the hydrogen adsorption energy of $0.12\ eV \cdot ML^{-1}$ on the (111) surfaces of Rh, Pt, and Au. This repulsive interaction has been explicitly calculated on Pt(111);[27,38] the same coverage dependence was assumed on Rh(111) and Au(111). It should be noted that Skúlason *et al.* show a slightly greater repulsion on Au(111) and weaker repulsion on Rh(111) than on Pt(111).[39] Consideration of these differences would yield a small change in the calculated surface energetics at low potentials (high hydrogen coverages). However, this change would only emphasize the trend in which (111) surface is the most stable (Rh > Pt > Au). As such, including these small differences in binding energy will not affect our conclusions. We also assume that adsorption between low and high coverage ($1\ ML$) on the (100) surfaces is independent of coverage on Rh(100), Pt(100), and Au(100), as has been found for Pt(100).[27,38]

Potential-dependent surface energies (with $1\ ML$ hydrogen adsorbed on the surface) were calculated as described previously, by adding the potential-dependent adsorption energy of hydrogen (normalized by surface area) to the surface energy of the

bare surface.[40] This procedure is outlined in Equations 4.1 and 4.2:

$$\gamma(U_{RHE}, \theta_{*H}) = \gamma_{bare} + \frac{\Delta G_{H_{ads}}(U_{RHE}, \theta_{*H})}{A} \tag{4.1}$$

$$\Delta G_{H_{ads}}(U_{RHE}, \theta_{*H}) = BE(\theta_{*H} = 0.25ML) + 0.5\Delta H_{H_2}^{form} + \\ \Delta ZPVE_{H_{ads}} - T\Delta S_{H_{ads}} + n|e|U_{RHE} + \omega\theta_{*H} \tag{4.2}$$

Here, $\gamma(U_{RHE}, \theta_{*H})$ is the surface energy of the hydrogen-covered surface as a function of potential (on a reversible hydrogen electrode scale, RHE) and hydrogen coverage ($\theta_{*H}$); $\gamma_{bare}$ is the surface energy of the bare surface;[36] $A$ is the area of the surface; $\Delta G_{H_{ads}}(U_{RHE}, \theta_{*H})$ is the free energy of hydrogen adsorption; $BE$ is the binding energy of hydrogen on the surface at low coverage (0.25 $ML$);[37] $\Delta H_{H_2}^{form}$ is the formation enthalpy of hydrogen gas at standard state ($-4.57$ $eV$);[37] $\Delta ZPVE_{H_{ads}}$ is the change in zero point vibrational energy of the hydrogen upon adsorption ($-0.008$ $eV$);[38] $T\Delta S_{H_{ads}}$ is the change in entropy of the hydrogen upon adsorption ($-0.00067$ $eV \cdot K^{-1}$);[38] $n$ is the number of hydrogen atoms adsorbed in the unit cell at the coverage of interest; $|e|U_{RHE}$ is the energy of an electron on the reversible hydrogen electrode scale; and $\omega$ is the *H-*H interaction term describing the interaction between adsorbed hydrogen on the surface (0.12 $eV \cdot ML^{-1}$ for *H on Pt(111), $\sim 0$ $eV \cdot ML^{-1}$ for *H on Pt(100)).[27,38] This difference in interaction energy is consistent with experimental estimates that indicate weaker (but non-zero) H-H interactions for Pt(100) than for Pt(111).[41,42] We assumed complete electron transfer between the adsorbing proton and the surface, so that all of the potential dependence arises from the electron being transferred as a reactant on proton adsorption. Additionally, we neglected the effects of near-surface solvation and electric field on hydrogen adsorption, since these effects have been shown previously to be small.[38]

As we have found hydrogen adsorption above 1 $ML$ (up to 1.25 $ML$) on Pt(100) to be favorable at low but positive potentials (near 0.1 $V$ vs. RHE),[40] we have extrapolated and included these data as well. Besides, we calculated the adsorption energy of hydrogen at 1.25 $ML$ on Rh(100) using the same methods defined previously for *H adsorption on Pt(100).[40] For this calculation, we used the PBE exchange-correlation functional, as was used to examine alkali metal cation adsorption. We find that the additional 0.25 $ML$ hydrogen prefers to adsorb in a bridge site (as do the hydrogen atoms between 0 and 1 $ML$) on Rh(100). As hydrogen adsorption is significantly weaker on Au(100) than on Pt(100) and Rh(100), a higher coverage (1.25 $ML$) was not considered on this surface.

While the bare surface energies are particularly sensitive to the functional used and the level of convergence defined, the relative stability of the (111) and (100) facets of each metal should be less sensitive. We therefore expect the trend in surface energies between (111) and (100) to be robust.

## 4.3 Results and discussion

In the following section, we will first describe the experimentally studied corrosion behavior of Pt, Rh and Au in LiOH, NaOH and KOH electrolytes. This description will be separate for each metal and will focus on the difference in corrosion behavior as a function of the electrolyte composition. This approach differs slightly from Chapter 2 & 3, which mainly described the corrosion behavior as a function of the corrosion potential. However, an electrochemical impression of the corrosion behavior as a function of the applied potential can be gained from Fig. A.4 through Fig. A.15 in Appendix A, which correspond to the figure format used in Chapter 2 & 3. Similarly, Fig. A.16 through Fig. A.27 display scanning electron micrographs of the electrodes as a function of the applied potential. Since Fig. A.4 through Fig. A.27 are designed to complement the figures in this chapter, the interested reader is referred to these supporting figures for a more complete impression of the experimental results on the corrosion behavior of the studied systems. These figures in the appendix are also accompanied by additional discussion of the presented results and conclusions.

After describing the experimental results, we will proceed by presenting our complementary theoretical results on the adsorption of Li, Na, K and H on Pt, Rh and Au. The experimental and theoretical results will be further interpreted and connected in the Discussion section.

### 4.3.1 Results

**Experimentally determined corrosion behavior**

The corrosion behavior of Pt, Rh and Au was studied through both cyclic voltammetry (CV) and scanning electron microscopy (SEM). As in the previous chapters, the metallic electrodes were treated by applying a constant cathodic voltage *versus* an internal reversible hydrogen electrode (RHE) for 60 seconds in a concentrated alkali metal hydroxide solution. Before and after this cathodic polarization, the electrodes were characterized by cyclic voltammetry in a sulfuric acid solution to monitor changes in the structure of the

electrode surface. Additionally, the electrodes were imaged by SEM after corrosion to identify etching features in the surface.

In these experiments, the applied corrosion potentials are purposefully spaced by $0.1\ V$ steps: the smallest interval at which we believe that differences in corrosion behavior can reliably be assessed with the current methodology. Given this potential spacing, our resolution in determining corrosion onset potentials is $0.1\ V$. Strictly speaking, this means that the 'true' corrosion onset potential will lie between the most negative potential where no corrosion can be detected and the least negative potential where corrosion can be detected. For consistency, however, we will follow Chapter 2 & 3 in defining the corrosion onset potential as the least negative potential where corrosion can be detected. This detection will rely predominantly on cyclic voltammetry.

### Platinum

For platinum, the use of cyclic voltammetry is well established as a quick and reliable method for characterizing electrode surfaces. This characterization relies on the so-called 'hydrogen region', which in $0.5\ M$ $H_2SO_4$ contains the following anodic features that are important for this work:[43]

1. A peak at $0.13\ V$ *vs.* RHE, corresponding to the substitution of *H by *OH on (110)-type sites.[44,45]

2. A peak at $0.27\ V$ *vs.* RHE, corresponding to (100)-type step sites near terrace borders.[44,45]

3. A broader feature between $0.3$ and $0.4\ V$ *vs.* RHE, corresponding to (100) terrace sites.

4. A broad feature between $0.06$ and $0.3\ V$ *vs.* RHE, corresponding to hydrogen desorption on (111) terraces. This feature is accompanied by a broad feature between $0.4$ and $0.55\ V$ *vs.* RHE, for (bi)sulfate adsorption on (111) terraces.

Since these features depend strongly on the presence and abundance of their corresponding surface sites, the use of cyclic voltammetry is extremely sensitive to small changes in the electrode structure. As such, CV measurements, complemented by SEM images, will be the primary method for quantifying the differences between corrosion in different electrolytes.
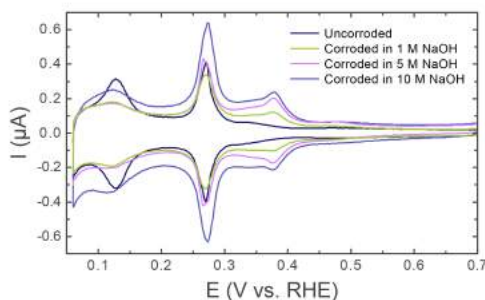
**Fig. 4.1** | Cyclic voltammograms of Pt corroded in NaOH of various concentrations, at −1.0 *V vs.* RHE. Voltammograms were recorded in 0.5 *M* H$_2$SO$_4$, at a scan rate of 50 *mV · s*$^{-1}$.

*Electrolyte concentration*

The differences are first explored as a function of cation concentration for NaOH electrolytes: in Fig. 4.1, voltammograms of electrodes corroded at −1 *V vs.* RHE in 1, 5 and 10 *M* NaOH are displayed in increasingly darker colors, with the uncorroded electrode displayed in dark blue. The comparison of these voltammograms reveals higher measured currents in the voltammograms of electrodes corroded in higher NaOH concentrations. This higher current corresponds to a larger hydrogen desorption charge, which in turn corresponds to more exposed surface area.[46] For the presented samples, this represents surface area increases of 28, 32 and 74% after corrosion in 1, 5 and 10 *M* NaOH, respectively. Higher electrolyte concentrations therefore induce more electrode roughening.

This increased roughness with increasing concentration correlates well with the corrosion onset potential. For Pt corrosion, this onset was shown in Chapter 2 to be signified by a decrease in (110) features at 0.13 *V vs.* RHE, which is accompanied by a minor increase in (100) features at 0.27 *V vs.* RHE. As can be seen in Fig. A.5 & A.8, these changes occur respectively after polarization at −0.6 *V vs.* RHE (−1.4 *V vs.* NHE) and −0.5 *V vs.* RHE (−1.4 *V vs.* NHE) in 1 and 5 *M* NaOH. These onset potentials are more negative than the −0.4 *V vs.* RHE (−1.3 *V vs.* NHE) observed in Chapter 2 for 10 *M* NaOH. This onset trend and the less substantial roughening in more dilute solutions indicate that the extent of corrosion correlates strongly with NaOH concentration.

Based on this trend as a function of concentration, one might expect the facet distribution to also change monotonically with regard to concentration. This is indeed the case for (100) features: both (100) step sites (0.27 *V vs.* RHE) and terrace sites (0.3–0.4 *V vs.*
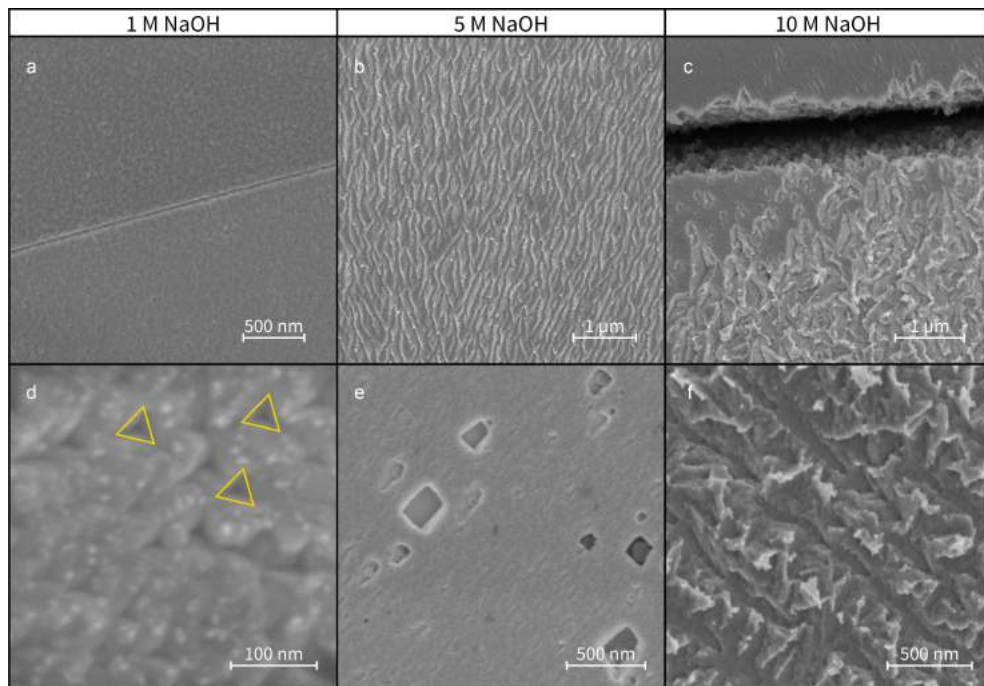
**Fig. 4.2 |** Scanning electron micrographs of Pt electrodes corroded at $-1$ *V* *vs.* RHE in 1 *M* NaOH **(a, d)**, 5 *M* NaOH **(b, e)** and 10 *M* NaOH **(c, f)**. Triangular features are highlighted in yellow.

RHE) increase with electrolyte concentration. However, the amount of (110) sites first decreases between 1 and 5 *M* NaOH, to then increase when corroding in 10 *M* NaOH. This indicates an interesting feature of cathodic corrosion in 10 *M* NaOH: the newly created surface area appears more disordered than that created at lower electrolyte concentrations, as is motivated in Appendix A.

Further indications of a rougher and more disordered surface follow from microscopy-based examination of the corroded electrodes, presented in Fig. 4.2. In this figure, Panels **a** and **d** display an electrode corroded in 1 *M* NaOH at $-1.0$ *V* *vs.* RHE. As can be seen in Panel **a**, which features the boundary between two crystal grains, the electrode appears predominantly roughened on the nano-scale, without the presence of well-defined etching features. However, small sections of the electrode feature triangular etch pits, which are (100)-oriented pits in (111)-like facets, as explained in Chapter 2 (model etch pit: Fig. A.28).

More severe corrosion features are present after cathodic treatment at $-1$ *V* *vs.* RHE

in 5 *M* NaOH (Fig. 4.2 **b**, **e**). This treatment causes the appearance of etch lines (Fig. 4.2 **b**) on large sections of the electrode and areas containing etch pits with more subtle roughening between them (Fig. 4.2 **e**). Many of these pits contain ∼90-degree angles and are assigned to (100)-type sites. This assignment is based on Chapter 2, but is also illustrated here by a model etch pit (Fig. A.28).

Finally, when increasing the NaOH concentration to 10 *M* (Fig. 4.2 **c**, **f**), the etch features increase further in size, thus indicating higher roughness. These features (Fig. 4.2 **f**) contain edges that are less straight than those after corrosion in less concentrated solutions. As such, the SEM images support the electrochemical observation that the increase from 5 to 10 *M* NaOH induces the formation of more disordered sites on the nano-level. Similarly, the SEM results corroborate the electrochemically observed roughness increase with cation concentration.

*Cation identity*

Besides being sensitive to the cation concentration, cathodic corrosion also responds strongly to the cation identity. This is illustrated in Fig. 4.3, which explores Pt corrosion as a function of cation type for electrolyte concentrations of 1 *M* (Panel **a**, **b**) and 5 *M* (Panel **c**, **d**). This exploration is further subdivided in mildly negative potentials (Panel **a**, **c**) and more negative corrosion potentials (Panel **b**, **d**).

At mildly negative potentials, the electrolyte cation appears to barely affect the facet preference after corrosion. At these potentials, the cyclic voltammograms for corroded Pt overlap quite well: the amount of created (100) terraces is similar for all electrolytes of similar concentrations. This overlap is particularly noteworthy because the corrosion onset potentials, derived from Fig. A.4–A.9, are not the same for all types of cations. For 1 *M* KOH, the onset potential is −0.5 *V* *vs.* RHE (−1.3 *V* *vs.* NHE), while it is −0.6 *V* *vs.* RHE (−1.4 *V* *vs.* NHE) for 1 *M* NaOH and LiOH. Similarly, for 5 *M* electrolytes, the onset potential is −0.4 *V* *vs.* RHE (−1.3 *V* *vs.* NHE) for KOH and at −0.5 *V* *vs.* RHE (−1.4 *V* *vs.* NHE) for NaOH and LiOH. This indicates that, at mildly negative potentials, the final facet distribution does not necessarily correlate with the cation-influenced onset potential, but rather with the applied electrode potential.

This observation contrasts with the behavior at more negative potentials, which depends strongly on the nature of the electrolyte cation. For 1 *M* corrosion electrolytes (Fig. 4.3 **c**), this dependence shows a clear trend between cations: larger cations remove more (110) sites and create more (100) step and terrace sites. This facet preference trend
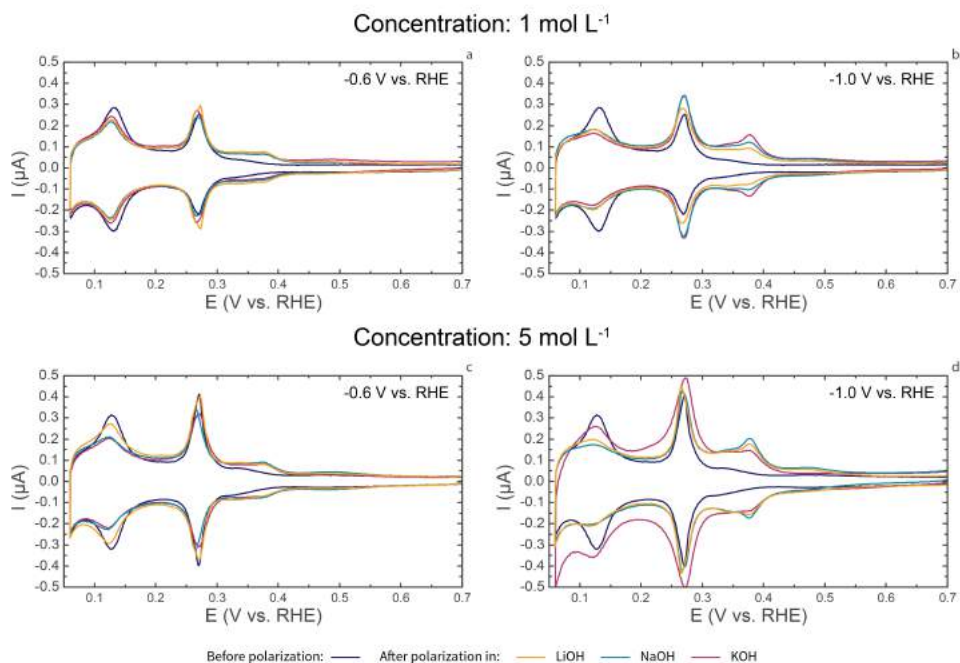
**Fig. 4.3 |** Cyclic voltammograms of Pt corroded in LiOH, NaOH and KOH at concentrations of 1 *M* **(a, b)** and 5 *M* **(c, d)**, at −0.6 *V* vs. RHE **(a, c)** and −1.0 *V* vs. RHE **(b, d)**. Voltammograms were recorded in 0.5 *M* $H_2SO_4$, at a scan rate of 50 $mV \cdot s^{-1}$.

is accompanied by a modest tendency for more surface area creation as the cation size increases.

The trend in surface area formation is sustained in more concentrated solutions, as can be seen in Fig. 4.3 **d**: at −1 *V* vs. RHE, most surface area is created in KOH solutions, followed respectively by NaOH and LiOH. Similarly, the facet preference trend is almost sustained in 5 *M* solutions. As in more dilute solutions, slightly more (100) terraces are created in NaOH electrolytes than in LiOH electrolytes. However, compared to these electrolytes, KOH causes an increase in (110) and (100) step sites and small decrease in (100) terraces. This increased step site formation is similar to that observed between 5 and 10 *M* NaOH. One can therefore also argue that moving from 5 *M* NaOH to 5 *M* KOH produces a more disordered surface after corrosion.

These electrochemical results can be analyzed in the light of scanning electron microscopy characterization. For 1 *M* electrolytes, SEM detects differences between cations,
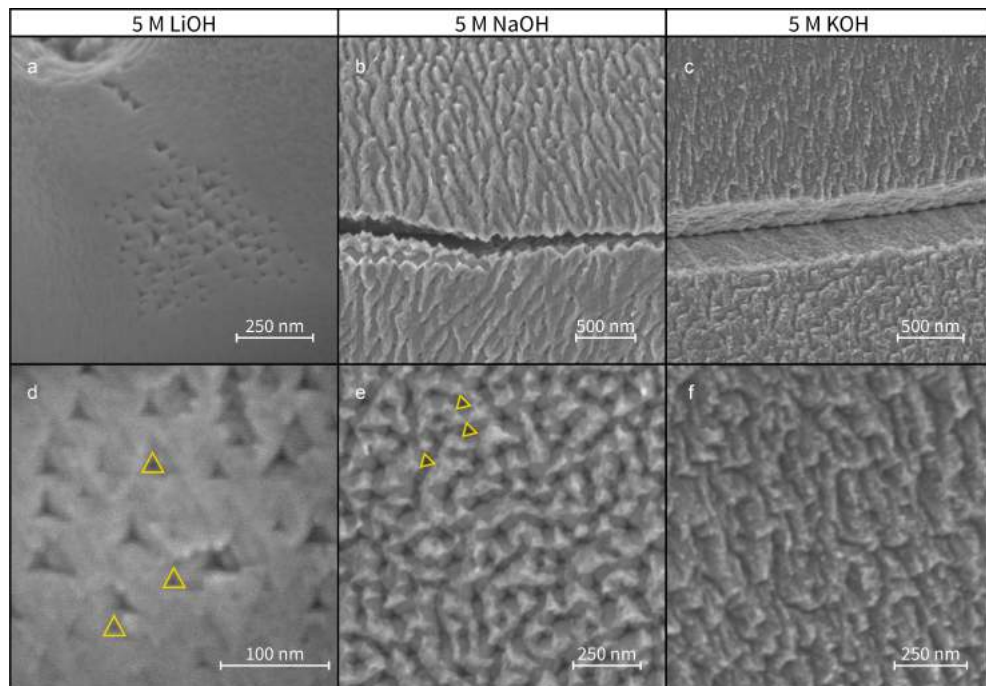
**Fig. 4.4 |** Scanning electron micrographs of Pt electrodes corroded at $-1$ $V$ vs. RHE in $5$ $M$ LiOH (**a**, **d**), $5$ $M$ NaOH (**b**, **e**) and $5$ $M$ KOH (**c**, **f**). Triangular features are highlighted in yellow.

with larger cations inducing more corrosion (Fig. A.16–A.18). This qualitatively matches the results in more concentrated electrolytes. As can be seen in Panels **a** and **d** of Fig. 4.4, corrosion in $5$ $M$ LiOH causes the formation of (100)-type triangular etch pits. These pits are present on small areas of the electrode; in other areas, any corrosion features are beyond the resolution of the SEM (Fig. A.19).

This differs significantly from corrosion in $5$ $M$ NaOH (Panels **b** and **e** of Fig. 4.2 and 4.4): etch lines are widespread and rectangular etch features can be seen in Fig. 4.2 **e**, underneath the grain boundary in Fig. 4.2 **b** and in Fig. A.20 **e**. In addition, the electrodes show significant corrugation that contains triangular features (Fig. 4.4 **e**), which resemble the triangular pits observed for less severe corrosion. These pits could serve as therefore initiation sites for more severe etching features, as is illustrated in Appendix A.

Finally, corroding in $5$ $M$ KOH creates rougher and less well-ordered features than those observed for LiOH and NaOH: large troughs are found along grain boundaries (Fig. 4.4 **c**) and significant roughness without straight features is found on crystal grains

(Fig. 4.4 **f**).

These SEM and voltammetry results create a coherent impression of cathodic corrosion. Corrosion in LiOH creates the least amount of surface area. This area is only slightly smaller than that created in NaOH electrolytes, while the electrodes appear markedly different in SEM. This indicates that corrosion in LiOH electrolytes creates roughness on scales below the SEM resolution. Corrosion in NaOH electrolytes then causes more macroscopic roughness. This roughness contains well-developed electrochemical (100) terrace features that correspond with the formation of straight, long-distance features in SEM. Such well-ordered sites are mostly absent from electrodes corroded in 5 *M* KOH, which appear the roughest and most disordered in both voltammetry and electron microscopy.

As such, a clear effect of the cation is present for both studied electrolyte concentrations. At low concentrations, the cation predominantly affects the surface facet distribution, causing most (100) sites to be formed in KOH, followed respectively by NaOH and LiOH. At higher concentrations, corrosion in NaOH and LiOH induces well-developed (100) features, with KOH leading to an increased amount of step sites. Corrosion furthermore produces more surface area with increasing cation size.

### *Rhodium*

In contrast with platinum voltammograms, rhodium voltammograms only feature one set of 'hydrogen' peaks.[47] Of this set, the cathodic peak corresponds to (bi)sulfate desorption, accompanied by hydrogen adsorption. Accordingly, the anodic peak corresponds to hydrogen desorption, accompanied by (bi)sulfate adsorption. The position of these peaks varies, depending on the exposed electrode facets. For the three basal planes, this yields the following peak positions in 0.1 *M* $H_2SO_4$:[47]

1. Rh(111) contains a sharp cathodic peak at 0.105 *V* *vs.* RHE and a sharp anodic peak at 0.122 *V* *vs.* RHE.

2. Rh(100) contains a sharp cathodic peak at 0.149 *V* *vs.* RHE and a sharp anodic peak at 0.157 *V* *vs.* RHE.

3. Rh(110) contains a broad cathodic peak at 0.107 *V* *vs.* RHE and a broad anodic peak at 0.120 *V* *vs.* RHE.

In line with our Chapter 3, we will primarily focus on the anodic peaks. The peaks are located around 0.121 *V vs.* RHE for the (111) and (110) facets, but situated approximately 35 *mV* more positive for the (100) facet. We used this peak position difference in Chapter 3 to determine the onset potential of rhodium: at the corrosion onset of −0.4 *V vs.* RHE (−1.3 *V vs.* NHE), the anodic hydrogen peak shifts positively by 2 *mV*. This positive shift signifies the formation of (100) sites. Because this peak shift is more abrupt than the gradual increase in electrode surface area, the same shift will be used here to determine the corrosion onset. We will focus exclusively on the effect of the cation identity in 5 *M* electrolytes, because cathodic corrosion of Rh in 1 *M* electrolytes is subtle and the spread in the data is too large to reliably establish onset potentials and facet preferences.

*Cation identity*

For 5 *M* electrolytes, the peak shift and surface area increase (as determined from the hydrogen desorption charge) after 60 seconds of cathodic polarization are presented in Fig. 4.5. In this figure, the anodic peak shift (Panel **b**) is approximately 2 *mV* in absence of cathodic corrosion. Though this 'baseline' shift is slightly higher than the < 1 *mV* shift in Chapter 3, it is reproducible for the presently studied electrolytes. The first electrolyte to exhibit a shift larger than 2 *mV* is 5 *M* KOH, for which a 4 *mV* peak shift marks the onset of cathodic corrosion at −0.4 *V vs.* RHE (−1.3 *V vs.* NHE). In agreement with Chapter 3, this 4 *mV* change represents an approximate 2 *mV* shift from the baseline change in peak position. Similar 3–4 *mV* total shifts occur at −0.5 *V vs.* RHE (−1.4 *V vs.* NHE) for LiOH and NaOH. These onset potentials match those for Pt corrosion, with corrosion in 5 *M* KOH starting at less negative potentials than corrosion in 5 *M* NaOH and LiOH.

Another similarity with Pt is that the initial surface area increase (Fig. 4.5 **a**) is similar at mildly negative potentials and starts diverging at approximately −0.7 *V vs.* RHE. However, the trend in surface area formation differs from platinum: most surface area is formed in NaOH, followed respectively by KOH and LiOH. Though the cause of this differing trend is unclear, it does match the observed peak shifts for Rh corrosion: the shift is highest for NaOH, with LiOH and KOH producing shifts that are 2 to 4 *mV* smaller, depending on the exact corrosion potential.

Such differences between cations in both surface area and peak shift are consistent with SEM characterization results, which are shown for the three electrolytes in Fig. 4.6. The electrolyte for which Fig. 4.5 **a** indicates the smallest surface area increase is 5 *M*
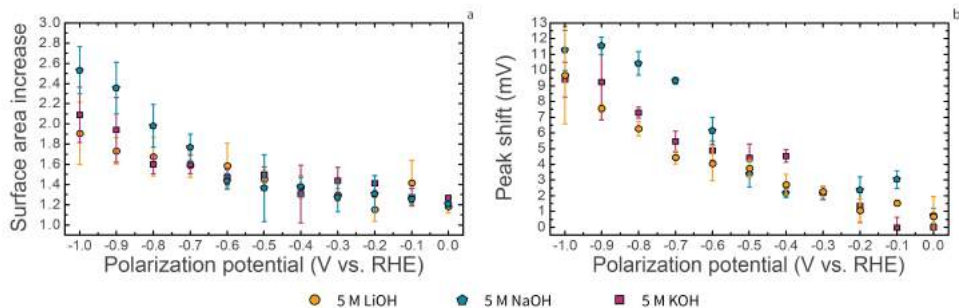
**Fig. 4.5 |** Relative rhodium surface area increase after cathodic polarization **(a)** and shift of the anodic hydrogen peak **(b)**, as a function of the applied polarization potential in 5 $M$ LiOH, 5 $M$ NaOH and 5 $M$ KOH. Each data point is the average of at least 3 independent experiments. Error bars represent one standard deviation; if an error bar is not visible, it falls within its corresponding data point.

LiOH. In electron microscopy (Fig. 4.6 **a, d**), Rh electrodes corroded in this electrolyte typically exhibit no signs of cathodic corrosion: with the exception of one electrode (Fig. A.22 **c**), the electrodes only contain ridges and cracks that align with the electrode, which Chapter 3 showed to not be caused by cathodic corrosion.

More signs of corrosion are visible for rhodium electrodes corroded in 5 $M$ KOH (Fig. 4.6 **c, f**), which is the electrolyte that ranks second in surface area creation. Interestingly, this electrolyte does not cause the formation of large etch pits, but instead creates a high coverage of small particles that are attached to the surface.

Finally, small particles can be observed after corrosion in 5 $M$ NaOH (Fig. 4.6 **b, e**) and large quasi-rectangular pits are found after corrosion at and below $-0.9$ $V$ *vs*. RHE. These pits match those created in 10 $M$ NaOH, and are assigned to (100) site formation (Chapter 3). They therefore match the CV peak shift ((100) preference) in Fig. 4.5 being highest for corrosion in NaOH. Additionally, the etch pits are the largest features observed for rhodium in this study, which correlates well with the electrochemical surface area increase being largest for 5 $M$ NaOH.
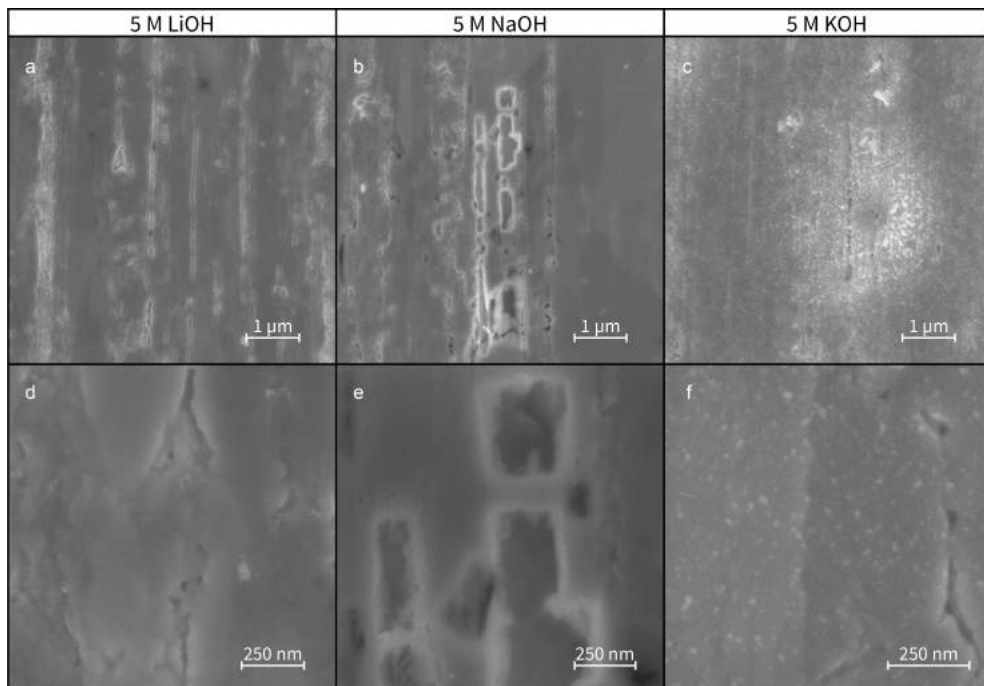
**Fig. 4.6 |** Scanning electron micrographs of Rh electrodes corroded at $-1$ *V* vs. RHE in $5$ *M* LiOH **(a, d)**, $5$ *M* NaOH **(b, e)** and $5$ *M* KOH **(c, f)**.

Summarizing, both electrochemistry and electron microscopy indicate the surface area increase to be smallest for LiOH, followed respectively by KOH and NaOH. Besides, electrochemistry indicates the largest amount of (100) sites to be formed in NaOH, which matches the occurrence of large, quasi-rectangular etch pits. Although these observations from CV and SEM lack the clear trends observed for platinum, both techniques produce mutually consistent results for the corrosion behavior of rhodium.

### Gold

For gold, the change in surface orientation will be studied by using the oxide region in the cyclic voltammogram. This region is situated approximately between 1.35 and 1.75 *V* vs. RHE and contains several overlapping peaks corresponding to the following three basal planes:[48,49]

1. Au(111) produces a peak at 1.58 *V* vs. RHE.

2. Au(100) produces a peak at 1.42 *V* vs. RHE.

3.  Au(110) produces a peak at 1.46 *V* *vs.* RHE.

Peaks corresponding to (100) and (111)/(110)-oriented steps are found respectively at 1.39 and 1.43 *V* *vs.* RHE.[48] Though some of the peaks are situated rather close to each other, they are reliable indicators of the amount of exposed basal planes.[16] The peaks will therefore be used to assess changes in the electrode surface after cathodic corrosion. As with rhodium, these changes are not reported for concentrations of 1 *M*; corrosion in these concentrations did not produce changes that were significant enough to reliably identify onset potentials and etching preferences.

*Cation identity*

Larger changes are observed for experiments in 5 *M* alkali metal hydroxides. For corrosion in these electrolytes, voltammograms before and after 60 seconds of corrosion at −1.5 *V* *vs.* RHE are shown in Fig. 4.7. The figure shows both the first (Panel **a**) and fourth (Panel **b**) voltammetric cycles after cathodic corrosion, because the electrode surface changes between cycles due to repetitive oxidation and reduction.[16] Such changes could obscure the difference between cations if only the fourth cycle were used for comparison. In addition, the displayed CVs are shown for a more negative corrosion potential (−1.5 *V* *vs.* RHE) than those shown for rhodium and platinum. This is because corrosion is significantly milder for gold, which causes smaller differences between the cations at less negative potentials; voltammograms of electrodes polarized around the corrosion onsets and at −3.0 *V* *vs.* RHE are available in Fig. A.13–A.15.

At −1.5 *V* *vs.* RHE, corrosion in all three electrolytes creates some extent of (111) features. These features, which are visible around 1.58 *V* *vs.* RHE, can be used to identify the onset potential of gold corrosion (Chapter 3). This analysis is presented in Fig. A.29, and indicates the onset potentials to be −0.9 *V* *vs.* RHE (−1.8 *V* *vs.* NHE) for 5 *M* LiOH and −0.8 *V* *vs.* RHE (−1.7 *V* *vs.* NHE) for 5 *M* NaOH and KOH. As for platinum and rhodium, these potentials are 0.1 to 0.2 *V* more negative than the corrosion onset potential found in Chapter 3 for 10 *M* NaOH: −0.7 *V* *vs.* RHE (−1.6 *V* *vs.* NHE). This indicates a later onset of cathodic corrosion for all three cations in more dilute electrolytes.

When the facet preference of the cations is compared, several interesting features stand out. These features are most clearly visible in the first cycle after corrosion (Fig.4.7 **a**). From this cycle, one can observe that LiOH induces the creation of only a small amount of (111) facets. Instead, the most-developed peak is the (100) peak at 1.41 *V* *vs.* RHE.
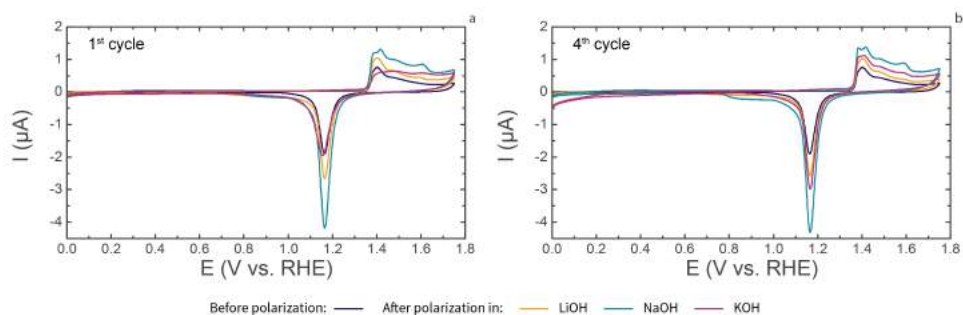
**Fig. 4.7 |** Cyclic voltammograms of Au, corroded in $5\,M$ LiOH, $5\,M$ NaOH and $5\,M$ KOH at $-1.5\,V$ vs. RHE. CVs shown are the first cycle **(a)** and the fourth cycle **(b)** after cathodic corrosion. Voltammograms were recorded in $0.1\,M$ H$_2$SO$_4$, at a scan rate of $50\,mV \cdot s^{-1}$.

This also holds true after 4 cycles (Fig. 4.7 **b**), with only small changes occurring between cycles.

The corrosion behavior in $5\,M$ LiOH is not matched by NaOH, which induces a strong development of (111) sites ($1.58\,V$ vs. RHE) in both the first and fourth characterization cycles. An additional difference with respect to LiOH is the amount of created surface area, which can primarily be assessed by the size of the oxide reduction peak at $1.16\,V$ vs. RHE.[50] A larger peak after corrosion in $5\,M$ NaOH indicates significantly more surface area formation than corrosion in $5\,M$ LiOH.

Finally, the created surface area in $5\,M$ KOH displays interesting behavior with respect to the other two electrolytes. During the first cycle after corrosion, it appears that virtually no surface area has been created: the oxide reduction peak is similar in height to the peak of a pristine electrode. Interestingly, this peak grows in size during characterization after cathodic corrosion, leading to a CV similar to that after corrosion in $5\,M$ LiOH, but with slightly more surface area, step sites, (110) terrace sites and (111) sites. Though these changes are discussed in more detail in Appendix A, the current analysis already indicates a strong difference in corrosion behavior for different cations.

As for Pt and Rh, these voltammetric changes correspond to changes observed with SEM. Scanning electron micrographs are shown for corrosion at $-3.0\,V$ vs. RHE in Fig. 4.8. This potential was chosen for SEM comparison because no corrosion could be detected by SEM for gold in $5\,M$ LiOH at $-1.5\,V$ vs. RHE (Fig. A.25). For this electrolyte, corrosion features were only visible near the tip of the electrode. These features consist predominantly of etch pits, of which a particularly interesting example is shown in Panel **a**. This
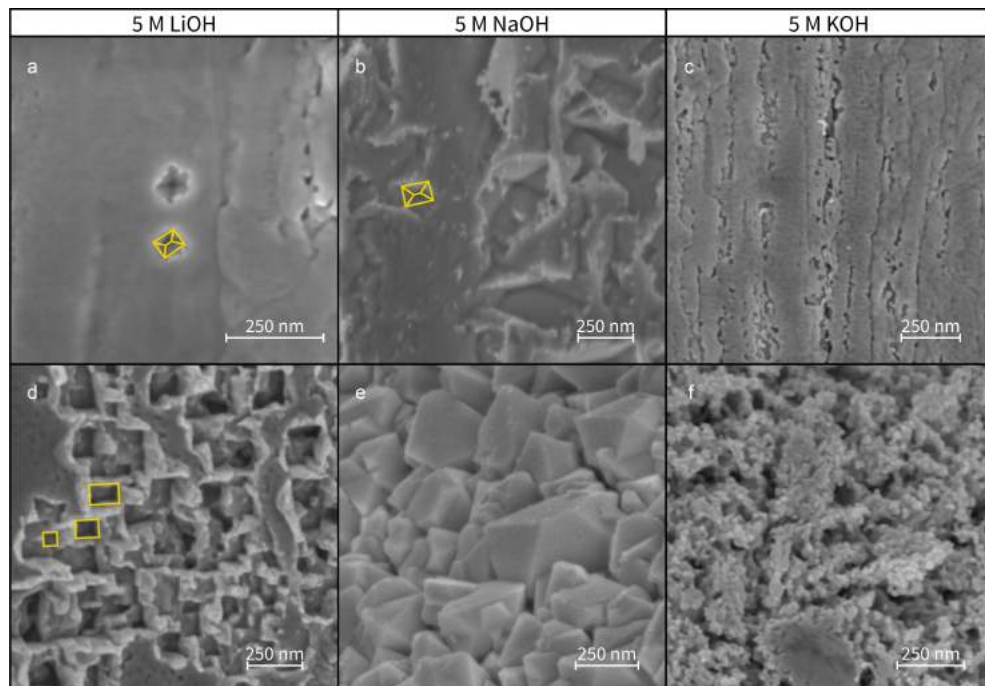
**Fig. 4.8 |** Scanning electron micrographs of Au electrodes corroded at −3 *V* vs. RHE in 5 *M* LiOH (**a**, **d**), 5 *M* NaOH (**b**, **e**) and 5 *M* KOH (**c**, **f**). Images in Panels **d**–**f** were taken at the tip of the electrode, whereas images in Panels **a**–**c** were taken further away from the tip. Representative etch pits have been highlighted in yellow.

type of etch pit is highlighted in yellow: it has outlines that appear to have roughly 90-degree angles and pit walls that slant inwards. This type of pit is therefore indicative of a (111)-type pit in a (100)-type surface, as can be rationalized using a model etch pit (Fig. A.28). In addition to these (111) sites, triangular and rectangular (100) pits are also visible in Fig. A.25 **c** and Fig. 4.8 **d**.

Pits are also observed after corrosion in 5 *M* NaOH, as is shown in Fig. 4.8 **b**. These features are larger than those seen for corrosion in 5 *M* LiOH, but match the orientation of (111)-type pits in (100)-type surfaces. The pits are accompanied by less well-defined roughness (Fig. A.26), but also by large, quasi-octahedral particles close to the tip of the electrode. These well-defined particles were previously observed after corrosion in 10 *M* NaOH and are strong indicators of the formation of (111) sites, as seen in Chapter 3.[8]

Well-defined particles and pits are absent for 5 *M* KOH. Corrosion in this electrolyte predominantly causes the etching of crystal grains, leading to the disordered features in

Fig. 4.8 **c**. In addition, cathodic corrosion creates disordered particles (Fig. 4.8 **f**); these particles are exclusively present at the tip of the electrode, where it is cut from the spool. As such, the presence of these small, disordered particles and etch pits supports the suggestion that corrosion in $5\,M$ KOH causes the formation of a more disordered type of gold surface.

Thus, SEM imaging reinforces the electrochemical observations for gold corrosion, indicating the following behaviors for the three electrolytes. Firstly, $5\,M$ LiOH is shown in both electrochemistry and electron microscopy to be the electrolyte in which the least surface area is created. When pronounced changes are present, both techniques can attribute them the formation of (triangular & rectangular) (100) sites and a small amount of (rectangular) (111) sites. Secondly, $5\,M$ NaOH is shown electrochemically to create the most new surface area, consisting predominantly of (111) sites. This agrees well with the (111)-type etch pits and quasi-octahedral particles observed in SEM. Finally, $5\,M$ KOH induces the formation of slightly more surface area than $5\,M$ LiOH. This surface area appears to be disordered, as is indicated by the lack of well-defined oxide features in the first cycle after corrosion. The observed disorder is reflected in the SEM by the formation of many small etch pits and the presence of small nanoparticles at the tip of the electrode. As such, the combination of CV and SEM characterization paints a consistent picture of the corrosion behavior of gold in $5\,M$ LiOH, NaOH and KOH.

**Computationally derived adsorption and surface energies**

After having experimentally mapped the corrosion behavior of Pt, Rh and Au, we exchange our experimental viewpoint for a computational perspective. From this perspective, we will first focus on the specific adsorption of alkali metal cations, followed by the surface energies of hydrogen-covered metals.

*Specific adsorption of cations*

We will focus first on the specific adsorption of Li$^+$, Na$^+$ and K$^+$ on Pt, Rh and Au. This approach extends from the work in Chapter 3 on sodium adsorption and initially considered adsorbed cations in vacuum, without including explicit solvation. However, explicit near-surface solvation was previously shown to significantly affect cation adsorption.[26] Explicit solvation was therefore included in the results in this chapter, whereas calculations without explicit solvation are shown for comparison in Fig. A.30–A.31. The presented calculations allowed us to calculate equilibrium adsorption potentials for cation
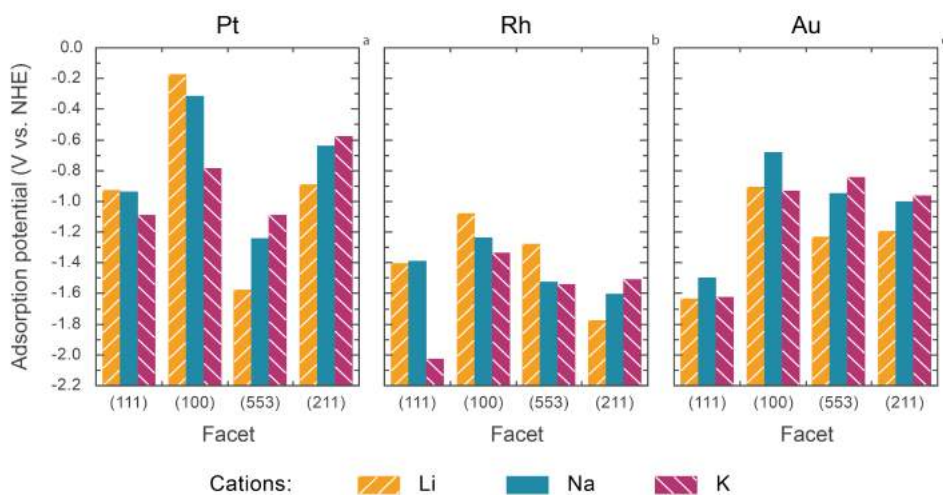
**Fig. 4.9 |** Equilibrium adsorption potentials for adsorption of Li, Na, and K on the (111), (100), (553) and (211) surfaces of Pt **(a)**, Rh **(b)**, and Au **(c)** from a 1 $M$ solution of alkali metal cation.

adsorption, facilitating a direct comparison with the experimentally determined onset potentials.

Calculated equilibrium adsorption potentials for Li$^+$, Na$^+$, K$^+$ onto the (111), (100), (553) and (211) facets of Pt, Rh and Au are displayed in Fig. 4.9. In this figure, cation adsorption is energetically favorable at potentials below the indicated equilibrium adsorption potential, as is signified by the bars covering the entire cation adsorption potential range. Though the cations transfer only a small part of their charge to the surface upon adsorbing, they do lose part of their solvation shell and interact directly with the metal surface. This therefore means that, within the context of this work, the cations are specifically adsorbed in the range covered by the bars in Fig. 4.9.

Importantly, the adsorption range starts at less negative potentials than the onset potential of cathodic corrosion for most of the metal facets. Therefore, the cations are favorably adsorbed to the metal surface at potentials where cathodic corrosion occurs. As such, the results in Fig. 4.9 support the importance of cation specific adsorption during cathodic corrosion. However, further assessment of the role of cations requires closer examination of adsorption trends across the different metal surface facets and between each of the alkali metal cations.

The trend in adsorption between facets is strongest for platinum, see Fig. 4.9 **a**: cation

adsorption is weakest on (111)-type sites. This follows from the adsorption potential being most negative on the (111) and on the (553) facet.[*] This relatively weak binding to (111)-type sites is contrasted by adsorption on (100)-type sites: the least negative adsorption potentials are found for the (100) facet and the (211) facet.[†] This strong binding on (100) sites *vs.* (111) sites might be related to the more open nature of (100)-type sites, which causes stronger binding for a variety of adsorbates.[51–53] Interestingly, this would imply an even stronger binding on step sites *versus* terrace sites, which is not observed. This apparent discrepancy is caused by a difference in cation coverage, as is discussed in more detail in Appendix A. Nonetheless, both Pt steps and terraces bind cations favorably to (100)-type sites, which correlates well with the experimentally observed preference for the creation of (100) sites on platinum.

While the adsorption energies for platinum show a clear trend that favors adsorption on (100) sites, there is no straightforward facet trend for Rh and Au (Fig. 4.9 **b, c**). Although these metals match Pt in exhibiting a strong preference for adsorption on (100) terraces over (111) terraces, they generally lack the significant difference between (553) and (211) that Pt exhibits.

Similarly, Pt is the only metal to exhibit clear trends in the calculated differences between cations. For Pt, steps and terraces behave oppositely; on terraces, Li adsorbs most strongly, followed respectively by Na and K. In contrast, Pt steps adsorb K most strongly, followed respectively by Na and Li. This difference between terraces and stepped surfaces arises from the different relative coverages of the cations on each surface, as is explained in Appendix A.

The trends with respect to cation identity for platinum are only partly upheld for Rh and Au: only the Rh(100), Rh(211), Au(553) and Au(211) trends behave similarly to their Pt counterparts. This absence of a calculated trend matches the experimental absence of a clear facet trend between cations for both Rh and Au.

### Energies of hydrogen-covered surfaces

In addition to examining alkali metal cation adsorption, we explored high coverages of adsorbed hydrogen which may be present on Pt, Rh and Au at cathodic corrosion potentials. We did so by calculating the surface energies of the (111) and (100) facets of

---

[*]  (553) facets contain 5-atom long (111) terraces and (111) steps to which cations adsorb.

[†]  (211) facets contain 3-atom long (111) terraces and (100) steps to which cations adsorb.

Pt, Rh and Au in the absence and presence of a monolayer ($ML$) of adsorbed hydrogen. These calculations were performed using values from literature DFT studies.[36,37] For (100) surfaces, we additionally found previously that the adsorption of as much as 1.25 monolayers of hydrogen is favorable at potentials near 0 *V vs.* RHE.[40] This data was therefore included, and the surface energy extrapolated to lower potentials in Fig. 4.10 **a**. Similarly high coverages were calculated in the current work for Rh(100) and included in Fig. 4.10 **b**, since the hydrogen binding strength of Rh is similar to that of Pt. Because the calculations for 1.25 $ML$ coverage on Pt(100) and Rh(100) used different protocols than the calculations of Ferrin *et al.*, our results were added to the graph as separate lines. Interestingly, our DFT data in Fig. 4.10 (dark purple) and calculations using literature values (pink) appear similar. This agreement inspires confidence in using Fig. 4.10 as a first-order approximation of the stabilizing effect of adsorbed hydrogen.

Fig. 4.10 indicates that, at potentials positive of hydrogen adsorption, the surface energy is constant as a function of potential. This constant energy is a result of ignoring electrolyte species like water or hydroxyl, which may adsorb to strongly-binding surfaces and lower the overall surface energy at positive potentials. At more cathodic potentials, adsorbed hydrogen is calculated to be stable. These potentials generally correspond with hydrogen adsorption features in the blank cyclic voltammograms of platinum and rhodium and initiate a decrease in surface energy in Fig. 4.10. This linear energy decrease is driven by hydrogen adsorption. This adsorption is increasingly favorable at lower potentials, which lowers the total energy of the system. Eventually, this constant decrease causes the surface energy to drop below zero $eV \cdot \text{Å}^{-2}$, as compared to bulk metal. When this happens, the creation of more surface area to facilitate hydrogen adsorption is energetically more favorable than the breaking of Pt-Pt bonds that such creation of surface area would require.

Importantly, this surface energy transition occurs at potentials that match the experimental corrosion onset potentials: approximately $-0.4$ to $-0.5$ *V vs.* RHE for Pt and Rh, and $-0.7$ *V vs.* RHE for Au. (Exact potentials are given in Table A.1.) Though it is important to emphasize that we calculated the curves in Fig. 4.10 using literature data that was obtained using different DFT methodologies,[36,37] the curves match our experimentally determined onset potentials rather well. As such, Fig. 4.10 indicates that high hydrogen coverages may be an energetic driving force for surface area creation and could therefore strongly affect the onset of cathodic corrosion.
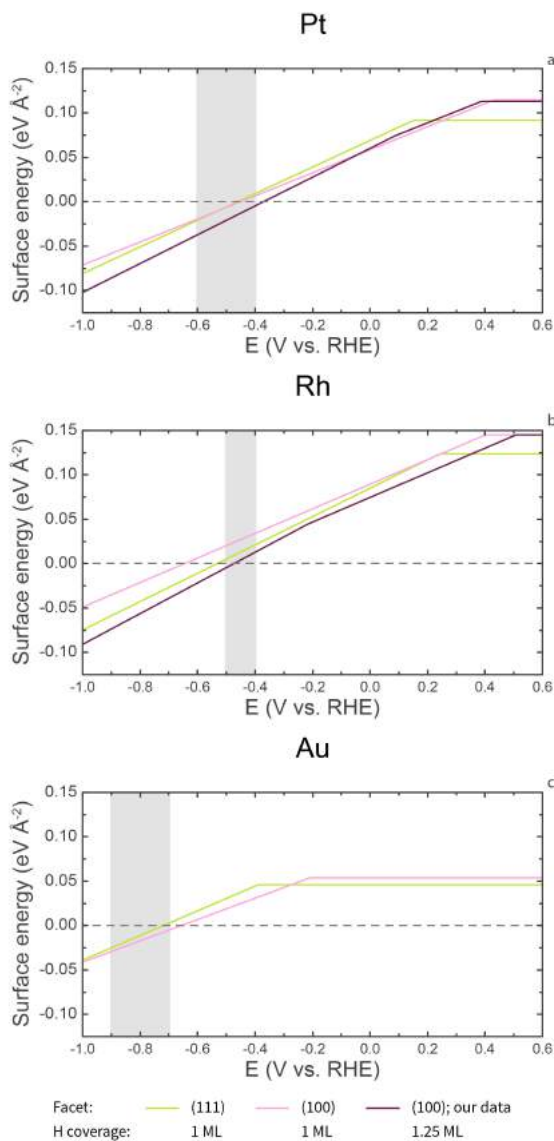
**Fig. 4.10 |** Potential-dependent surface energy of the (111) and (100) facets of Pt **(a)**, Rh **(b)**, and Au **(c)** in the absence and presence of 1 $ML$ *H. On Pt(100) and Rh(100), we have additionally considered the adsorption of 1.25 $ML$ *H. Our own data for Rh(100) was calculated with the PBE exchange-correlation functional instead of PW91. The range of experimentally determined onset potentials from this thesis is marked in grey.

### 4.3.2  Discussion

**Onset potential**

In the current chapter, we established onset potentials for cathodic corrosion of Pt, Rh and Au in various concentrations of LiOH, NaOH and KOH. Additionally, we explored the role of cation and hydrogen adsorption through theoretical calculations. Though this combination of theory and experiment does not unambiguously explain the nature of cathodic corrosion, it does provide valuable new clues towards elucidating this puzzling (electro)chemical phenomenon. Perhaps the most concrete of these clues are related to the onset potential of cathodic corrosion.

The onset potential depends strongly on the electrolyte concentration: corrosion takes place at less negative potentials as the concentration increases. This trend is valid for Pt, Rh and Au, as can be seen by comparing the current results with those in Chapter 2 & 3 for more concentrated electrolytes. The corrosion onset is similarly sensitive to the nature of the electrolyte cation: it generally starts at the least negative potentials for $K^+$, followed respectively by $Na^+$ and $Li^+$.

Though these experimental trends appear robust, they cannot conclusively be explained by the corresponding DFT results on cation adsorption. We therefore restrict this comparison of theory and experiment to two observations. First of all, larger cations are calculated to bind stronger to step edges. This could matter if cathodic corrosion were initiated at high-energy defect or step sites on the electrodes. Secondly, we calculate that larger cations retain more of their charge upon adsorption. This could shift the onset potential if cations were required to electrostatically stabilize an anionic reaction intermediate. Though speculative in nature, these computational suggestions parallel the observed effects of cations on the corrosion onset potential. These suggestions are therefore worthy of consideration in further mechanistic studies of cathodic corrosion.

In addition to the influence of cations on the corrosion onset, a similar role might be played by hydrogen: hydrogen is adsorbed on most metal surfaces at potentials where cathodic corrosion occurs. Exploring the effect of adsorbed hydrogen on the potential-dependent surface energy (Fig. 4.10), we found an energetic driving force for the creation of surface area. This driving force appears at potentials that correspond remarkably well with the experimental cathodic corrosion onset potentials. Importantly, this agreement was established without making any kinetic or mechanistic assumptions: it simply indicates a thermodynamic driving force for creating more surface area around the corrosion

onset potential.

The onset potential of cathodic corrosion therefore appears to depend on three major actors:

1. The corroded metal.

2. The electrolyte cation, which also affects various other factors of corrosion (Chapter 2 & 3).[9–13]

3. Adsorbed hydrogen.

Given the pronounced effect of each of these actors on the location of the corrosion onset, it is likely that each of them is involved in creating the elusive intermediate species that underlies cathodic corrosion. A possible class of species that contains all three actors and has been observed experimentally is ternary metal hydrides.

In brief, ternary metal hydrides are compounds with the general formula $A_x M_y H_z$, where $A$ is an alkali or alkaline earth metal and $M$ is a transition metal.[54] In the solid state, these compounds contain anionic $[MH_n]^{\delta-}$ clusters, which are stabilized by surrounding cations.[55] As such, these hydrides contain both ionic (or coulombic) interactions between the cation and the anionic cluster, and covalent (or coordination) bonds between the metal center and the hydrogen atoms.[56] A variety of these hydrides with Pt and Rh centers have been synthesized and fully characterized.[55,57] Though similar solid-state examples of ternary gold hydrides are unavailable, their existence is not unlikely: $AuH_2^-$ and $AuH_4^-$ have been generated with laser ablation,[58] and theoretical calculations suggest that such $AuH_2^-$ clusters could be stabilized by alkali metal cations.[59] Given these examples of ternary hydrides of Pt, Rh and Au, such compounds might be the elusive intermediate that underlies cathodic corrosion.

The presence of these species would match the suggested simultaneous importance of the corroded metal, electrolyte cations and adsorbed hydrogen. However, ternary metal hydrides are extremely sensitive to moisture and air,[55,60] which would make them highly unstable in our working electrolyte. Interestingly, this instability is consistent with current and previous experimental results. After all, during cathodic corrosion, only the reacting material (e.g. Pt, Rh, Au) and produced material (e.g. corroded Pt, Rh & Au surfaces and nanoparticles) have explicitly been identified: the intermediate species is highly unstable and has, as of now, escaped direct detection and chemical isolation.

In short, these hydrides are unstable enough to explain their elusiveness during experiments, yet have been studied and characterized to such an extent that their existence is plausible in our system. Additionally, they require the presence of a metal center, hydrogen *and* a stabilizing cation. As such, these hydrides are, in our opinion, prime targets for future mechanistic studies of the reaction intermediates of cathodic corrosion.

**Electrode area and facet distribution**

Besides considering these mechanistic insights, it is instructive to evaluate the role of cations in the final surface structure of the corroded electrodes. This role is relatively clear when considering cation concentration: higher concentrations lead to more severe changes in the facet distribution and the amount of created surface area for Pt (Fig. 4.1 & 4.2). Rh and Au behave similarly in that corrosion is rather mild at lower cation concentrations.

These effects of cation concentration appear to be thermodynamic in nature, meaning here that prolonged corrosion in dilute electrolytes is not likely to produce similar results as shorter corrosion in more concentrated electrolytes. This is illustrated by the corrosion of electrodes in $5\ M$ NaOH for various amounts of time (Fig. A.32): the difference between 1 and 10 minutes of corrosion is minimal, if at all present. As such, the presented corroded electrodes appear to have reached a stable state and the differences in Fig. 4.1 are strictly a consequence of the cation concentration.

Similar to the cation concentration, the cation identity also affects the final state of the corroded electrodes. However, this effect appears to vary with the applied potential. At the most negative potentials, both the facet distribution and surface area creation are strongly affected by the cation identity for all three metals.

The strongest trend in facet preference is observed for the corrosion of Pt: a monotonic (100) preference is observed when increasing the cation size in $1\ M$ electrolyte concentrations. This trend is captured well by our DFT results, which indicate the strongest binding on (100)-type steps ((211) facets) for K, followed by Na and Li. This trend is matched by (110)-type steps ((553) facets), which might explain why more step sites and more general surface area are produced in $5\ M$ KOH, compared to LiOH and NaOH. As such, the DFT results for cation adsorption agree well with the experimental corrosion behavior of Pt.

However, the calculated cation adsorption strengths match less well with the corrosion behavior of Rh and Au: they do not explain the observed facet distributions or why

most area is created in NaOH. At best, the absence of a clear trend in DFT resembles the absence of a clear trend in experimental facet distribution. The lack of overlap between experiment and theory can be attributed to the calculations in Fig. 4.9 only capturing cation adsorption. Other factors, like hydrogen adsorption, are not captured in these calculations. Cation adsorption therefore only partly determines the corrosion behavior at more negative potentials and hydrogen co-adsorption might improve the predictions.

At milder negative potentials, the cation identity appears unimportant in determining the electrode structure for all three metals:

- For Pt, the CVs of electrodes corroded at mildly negative potentials show great similarity (Fig. 4.3), especially when comparing the amount of created (100) terraces. In addition, close comparison of the micrographs in Fig. 4.2, Fig. 4.4 and Fig. A.16–A.21 reveals that the earliest indications of corrosion are typically (100)-oriented triangular etch pits, regardless of the identity and concentration of the electrolyte cation.

- For Rh, both the surface area increase and hydrogen desorption peak shift (Fig. 4.5) are similar for all three electrolytes at mildly negative potentials (approximately $-0.6\ V$ *vs.* RHE) before diverging at more negative potentials.

- For Au, the facet distribution after corrosion (Fig. A.29) is virtually identical for corrosion in both $5\ M$ NaOH and KOH.

These observations suggest that the cation is of limited relevance in determining the electrode structure at mildly negative potentials, but of large significance at more negative potentials. This might be due to an increased adsorbed cation coverage at more negative potentials, as is explained in Appendix A. Such a coverage dependence might imply an interplay between both adsorbed cations and adsorbed hydrogen. This would be consistent with our mechanistic hypothesis regarding ternary metal hydrides.

**Implications for electrode structuring**

Regardless of the exact mechanisms that underlie the final structure of corroded electrodes, the current work provides a detailed characterization of the cathodic corrosion behavior of various combinations of electrode materials and electrolyte alkali metal cations. These results are particularly relevant when employing cathodic corrosion to

alter the surface of metallic electrodes. Hence, we will end our discussion with recommendations for structuring electrodes by cathodic corrosion. The first three sets of recommendations are metal-specific:

– Platinum generally prefers forming (100) sites during cathodic corrosion. However, the extent of this preference can be significantly tuned by varying both the identity and concentration of the alkali metal cations in the electrolyte. The strongest preference for forming well-defined (100) terraces without creating steps is found for corrosion in $5\,M$ NaOH. If LiOH is used instead, the corroded electrodes appear smoother in SEM (Fig. 4.4, Fig. A.16 and Fig. A.19) and expose slightly less (100) terraces in voltammetry. Accordingly, changing the cation to K$^+$ induces the formation a rougher and (at $5\,M$ concentrations) more disordered surface.

– Rhodium exhibits a minor (100) preference, which is strongest in NaOH. NaOH is also the electrolyte of choice when a large surface area increase is desired. If less surface area and (100) preference are required, LiOH and KOH are more appropriate working electrolytes: corrosion in LiOH creates surfaces that appear in SEM to retain most of their original morphology, while KOH induces nano-sized corrugation and slightly more roughness on the electrode.

– For gold, cathodic corrosion should be carried out at more negative potentials than for platinum and rhodium. When doing so, corrosion in LiOH creates electrodes with moderate roughening, exhibiting some well-defined (100) and (111) etch pits. More severe roughening is present after corrosion in NaOH, which creates most roughening and large (111)-oriented particles. Newly formed (111) sites are most clearly expressed in $10\,M$ NaOH, where the (111) oxide peak can be quite well-defined (Chapter 3). Finally, corrosion in KOH creates intermediate degrees of surface area, accompanied by corrugation along grain boundaries.

Finally, we will conclude our recommendations with three more general notes:

– Both this chapter and Chapter 2 & 3 indicate crystallographic preferences in cathodic corrosion: clear facet preferences can be identified and corrosion appears most pronounced around grain boundaries and, in case of un-annealed Rh & Au electrodes, in areas close to where the electrodes were cut from the spool with wire cutters. This parallels previous findings in nanoparticle synthesis through cathodic corrosion, which achieved the most well-defined nanoparticles after pro-

longed annealing of the parent electrode.[12] The extent of corrosion may therefore vary, depending on the initial state of the electrode: more or less corrosion than found in the current work may be observed if mechanical stress is reduced by annealing or introduced by methods like mechanical polishing.

– Our recommendations are strictly valid in the studied potential range. Though more negative potentials will likely just emphasize the findings in the current work, exploring such potentials is encouraged when aiming to create an optimal surface structure. Similarly, if the target surface structure requires less corrosion, lower potentials can be chosen by consulting Fig. A.4 through Fig. A.27.

– Though the current work focuses on using pure alkali metal hydroxides to avoid overcomplicated analyses, different electrolytes might generate different and interesting results. Mixing cations to combine or balance their effects might be effective, as well as using entirely different cations. However, care should be taken not to choose cations that electrodeposit under the chosen corrosion conditions, in order to avoid the possible formation of metal overlayers or even alloy phases.[61]

## 4.4   Conclusions

The current work has explored the cathodic corrosion behavior of Pt, Rh and Au in LiOH, NaOH and KOH, in order to systematically assess the effect of the electrolyte cation. In doing so, it was found experimentally that both the concentration and identity of the cation can strongly affect the surface area and facet distribution of corroded electrodes, as well as the cathodic corrosion onset potential. These experimental results led to a set of concrete recommendations for employing cathodic corrosion to modify the structure of metallic electrodes for a specific purpose.

In addition to producing guidelines, we rationalized our experimental results by using first-principles calculations of cation adsorption. Importantly, the calculations indicate that cations are adsorbed at potentials where cathodic corrosion occurs. Though the calculations also satisfactorily reproduce the trend for (100) site formation for Pt in $1\,M$ LiOH, NaOH and KOH, they do not conclusively explain other trends in the onset potential, facet distribution and surface area increase after cathodic corrosion. More mechanistic information on cathodic corrosion is therefore required to explain the strong effect of cations on these factors.

Equally relevant for the onset of corrosion is perhaps the adsorption of hydrogen; an analysis of literature hydrogen adsorption values indicates a thermodynamic driving force for the creation of surface area. Importantly, this driving force matches the experimental trend in onset potentials between metals, *without* making any mechanistic assumptions.

By combining the observed relevance of hydrogen, electrolyte cations and the corroded electrode material, we postulate that the key reaction intermediate of cathodic corrosion might be a ternary metal hydride. Though the current work provides no direct evidence for such metal hydrides, their solid-state properties have been extensively studied and their occurrence would match several experimental observations. Notably, ternary metal hydrides would explain the importance of cations that has been explored in previous work and reaffirmed in the presented research. Ternary metal hydrides are therefore plausible reaction intermediates, which could serve as a starting point for further mechanistic studies of cathodic corrosion.

In conclusion, the current work on cathodic corrosion provides recommendations for electrode surface structuring, extensive information on the role of cations during DC cathodic corrosion and a testable hypothesis for the nature of the elusive cathodic corrosion reaction intermediate. As such, the work presented here is an essential step in both understanding and applying cathodic corrosion.

## 4.5   Acknowledgements

## References

1.   Haber, F. The Phenomenon of the Formation of Metallic Dust from Cathodes. *Transactions of the American Electrochemical Society* **2,** 189–196 (1902).

2.   Kabanov, B. N., Astakhov, I. I. & Kiseleva, I. G. Formation of crystalline intermetallic compounds and solid solutions in electrochemical incorporation of metals into cathodes. *Electrochimica Acta* **24,** 167–171 (1979).

3.   Liu, J., Huang, W., Chen, S. & Hu, S. Facile electrochemical dispersion of bulk Rh into hydrosols. *Int. J. Electrochem. Sci.* **4,** 1302–1308 (2009).

4.   Huang, W., Chen, S., Zheng, J. & Li, Z. Facile preparation of Pt hydrosols by dispersing bulk Pt with potential perturbations. *Electrochemistry Communications* **11,** 469–472 (2009).

5.  Leontyev, I., Kuriganova, A., Kudryavtsev, Y., Dkhil, B. & Smirnova, N. New life of a forgotten method: Electrochemical route toward highly efficient Pt/C catalysts for low-temperature fuel cells. *Applied Catalysis A: General* **431-432,** 120–125 (2012).

6.  Yanson, A. I. *et al.* Cathodic Corrosion: A Quick, Clean, and Versatile Method for the Synthesis of Metallic Nanoparticles. *Angewandte Chemie International Edition* **50,** 6346–6350 (2011).

7.  Gangal, U., Srivastava, M. & Sen Gupta, S. K. Mechanism of the Breakdown of Normal Electrolysis and the Transition to Contact Glow Discharge Electrolysis. *Journal of The Electrochemical Society* **156,** F131–F136 (2009).

8.  Strasser, P., Gliech, M., Kuehl, S. & Moeller, T. Electrochemical processes on solid shaped nanoparticles with defined facets. *Chemical Society Reviews* **47,** 715–735 (2018).

9.  Yanson, A., Antonov, P., Rodriguez, P. & Koper, M. Influence of the electrolyte concentration on the size and shape of platinum nanoparticles synthesized by cathodic corrosion. *Electrochimica Acta* **112,** 913–918 (2013).

10. Yanson, A., Antonov, P., Yanson, Y. & Koper, M. Controlling the size of platinum nanoparticles prepared by cathodic corrosion. *Electrochimica Acta* **110,** 796–800 (2013).

11. Feng, J. *et al.* Cathodic Corrosion of a Bulk Wire to Nonaggregated Functional Nanocrystals and Nanoalloys. *ACS Applied Materials & Interfaces* **10,** 9532–9540 (2018).

12. Duca, M., Rodriguez, P., Yanson, A. I. & Koper, M. T. M. Selective Electrocatalysis on Platinum Nanoparticles with Preferential (100) Orientation Prepared by Cathodic Corrosion. *Topics in Catalysis* **57,** 255–264 (2014).

13. Yanson, A. I. & Yanson, Y. I. Cathodic corrosion. II. Properties of nanoparticles synthesized by cathodic corrosion. *Low Temperature Physics* **39,** 312–317 (2013).

14. Peng, Z. & Yang, H. Designer platinum nanoparticles: Control of shape, composition in alloy, nanostructure and electrocatalytic property. *Nano Today* **4,** 143–164 (2009).

15. Van de Krol, R. in *Photoelectrochemical Hydrogen Production* (eds Van de Krol, R. & Grätzel, M.) 109 (Springer, Boston, MA, 2012).

16. Jeyabharathi, C., Ahrens, P., Hasse, U. & Scholz, F. Identification of low-index crystal planes of polycrystalline gold on the basis of electrochemical oxide layer formation. *Journal of Solid State Electrochemistry* **20,** 3025–3031 (2016).

17. Kresse, G. Ab initio molecular dynamics for liquid metals. *Journal of Non-Crystalline Solids* **192-193,** 222–229 (1995).

18. Kresse, G. & Furthmüller, J. Efficiency of ab-initio total energy calculations for metals and semiconductors using a plane-wave basis set. *Computational Materials Science* **6,** 15–50 (1996).

19. Kresse, G. & Furthmüller, J. Efficient iterative schemes for ab initio total-energy calculations using a plane-wave basis set. *Physical Review B* **54,** 11169–11186 (1996).

20. Perdew, J. P., Burke, K. & Ernzerhof, M. Generalized Gradient Approximation Made Simple. *Physical Review Letters* **77,** 3865–3868 (1996).

21. Perdew, J. P., Burke, K. & Ernzerhof, M. Generalized Gradient Approximation Made Simple [Phys. Rev. Lett. 77, 3865 (1996)]. *Physical Review Letters* **78,** 1396–1396 (1997).

22. Blöchl, P. E. Projector augmented-wave method. *Physical Review B* **50,** 17953–17979 (1994).

23. Kresse, G. & Joubert, D. From ultrasoft pseudopotentials to the projector augmented-wave method. *Physical Review B* **59,** 1758–1775 (1999).

24. Monkhorst, H. J. & Pack, J. D. Special points for Brillouin-zone integrations. *Physical Review B* **13,** 5188–5192 (1976).

25. Bengtsson, L. Dipole correction for surface supercell calculations. *Physical Review B - Condensed Matter and Materials Physics* **59,** 12301–12304 (1999).

26. Mills, J. N., McCrum, I. T. & Janik, M. J. Alkali cation specific adsorption onto fcc(111) transition metal electrodes. *Phys. Chem. Chem. Phys.* **16,** 13699–13707 (2014).

27. McCrum, I. T. & Janik, M. J. pH and Alkali Cation Effects on the Pt Cyclic Voltammogram Explained Using Density Functional Theory. *The Journal of Physical Chemistry C* **120,** 457–471 (2016).

28. Ogasawara, H. *et al.* Structure and Bonding of Water on Pt(111). *Physical Review Letters* **89,** 276102 (2002).

29. He, Z.-D., Hanselman, S., Chen, Y.-X., Koper, M. T. M. & Calle-Vallejo, F. Importance of Solvation for the Accurate Prediction of Oxygen Reduction Activities of Pt-Based Electrocatalysts. *The Journal of Physical Chemistry Letters* **8,** 2243–2246 (2017).

30. Han, B., Viswanathan, V. & Pitsch, H. First-Principles Based Analysis of the Electrocatalytic Activity of the Unreconstructed Pt(100) Surface for Oxygen Reduction Reaction. *The Journal of Physical Chemistry C* **116,** 6174–6183 (2012).

31. Kolb, M. J. *et al.* Double-Stranded Water on Stepped Platinum Surfaces. *Physical Review Letters* **116,** 136101 (2016).

32. Momma, K. & Izumi, F. VESTA 3 for three-dimensional visualization of crystal, volumetric and morphology data. *Journal of Applied Crystallography* **44,** 1272–1276 (2011).

33. Varma, S. & Rempe, S. B. Coordination numbers of alkali metal ions in aqueous solutions. *Biophysical Chemistry* **124,** 192–199 (2006).

34. Resasco, J. *et al.* Promoter Effects of Alkali Metal Cations on the Electrochemical Reduction of Carbon Dioxide. *Journal of the American Chemical Society* **139,** 11277–11287 (2017).

35. Pérez-Gallent, E., Marcandalli, G., Figueiredo, M. C., Calle-Vallejo, F. & Koper, M. T. M. Structure- and Potential-Dependent Cation Effects on CO Reduction at Copper Single-Crystal Electrodes. *Journal of the American Chemical Society* **139,** 16412–16419 (2017).

36. Tran, R. *et al.* Surface energies of elemental crystals. *Scientific Data* **3,** 160080 (2016).

37. Ferrin, P., Kandoi, S., Nilekar, A. U. & Mavrikakis, M. Hydrogen adsorption, absorption and diffusion on and in transition metal surfaces: A DFT study. *Surface Science* **606,** 679–689 (2012).

38. Karlberg, G. S. *et al.* Cyclic Voltammograms for H on Pt(111) and Pt(100) from First Principles. *Physical Review Letters* **99,** 126101 (2007).

39. Skúlason, E. *et al.* Modeling the Electrochemical Hydrogen Oxidation and Evolution Reactions on the Basis of Density Functional Theory Calculations. *The Journal of Physical Chemistry C* **114,** 22374–22374 (2010).

40. McCrum, I. T., Hickner, M. A. & Janik, M. J. First-Principles Calculation of Pt Surface Energies in an Electrochemical Environment: Thermodynamic Driving Forces for Surface Faceting and Nanoparticle Reconstruction. *Langmuir* **33,** 7043–7052 (2017).

41. Koper, M. T. & Lukkien, J. J. Modeling the butterfly: the voltammetry of $(\sqrt{3} \times \sqrt{3})$R30° and p$(2 \times 2)$ overlayers on (111) electrodes. *Journal of Electroanalytical Chemistry* **485,** 161–165 (2000).

42. Garcia-Araez, N., Lukkien, J. J., Koper, M. T. & Feliu, J. M. Competitive adsorption of hydrogen and bromide on Pt(100): Mean-field approximation vs. Monte Carlo simulations. *Journal of Electroanalytical Chemistry* **588,** 1–14 (2006).

43. Solla-Gullón, J., Rodríguez, P., Herrero, E., Aldaz, A. & Feliu, J. M. Surface characterization of platinum electrodes. *Phys. Chem. Chem. Phys.* **10,** 1359–1373 (2008).

44. Chen, X., McCrum, I. T., Schwarz, K. A., Janik, M. J. & Koper, M. T. M. Co-adsorption of Cations as the Cause of the Apparent pH Dependence of Hydrogen Adsorption on a Stepped Platinum Single-Crystal Electrode. *Angewandte Chemie International Edition* **56,** 15025–15029 (2017).

45. McCrum, I. T. & Janik, M. J. First Principles Simulations of Cyclic Voltammograms on Stepped Pt(553) and Pt(533) Electrode Surfaces. *ChemElectroChem* **3,** 1609–1617 (2016).

46. Vidal-Iglesias, F. J., Arán-Ais, R. M., Solla-Gullón, J., Herrero, E. & Feliu, J. M. Electrochemical Characterization of Shape-Controlled Pt Nanoparticles in Different Supporting Electrolytes. *ACS Catalysis* **2,** 901–910 (2012).

47. Xu, Q., Linke, U., Bujak, R. & Wandlowski, T. Preparation and electrochemical characterization of low-index rhodium single crystal electrodes in sulfuric acid. *Electrochimica Acta* **54,** 5509–5521 (2009).

48. Štrbac, S., Adžić, R. & Hamelin, A. Oxide formation on gold single crystal stepped surfaces. *Journal of Electroanalytical Chemistry and Interfacial Electrochemistry* **249,** 291–310 (1988).

49. Kibler, L. A. *Preparation and Characterization of Noble Metal Single Crystal Electrode Surfaces* 2003.

50. Trasatti, S. & Petrii, O. Real surface area measurements in electrochemistry. *Pure and applied chemistry* **63,** 711–734 (1991).

51. Li, H. *et al.* Why (1 0 0) Terraces Break and Make Bonds: Oxidation of Dimethyl Ether on Platinum Single-Crystal Electrodes. *Journal of the American Chemical Society* **135,** 14329–14338 (2013).

52. Li, H., Li, Y., Koper, M. T. M. & Calle-Vallejo, F. Bond-Making and Breaking between Carbon, Nitrogen, and Oxygen in Electrocatalysis. *Journal of the American Chemical Society* **136,** 15694–15701 (2014).

53. Calle-Vallejo, F., Loffreda, D., Koper, M. T. M. & Sautet, P. Introducing structural sensitivity into adsorption–energy scaling relations by means of coordination numbers. *Nature Chemistry* **7,** 403–410 (2015).

54. Firman, T. K. & Landis, C. R. Structure and Electron Counting in Ternary Transition Metal Hydrides. *Journal of the American Chemical Society* **120,** 12650–12656 (1998).

55. Yvon, K. & Renaudin, G. in *Encyclopedia of Inorganic Chemistry* (eds King, R. B., Crabtree, R. H., Lukehart, C. M., Atwood, D. A. & Scott, R. A.) 2nd ed., 1814–1846 (John Wiley & Sons, Ltd, Chichester, UK, 2006).

56. Orgaz, E. & Gupta, M. Chemical bonding features of the ternary alkali metal platinum and palladium hydrides. *International Journal of Quantum Chemistry* **80,** 141–152 (2000).

57. Bronger, W., Müller, P., Schmitz, D. & Spittank, H. Synthese und Struktur von Na2PtH4, einem ternären Hydrid mit quadratisch planaren PtH42-Baugruppen. *Zeitschrift für anorganische und allgemeine Chemie* **516,** 35–41 (1984).

58. Wang, X. & Andrews, L. Gold Is Noble but Gold Hydride Anions Are Stable. *Angewandte Chemie International Edition* **42,** 5201–5206 (2003).

59. Rahm, M., Hoffmann, R. & Ashcroft, N. W. Ternary Gold Hydrides: Routes to Stable and Potentially Superconducting Compounds. *Journal of the American Chemical Society* **139,** 8740–8751 (2017).

60. Suchanek, E., Lange, N., Auffermann, G., Bronger, W. & Lutz, H. D. Raman spectroscopic studies on palladium and platinum hydrido complexes. *Journal of Raman Spectroscopy* **30,** 981–986 (1999).

61. Bennett, E. *et al.* A Synthetic Route for the Effective Preparation of Metal Alloy Nanoparticles and Their Use as Active Electrocatalysts. *ACS Catalysis* **6,** 1533–1539 (2016).
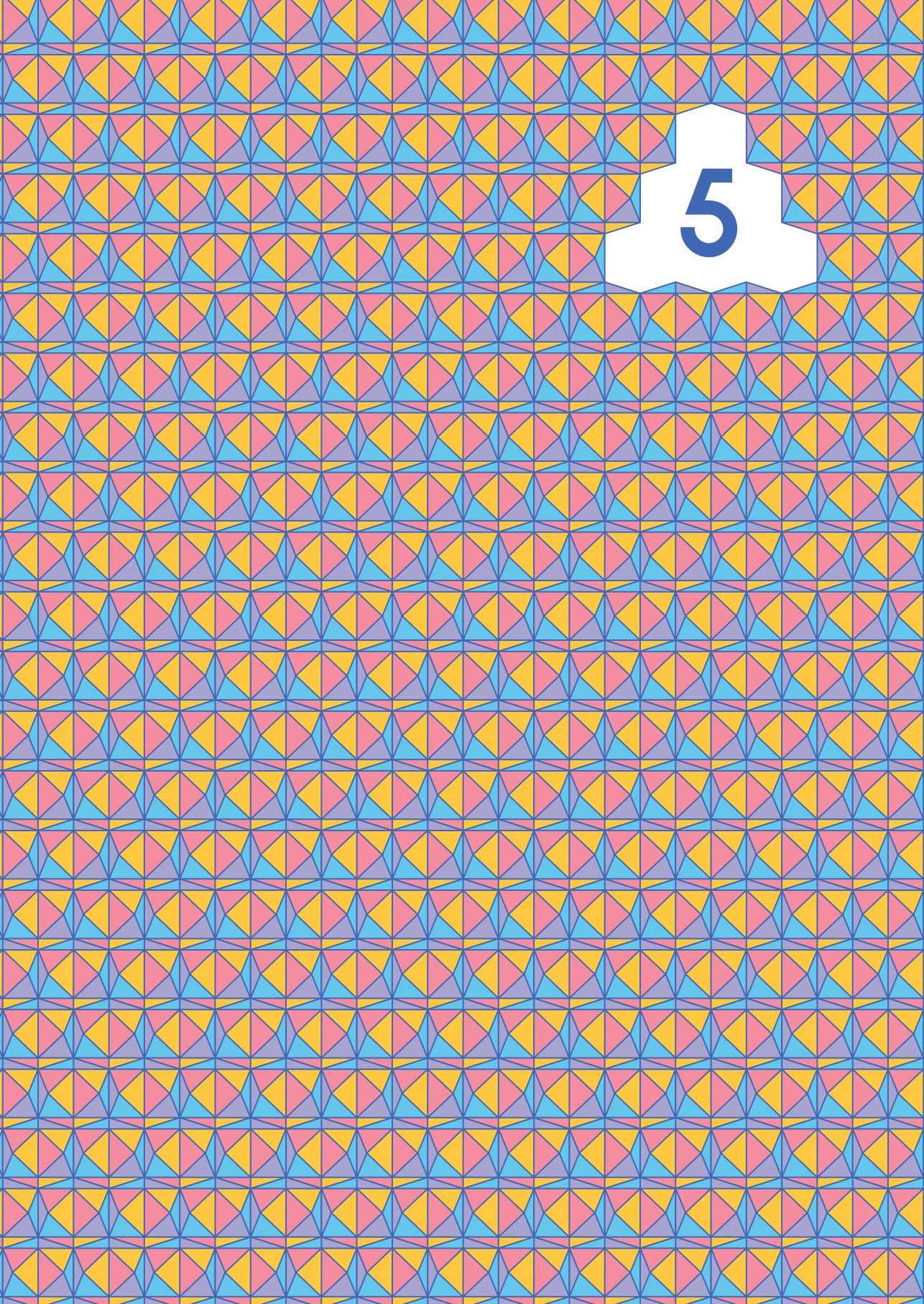
5

# *Operando* HERFD-XANES Investigation of Pt during Cathodic Corrosion

*Cathodic corrosion is a chemical etching phenomenon that likely occurs by forming a metal-containing anion. Though such an anion would be consistent with all experiments of cathodic corrosion, there is currently no direct evidence for its existence. The current chapter aims to provide this evidence by using X-ray absorption spectroscopy (XAS). XAS will be used to characterize platinum nanoparticles during cathodic corrosion in 10 M NaOH. The chemical state of these particles is characterized using the X-ray absorption near edge structure (XANES), which is recorded in the high-energy resolution fluorescence detection (HERFD) configuration. This experimental design can detect small changes in the Pt sample during corrosion. These changes are quantified and compared to theoretically simulated X-ray absorption spectra. This analysis supports the existence of $Na_2PtH_6$ during cathodic corrosion. As such, the presented work provides experimental results that indicate the nature of the enigmatic cathodic corrosion immediate. In addition, the current results are, to our best knowledge, the first measurements indicating the generation of ternary metal hydrides in water.*

## 5.1   Introduction

Cathodic corrosion is a chemical process that dramatically etches surfaces of many metals.[1–4] Though this enigmatic phenomenon has been the subject of persistent fundamental characterization efforts, its underlying reaction mechanism is still unknown. An important reason for this lack of understanding is the short-lived nature of the main reaction intermediate. This reaction intermediate cannot be isolated for *ex-situ* characterization; instead, only cathodically corroded metallic surfaces (Chapter 2–4) or the metal (oxide) nanoparticle products of cathodic corrosion have been studied.[2,5–9] To characterize the elusive reaction intermediate, it is therefore imperative to use *operando* techniques that probe the intermediate while it is being generated during cathodic corrosion.

Typical *operando* or *in-situ* characterization techniques rely on spectroscopy to probe either the oxidation state or chemical environment of a sample. In the present case, this would allow for identifying whether the corroding species resembles a metallic anion or perhaps a ternary metal hydride, as suggested in Chapter 4. However, many spectroscopic techniques are incompatible with the challenging electrode environment during cathodic corrosion.

For example, a technique such as Fourier-transform infrared spectroscopy (FTIR) can detect adsorbed species like hydrogen,[10] but it is generally incompatible with hydrogen bubbles that form during cathodic corrosion.[11] Hydrogen bubbles are less problematic for techniques such as surface-enhanced Raman spectroscopy (SERS), but bubble-compatible SERS requires the use of atomically thin metallic layers that will likely degrade quickly during cathodic corrosion.[12,13] A third spectroscopic technique is Mössbauer spectroscopy, which can detect oxidation state changes of elements such as gold,[14] but cannot detect dissolved species such as the species of interest during cathodic corrosion.[15]

A more suitable spectroscopic technique for studying cathodic corrosion is X-ray absorption spectroscopy (XAS).[16] XAS and, more specifically, X-ray absorption near edge structure (XANES) experiments can generate a wealth of information on both the oxidation state and presence of adsorbates of the sample of interest: *in-situ* XANES studies of Pt samples have previously been used assess the Pt d-band filling, Pt oxidation state and the presence of adsorbed species like *H, and *CO.[17–21] XANES can also be used during electrochemical measurements if the experimental setup is carefully designed.[22–26]

*Operando* XANES is therefore used in this chapter to study Pt nanoparticles during cathodic corrosion. These experiments are carried out in a flow cell, to reduce interference by bubble formation during experiments. Furthermore, the experiments are performed in the high-energy resolution fluorescence detection (HERFD) configuration, which significantly improves important features in the XANES spectrum.[21,26] In doing so, we can detect a subtle shift in the absorption edge position and decrease in white line intensity during cathodic corrosion. Further analysis of these spectral changes and theoretical modeling of XANES spectra suggests the existence of $Na_2PtH_6$ during cathodic corrosion. Though definitive proof of $Na_2PtH_6$ during cathodic corrosion requires further theoretical and experimental efforts, the results presented here support the "ternary metal hydride" hypothesis for cathodic corrosion.

## 5.2   Materials and methods

### 5.2.1   *Operando* XANES measurements

*Operando* HERFD-XANES experiments of the platinum L$_{III}$ edge were carried out at beamline 6-2 of the Stanford Synchrotron Radiation Lightsource (SSRL). At this beamline, the incoming photon beam was passed through a double-crystal Si(311) monochromator. After the monochromation, the beam was reflected by a Rh-coated mirror. This parabolic mirror rejected harmonic photons from the beam and focused the beam onto the sample with a beam height of 420 $\mu m$ full width at half maximum (FWHM) and a beam width of 129 $\mu m$ FWHM. The incoming beam and the sample were aligned in grazing incidence, with the electric field vector of the beam parallel to the sample surface. The beam energy was calibrated before measurements with respect to a metallic Pt foil; for calibration, the first inflection point of the Pt L$_{III}$ edge was assigned a value of 11563.7 $eV$.

After absorption of the X-rays by the sample, the fluorescent Pt $L_{\alpha 1}$ X-rays with an energy of 9442 $eV$ were detected with a Johann-type X-ray spectrometer.[27] These X-rays were selectively diffracted onto the X-ray detector by using the (660) Bragg reflection of five Ge(110) crystals with a radius of curvature of 1 $m$. This setup had a combined monochromator and detector resolution of 1.0 $eV$.

### 5.2.2   Electrochemical XANES cell

For the *operando* XAS measurements, a home-made flow cell was used. In this cell, displayed in Fig. 5.1, the working electrode was the lowest point, such that the incoming beam (shown in red) could hit the sample unimpaired. Similarly, the detected outgoing Pt $L_{\alpha 1}$ X-rays (shown in grey) were able to travel towards the detector without hitting parts of the cell. More detailed descriptions and schematic drawings of the cell are given in Appendix B.

The working electrolyte was 10 $M$ NaOH (Merck, Suprapur), which was stored in a fluorinated ethylene propylene (FEP) bottle and pumped into the cell through perfluoroalkoxy alkane (PFA) tubing. The electrolyte was pumped through the cell with a peristaltic pump (Ismatec IP-N), which was fitted with $\varnothing = 3.17\ mm$ phthalate-free polyvinyl chloride (PVC) tubing and operated at a flow rate of 10 $mL \cdot min^{-1}$.

Within the cell channel, a thin Pt (Mateck, 99.9%) counter electrode strip was placed alongside the working electrode and a Gaskatel 'HydroFlex' reversible hydrogen electrode (RHE) was placed downstream from the working electrode. The working electrode
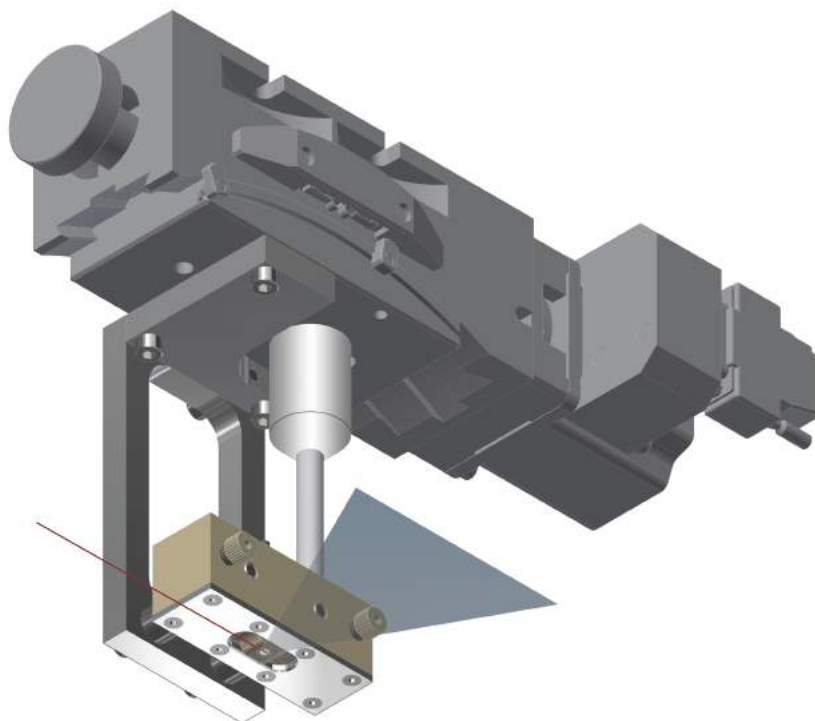
**Fig. 5.1 |** Schematic view of the *operando* XANES cell. The ingoing X-ray beam is indicated by the thin red line, while the detected outgoing fluorescent X-rays are visualized in grey.

consisted of a $\varnothing = 3\ mm$ gold (Alfa Aesar, 99.9985%) disk. The electrode contained a $22.5\ \mu g$ loading of surfactant-free Pt nanoparticles, which was drop-casted onto the electrode from a $0.5\ mg \cdot mL^{-1}$ solution in water. These nanoparticles were dried under a helium stream.

### 5.2.3 Nanoparticle preparation

The nanoparticles were prepared through cathodic corrosion,[2] by applying a $100\ Hz$ square wave potential with $-5V/+2V$ *vs.* RHE potential limits. This potential program was 85% IR corrected and applied by a Bio-Logic SP-300 potentiostat (connected to a $2A/30V$ booster board), using a HydroFlex RHE electrode (Gaskatel) and a graphite rod (Alfa Aesar, Ultra "F" purity) counter electrode. The corrosion electrolyte was $5\ M$ KOH (Sigma-Aldrich, 99.99% trace metals basis), held within an FEP container. Using this configuration, a $\varnothing = 0.1\ mm$ Pt wire (Mateck, 99.99%) was immersed for $1\ mm$ and cor-

roded until the entire wire was consumed. This step was repeated twice, after which the nanoparticles were purified through ultracentrifugation: the particles were centrifuged and the supernatant was replaced with clean water. The latter step was repeated until the supernatant pH was neutral.

### 5.2.4 Cleaning and experiment preparation

The abovementioned electrochemical setups were cleaned by storing the relevant parts overnight in a solution of $1\ g \cdot L^{-1}$ $KMnO_4$ (Fluka, ACS reagent) and $0.5\ M$ $H_2SO_4$ (Fluka, ACS reagent). This solution was removed before experiments, and any $KMnO_4$ residues were decomposed with dilute $H_2O_2$ (Merck, Emprove exp). This solution was then also removed, after which the parts were boiled five times in water. All water used in this work (resistivity $> 18.2\ M\Omega \cdot cm$, TOC $< 5\ ppb$) was cleaned using a Millipore MilliQ system. During *operando* experiments, all potentials were 85% IR corrected and applied by a Bio-Logic SP-300 potentiostat. Use of a booster board was not necessary.

### 5.2.5 Data processing and normalization

Using the aforementioned cell and preparation procedure, X-ray absorption spectra could be measured during electrochemical experiments. Low-noise spectra were achieved in absence of gas evolution on the working electrode, such that only four spectra needed to be recorded and averaged to yield the presented spectra. More spectra were recorded during significant gas evolution ($-0.4\ V$ *vs.* RHE and below), to compensate for noise due to bubble formation and breaking. If bubble formation led to anomalous features in spectra, these spectra were eliminated from the analysis; about 8 scans were averaged per applied potential to yield the presented data. In total, two samples, denoted sample 1 and 2 were measured at various potentials. Though both samples yielded qualitatively similar data, sample 1 is the one presented here because its spectra contained the least bubble-induced noise.

Data alignment was performed to account for shifts in the monochromator position during experiments. This was done in IgorPro by shifting the crystal glitch position to a known value. The spectra were subsequently averaged, flattened and normalized by setting the edge jump to one in ATHENA.[28] To explicitly express this normalization, all absorption spectra are plotted in y-axis units of 'edge fraction', where a value of one equals the edge jump.[16]

### 5.2.6   Theoretical modeling of X-ray absorption spectra

Calculations of the core edge spectroscopy were performed within the OCEAN package.[29,30] This first principles code generates X-ray absorption spectra based on both ground-state density functional theory (DFT) and the numerical solution of the Bethe-Salpeter equation (BSE) within a basis of electron and hole states (and associated core-hole dielectric screening) provided by the DFT Kohn-Sham orbitals.[31,32] The DFT electronic structure was calculated within the generalized gradient approximation using the Quantum ESPRESSO code,[33] and the BSE equation was solved with the NBSE program.[30] Efficient numerical sampling of the Brillouin zone was enabled through the use of the Shirley interpolation scheme.[34] The DFT plane-wave basis cut-off energy was set to $100\ Ry$ using the Perdew-Berke-Ernzerhof (PBE) functional within the generalized gradient approximation (GGA).[35,36] The final states were included up to an energy range of 150 eV. The k-points used in the calculations were $12 \times 12 \times 12$, $12 \times 12 \times 12$, $6 \times 6 \times 6$, and $6 \times 6 \times 6$ for bulk Pt metal,[37] $\alpha$-$PtO_2$,[38] $Na_2HPt_4$,[39] and $Na_2HPt_6$,[40] respectively. The real-space mesh for the BSE calculation was $12 \times 12 \times 12$, $12 \times 12 \times 12$, $6 \times 6 \times 6$, and $6 \times 6 \times 6$ for bulk Pt metal, $\alpha$-$PtO_2$, $Na_2HPt_4$, and $Na_2HPt_6$, respectively. The radius of the sphere in which the local basis is calculated was set to $5\ Bohr$ to construct the PAW-style optimal projector functions (OPF). The screening of the core-hole interaction was done in real space using the random phase approximation up to a radius around the core of $5\ Bohr$.[41] The calculated Pt $L_{III}$ edge spectra were numerically broadened via convolution with a Lorentzian with a half width at half maximum (HWHM) of $1.3\ eV$ to match the broadening obtained from the HERFD mode utilized in the XAS experiments. The core-level shift was obtained through calculations for the Pt metal and then applied to the other Pt compounds. The simulated spectra were normalized with ATHENA.[28] Then, a single constant energy shift was applied to these simulated spectra to align them with the experimental data. Specifically, the calculated Pt spectrum was shifted to have the first inflection point match that of the experimental spectrum at a potential of $0.4\ V$ *vs.* RHE: $11564.4\ eV$. The absolute shift to achieve this value was then applied to the other calculated spectra.

## 5.3   Results and discussion

In this section, we will first present X-ray absorption spectra of Pt nanoparticles at both cathodic and anodic potentials. We will then analyze these spectra qualitatively through the use of difference spectra and quantitatively by peak fitting. The spectra will then be
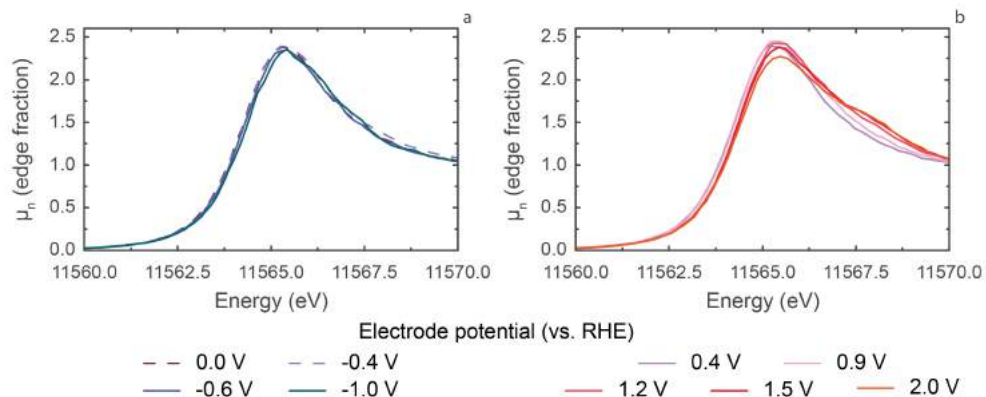
**Fig. 5.2 |** HERFD-XANES spectra of electrodes polarized at cathodic potentials **(a)** and anodic potentials **(b)**.

compared to modeled spectra of ternary metal hydrides, which we consider plausible reaction intermediates (Chapter 4).

### 5.3.1   Absorption spectra at anodic and cathodic potentials

Fig. 5.2 displays XANES spectra of the studied nanoparticles at both anodic and cathodic potentials. The same spectra are shown in a wider energy range in Fig. B.3.

We will first focus on the spectra taken at anodic potentials (Fig. 5.2 **b**), because these spectra can be compared with previous HERFD-XANES studies for Pt nanoparticle oxidation. The spectra in Fig. 5.2 **b** gradually shift towards more positive energies as the electrode potential increases. This shift is well documented and is related to interactions between the Pt particles and oxygen.[22–26] The small initial shift between 0.4 and 0.9 *V vs.* RHE is subtle and corresponds to the adsorption of oxygen-containing species, such as *OH,[42,43] onto the electrode.[22] The more substantial shifts at more anodic potentials correspond to oxidation of the surface and the formation of platinum oxides.[22]

The aforementioned shifts are accompanied by the formation of a shoulder between 11567.5 and 11570 *eV*. This shoulder is located approximately 2 *eV* above the white line absorption peak and therefore likely corresponds to the formation of $\alpha$-PtO$_2$:[26] the most likely oxide phase for thermally and electrochemically oxidized platinum.[23,44,45]

Interestingly, this shoulder is smaller in magnitude than previously reported peaks for electrochemically oxidized platinum nanoparticles and monolayers.[22–26] We ascribe this difference to a significant amount of Pt atoms remaining un-oxidized in the current

experiment. Oxidation of the nanoparticles was therefore likely restricted to the outer nanoparticle shell. This could partly be due to the difference between our 10 *M* NaOH electrolyte and the 0.01–0.1 *M* HClO$_4$ electrolytes used in previous literature experiment. However, the most probable reason for the lower degree of oxidation is a difference in nanoparticle size. Our particles are likely between 6 and 11 *nm* in size,[46] which is much larger than the previously studied 1.2 *nm* particles.[25] Our particles therefore possess a much lower surface-to-bulk atom ratio and, thus, are not oxidized as much as smaller nanoparticles, monolayers and nano-islands.[22–26] Nonetheless, the particles studied here exhibit detectable shifts in the absorption spectrum that match the available literature. This confirms that the current setup is sensitive towards changes in the platinum oxidation state.

After confirming that the current system can reproduce the known oxidative behavior of Pt, we can now explore the spectral changes under cathodic potentials. These results are shown in Fig. 5.2 **a**. In this panel, the most positive spectrum was recorded at 0 *V vs.* RHE. This spectrum overlaps well with the spectrum at 0.4 *V vs.* RHE, as can be seen in Fig. B.4. Though both spectra are rather similar, the spectrum at 0 *V vs.* RHE has a slightly lower white line intensity and is slightly broader than the spectrum at 0.4 *V vs.* RHE. This subtle broadening is due to adsorbed hydrogen, which covers 60 to 100% of the electrode surface at 0 *V vs.* RHE:[42,47–49] electrochemically adsorbed hydrogen broadens the XANES spectrum of platinum.[24,25] The broadening observed in Fig. B.4 is more subtle than the previously reported broadening, which again indicates a lower surface sensitivity due to a larger nanoparticle size in the current experiments.

The broadening in Fig. B.4 is also present at more cathodic potentials (Fig. 5.2 **a**). However, more cathodic potentials also cause a constant and small positive absorption edge shift. This edge shift appears subtle, yet consistent.

### 5.3.2 Difference spectra

To emphasize changes in the absorption edge, difference XANES spectra were created. Such spectra have previously been used to detect adsorbed species on Pt.[19,20] In the present case, difference spectra were obtained by subtracting the XANES spectrum at 0.4 *V vs.* RHE from the other spectra. The result of this data treatment is presented in Fig. 5.3.

We will first comment on changes in the Pt difference spectrum at anodic potentials (Fig. 5.3 **b**). At moderate anodic potentials (0.9 *V*), the small positive peak in the differ-
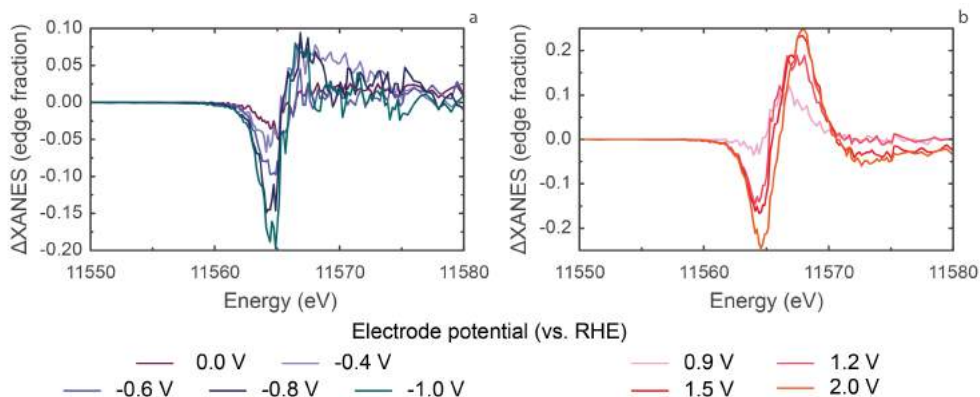
**Fig. 5.3 |** Difference spectra of electrodes polarized at cathodic potentials **(a)** and anodic potentials **(b)**. The reference spectrum for background subtraction was recorded at an applied potential of 0.4 *V vs.* RHE.

ence spectrum corresponds to a small shoulder in the normal spectrum (Fig. 5.2 **b**) that corresponds to the adsorption of *O or *OH.[22] At more anodic potentials, the growth of this peak is accompanied by a negative feature in the difference spectrum. This negative feature matches the corresponding edge shift in the normal XANES spectrum upon oxidation of the Pt nanoparticles. These negative and positive features in the difference spectra therefore facilitate the observation of more subtle features in the absolute absorption spectrum.

This enhancement also applies to spectra obtained at cathodic potentials, for which difference spectra are shown in Fig. 5.3 **a**. In these spectra, a negative peak is present at and below 0 *V vs.* RHE. This negative feature gradually develops at more cathodic potentials. At the most cathodic potentials, the negative feature appears to be accompanied by a positive feature between 11566 and 11567 *eV*. A more quantitative analysis is necessary to determine whether this positive feature is related to actual spectral changes, or rather due to random fluctuations in the absorption spectra.

### 5.3.3   Peak fitting

To quantitatively assess the data, we fitted several peaks to the spectra. Specifically, we fitted one pseudo-Voigt function at lower energies to account for the white line and one peak at higher energies to account for broadening of the spectra. These peaks will be referred to as the 'low-energy peak' and the 'high-energy peak', respectively. When fitting

these peaks, we accounted for the edge jump by including an arctangent function in the fitting procedure. This procedure and the fit parameters were based on a previous study of electrochemical Pt oxidation;[25] more details, all fit results and four representative fits are given in Appendix B. A summary of the fit results is given in Fig. 5.4. This figure presents the area of each of the peaks and the area of the sum of these peak, as a function of the applied potential.

In Fig. 5.4, the highest area is consistently found for the low-energy peak. This peak was previously ascribed to metallic Pt.[25] As such, Fig. 5.4 confirms that a significant part of the Pt nanoparticles remains metallic during the electrochemical experiments. The highest amount of metallic platinum is found at $0.4$ *V vs.* RHE. This is the expected state for Pt at this potential.[50]

At more anodic potentials, the area of the low-energy peak decreases, while the area of the high-energy peak increases. This increase of the high-energy peak agrees well with the oxidation of platinum, because this peak is located at energies where platinum oxides are generally observed.[22–26] The high-energy peak increase coincides with an increased sum of the peak areas. This peak area sum can be used as an indicator of the empty d-states and, by extension, the Pt oxidation state.[25] The increase of this peak therefore corresponds well with the expected oxidation of Pt at anodic potentials.

Accordingly, the peak sum decreases subtly at cathodic potentials. This has been observed before at $-0.04$ *V vs.* RHE in $0.1$ *M* $HClO_4$[25] and would suggest some degree of d-band filling with respect to Pt at $0.4$ *V vs.* RHE. Interestingly, the subtle decrease in sum peak area is accompanied by a decrease in the low-energy peak and an increase in the high-energy peak area. This indicates that the white line decrease and peak broadening in Fig. 5.2 are indeed caused by changes in the chemical nature of the Pt electrode.

### 5.3.4  Modeled XANES spectra

To explore these chemical changes, HERFD-XANES spectra were modeled using the OCEAN package.[29,30] We first modeled Pt and $\alpha$-$PtO_2$ spectra for comparison with the known anodic behavior of Pt. We then additionally modeled spectra of two candidate ternary metal hydrides: $Na_2PtH_4$ and $Na_2PtH_6$. These hydrides were chosen based on the suggestion of their existence in Chapter 4. The resulting calculated X-ray absorption spectra and corresponding difference spectra are plotted in Fig. 5.5. In this figure, Panel **a** features an energy range that matches the energy range in Fig. 5.2; expanded spectra are shown in Fig. B.6.
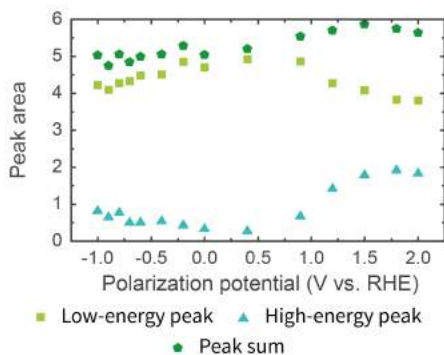
**Fig. 5.4** | Areas of the fitted low-energy peak, high-energy peak and the sum of both peaks. Full fit results are given in Appendix B.

For assessing the quality of the modeled spectra, it is instructive to evaluate the difference between Pt and $PtO_2$. This assessment is facilitated by aligning the first inflection point of the modeled Pt absorption edge with that of the experimental spectrum at 0.4 *V* *vs.* RHE. The relative shift in the white line maximum between our Pt and $\alpha$-$PtO_2$ models is 1.6 *eV*, which agrees well with the $\sim$ 2 *eV* shift observed experimentally. Our modeled Pt spectra also reproduce the positions of the various peaks in the experimental absorption spectrum, although the normalized intensity of peak features is overestimated. Finally, the difference spectrum of $PtO_2$ with a Pt background matches the anodic difference spectra in Fig. 5.2 **b** reasonably well: it crosses zero at 11565.6 *eV* (compared to our experimental 11565.3–11566.0 *eV*), and its peaks are 2.2 *eV* apart (compared to the experimental 3.1–3.4 *eV*). Based on these comparisons, our OCEAN simulations reasonably reproduce the experimental reference spectra.

Having established the applicability of our simulations, we will compare the theoretically modeled spectra for $Na_2PtH_4$ and $Na_2PtH_6$ with those of Pt. This comparison indicates that both hydrides have edge positions that are positive of the Pt edge position. Both hydrides also exhibit a white line peak, about 2.2–2.4 *eV* above that of Pt. Thirdly, both hydrides have isobestic points with Pt, at about 11567.2 *eV* ($Na_2PtH_4$ and 11566.6 *eV* ($Na_2PtH_6$). These isobestic points correspond to x-axis intercepts at the same positions in the difference spectra (Fig. 5.5 **b**). These difference spectra also contain a well-developed negative peak for both hydrides. A sharp positive peak is only present for $Na_2PtH_6$, after which the difference spectra slowly decreases to 0 at 11580 *eV*. In contrast, a broader positive peak is present for $Na_2PtH_4$. These features will be compared
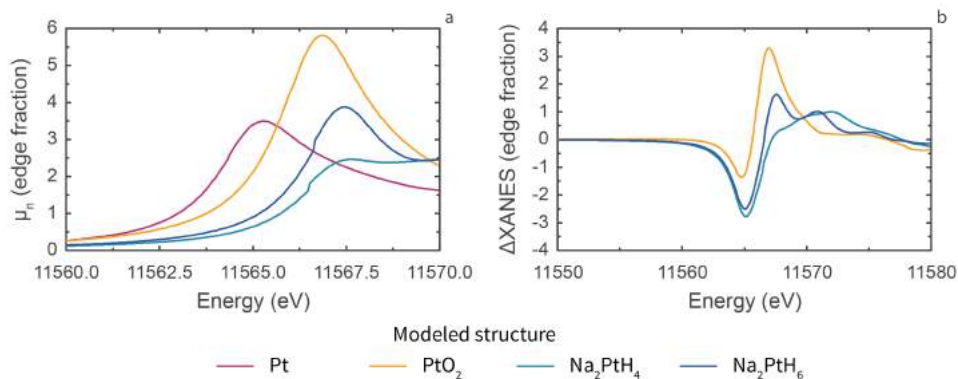
**Fig. 5.5 |** Modeled HERFD-XANES spectra **(a)** and difference spectra **(b)** for bulk Pt, $PtO_2$, $NaPtH_4$ and $Na_2PtH_6$. The reference spectrum for background subtraction in Panel **b** is the modeled spectrum for bulk Pt.

with the experimental difference spectra in the Discussion section.

### 5.3.5   Discussion

We established that the spectra of our Pt nanoparticles shift positive and a high-energy shoulder develops as the nanoparticles are partly oxidized to $\alpha$-$PtO_2$. The observed behavior of the nanoparticles is consistent with previous literature reports and supports the validity of the spectral changes at cathodic potentials.

It would be appealing to ascribe these changes to additional adsorbed hydrogen Under cathodic polarization, the Pt $L_{III}$ XANES (Fig. 5.2 **a**) show a small positive edge shift and subtle whiteline decrease; Fig. 5.3 **a** emphasizes this shift at all cathodic potentials. These difference spectra also reveal a small shoulder above $11566\,eV$. Though the shape of this shoulder is affected by the formation of hydrogen bubbles during cathodic corrosion, the peak appears to be a significant feature of the data. This is indicated by Fig. 5.4, in which a constantly increasing high-energy peak is required to fit the cathodic XANES spectra.

It would be appealing to ascribe these changes to additional adsorbed hydrogen at more cathodic potentials; such "overpotential adsorbed hydrogen" ($H_{OPD}$) has been detected at cathodic potentials through vibrational spectroscopy.[12,49] The presence of $H_{OPD}$ might even be inferred by the difference spectra (Fig. 5.3 **a**), which have similarly shaped difference spectra of Pt nanoparticles in a $H_2$ atmosphere.[19,20] However, adsorbed $H_{OPD}$ does not appear consistent with the experimental observations upon closer inspection of the presented data. Specifically, the shape of the difference spectra appears

quantitatively different from those of hydrogen-covered Pt nanoparticles.[19,20] For these previously studied particles, the difference spectra indeed contain a positive and negative peak, but the peaks are approximately $6\ eV$ apart and equal in magnitude. This contrasts with the peaks in Fig. 5.3, for which the negative peak can be more than twice as intense as the broad positive feature and the peaks are located more closely to each other.

A perhaps even more important observation is the magnitude of the observed difference spectra. For instance, the difference spectrum for $0\ V$ vs. RHE (Fig. 5.3 **a**) corresponds to adsorption of 0.6 to 1 monolayer of hydrogen. This spectrum is much more subtle than those at the most cathodic potentials, which have magnitudes up to 4.5 times as high. Similarly, the high-energy peak in Fig. 5.4 increases in area from $0.33\pm0.05$ to $0.81\pm0.09$. If these changes were caused by $H_{OPD}$ alone, the coverage would have to be in the order of several monolayers.

Therefore, it seems useful to explore alternative chemical species and compare the spectra in Fig. 5.3 to the modeled ternary metal hydride spectra in Fig. 5.5. At first glance, the $Na_2PtH_6$ spectrum in Fig. 5.5 appears most similar to the data. We therefore calculated linear combinations of the Pt and $Na_2PtH_6$ spectra to approximate nanoparticles that may be partly converted to $Na_2PtH_6$ during cathodic corrosion. These spectra were then converted into difference spectra by subtracting the modeled Pt spectrum from Fig. 5.5. An exemplary difference spectrum is plotted alongside two experimental spectra in Fig. 5.6.

The modeled difference spectrum in Fig. 5.6 corresponds to a linear combination of 94% Pt and 6% $Na_2PtH_6$. This difference spectrum matches the experimental cathodic spectra relatively well: it reproduces the difference between the negative and positive peak, the intensity ratio between both peaks, and the gradual decrease of the positive feature at higher absorption energies. The model spectrum might therefore be a reasonable approximation of Pt nanoparticles during cathodic corrosion in $10\ M$ NaOH.

The match between the data and modeled spectra in Fig. 5.6 and the arguments preceding this figure provide important indications towards the existence of a ternary metal hydride during cathodic corrosion. However, two considerations prevent us from conclusively claiming the presence of a hydride like $Na_2PtH_6$. Firstly, our current theoretical efforts do not contain a modeled spectrum of adsorbed hydrogen on Pt. Such a spectrum would be essential in a systematic comparison of model candidate reaction intermediates. OCEAN calculations regarding these spectra are currently being performed and will be reported when they are finished. Secondly, the current experiments are not immune to
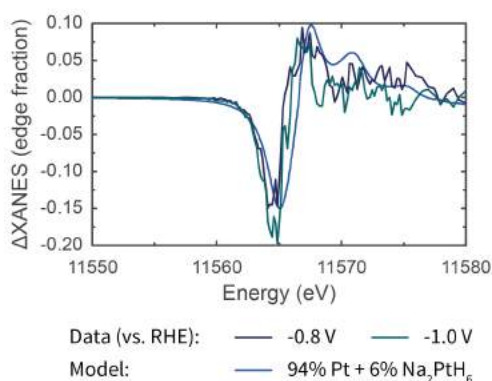
**Fig. 5.6 |** Difference spectra of electrodes polarized at −0.8 and −1.0 *V* vs. RHE. These spectra are plotted alongside a difference spectrum that is a linear combination of 94% of the modeled Pt spectrum and 6% of the modeled $Na_2PtH_6$ spectrum. For the data, the reference spectrum was that at 0.4 *V* vs. RHE. For the model, the reference spectrum is the modeled spectrum for pure Pt.

the effects of hydrogen bubbles. Though the use of a flow cell has significantly improved the signal-to-noise ratio when compared to initial experiments in a hanging-meniscus cell, the effect of bubbles is still visible in the presented spectra. These detrimental effects are amplified in further analysis using difference XANES spectra. The presented results might be improved by repeating them with samples that produce larger relative changes in the absorption spectrum. Such larger changes would then be more clearly distinguishable from noise due to hydrogen bubble formation. These pronounced changes could be achieved by using smaller nanoparticles, which should produce more clearly distinguishable spectral features.[25]

## 5.4 Conclusions

The current chapter has presented an *operando* HERFD-XANES investigation of Pt nanoparticles during cathodic corrosion. The chapter first established the proper functioning of the working setup by reproducing reported results on the anodic oxidation of Pt. After doing so, the cathodic behavior of Pt was studied.

This study of cathodically polarized Pt established a gradual shift in the Pt $L_{III}$ absorption edge. This shift was accompanied by a shoulder at higher absorption energies. These changes were corroborated by further analysis using difference absorption spec-

tra and a peak fitting procedure. These results could then be compared to first principles calculations of XANES spectra of ternary metal hydrides. From these simulated spectra, the spectrum of the $Na_2PtH_6$ model reproduced several key features in the experimental absorption spectra.

Though further theoretical computations of hydrogen-covered Pt are necessary and experiments with smaller nanoparticles would be desirable, the current results provide the first experimental indications of the existence of $Na_2PtH_6$ during cathodic corrosion. If proven correct, the presence of $Na_2PtH_6$ would, to our knowledge, be the first report of such ternary metal hydrides at the water-platinum interface. The presented results are therefore relevant for both cathodic corrosion and electrochemistry as a whole.

## 5.5   Acknowledgements

## References

1.   Haber, F. The Phenomenon of the Formation of Metallic Dust from Cathodes. *Transactions of the American Electrochemical Society* **2,** 189–196 (1902).

2.   Yanson, A. I. *et al.* Cathodic Corrosion: A Quick, Clean, and Versatile Method for the Synthesis of Metallic Nanoparticles. *Angewandte Chemie International Edition* **50,** 6346–6350 (2011).

3.   Yanson, Y. I. & Yanson, A. Cathodic corrosion. I. Mechanism of corrosion via formation of metal anions in aqueous medium. *Low Temperature Physics* **39,** 304–311 (2013).

4.   Yanson, A., Antonov, P., Rodriguez, P. & Koper, M. Influence of the electrolyte concentration on the size and shape of platinum nanoparticles synthesized by cathodic corrosion. *Electrochimica Acta* **112,** 913–918 (2013).

5.   Rodriguez, P., Tichelaar, F. D., Koper, M. T. M. & Yanson, A. I. Cathodic Corrosion as a Facile and Effective Method To Prepare Clean Metal Alloy Nanoparticles. *Journal of the American Chemical Society* **133,** 17626–17629 (2011).

6.   Bennett, E. *et al.* A Synthetic Route for the Effective Preparation of Metal Alloy Nanoparticles and Their Use as Active Electrocatalysts. *ACS Catalysis* **6,** 1533–1539 (2016).

7.   Kromer, M. L. *et al.* High-Throughput Preparation of Metal Oxide Nanocrystals by Cathodic Corrosion and Their Use as Active Photocatalysts. *Langmuir* **33,** 13295–13302 (2017).

8.  Feng, J. *et al.* Cathodic Corrosion of a Bulk Wire to Nonaggregated Functional Nanocrystals and Nanoalloys. *ACS Applied Materials & Interfaces* **10,** 9532–9540 (2018).

9.  Lawrence, M. J. *et al.* Electrochemical Synthesis of Nanostructured Metal-Doped Titanates and Investigation of Their Activity as Oxygen Evolution Photoanodes. *ACS Applied Energy Materials,* acsaem.8b00873 (2018).

10. Diaz-Morales, O., Hersbach, T. J. P., Badan, C., Garcia, A. C. & Koper, M. T. Hydrogen adsorption on nano-structured platinum electrodes. *Faraday Discussions* **210,** 301–315 (2018).

11. Nichols, R. & Bewick, A. Spectroscopic identification of the adsorbed intermediate in hydrogen evolution on platinum. *Journal of Electroanalytical Chemistry and Interfacial Electrochemistry* **243,** 445–453 (1988).

12. Jiang, Y.-X. *et al.* Characterization of surface water on Au core Pt-group metal shell nanoparticles coated electrodes by surface-enhanced Raman spectroscopy. *Chemical Communications,* 4608 (2007).

13. Wu, D.-Y., Li, J.-F., Ren, B. & Tian, Z.-Q. Electrochemical surface-enhanced Raman spectroscopy of nanostructures. *Chemical Society Reviews* **37,** 1025 (2008).

14. Dietzel, P. & Jansen, M. Synthesis and crystal structure determination of tetramethylammonium auride. *Chemical Communications* **21,** 2208–2209 (2001).

15. Long, G. & Grandjean, F. in *Comprehensive Coordination Chemistry II* 269–277 (Elsevier, 2003).

16. Calvin, S. *XAFS for Everyone* 1st ed. **1,** 427 (CRC Press, Boca Raton, FL, 2013).

17. Samant, M. G. & Boudart, M. Support effects on electronic structure of platinum clusters in Y zeolite. *The Journal of Physical Chemistry* **95,** 4070–4074 (1991).

18. Ichikuni, N. & Iwasawa, Y. In situ d electron density of Pt particles on supports by XANES. *Catalysis Letters* **20,** 87–95 (1993).

19. Behafarid, F. *et al.* Electronic properties and charge transfer phenomena in Pt nanoparticles on γ-Al2O3: size, shape, support, and adsorbate effects. *Physical Chemistry Chemical Physics* **14,** 11766 (2012).

20. Small, M. W., Sanchez, S. I., Marinkovic, N. S., Frenkel, A. I. & Nuzzo, R. G. Influence of Adsorbates on the Electronic Structure, Bond Strain, and Thermal Properties of an Alumina-Supported Pt Catalyst. *ACS Nano* **6,** 5583–5595 (2012).

21. Frenkel, A. I. *et al.* An in Situ Study of Bond Strains in 1 nm Pt Catalysts and Their Sensitivities to Cluster–Support and Cluster–Adsorbate Interactions. *The Journal of Physical Chemistry C* **117,** 23286–23294 (2013).

22. Friebel, D. *et al.* In situ X-ray probing reveals fingerprints of surface platinum oxide. *Phys. Chem. Chem. Phys.* **13,** 262–266 (2011).

23. Friebel, D., Miller, D. J., Nordlund, D., Ogasawara, H. & Nilsson, A. Degradation of Bimetallic Model Electrocatalysts: An In Situ X-Ray Absorption Spectroscopy Study. *Angewandte Chemie International Edition* **50,** 10190–10192 (2011).

24. Friebel, D. *et al.* Balance of Nanostructure and Bimetallic Interactions in Pt Model Fuel Cell Catalysts: In Situ XAS and DFT Study. *Journal of the American Chemical Society* **134,** 9664–9671 (2012).

25. Merte, L. R. *et al.* Electrochemical Oxidation of Size-Selected Pt Nanoparticles Studied Using in Situ High-Energy-Resolution X-ray Absorption Spectroscopy. *ACS Catalysis* **2,** 2371–2376 (2012).

26. Cui, Y.-T. *et al.* Wetting Induced Oxidation of Pt-based Nano Catalysts Revealed by In Situ High Energy Resolution X-ray Absorption Spectroscopy. *Scientific Reports* **7,** 1482 (2017).

27. Sokaras, D. *et al.* A seven-crystal Johann-type hard x-ray spectrometer at the Stanford Synchrotron Radiation Lightsource. *Review of Scientific Instruments* **84,** 053102 (2013).

28. Ravel, B. & Newville, M. ATHENA , ARTEMIS , HEPHAESTUS: data analysis for X-ray absorption spectroscopy using IFEFFIT. *Journal of Synchrotron Radiation* **12,** 537–541 (2005).

29. Vinson, J., Rehr, J. J., Kas, J. J. & Shirley, E. L. Bethe-Salpeter equation calculations of core excitation spectra. *Physical Review B* **83,** 115106 (2011).

30. Gilmore, K. *et al.* Efficient implementation of core-excitation Bethe–Salpeter equation calculations. *Computer Physics Communications* **197,** 109–117 (2015).

31. Kohn, W. & Sham, L. J. Self-Consistent Equations Including Exchange and Correlation Effects. *Physical Review* **140,** A1133–A1138 (1965).

32. Schwartz, C. P. *et al.* Temperature and radiation effects at the fluorine K-edge in LiF. *Journal of Electron Spectroscopy and Related Phenomena* **218,** 30–34 (2017).

33. Giannozzi, P. *et al.* QUANTUM ESPRESSO: a modular and open-source software project for quantum simulations of materials. *Journal of Physics: Condensed Matter* **21,** 395502 (2009).

34. Shirley, E. L. Optimal basis sets for detailed Brillouin-zone integrations. *Physical Review B* **54,** 16464–16469 (1996).

35. Perdew, J. P., Burke, K. & Ernzerhof, M. Generalized Gradient Approximation Made Simple. *Physical Review Letters* **77,** 3865–3868 (1996).

36. Perdew, J. P., Burke, K. & Ernzerhof, M. Generalized Gradient Approximation Made Simple [Phys. Rev. Lett. 77, 3865 (1996)]. *Physical Review Letters* **78,** 1396–1396 (1997).

37. Swanson, H. E. & Tatge, E. *Standard X-ray Diffraction Powder Patterns* (eds Swanson, H. E. & Tatge, E.) (U.S. Government Printing Office, Washington, 1953).

38. McBride, J. R., Graham, G. W., Peters, C. R. & Weber, W. H. Growth and characterization of reactively sputtered thin-film platinum oxides. *Journal of Applied Physics* **69,** 1596–1604 (1991).

39. Bronger, W., Müller, P., Schmitz, D. & Spittank, H. Synthese und Struktur von Na2PtH4, einem ternären Hydrid mit quadratisch planaren PtH42-Baugruppen. *Zeitschrift für anorganische und allgemeine Chemie* **516,** 35–41 (1984).

40. Ghebouli, M. *et al.* Theoretical prediction of the fundamental properties for the ternary Li2PtH6 and Na2PtH6. *Journal of Solid State Chemistry* **196,** 498–503 (2012).

41. Shirley, E. L. Local screening of a core hole: A real-space approach applied to hafnium oxide. *Ultramicroscopy* **106,** 986–993 (2006).

42. McCrum, I. T., Hickner, M. A. & Janik, M. J. First-Principles Calculation of Pt Surface Energies in an Electrochemical Environment: Thermodynamic Driving Forces for Surface Faceting and Nanoparticle Reconstruction. *Langmuir* **33,** 7043–7052 (2017).

43. Chen, X., McCrum, I. T., Schwarz, K. A., Janik, M. J. & Koper, M. T. M. Co-adsorption of Cations as the Cause of the Apparent pH Dependence of Hydrogen Adsorption on a Stepped Platinum Single-Crystal Electrode. *Angewandte Chemie International Edition* **56,** 15025–15029 (2017).

44. Miller, D. J. *et al.* Oxidation of Pt(111) under Near-Ambient Conditions. *Physical Review Letters* **107,** 195502 (2011).

45. Huang, Y.-F., Kooyman, P. J. & Koper, M. T. M. Intermediate stages of electrochemical oxidation of single-crystalline platinum revealed by in situ Raman spectroscopy. *Nature Communications* **7,** 12440 (2016).

46. Yanson, A., Antonov, P., Yanson, Y. & Koper, M. Controlling the size of platinum nanoparticles prepared by cathodic corrosion. *Electrochimica Acta* **110,** 796–800 (2013).

47. Koper, M. T. & Lukkien, J. J. Modeling the butterfly: the voltammetry of $(\sqrt{3} \times \sqrt{3})$R30° and p(2 × 2) overlayers on (111) electrodes. *Journal of Electroanalytical Chemistry* **485,** 161–165 (2000).

48. Garcia-Araez, N., Lukkien, J. J., Koper, M. T. & Feliu, J. M. Competitive adsorption of hydrogen and bromide on Pt(100): Mean-field approximation vs. Monte Carlo simulations. *Journal of Electroanalytical Chemistry* **588,** 1–14 (2006).

49. Jerkiewicz, G. Electrochemical Hydrogen Adsorption and Absorption. Part 1: Under-potential Deposition of Hydrogen. *Electrocatalysis* **1,** 179–199 (2010).

50. Pourbaix, M. *Atlas of electrochemical equilibria in aqueous solutions* 2nd ed., 644 (National Association of Corrosion Engineers, 1974).
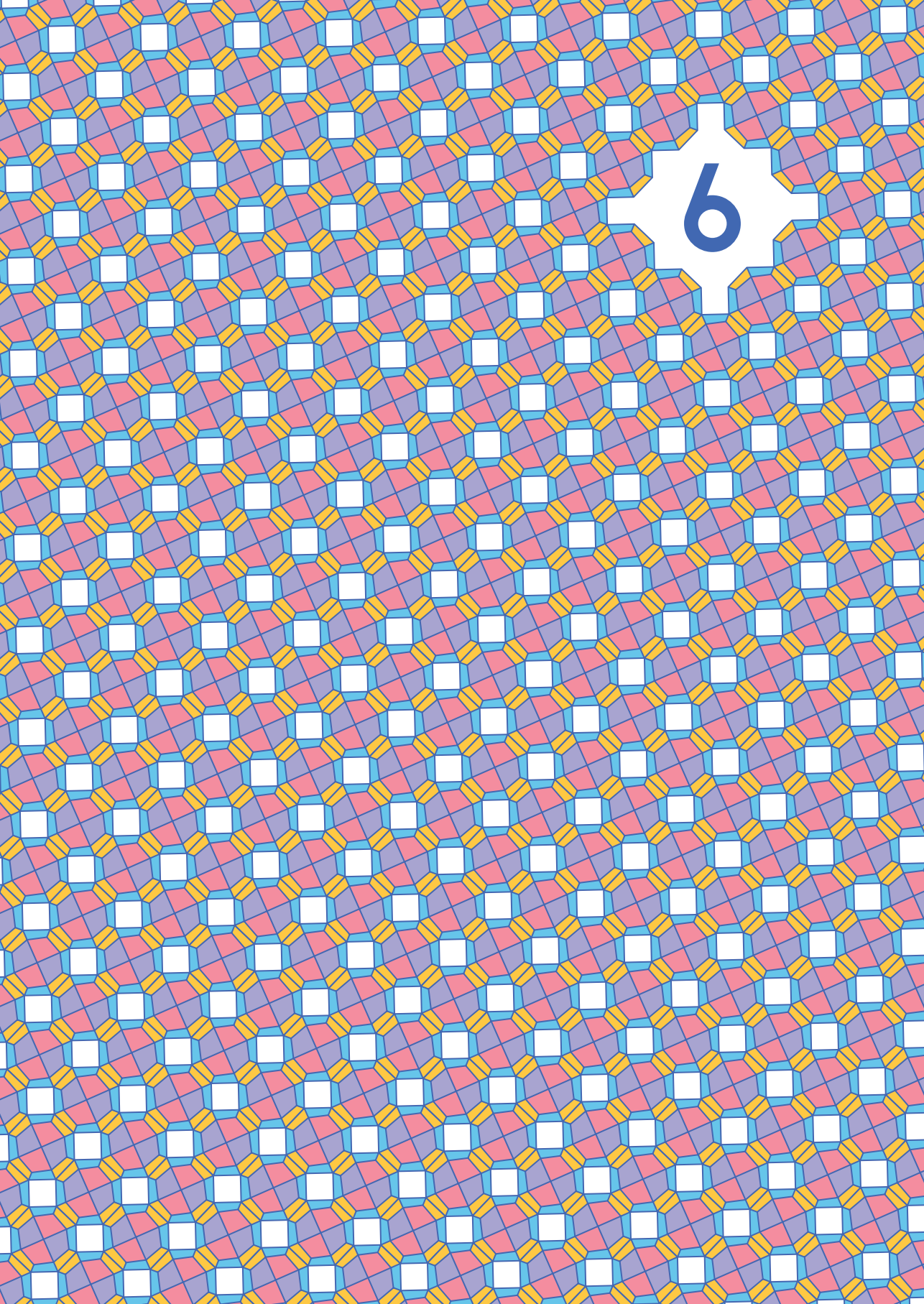
6

# Enhancement of Oxygen Reduction Activity of Pt(111) through Mild Cathodic Corrosion

*The oxygen reduction reaction (ORR) is a crucial half-reaction of fuel cells. Effectively promoting the ORR is therefore of prime importance in developing commercially viable fuel cells. Unfortunately, many common ORR catalysts have activities that are well below the theoretically predicted optimum. This is due to many catalysts binding reaction intermediates like adsorbed hydroxide (\*OH) too strongly. In the current chapter, we explore a new approach to optimizing \*OH binding on existing catalysts: catalyst pretreatment with cathodic corrosion. We do this by mildly cathodically corroding a Pt(111) single crystal, in an effort to create catalytic sites with optimized \*OH binding strength. Electrochemical characterization of the corroded Pt(111) electrode reveals the creation of step sites on the surface. These sites appear more active towards the ORR than 'normal' stepped sites. They are therefore likely concave sites with optimized \*OH binding properties. This result presents cathodic corrosion as a method to optimize existing catalysts for the ORR and other structure-sensitive reactions.*

## 6.1   Introduction

Anthropogenic climate change has stimulated large-scale efforts to shift from fossil to renewable sources of energy.[1,2] A prominent approach for achieving this shift is the 'hydrogen economy', in which renewable energy is used to generate hydrogen from water.[3,4] This hydrogen could be stored, transported and later oxidized in fuel cells to generate electricity where it is needed. Unfortunately, the performance of fuel cells is currently severely limited by the counter reaction of hydrogen oxidation: the oxygen reduction

---

This chapter will form the basis of a manuscript that will be submitted to a peer-reviewed scientific journal.

reaction (ORR).[5] Catalyzing this reaction with high current densities and at low overpotentials is therefore an important focus area in electrochemistry.

The most active metallic ORR catalysts are platinum group metals.[6] However, even these active catalysts are typically limited in their performance, because they bind reaction intermediates like adsorbed oxygen (*O) and adsorbed hydroxide (*OH) too strongly.[5] For example, theoretical calculations indicate the binding of *OH on the (111) facet of platinum to be too strong by approximately 0.1 $eV$.[7] This would suggest that the activity of platinum-group metals can be enhanced by weakening the *OH binding strength.[8]

The *OH binding strength can be weakened by creating alloy catalysts:[9] model alloys, like $Pt_3Ni$(111) and PtCo(111), show strongly improved activity with regard to Pt(111).[10–12] However, translating these model catalysts into their industrially relevant nanoparticle equivalents is not straightforward, with many alloy nanoparticles being unstable and changing their composition under ORR conditions.[4,7,13,14] It might therefore be more prudent to generate active ORR catalysts from single elements like platinum.

This approach would rely on tuning the catalyst's surface structure, since the platinum ORR activity is sensitive to the exposed surface sites: in $HClO_4$, the three Pt basal planes increase in activity in the order (100) < (111) < (110).[15] Even more active are stepped surfaces.[16–18] Though steps contain strongly *OH-binding sites at the top of the step, they also contain concave sites at the bottom of the step which bind *OH weaker than Pt(111).[19] Notably though, most of these concave sites bind *OH slightly too weakly and thus overshoot the activity optimum for the ORR.[20] Instead, optimal activity can be achieved by removing atoms from flat platinum surfaces to create sites that bind *OH nearly optimally.[20]

Atom removal to optimize *OH binding may be achieved by cathodic corrosion, since Chapter 2 and 4 identified the creation of etch pits during cathodic corrosion. Though these roughly 30 $nm$-wide pits are larger than the optimal 1 $nm$-wide pits,[20] the aforementioned chapters also indicate the presence of smaller etching features that are undetectable in scanning electron microscopy. In an effort to generate these smaller sites with optimal ORR reactivity, the current chapter focuses on modifying Pt(111) through mild cathodic corrosion in 1 $M$ NaOH. As will be demonstrated, this approach indeed enhances the ORR activity of Pt(111); this enhancement is likely caused by creating sites with more optimal *OH binding. These results present cathodic corrosion as a viable method to enhance the activity of monometallic platinum electrocatalysts. As such, the present work opens up strategies for modifying commercial catalysts to generate optimum binding

sites with superior catalytic activity.[19]

## 6.2 Materials and methods

### 6.2.1 Cleaning and sample preparation

All water used in this work (resistivity $> 18.2\ M\Omega \cdot cm$, TOC $< 5\ ppb$) was purified with a Millipore MilliQ system. All glassware was cleaned from organic contamination by soaking overnight in an aqueous solution of $1\ g \cdot L^{-1}$ $KMnO_4$ (Fluka, ACS reagent) and $0.5\ M$ $H_2SO_4$ (Fluka, ACS reagent). Before experiments, this solution was drained and residual $MnO_4^-$ was decomposed by immersing the glassware in dilute $H_2O_2$ (Merck, Emprove exp). This solution was subsequently drained and all glassware was boiled in water six times to remove inorganic contaminations, including (bi)sulfate from the cleaning solution.

After cleaning, two three-electrode glass cells were prepared: one cell for sample characterization and one cell for ORR catalysis. These cells were filled with $0.1\ M$ $HClO_4$ (Fluka, TraceSelect) and each contained a Pt counter electrode (Mateck, 99.9%) and an internal reversible hydrogen electrode (RHE) which used a constant hydrogen (Linde, 6.0 purity) flow. The RHE was connected to an auxiliary Pt electrode in the main cell compartment with a $4\ \mu F$ capacitor, in order to reduce high-frequency noise during electrochemical experiments.[21]

In addition to these two glass cells, a third single-compartment cell made of fluorinated ethylene propylene (FEP) was used for cathodic corrosion. This cell was filled with $1\ M$ NaOH (Merck, Suprapur), contained a commercial 'Hydroflex' RHE (Gaskatel) and a dimensionally stable anode counter electrode, provided by Magneto Special Anodes. This staff-shaped anode consisted of titanium, coated with a porous iridium mixed metal oxide. Before use, this electrode was cleaned by rinsing it with $H_2O_2$, since it could not be cleaned by flame-annealing or soaking in the $KMnO_4$ cleaning solution; annealing would destroy the electrode, whereas soaking led to $KMnO_4$ being absorbed into the oxide. This $KMnO_4$ could not be removed by boiling the electrode and would therefore be expelled into the working solution when experiments induced oxygen evolution on the counter electrode. Fortunately, the $H_2O_2$ rinsing procedure proved adequate in cleaning the electrode, since no onset shifts like those observed in Chapter 4 were observed.

Prior to each experiment, working electrodes were prepared by flame-annealing them with a propane torch for approximately 20 seconds. The electrodes were then cooled down in a glass cooler in a reducing $H_2/Ar$ (Linde, 6.0 purity) atmosphere. After cooling,

the electrodes were protected with a droplet of deoxygenated water from the cooling flask and transferred to one of the electrochemical cells. The electrodes used in this study were a home-made 2.3 $mm$ diameter bead-type polycrystalline Pt electrode (Pt(poly)); a 2.1 $mm$ diameter bead-type Pt(100) electrode (iCryst); a 2.5 $mm$ diameter bead-type Pt(110) electrode (iCryst); and a 3 $mm$ diameter, 2 $mm$ high cylindrical Pt(111) crystal (Surface Preparation Laboratory). Cyclic voltammograms for these electrodes are shown in Fig. C.1.

## 6.2.2   Electrochemistry

Electrochemical experiments were performed with a Bio-Logic VSP-300 potentiostat. After setting up the glassware, cyclic voltammograms were run in both glass cells to ensure the cleanliness of the working solutions. Specifically, each cell was deaerated by purging the electrolyte with argon (Linde, 6.0 purity) for at least 30 minutes. Then, 4 cyclic voltammograms (CVs) of the Pt(111) electrode were recorded in hanging meniscus configuration at a scan rate of 50 $mV \cdot s^{-1}$, between 0.06 and 0.9 $V$ vs. RHE, while maintaining deaeration by flowing argon over the working electrode. Special attention was paid to the presence of (bi)sulfate, which significantly affects the oxygen reduction activity.[16,17] (Bi)sulfate can easily be detected in Pt(111) voltammograms, since it causes a distinct reductive feature between 0.45 and 0.55 $V$ vs. RHE at concentrations as low as $10^{-6}$ $M$.[22] If no signs of (bi)sulfate were present and the voltammograms did not change shape between cycles, the cells were considered to be clean. After establishing cleanliness, the argon flow in the catalysis cell was replaced by O$_2$ (Linde, 6.0 purity), which was bubbled through the working electrolyte for at least 10 minutes to ensure oxygen saturation.

Each experiment started by running 4 Pt(111) CVs in the characterization cell as described above, to validate the cleanliness and ordering of the surface. The Pt(111) electrode was then rinsed and immersed for at least 1 $mm$ in the corrosion cell. In this cell, the cell resistance was determined through impedance spectroscopy at 0.5 $V$ vs. RHE, at a 100 $kHz$ frequency and a 20 $mV$ sine wave amplitude.[23] This resistance value was used to subsequently apply a 85% IR-corrected potential to the electrode for 60 seconds, in order to modify the electrode through cathodic corrosion. Following modification, the electrode was removed under potential control, rinsed and moved to the characterization cell. In this cell, the state of the electrode surface was characterized by running 4 cyclic voltammograms between 0.06 and 0.7 $V$ vs. RHE. The 0.7 $V$ potential bound was chosen as a safe upper limit where none of the cathodically produced sites would be

removed through oxidation of the surface.

After characterization, the ORR activity of the modified electrode was assessed in the hanging meniscus rotating disk (HMRD) configuration.[24] To this end, the electrode was mounted in a home-made electrode holder that was subsequently screwed into the shaft of a Pine rotator. The electrode was lowered into the catalysis cell, where the oxygen now flowed over the electrolyte solution to maintain oxygen saturation during experiments. In this cell, a meniscus was made between the electrode and the electrolyte while polarizing the electrode at $0.06$ *V* vs. RHE. After making contact, the cell resistance was determined through impedance spectroscopy at $0.9$ *V* vs. RHE. The electrode potential was then held at $0.06$ *V* vs. RHE for 5 seconds before testing the catalytic activity of the electrode with cyclic voltammetry; two CVs were run between $0.06$ and $0.9$ *V* vs. RHE, at a scan rate of $50$ $mV \cdot s^{-1}$. The electrode rotation rate was then automatically changed by the potentiostat to $200$ $rpm$, the current was allowed to stabilize for 5 seconds at $0.06$ *V* vs. RHE and two CVs were run between $0.06$ and $0.9$ *V* vs. RHE. This step was repeated to obtain additional CVs at rotation rates of $400$, $900$, $1600$ and $2500$ $rpm$.

## 6.3 Results and discussion

In this chapter, we assess the effect of mild cathodic corrosion and the subsequent change in ORR activity for Pt(111) as follows. First, as in previous chapters, blank cyclic voltammograms (CVs) of corroded and uncorroded Pt(111) were recorded. These CVs are presented first. Then, the activity activity of the Pt(111) electrode was studied in the hanging meniscus rotating disk (HMRD) configuration.[24] The proper functioning of the HMRD setup will be discussed briefly, followed by the recorded ORR activity and discussion of the presented results.

### 6.3.1 Cathodic corrosion of Pt(111)

Blank CVs of Pt(111), before and after cathodic polarization in $1$ *M* NaOH are presented in Fig. 6.1. As can be seen, the uncorroded Pt(111) electrode contains the characteristic hydrogen adsorption and desorption features between $0.06$ and $0.4$ *V* vs. RHE, followed by the double layer region and subsequent adsorption and desorption of OH between $0.5$ and $0.9$ *V* vs. RHE.[25] Importantly, no peaks are visible at $0.13$ and $0.29$ *V* vs. RHE. This indicates that no electrochemically observable peak sites are present on the electrode before cathodic polarization.[26]
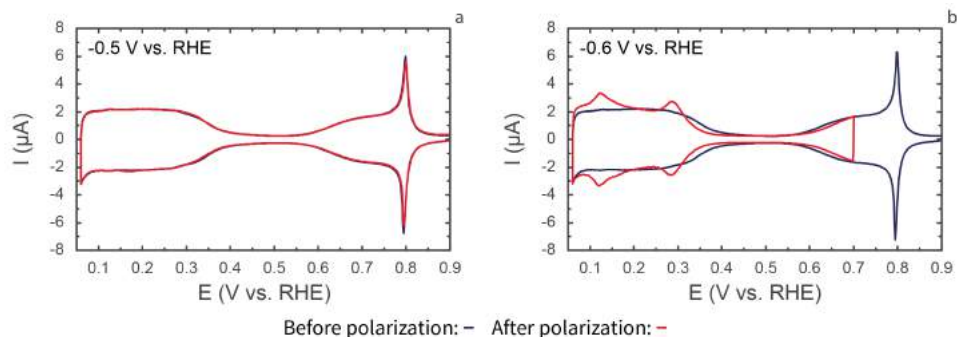
**Fig. 6.1 |** Cyclic voltammograms of Pt(111) before (blue trace) and after (red trace) cathodic polarization in 1 $M$ NaOH at $-0.5$ $V$ *vs.* RHE **(a)** and $-0.6$ $V$ *vs.* RHE **(b)**. Voltammograms were recorded in 0.1 $M$ HClO$_4$, at a scan rate of 50 $mV \cdot s^{-1}$.

Similarly, no additional peaks are present after polarizing Pt(111) at $-0.5$ $V$ *vs.* RHE in 1 $M$ NaOH. This indicates no change in the electrode structure when polarizing it before the cathodic corrosion onset potential. In contrast, pronounced changes are visible after polarizing the electrode at the onset potential found in Chapter 4: $-0.6$ $V$ *vs.* RHE. This treatment causes the formation of both (110) steps (0.13 $V$ *vs.* RHE) and (100) steps (0.29 $V$ *vs.* RHE). These changes appear to be largely independent of the corrosion potential, as is illustrated in Fig. C.2 Additionally, the onset of OH adsorption has shifted positively by about 0.02 $V$, which indicates a slightly weakened *OH adsorption strength on the (111) terrace of the corroded surface.[20] Such weakened binding should promote the ORR activity for the corroded electrode.

### 6.3.2  HMRD configuration

The ORR activity is assessed in the HMRD configuration.[24] This configuration differs from the conventional rotating disk electrode (RDE) configuration, because the working electrode is not encased in a shaft and submerged into the working solution. Instead, the bead- or cylinder-type crystal is mounted in a modified RDE rotator and contact with the side of the electrode is prevented by elevating the electrode into a hanging meniscus configuration. Though this configuration allows for the convenient use of standard single crystal electrodes, care has to be taken to make sure that the HMRD behaves like a classical RDE electrode.

Specifically, the height of the electrode has to be controlled carefully:[24] if the electrode were too low, wetting of the side would occur and the catalytic activity of sites other

than the desired facet would be probed. This would cause an increased absolute slope in the Levich plot. In contrast, if the electrode were too high, the meniscus would be constrained. This would lead to reduced mass transport and an offset in the ORR Levich plots.

Levich plots were therefore constructed for each electrode to verify the validity of the HMRD setup for the investigated system. A set of ORR voltammograms used for these Levich plots is displayed in Fig. C.3. Additional exemplary Levich plots are displayed for each electrode in Fig. C.4. All reported data were measured on electrodes with zero or near-zero Levich plot offsets and Levich slopes within several percent of the theoretically expected value, based on literature parameters for the solubility and diffusion coefficient of oxygen in $0.1$ *M* HClO$_4$.[27] A notable exception to this statement is the employed Pt(110) electrode, which consistently had *lower* Levich slopes. We attribute this to an unexpected decrease in the effective electrode surface area, which is compensated for in the following normalized ORR activity assessment. With the exception of this electrode, all electrodes behaved as expected, such that the HMRD setup can be used to accurately assess the ORR activity of the corroded Pt(111) electrodes.

### 6.3.3   ORR enhancement by cathodic corrosion

The ORR activity for a corroded Pt(111) electrode, a polycrystalline electrode and the three basal planes of platinum is displayed in Fig. 6.2. In this plot, all currents are normalized by the absolute limiting current density for each electrode. This normalization accounts for minor variations in the limiting current due to small variations in the meniscus height[18] and small deviations in the alignment of the electrode.[12] The normalization therefore allows for objective comparison of the ORR activity in the HMRD configuration.[18]

As can be seen in Fig. 6.2, the ORR activity at $0.9$ *V vs.* RHE follows the order Pt(100) < Pt(111) < Pt(110). This activity trend is in good agreement with both experimental results and recent density functional theory calculations.[15,19,20,28] A similar activity is achieved for Pt(poly), which has comparable activity to Pt(111). However, the corroded Pt(111) electrode is more active than any of the other studied crystals. This indicates that cathodic corrosion is indeed able to enhance the ORR activity of a Pt(111) electrode.

The activity enhancement through cathodic corrosion is more readily apparent from the quantitative activity assessment in Fig. 6.3. In Fig. 6.3, the absolute normalized current at $0.9$ *V* is plotted for each electrode. In Panel **b** of this figure, the activity of both Pt(111) and (100) show excellent quantitative agreement with well-prepared electrodes
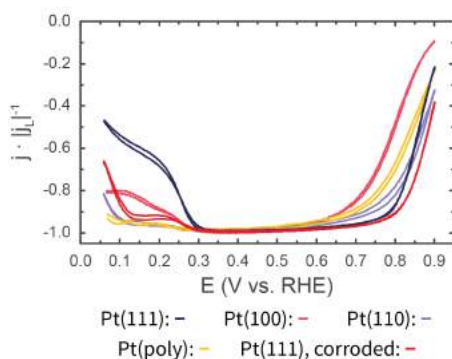
**Fig. 6.2 |** Cyclic voltammograms for oxygen reduction on Pt(111), Pt(100), Pt(110), Pt(poly) and Pt(111) which was corroded at $-0.6$ *V* *vs.* RHE in 1 *M* NaOH. The electrode rotation rate was 1600 *rpm*. Voltammograms were recorded in oxygen-saturated 0.1 *M* HClO$_4$, at a scan rate of 50 *mV* $\cdot$ *s*$^{-1}$.

from the work from Feliu *et al.*[28] A more qualitative agreement is obtained for Pt(poly) and Pt(110), which are respectively more and less active than similar previously studied electrodes.[28,29] The increased Pt(poly) activity can be ascribed to a slightly different state of the surface, which can be expected for different polycrystalline electrodes. Similarly, the reduced activity of Pt(110) is caused by the crystal's high sensitivity to reconstructed 1×2 domains on the surface: if less reconstructed domains are formed during the cooling of the crystal, the ORR activity is reduced as well.[30] This remarkable sensitivity of Pt(110) to variations in the crystal cooling conditions is also responsible for the slightly larger error bar for Pt(110) in Fig. 6.3 **b**. From Panel **b**, it therefore appears that all electrodes are as active as expected from literature.

With all uncorroded single crystals behaving in accordance with previous literature, the activity of cathodically treated Pt(111) can be assessed quantitatively (Fig. 6.3 **a**). In Fig. 6.3 **a**, it can be seen that the activity of Pt(111) is not enhanced if the polarization potential is below the onset potential that was established in Chapter 4. However, the Pt(111) ORR activity at 0.9 *V* *vs.* RHE increases sharply after cathodic treatment at or below the onset potential of $-0.6$ *V* *vs.* RHE: the normalized activity improves from 0.22 to 0.38. This improvement corresponds to an increase in the kinetic current density ($j_k$) from 2.8 to 6.6 *mA* $\cdot$ *cm*$^{-2}$, as can be seen in Fig. C.5. This enhancement of both $j_k$ and the normalized activity decreases slightly at more negative corrosion potentials, but increases again to 0.37 (6.4 *mA* $\cdot$ *cm*$^{-2}$) at $-1.0$ *V* *vs.* RHE. It therefore appears that electrode
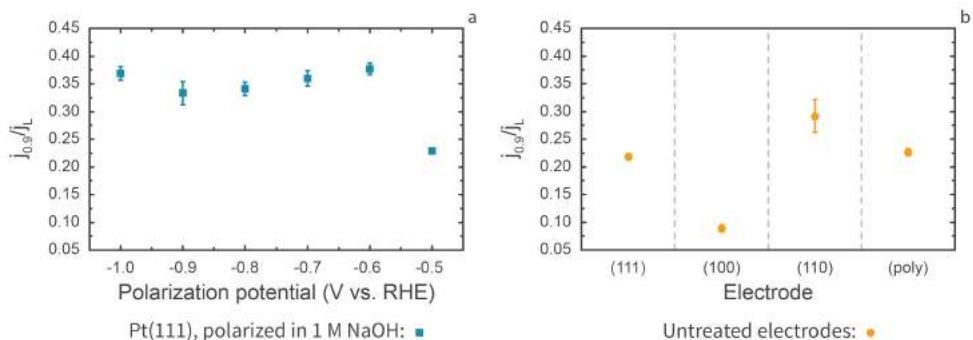
**Fig. 6.3 |** Normalized ORR activity of corroded Pt(111) (blue squares), as function of the polarization potential **(a)** and of uncorroded electrodes (yellow circles) **(b)**. Rotation rate: 1600 *rpm*. Each data point is the average of 3 or more experiments. Error bars represent one standard deviation.

pretreatment with cathodic corrosion can strongly enhance the oxygen reduction activity of Pt(111).

### 6.3.4  Discussion

Though the data in Fig. 6.3 and Fig. C.5 indicate that cathodic corrosion can more than double the kinetic ORR current density of Pt(111), it is instructive to rationalize the exact cause of this improvement. Specifically, one might wonder whether the improvement is simply caused by the creation of step sites or by the formation of sites with optimal generalized coordination numbers.

The presence of step sites on Pt(111) is known to enhance the ORR activity.[16–18] If the presence of 'normal' (110) and (100) sites were the cause of the presently reported activity enhancement, the enhancement should therefore correlate roughly to the amount of steps.[18] However, the corroded step sites appear to have much higher activities than most stepped single crystals:[28] only crystals with very high step densities surpass the normalized activity of the corroded electrodes. For example, our most active electrodes are as active as Pt(332), which has one (110) step for every five (111) terrace atoms[31] and a normalized activity of 0.38.[28] By qualitatively comparing the CVs of Pt(332) and other stepped single crystals with those in Fig. 6.1, one can conclude that the stepped crystals possess a much higher step density than the corroded (111) electrodes.[31,32] Each step on a stepped single crystal therefore has a *lower* ORR activity contribution than a step on corroded Pt(111).

This reduced contribution of steps on stepped single crystals is likely due to those

steps binding *OH too weakly and thus overshooting the per-step ORR activity optimum.[20] Since these steps are less active than those created in the current work, it appears that the current steps possess a more optimized *OH binding strength. In fact, the cathodically created steps are approximately as active as optimal binding sites that can be created through anodic cycling.[20] Through such cycling, a 15 % surface area increase through active site formation led to a current densities of approximately $7.4 \ mA \cdot cm^{-2}$. Such area increases and current densities are comparable to those presented here. It is therefore highly likely that both the previously reported anodically created sites[20] and the cathodically created sites presented here have similar concave geometries with optimized *OH binding.

A final argument for this conclusion is that optimized concave pits are rather small,[20] being approximately 3 atoms ($\sim 0.9 \ nm$)[33] wide and having the optimally coordinated atom at the bottom of the pit. Such sites should only be present after mild cathodic corrosion, where no etch pits are detectable in SEM yet. Accordingly, more pronounced corrosion will create overlapping etch pits, which contain less optimally coordinated Pt atoms per square nanometer. Such strongly corroded electrodes should then have a lower ORR activity than those in Fig. 6.3. This is demonstrated in Fig. C.6, which displays exploratory experiments of Pt(111), corroded in $10 \ M$ NaOH. As the figure shows, corrosion at $-0.4 \ V$ *vs.* RHE creates a surface that is similar to those created in $1 \ M$ NaOH. This surface also has a comparable normalized activity of 0.32. However, a monotonic activity decrease is observed for more pronounced cathodic corrosion at $-0.5 \ V$ *vs.* RHE and below. This indicates that the creation of more step sites through cathodic corrosion does not necessarily correlate to an enhanced activity, since Chapter 2 and 4 indicate this corrosion to create large sites overlapping sites that are not beneficial to the overall ORR activity.

Based on the aforementioned considerations, it appears that cathodic corrosion is a suitable technique for creating active ORR sites. This opens possibilities for creating active sites on nanocatalysts such as (111)-oriented nano-octahedra that could benefit from the presence of additional concave sites.[14,19] Though modifying nanocatalysts will require overcoming challenges like ensuring nanoparticle adhesion during cathodic corrosion, such modification might be a viable strategy for producing industrially relevant ORR catalysts. This reasoning is supported by encouraging recent results, where cathodic corrosion in methanol was shown to improve the distribution of various types of metallic nanoparticles.[34]

Cathodic corrosion as a catalyst enhancement strategy is not limited to oxygen reduction on platinum. The current approach can easily be extended to structure-sensitive reactions like glycerol oxidation and ammonia oxidation,[35,36] or to different metal catalysts. These applications of cathodic corrosion can further be directed by the guidelines in Chapter 4.

## 6.4   Conclusions

Summarizing, the current chapter has demonstrated that the oxygen reduction activity can be significantly enhanced by cathodic corrosion. This enhancement is likely not caused by the creation of 'normal' step sites, but instead by the formation of active concave sites on the Pt(111) surface.[20] These results strongly support the notion that cathodic corrosion can be used to pre-treatreat metallic nanoparticles to improve catalytic activity and selectivity. As such, cathodic corrosion may play a vital role in future electrocatalyst improvement.

## 6.5   Acknowledgements

## References

1.   Anderson, K. & Peters, G. The trouble with negative emissions. *Science* **354** (2016).

2.   Oreskes, N. in *Climate Modelling* (eds Lloyd, E. A. & Winsberg, E.) 31–64 (Palgrave Macmillan, Cham, 2018).

3.   Bockris, J. O. A Hydrogen Economy. *Science* **176,** 1323–1323 (1972).

4.   Katsounaros, I. & Koper, M. T. M. in *Electrochemical Science for a Sustainable Society* 23–50 (Springer International Publishing, Cham, 2017).

5.   Nørskov, J. K. *et al.* Origin of the overpotential for oxygen reduction at a fuel-cell cathode. *Journal of Physical Chemistry B* **108,** 17886–17892 (2004).

6.   Markovic, N. Surface science studies of model fuel cell electrocatalysts. *Surface Science Reports* **45,** 117–229 (2002).

7.   Stephens, I. E. L., Bondarenko, A. S., Grønbjerg, U., Rossmeisl, J. & Chorkendorff, I. Understanding the electrocatalysis of oxygen reduction on platinum and its alloys. *Energy & Environmental Science* **5,** 6744 (2012).

8.   Kulkarni, A., Siahrostami, S., Patel, A. & Nørskov, J. K. Understanding Catalytic Activity Trends in the Oxygen Reduction Reaction. *Chemical Reviews* **118,** 2302–2312 (2018).

9.   Greeley, J. *et al.* Alloys of platinum and early transition metals as oxygen reduction electrocatalysts. *Nature Chemistry* **1,** 552–556 (2009).

10. Stamenkovic, V. R. *et al.* Improved Oxygen Reduction Activity on Pt3Ni(111) via Increased Surface Site Availability. *Science* **315,** 493–497 (2007).

11. Stamenkovic, V. R. *et al.* Trends in electrocatalysis on extended and nanoscale Pt-bimetallic alloy surfaces. *Nature Materials* **6,** 241–247 (2007).

12. Wakisaka, M. *et al.* Unprecedented dependence of the oxygen reduction activity on Co content at Pt Skin/Pt-Co(111) single crystal electrodes. *Electrochemistry Communications* **67,** 47–50 (2016).

13. Greeley, J. & Nørskov, J. K. Combinatorial Density Functional Theory-Based Screening of Surface Alloys for the Oxygen Reduction Reaction. *The Journal of Physical Chemistry C* **113,** 4932–4939 (2009).

14. Strasser, P., Gliech, M., Kuehl, S. & Moeller, T. Electrochemical processes on solid shaped nanoparticles with defined facets. *Chemical Society Reviews* **47,** 715–735 (2018).

15. Marković, N., Adžić, R., Cahan, B. & Yeager, E. Structural effects in electrocatalysis: oxygen reduction on platinum low index single-crystal surfaces in perchloric acid solutions. *Journal of Electroanalytical Chemistry* **377,** 249–259 (1994).

16. Maciá, M. D., Campiña, J. M., Herrero, E. & Feliu, J. M. On the kinetics of oxygen reduction on platinum stepped surfaces in acidic media. *Journal of Electroanalytical Chemistry* **564,** 141–150 (2004).

17. Kuzume, A., Herrero, E. & Feliu, J. M. Oxygen reduction on stepped platinum surfaces in acidic media. *Journal of Electroanalytical Chemistry* **599,** 333–343 (2007).

18. Gómez-Marín, A. M. & Feliu, J. M. Oxygen reduction on nanostructured platinum surfaces in acidic media: Promoting effect of surface steps and ideal response of Pt(111). *Catalysis Today* **244,** 172–176 (2015).

19. Calle-Vallejo, F. *et al.* Why conclusions from platinum model surfaces do not necessarily lead to enhanced nanoparticle catalysts for the oxygen reduction reaction. *Chemical Science* **8,** 2283–2289 (2017).

20. Calle-Vallejo, F. *et al.* Finding optimal surface sites on heterogeneous catalysts by counting nearest neighbors. *Science* **350,** 185–189 (2015).

21. Van de Krol, R. in *Photoelectrochemical Hydrogen Production* (eds Van de Krol, R. & Grätzel, M.) 109 (Springer, Boston, MA, 2012).

22. Attard, G. A., Brew, A., Hunter, K., Sharman, J. & Wright, E. Specific adsorption of perchlorate anions on Pt{hkl} single crystal electrodes. *Phys. Chem. Chem. Phys.* **16,** 13689–13698 (2014).

23. Jung, S., McCrory, C., Ferrer, I. M., Peters, J. C. & Jaramillo, T. F. Benchmarking Nanoparticulate Metal Oxide Electrocatalysts for the Alkaline Water Oxidation Reaction. *J. Mater. Chem. A* (2015).

24. Villullas, H. & Teijelo, M. The hanging-meniscus rotating disk (HMRD) Part 1. Dependence of hydrodynamic behavior on experimental variables. *Journal of Electroanalytical Chemistry* **384,** 25–30 (1995).

25. Gomez, R., Orts, J. M., Alvarez-Ruiz, B. & Feliu, J. M. Effect of Temperature on Hydrogen Adsorption on Pt(111), Pt(110), and Pt(100) Electrodes in 0.1 M HClO4. *The Journal of Physical Chemistry B* **108,** 228–238 (2004).

26. Vidal-Iglesias, F. J., Arán-Ais, R. M., Solla-Gullón, J., Herrero, E. & Feliu, J. M. Electrochemical Characterization of Shape-Controlled Pt Nanoparticles in Different Supporting Electrolytes. *ACS Catalysis* **2,** 901–910 (2012).

27. Wakabayashi, N., Takeichi, M., Itagaki, M., Uchida, H. & Watanabe, M. Temperature-dependence of oxygen reduction activity at a platinum electrode in an acidic electrolyte solution investigated with a channel flow double electrode. *Journal of Electroanalytical Chemistry* **574,** 339–346 (2005).

28. Gómez-Marín, A. M., Rizo, R. & Feliu, J. M. Oxygen reduction reaction at Pt single crystals: a critical overview. *Catalysis Science & Technology* **4,** 1685 (2014).

29. Gómez-Marín, A., Feliu, J. & Edson, T. Reaction Mechanism for Oxygen Reduction on Platinum: Existence of a Fast Initial Chemical Step and a Soluble Species Different from H2O2. *ACS Catalysis* **8,** 7931–7943 (2018).

30. Attard, G. A. & Brew, A. Cyclic voltammetry and oxygen reduction activity of the Pt{110}-(1×1) surface. *Journal of Electroanalytical Chemistry* **747,** 123–129 (2015).

31. Armand, D. & Clavilier, J. Electrochemical behaviour of the (110) orientation of a platinum surface in acid medium: the role of anions. *Journal of Electroanalytical Chemistry and Interfacial Electrochemistry* **263,** 109–126 (1989).

32. Clavilier, J., El Achi, K. & Rodes, A. In situ probing of step and terrace sites on Pt(S)-[n(111) × (111)] electrodes. *Chemical Physics* **141,** 1–14 (1990).

33. Arblaster, J. W. Crystallographic Properties of Platinum. *Platinum Metals Review* **41,** 12–21 (1997).

34. Vanrenterghem, B. *et al.* Cutting the Gordian Knot of electrodeposition via controlled cathodic corrosion enabling the production of supported metal nanoparticles below 5 nm. *Applied Catalysis B: Environmental* **226,** 396–402 (2018).

35. Garcia, A. C. *et al.* Strong Impact of Platinum Surface Structure on Primary and Secondary Alcohol Oxidation during Electro-Oxidation of Glycerol. *ACS Catalysis* **6,** 4491–4500 (2016).

36. Vidal-Iglesias, F. J. *et al.* Shape-dependent electrocatalysis: Ammonia oxidation on platinum nanoparticles with preferential (100) surfaces. *Electrochemistry Communications* **6,** 1080–1084 (2004).
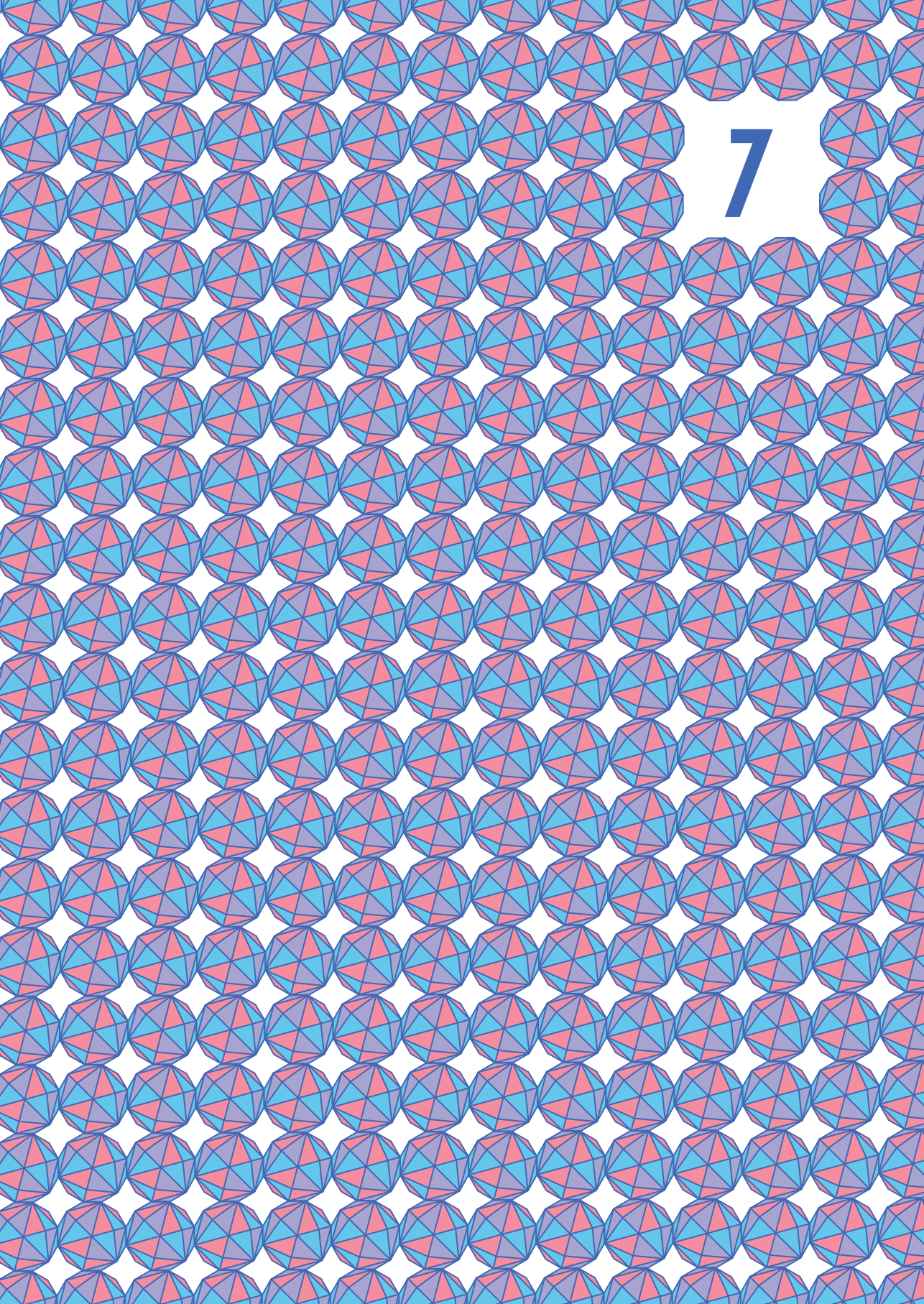
# Local Structure and Composition of PtRh Nanoparticles Produced through Cathodic Corrosion

*Alloy nanoparticles fulfill an important role in catalysis. These particles can be produced by cathodic corrosion, through applying an AC voltage to an alloy electrode. However, this harsh AC potential program might affect the final nanoparticle elemental distribution. Here, we explore this issue by characterizing the time required to create $1\ \mu mol$ of Rh, $Pt_{12}Rh_{88}$, $Pt_{55}Rh_{45}$ and Pt nanoparticles under various applied potentials. The corrosion time measurements are complemented by characterization through transmission electron microscopy, X-ray diffraction and X-ray absorption spectroscopy. The corrosion times indicate that platinum and rhodium corrode at different rates and that the alloy corrosion rates are dominated by platinum. In addition, structural characterization reveals that the created alloy nanoparticles indeed exhibit small degrees of elemental segregation. These results indicate that the atomic alloy structure is not always preserved during cathodic corrosion.*

## 7.1 Introduction

In heterogeneously catalyzed processes, a high activity per gram of catalyst is desired. This requires a maximization of active surface area, which is why heterogeneous catalysts are typically processed to become (supported) nanoparticles.[1] Such particles can take on various manifestations, including alloys. These metal alloys are of great interest, since their composition can be varied to optimize catalysis.[2] In such an optimized alloy catalyst, the bonding of reaction intermediates to the catalyst can be tuned such that a reaction is catalyzed with minimal energy losses.[3–5] Though this optimization strategy has led to significant advances in catalyzing various reactions,[6–9] preparing alloy nanoparticles with

a tuned composition is often challenging. Therefore, finding new ways to prepare alloy nanoparticles is potentially of great interest.

Among the various chemical,[10–14] biochemical[15] and physical[16–18] processes used to create metal alloy nanoparticles, a promising candidate is cathodic corrosion. This method, which was first observed by Haber,[19] revisited by Kabanov *et al.*[20] and studied again more recently,[21–26] involves making nanoparticles by applying a cathodic voltage to a sacrificial electrode. During this cathodic polarization, nanoparticles will form near and on the electrode. The majority of these particles generally remains attached to the sacrificial electrode, which is why a more positive voltage is typically introduced to disperse the nanoparticles into the working solution and allow the particles to be collected.[23] By alternating these positive and negative polarizations, one obtains an AC potential program. Such programs are the basis of most practical cathodic corrosion setups,[27–29] which can be used to produce nanoparticles of most metals and alloys in a relatively fast and clean way.

Producing alloy nanoparticles by cathodic corrosion should only require a sacrificial electrode of the right composition, and should be able to convert the electrode into nanoparticles with the same composition. This was demonstrated by manufacturing a variety of PtRh alloy nanoparticles that exhibited superior catalytic activity for various reactions.[27] Cyclic voltammetry (CV), X-ray diffraction (XRD) and energy-dispersive X-ray spectroscopy (EDX) analysis indicated that these particles had the same structure and composition as their sacrificial electrodes.

However, platinum and rhodium vary in their surface energy and resistance to oxidation,[30,31] which can lead to sub-nanometer-scale surface segregation of the nanoparticles.[32] Because the expected length scale of surface segregation falls beyond the resolution of the previously employed techniques, segregation might have gone unnoticed. In addition, platinum and rhodium were recently shown to behave subtly differently during cathodic corrosion: though both metals were shown in Chapter 2 & 3 to start corroding at similar potentials, rhodium was the only metal from which nanoparticle dispersion could be observed visibly during constant polarization at mild potentials. It is therefore not immediately apparent why cathodic corrosion should preserve the atomic structure and composition of the sacrificial electrode during the formation of nanoparticles.

To bridge this gap in the understanding of cathodic corrosion, we present a detailed study of cathodic nanoparticle formation of PtRh alloys. Cathodic corrosion of Pt, $Pt_{55}Rh_{45}$, $Pt_{12}Rh_{88}$ and Rh electrodes is combined with three structural characteriza-

tion methods of the resulting nanoparticles: visual characterization through transmission electron microscopy (TEM), long-range structural characterization through XRD and local structural characterization through extended X-ray absorption fine structure (EXAFS) measurements. As we will show, these complementary techniques detect small differences in nanoparticle size and composition, which indicate the coexistence of a crystalline and an amorphous set of particles that exhibit a minor degree of elemental segregation.

## 7.2 Materials and methods

### 7.2.1 Nanoparticle synthesis

All electrochemical experiments were performed in a two-electrode setup, using a graphite rod (Alfa Aesar, Ultra "F" purity) as the counter electrode. Working electrodes were either of the following wires: Pt (Mateck, 99.99%; $\varnothing = 0.1\ mm$), $Pt_{55}Rh_{45}$ (Goodfellow; $\varnothing = 0.1\ mm$), $Pt_{12}Rh_{88}$ (Highways International; $\varnothing = 0.1\ mm$) and Rh (Mateck, 99.9%; $\varnothing = 0.125\ mm$). All alloy compositions in this work are given as atomic ratios. The working electrolyte consisted of saturated NaOH (Acros, for analysis). All water used in this study was demineralized and ultrafiltered by a Millipore MilliQ system (resistivity $> 18.2\ M\Omega \cdot cm$, TOC $< 5\ ppb$). For each measurement, a micrometer screw was used to carefully control the working electrode immersion depth, such that 1 $\mu mol$ of material was immersed. Next, a 100 $Hz$ square wave potential was applied until corrosion was completed. The square wave potential limits were either $-20\ V$ and $+10\ V$; $-15\ V$ and $+10\ V$; $-10\ V$ and $+10\ V$; $-10\ V$ and $+15\ V$; or $-10\ V$ and $+20\ V$. These potentials were applied using a power amplifier that was controlled by LabVIEW. The produced particles were purified using repeated centrifuging/rinsing cycles, until the pH of the supernatant was neutral.

### 7.2.2 Structural characterization

Crystallinity and coherent domain size of the original alloys and of the nanoparticle alloy samples were characterized by X-ray diffraction (XRD) and X-ray absorption spectroscopy (XAS). Before characterization, the nanoparticle samples were embedded in a boron nitride matrix: for each sample, approximately 10 $mg$ of PtRh nanoparticles was mixed with 200 $mg$ of boron nitride (Wako Chemicals, Japan, ACS grade) and compressed into pellets.

**X-ray diffraction**

X-ray diffraction patterns of the nanoparticles were measured with a Rigaku Miniflex powder X-ray diffractometer, which uses a Cu K$_\alpha$ X-ray source. From these diffraction patterns, coherent domain sizes were calculated from the peak shape of the (111) diffraction peaks. In this calculation, the Scherrer formula was used and the shape of the diffraction peaks was assumed to conform to the Voigt function. X-ray diffraction patterns of the alloy wires were measured on a Philips X'pert diffractometer, which was equipped with an X'celerator and used a Cu K$_\alpha$ source.

**X-ray absorption spectroscopy**

Local structure information of the prepared alloy nanoparticles was obtained with XAS. The X-ray absorption spectra were collected in transmission mode in the Pt L$_\mathrm{III}$ and Rh K edge regions at the BL12 (Si(111) monochromator) and BLNW10 (Si(311) monochromator) beamlines of the Photon Factory synchrotron (Japan Institute for High Energy Physics (KEK)). The Rh K-scans extended to 20 Å$^{-1}$ and Pt L$_\mathrm{III}$ data were limited to 15 Å$^{-1}$. Each spectrum was recorded at four different scanning step sizes: the pre-edge region (between 500 to 50 $eV$ before the absorption edge) was scanned in 6.5 $eV$ steps to enable background subtraction. In the 50 $eV$ pre-edge to 100 $eV$ post-edge range, a step size of 0.4 to 0.5 $eV$ was used to acquire the XANES part of the spectra. Finally, 2.5 to 3.0 $eV$ scanning steps were used in the 100 to 500 $eV$ post-edge reason, while 7.0 $eV$ steps were maintained in the post-edge region above 500 $eV$. The experimental beamtime was provided by the Photon Factory within project 2014G181.

All data processing prior to the local structure refinement of the EXAFS functions was done using version 1.2.10 of the IFEFFIT software package.[33] This processing involved data normalization, smoothing, background subtraction, Fourier transformation of the spectra and windowing of the transform. The photoelectron wave vector (k) for the Fourier transforms was kept within the range of $k = 3$–18 Å$^{-1}$ for Rh-EXAFS and $k = 3$–13 Å$^{-1}$ for Pt-EXAFS. A k-weighting factor of 2 was applied. For presenting EXAFS functions in real space (R-space), the ranges of $R = 1$–6 Å and $R = 1$–4 Å were used for Rh and Pt EXAFS, respectively. The EXAFS functions in R-space are displayed in Fig. D.1.

After data processing, the local structure of the materials was analyzed using the ARTEMIS non-linear least squares (NLLLS) minimization module of the IFEFFIT package.[34] This was done by performing full-profile refinement of the EXAFS spectra by NLLS mini-
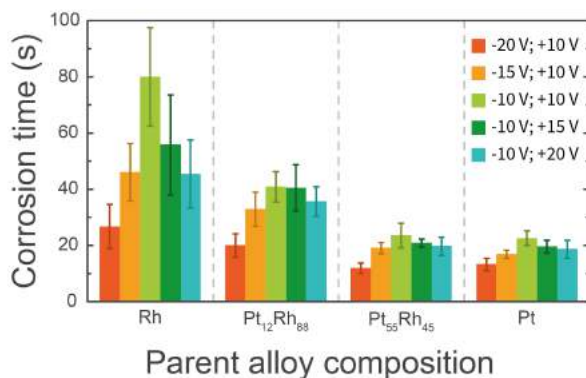
**Fig. 7.1 |** : Time required to produce 1 $\mu mol$ of nanoparticles, using square wave potentials with various limits. Reported corrosion times are averages of 10 measurements. The error bars represent a 95% confidence interval.

mization in R-space with a k-weighting factor of 2. The theoretical model was generated using the FEFF6.2 library with structural parameters derived from an ideal face-centered cubic *(fcc)* metal with a random distribution of the constituting elements. The coordination numbers and bonding distances of Pt and Rh in each coordination shell were refined independently without additional constraints.

## 7.3 Results and discussion

### 7.3.1 Corrosion rate

In order to study the various factors influencing the rate of nanoparticle production, the time required to corrode 1 $\mu mol$ of wire was measured for each metal and alloy. This time, which will be referred to as corrosion time, should be related inversely to the corrosion rate and is displayed in Fig. 7.1 for all tested materials and potential limits. The corrosion treatment with $-10\,V$ negative and $+10\,V$ positive limits, shown in light green in Fig. 7.1, will be used as a reference for the comparison with the other treatments. This treatment is therefore shown as the middle bar for each alloy in Fig. 7.1.

Comparing the corrosion time for the different alloys, this time is highest for rhodium and decreases with increasing platinum content. Equivalently, the corrosion rate is lowest for rhodium and increases with increasing platinum content. This effect of platinum appears more pronounced for smaller amounts of platinum; the corrosion rate roughly

doubles when 12 percent of platinum is present and increases further for a platinum content of 55 percent. In contrast, the corrosion rate increases only marginally between $Pt_{55}Rh_{45}$ and pure platinum. Thus, the corrosion rate appears to depend nonlinearly on the platinum content of the alloy, with smaller platinum ratios having a more pronounced effect on the corrosion rate.

Another factor influencing the corrosion rate is the negative potential limit. The corrosion time as a function of the negative potential limit is depicted with the dark and light orange bars in Fig. 7.1. When lowering the negative limit from $-10$ *V* to $-20$ *V*, the corrosion time goes down drastically; it decreases from 23 seconds to 13 seconds in the case of platinum and drops sharply from 80 seconds to 27 seconds for rhodium. The alloys exhibit a similar degree of enhancement. This enhancement has been observed before and can be explained quite readily by realizing that the nanoparticles are produced through a cathodic process.[23] The rate for this process will be influenced by its driving force: the negative potential limit. Hence, a more negative potential limit will speed up the corrosion and lower the corresponding corrosion time.

The dark green and blue bars in Fig. 7.1 illustrate the effect of the positive potential limit on the corrosion rate. The corrosion rate is only enhanced significantly by the positive potential limit in the case of pure rhodium: the average corrosion time decreases from 80 to 45 seconds when increasing the positive potential limit from 10 to 20 *V*. The observed change of the corrosion time is negligible for all other materials. This difference in corrosion time may be explained by the differing anodic dissolution kinetics of platinum and rhodium.

To properly assess these kinetics, one should distinguish between transient and steady-state dissolution.[35] Transient dissolution takes place when metal oxides are created and consecutively reduced. In our system, transient dissolution therefore occurs when switching between positive and negative polarization. As such, the transient dissolution rate should primarily depend on how often positive and negative polarizations are alternated, which is determined by the frequency of the applied square wave potential. Since this frequency is kept constant, the transient dissolution rate should be constant in all experiments as well. In contrast with transient dissolution, steady-state dissolution occurs during constant positive polarization and takes place concurrently with oxygen evolution.[35] Both the oxygen evolution rate and the steady-state dissolution rate are expected to increase with a more positive potential limit. Based on the characteristics of transient and steady-state dissolution, it is therefore expected that only the steady-state

dissolution rate should increase when the positive potential limit is increased.

These two dissolution mechanisms are of differing importance for platinum and rhodium. On the one hand, rhodium dissolves through both the transient and steady-state mechanisms. Its dissolution rate should therefore increase when the positive potential limit is increased. On the other hand, platinum is virtually unaffected by steady-state dissolution.[35] This would explain why the dissolution rate of platinum and platinum-containing alloys appears to be largely unaffected by increasing the positive potential limit.

The observed trends in the corrosion rate underscore the importance of platinum in the cathodic corrosion of PtRh alloys. Without platinum, rhodium exhibits a slow corrosion rate which can be enhanced by increasing the positive potential limit. The presence of 12 percent of platinum leads to a dramatic increase in the corrosion rate and shifts the corrosion behavior towards that of pure platinum, while simultaneously diminishing the influence of the positive potential limit on the corrosion rate. With a platinum content of 55 percent, the alloy corrodes virtually identically to pure Pt: it exhibits similar corrosion rates and barely responds to variations of the positive potential limit. Based on these observations, we conclude that platinum dominates the corrosion behavior of the PtRh alloys.

### 7.3.2  Alloy nanoparticle structure

Further insight into the corrosion behavior of the alloys can be gained by comparing the structure of the prepared alloy nanoparticles with that of the parent alloys. Such a comparison is essential, since the local structure of a nanoparticle has a major effect on its catalytic activity. Because the prepared nanoparticles may consist of both crystalline and amorphous phases, one needs to combine several structure-sensitive techniques to probe the relation between the structure of nanoparticles and the conditions under which these particles were synthesized.

The crystalline nanoparticle phases can conveniently be probed by using X-ray diffraction, since this technique exclusively detects crystalline phases. Additionally, both crystalline and non-crystalline phases of the nanoparticles can be detected by EXAFS. This technique probes the local chemical composition, provides information on the average coordination number of the alloy components and is able to resolve average interatomic bonding distances. This information reflects the average local environment around both rhodium and platinum atoms, since both the Pt $L_{III}$ edge and the Rh K edge are probed
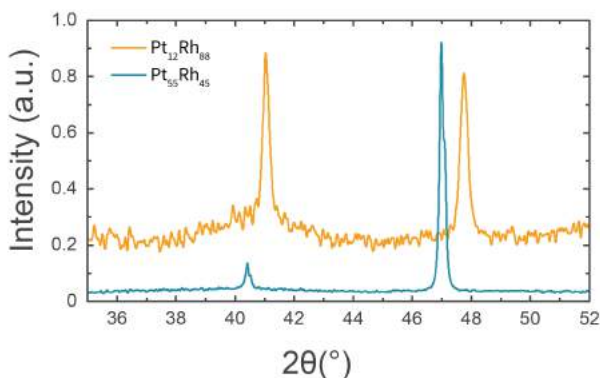
**Fig. 7.2 |** : X-ray diffraction patterns of the parent alloy wires

independently.

## Crystalline phase characterization

Before analyzing the produced nanoparticles, we will briefly discuss the structure of the parent electrodes. Since both parent electrodes exhibit diffraction patterns with well-developed peaks (Fig. 7.2), both parent bulk alloys are crystalline. The peak positions match those of the *fcc* structure, which is the native crystal structure of both platinum and rhodium.[36,37] For both alloys, this structure generates a (111) reflection at $2\theta$-angles between 40 and 42 degrees, along with a (200) reflection peak between 47 and 48 degrees. The well-defined peaks in the $Pt_{12}Rh_{88}$ alloy diffraction pattern suggest the presence of a single crystalline phase. In contrast, the peaks in the $Pt_{55}Rh_{45}$ pattern contain a small shoulder at higher reflection angles. The presence of this shoulder indicates that each peak is actually the product of two overlapping peaks, which points towards a co-existence of two crystalline phases of similar chemical compositions. The chemical composition of both alloys, which can be determined from Vegard's law, agrees well with the expected chemical compositions.

More unexpected is the observation that, for $Pt_{55}Rh_{45}$, the (200) reflection intensity is significantly higher than one would expect from the (111) intensity. This can be attributed to the wire nature of the parent alloy sample, since many wires are oriented along a crystallographic axis;[38] such a preferential orientation should lead to an enhancement of specific peaks in the diffraction pattern of the parent alloy.

XRD was also employed to analyze the produced nanoparticles. For these nanoparticles, the presence of diffraction patterns (Fig. D.2) demonstrates that they are at least partially crystalline. All diffraction peaks conform to the *fcc* structure, which indicates that no crystalline bulk oxide is present in the nanoparticles. Though all of the diffraction patterns match the *fcc* structure, the relative intensities of the patterns differ between Pt-rich and Pt-poor materials. On the one hand, Rh and $Pt_{12}Rh_{88}$ nanoparticles show a disproportionally suppressed scattering in the (200) direction, which suggests a preferential orientation of the formed nanoparticles. On the other hand, the Pt and $Pt_{55}Rh_{45}$ alloys exhibit a more conventional reflection intensity in the (200) direction, which suggests that these particles grew more isotropically.

For all nanoparticles, one can use the X-ray diffraction data to determine the particles' average coherent domain size. This domain size should ideally approach the nanoparticle size and is displayed in Fig. 7.3. The coherent domain sizes in Fig. 7.3 range between *9* and *11 nm* for the pure platinum particles and *3.5* and *5.5 nm* for Rh and the Pt-Rh alloys, respectively. The coherent domain sizes decrease with increasing rhodium content.

Interestingly, the coherent domain sizes of the rhodium-containing particles exceed the average particle sizes obtained in transmission electron microscopy (Table D.1). This apparent discrepancy can be reconciled by examining the particle size distributions in Fig. D.3–D.6, which show that a large fraction of the nanoparticles is smaller than the limit of the diffraction approach in the XRD setup (*ca. 5 nm*). Since this fraction of particles is not detected by X-ray diffraction, XRD detects a disproportionally large amount of big particles. The obtained domain size is therefore an overestimate of the actual particle size.

**Crystalline and amorphous phase characterization**

The discrepancy between the coherent domain size and the TEM-based particle size suggests the presence of a significant amount of amorphous or crystallographically amorphous nanoparticles in the studied samples. In this context, 'crystallographically amorphous' is used to indicate particles that are too small to be detected by XRD. For this reason, it is insightful to study the nanoparticles with EXAFS, which does not require crystallinity and probes the local nanoparticle structure. A combination of EXAFS and XRD will be used in this section to assess the composition of the produced nanoparticles. To simplify the discussion, $Pt_{12}Rh_{88}$ and $Pt_{55}Rh_{45}$ will be discussed separately. Each
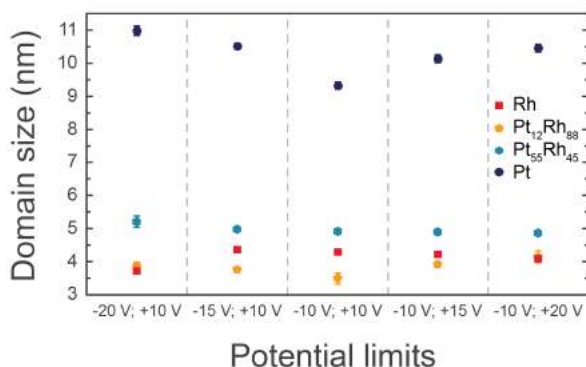
**Fig. 7.3 |** : Coherent domain sizes of the prepared nanoparticles. Error bars represent two standard deviations. If an error bar is not visible, it overlaps with its corresponding data point.

alloy system will be referred to by the composition of the parent alloy, even though the following discussion will demonstrate that the original alloy composition is not always completely preserved in the nanoparticles.

In the case of $Pt_{12}Rh_{88}$, XRD detects a slight platinum enrichment in the produced nanoparticles (Fig. 7.4 **a**). A similar enrichment in platinum is obtained from refinement of the $Pt_{12}Rh_{88}$ EXAFS data (Fig. 7.4 **b**). The rhodium K edge data suggest that the platinum content in the Rh local environment ranges between 13 and 18 percent, while the platinum $L_{III}$ edge data point towards a higher Pt concentration in the local environment of platinum (22 to 27 percent). Though the XRD- and EXAFS-based compositions deviate slightly in samples like the one prepared at $-10\,V$; $+10\,V$, they generally match well.

A less satisfactory agreement between XRD- and EXAFS-based compositions is found for $Pt_{55}Rh_{45}$ (Fig. 7.4 **c, d**): XRD indicates a platinum content that is markedly higher than in the parent alloy (71 to 75 percent), while EXAFS generally indicates a more expected Pt content of 52 to 53 percent in the Rh environment and 59 to 61 percent in the Pt environment. Though the EXAFS-based compositions point towards a minor platinum enrichment with respect to the parent alloy, this enrichment is not as dramatic as suggested by the XRD.

This mild platinum enrichment, which is detected by both techniques and for both alloys, points towards a minor loss of rhodium. Such a loss can be accounted for by noticing that Fig. 7.3 and Fig. D.3–D.6 indicate that rhodium-rich particles are generally smaller than rhodium-poor particles. These small-size rhodium-rich nanoparticles are lost more easily during the purifying centrifuging/rinsing cycles. In addition, a dispro-
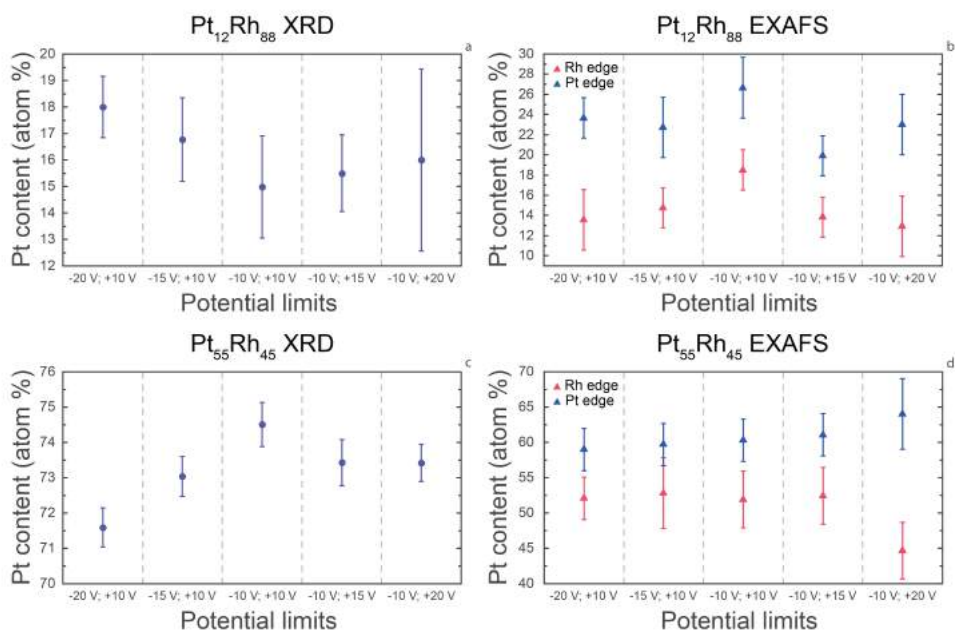
**Fig. 7.4 |**: Composition of nanoparticles produced from $Pt_{12}Rh_{88}$ **(a, b)** and $Pt_{55}Rh_{45}$ **(c, d)** wires, as determined by XRD **(a, c)** and EXAFS **(b, d)**. Error bars represent one standard deviation.

portional amount of rhodium might have been lost through the formation of cationic rhodium during steady-state dissolution.

A more paradoxical observation is the difference between the compositions found by XRD and EXAFS. This discrepancy, which occurs in all $Pt_{55}Rh_{45}$ samples and several $Pt_{12}Rh_{88}$ samples, is another indication of the coexistence of a crystalline and an amorphous phase. Of these two phases, the crystalline one is the only phase that is detectable by XRD. Therefore, the crystalline phase is overrepresented in both the XRD-based particle size and composition data. If this crystalline phase has a different composition than the amorphous phase, a difference between EXAFS and XRD is indeed expected. By combining this result with the observed size difference between XRD and TEM, one can deduce that this crystalline phase has a bigger particle size than the amorphous phase, in addition to the different content that can be deduced from the difference between EXAFS and XRD.

Another hint for the co-existence of a crystalline and amorphous phase follows from a closer scrutiny of the compositions that are found from EXAFS analysis of the Pt $L_{III}$ and

Rh K edge. These compositions indicate that the average local platinum content is higher around platinum atoms and that the average local rhodium content is higher around rhodium. This implies minor clustering of platinum and rhodium, which is a sign of elemental segregation. This segregation might be present as either surface segregation within particles (intra-particle segregation) or as the coexistence of two types of particles with different compositions (inter-particle segregation). These types of segregation cannot be distinguished with EXAFS, since the X-ray beam typically probes sample areas between 0.4 and 1 $mm^2$ and thus provides insufficient spatial resolution. Nonetheless, the EXAFS data clearly indicate a minor degree of elemental segregation. This segregation can be interpreted in a visual manner by using 2D nanoparticle models, which are presented in Fig. D.7.

Further evidence for elemental segregation follows from the inhomogeneous distribution of oxygen on the alloy nanoparticles; approximately $0.8 \pm 0.3$ oxygen atoms per rhodium atom can be refined from the Rh K edge EXAFS data. This oxygen can be attributed to surface oxygen species, since no evidence for the formation of bulk oxides is present in the XRD data. More specifically, this oxygen is likely chemisorbed on the nanoparticles, since the amount of oxygen is independent of the potential limits that were used during particle synthesis. In contrast with oxygen on rhodium, no statistically significant signs of oxygen can be found from the refined Pt $L_{III}$ edge EXAFS data. The absence of chemisorbed surface oxygen species around Pt and presence of these species around Rh suggests a preferential confinement of rhodium to the surface of the produced nanoparticles. As such, this oxygen distribution is an additional sign of a small degree of elemental inhomogeneity in the produced nanoparticles.

**Coordination numbers**

Another indicator of alloy homogeneity is the overall coordination number of each element, which is shown in Fig. 7.5. This quantity can be used as an indicator of surface segregation of the alloy components, since a significantly lower coordination number can be related to the preferential surface confinement of an alloy component.

The $Pt_{12}Rh_{88}$ alloy nanoparticles show reasonable similarity of the platinum and rhodium coordination numbers, which range between 8.5 and 10.0. This indicates that both components are distributed homogeneously throughout the nanoparticles. However, the coordination numbers differ from 12, which is the coordination number of a bulk *fcc* metal. This can be attributed to the rather small size of the prepared nanoparticles,
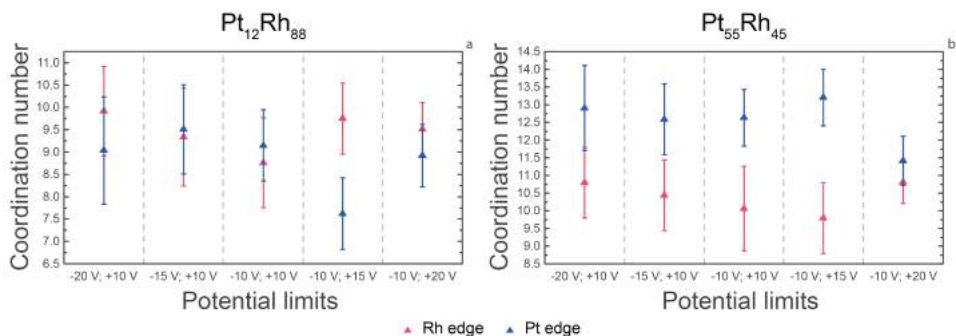
**Fig. 7.5 |** : Average coordination numbers of Pt and Rh in $Pt_{12}Rh_{88}$ **(a)** and $Pt_{55}Rh_{45}$ **(b)**. Error bars represent one standard deviation.

which is in the order of 1.5–2.5 *nm*. In such small particles, 40 to 60 percent of the atoms are at the surface.[39] These atoms have fewer neighboring atoms than those in the bulk, which leads to a lower overall coordination number.

The coordination number of Pt in the $Pt_{55}Rh_{45}$ alloys is closer to 12, which is in agreement with the larger particle sizes of these alloys. However, the average coordination number of Rh is markedly different and appears closer to 10. This suggests predominant confinement of Rh into the particle surface. This surface confinement could again point to both intra- and inter-particle segregation. Intra-particle segregation is plausible, since rhodium can preferentially be present at the surface of an otherwise homogeneous nanoparticle.[40] Similarly plausible is inter-particle segregation as the cause of a lowered coordination number for rhodium: if small rhodium-rich particles coexist with larger platinum-rich particles, one will expect a lower coordination number of rhodium due to the difference in particle size.

**Bond distances**

Another parameter that follows from the EXAFS refinement is the average bonding distance between the various elements in the alloy. These refined metal-metal distances are compared in Fig. 7.6, providing insight into the amount of strain in the prepared nanoparticles.

Surprisingly, the refinement of these distances indicates no variability of the Pt-Pt, Pt-Rh and Rh-Rh bond distances in the $Pt_{12}Rh_{88}$ nanoparticles; both Rh K edge and Pt $L_{III}$ edge data indicate a bond distance of 2.69 Å. This indicates that the Pt atoms in the
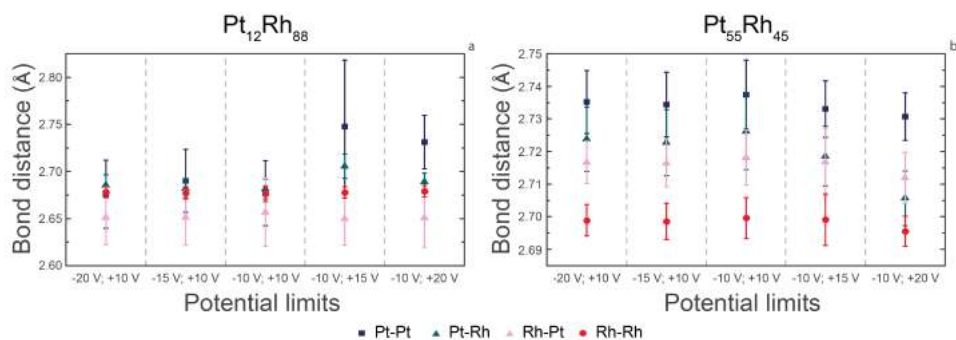
**Fig. 7.6 |** : Average bond distances of Pt and Rh in $Pt_{12}Rh_{88}$ **(a)** and $Pt_{55}Rh_{45}$ **(b)**. The Pt-Rh and Rh-Pt distances both represent the same distance, measured on a different absorption edge. The Pt-Rh data points were measured on the Pt $L_{III}$ edge, while the Rh-Pt points were measured on the Rh K edge. Error bars represent one standard deviation.

prepared nanoparticles reside in rather compressed environments, which agrees well with the fact that the nanoparticles contain more than 80 percent of rhodium. Though this is less rhodium than was present in the parent alloy wires, the rhodium content appears to be high enough to cause strain on the platinum atoms.

In contrast, the metal-metal distances in $Pt_{55}Rh_{45}$ indicate a relaxed structure with well-distinguished bond distances between Pt-Pt and Rh-Rh bonding pairs. These bond distances agree well with those reported in bulk Pt and Rh.[36,37] A similar agreement is obtained for the Pt-Rh bond distances, which fall between those of Pt-Pt and Rh-Rh. This indicates a small degree of element segregation, which matches well with earlier observations from the local platinum content, oxygen distribution and average coordination numbers.

### 7.3.3   Discussion

The electrochemical cathodic corrosion behavior of the studied PtRh systems indicates that platinum electrodes are converted to nanoparticles at a higher rate than rhodium electrodes. The corrosion rate of alloy nanoparticles appears to be dominated by platinum, since the corrosion behavior is sensitive to the alloy composition at low platinum contents and less sensitive to the composition at high platinum contents.

In addition, electrochemical characterization reveals that the corrosion rate of rhodium is strongly affected by the value of the positive potential limit. This indicates a pronounced role of anodic steady-state rhodium dissolution in the overall nanoparticle

production rate. In contrast, the role of steady-state dissolution is strongly diminished for platinum and platinum-containing alloys.

The electrochemically observed steady-state rhodium dissolution is paralleled by a minor loss of rhodium that is indicated by both XRD and EXAFS. This rhodium loss can occur during steady-state dissolution of cationic rhodium at positive polarization. Though it is likely that part of this ionic rhodium will redeposit during the consecutive negative polarization, rhodium loss through steady-state dissolution can currently not be excluded. Alternatively, it is possible that small rhodium-rich particles are lost during particle purification.

Further structural characterization of the PtRh nanoparticles through XRD, TEM and EXAFS provides several insights. Firstly, X-ray diffraction detects nanoparticles that are significantly bigger than transmission electron microscopy would suggest. This indicates that XRD does not detect all produced nanoparticles. In a similar vein, XRD and EXAFS detect different nanoparticle compositions: XRD detects platinum contents that differ significantly from the expected content, while EXAFS matches the expected content relatively well. Combining these observations, it appears that the produced nanoparticle samples contain crystallographically amorphous particles that are undetectable by XRD, have sub-average particle sizes and differ in composition from the nanoparticles that can be detected by XRD.

Secondly, the analysis of the EXAFS data reveals an increased average Pt content around Pt atoms and an increased average Rh content around Rh atoms. This indicates segregation of platinum and rhodium. Elemental segregation is also expressed in the average coordination numbers of platinum and rhodium in the alloy nanoparticles. Though these coordination numbers are similar in $Pt_{12}Rh_{88}$, they differ in $Pt_{55}Rh_{45}$: the lower coordination number of rhodium is a sign of confinement of rhodium to the surface of the nanoparticles, which is underscored by chemisorbed oxygen only being detectable around rhodium. Similarly, the refined bond distances are similar for both elements in $Pt_{12}Rh_{88}$, but are different in $Pt_{55}Rh_{45}$. These differing bond distances are another indication of element segregation in $Pt_{55}Rh_{45}$. This segregation can be a sign of both intra-particle and inter-particle segregation.

## 7.4 Conclusions

This study presents an analysis of nanoparticles of four PtRh systems synthesized by the cathodic corrosion method using various AC potential programs. By studying these obtained nanoparticles with complementary characterization techniques, various insights are obtained.

First of all, electrochemistry indicates that the corrosion behavior of alloys is dominated by the behavior of platinum, which is the component with the fastest corrosion rate. Secondly, XRD and TEM suggest the coexistence of larger crystalline and smaller crystallographically amorphous nanoparticles. This suggestion is confirmed by the difference between XRD and EXAFS data: while the EXAFS data detect an overall composition that is as expected, XRD only detects a crystalline subset of nanoparticles. Finally, the EXAFS-based compositions, coordination numbers and bond lengths indicate that the produced nanoparticles exhibit intra- or inter-particle elemental segregation.

Since this segregation might be induced by the presence of positive potentials during the corrosion protocol in this study, excluding these anodic potentials in a future study might yield additional valuable insights into cathodic corrosion. We do note that the exclusion of anodic potentials would likely lead to longer corrosion times that would be impractical when upscaling cathodic corrosion as a feasible nanoparticle production method.

A more pragmatic avenue for future studies would therefore be to study other alloy systems. The insights obtained in the current work are based exclusively on the PtRh system, in which rhodium is the component that is most prone to steady-state dissolution and has the lowest reduction potential. Research on the corrosion behavior of different alloys should allow for the distinguishment between the importance of these parameters. An ideal first candidate for this study would be the AuPt system, in which gold is more prone to steady-state dissolution,[35] but has a higher reduction potential than platinum.[31]

Though the conclusions from these possible future studies might ultimately lead to a more complete understanding of cathodic corrosion, the current study reaffirms the potential of cathodic corrosion to be a relatively straightforward technique to create alloy nanoparticles.[27,29] At the same time, these insights indicate that cathodic corrosion does not always preserve the alloy composition on an atomic level. It is therefore essential to characterize cathodically created nanoparticles with various complementary techniques, in order to confirm the homogeneity of the final nanoparticle product.

# References

1. Zaera, F. Shape-Controlled Nanostructures in Heterogeneous Catalysis. *ChemSusChem* **6,** 1797–1820 (2013).

2. Ferrando, R., Jellinek, J. & Johnston, R. L. Nanoalloys: From Theory to Applications of Alloy Clusters and Nanoparticles. *Chemical Reviews* **108,** 845–910 (2008).

3. Medford, A. J. *et al.* From the Sabatier principle to a predictive theory of transition-metal heterogeneous catalysis. *Journal of Catalysis* **328,** 36–42 (2015).

4. Vojvodic, A. & Nørskov, J. K. New design paradigm for heterogeneous catalysts. *National Science Review* **2,** 140–149 (2015).

5. Nørskov, J. K. *et al.* Origin of the overpotential for oxygen reduction at a fuel-cell cathode. *Journal of Physical Chemistry B* **108,** 17886–17892 (2004).

6. Shao, M.-H., Sasaki, K. & Adzic, R. R. Pd-Fe Nanoparticles as Electrocatalysts for Oxygen Reduction. *Journal of the American Chemical Society* **128,** 3526–3527 (2006).

7. Cui, C. *et al.* Octahedral PtNi Nanoparticle Catalysts: Exceptional Oxygen Reduction Activity by Tuning the Alloy Particle Surface Composition. *Nano Letters* **12,** 5885–5889 (2012).

8. Kortlever, R., Peters, I., Koper, S. & Koper, M. T. M. Electrochemical $CO_2$ Reduction to Formic Acid at Low Overpotential and with High Faradaic Efficiency on Carbon-Supported Bimetallic Pd–Pt Nanoparticles. *ACS Catalysis* **5,** 3916–3923 (2015).

9. Zhang, T. *et al.* Shape-tunable Pt–Ir alloy nanocatalysts with high performance in oxygen electrode reactions. *Nanoscale* **9,** 1154–1165 (2017).

10. Peng, Z. & Yang, H. Designer platinum nanoparticles: Control of shape, composition in alloy, nanostructure and electrocatalytic property. *Nano Today* **4,** 143–164 (2009).

11. Kim, M.-J., Na, H.-J., Lee, K. C., Yoo, E. A. & Lee, M. Preparation and characterization of Au–Ag and Au–Cu alloy nanoparticles in chloroform. *J. Mater. Chem.* **13,** 1789–1792 (2003).

12. Raveendran, P., Fu, J. & Wallen, S. L. A simple and "green" method for the synthesis of Au, Ag, and Au–Ag alloy nanoparticles. *Green Chem.* **8,** 34–38 (2006).

13. Choi, H., Al-Abed, S. R., Agarwal, S. & Dionysiou, D. D. Synthesis of Reactive Nano-Fe/Pd Bimetallic System-Impregnated Activated Carbon for the Simultaneous Adsorption and Dechlorination of PCBs. *Chemistry of Materials* **20,** 3649–3655 (2008).

14. Deng, Y.-J. *et al.* Alloy tetrahexahedral Pd–Pt catalysts: enhancing significantly the catalytic activity by synergy effect of high-index facets and electronic structure. *Chemical Science* **3,** 1157 (2012).

15. Schröfel, A. *et al.* Applications of biosynthesized metallic nanoparticles – A review. *Acta Biomaterialia* **10,** 4023–4042 (2014).

16. Koch, C. C. Synthesis of nanostructured materials by mechanical milling: problems and opportunities. *Nanostructured Materials* **9,** 13–22 (1997).

17. Lee, I., Han, S. W. & Kim, K. Production of Au–Ag alloy nanoparticles by laser ablation of bulk alloys. *Chemical Communications* **3,** 1782–1783 (2001).

18. He, T., Kreidler, E., Xiong, L., Luo, J. & Zhong, C. J. Alloy Electrocatalysts. *Journal of The Electrochemical Society* **153,** A1637–A1643 (2006).

19. Haber, F. The Phenomenon of the Formation of Metallic Dust from Cathodes. *Transactions of the American Electrochemical Society* **2,** 189–196 (1902).

20. Kabanov, B. N., Astakhov, I. I. & Kiseleva, I. G. Formation of crystalline intermetallic compounds and solid solutions in electrochemical incorporation of metals into cathodes. *Electrochimica Acta* **24,** 167–171 (1979).

21. Huang, W., Chen, S., Zheng, J. & Li, Z. Facile preparation of Pt hydrosols by dispersing bulk Pt with potential perturbations. *Electrochemistry Communications* **11,** 469–472 (2009).

22. Liu, J., Huang, W., Chen, S. & Hu, S. Facile electrochemical dispersion of bulk Rh into hydrosols. *Int. J. Electrochem. Sci.* **4,** 1302–1308 (2009).

23. Yanson, A. I. *et al.* Cathodic Corrosion: A Quick, Clean, and Versatile Method for the Synthesis of Metallic Nanoparticles. *Angewandte Chemie International Edition* **50,** 6346–6350 (2011).

24. Leontyev, I., Kuriganova, A., Kudryavtsev, Y., Dkhil, B. & Smirnova, N. New life of a forgotten method: Electrochemical route toward highly efficient Pt/C catalysts for low-temperature fuel cells. *Applied Catalysis A: General* **431-432,** 120–125 (2012).

25. Lu, F., Ji, X., Yang, Y., Deng, W. & Banks, C. E. Room temperature ionic liquid assisted well-dispersed core-shell tin nanoparticles through cathodic corrosion. *RSC Advances* **3,** 18791–18793 (2013).

26. Najdovski, I., Selvakannan, P. & O'Mullane, A. P. Cathodic Corrosion of Cu Substrates as a Route to Nanostructured Cu/M (M=Ag, Au, Pd) Surfaces. *ChemElectroChem* **2,** 106–111 (2015).

27. Rodriguez, P., Tichelaar, F. D., Koper, M. T. M. & Yanson, A. I. Cathodic Corrosion as a Facile and Effective Method To Prepare Clean Metal Alloy Nanoparticles. *Journal of the American Chemical Society* **133,** 17626–17629 (2011).

28. Duca, M., Rodriguez, P., Yanson, A. I. & Koper, M. T. M. Selective Electrocatalysis on Platinum Nanoparticles with Preferential (100) Orientation Prepared by Cathodic Corrosion. *Topics in Catalysis* **57,** 255–264 (2014).

29. Bennett, E. *et al.* A Synthetic Route for the Effective Preparation of Metal Alloy Nanoparticles and Their Use as Active Electrocatalysts. *ACS Catalysis* **6,** 1533–1539 (2016).

30. Vitos, L., Ruban, A. V., Skriver, H. L. & Kollár, J. The surface energy of metals. *Surface Science* **411,** 186–202 (1998).

31. Vanýsek, P. in *CRC Handbook of Chemistry and Physics* (ed Haynes, W. M.) 96th ed., 5–80 – 5–89 (CRC Press, Boca Raton, FL, 2015).

32. Zafeiratos, S., Piccinin, S. & Teschner, D. Alloys in catalysis: phase separation and surface segregation phenomena in response to the reactive environment. *Catalysis Science & Technology* **2,** 1787–1801 (2012).

33. Newville, M. IFEFFIT : interactive XAFS analysis and FEFF fitting. *Journal of Synchrotron Radiation* **8,** 322–324 (2001).

34. Ravel, B. & Newville, M. ATHENA , ARTEMIS , HEPHAESTUS: data analysis for X-ray absorption spectroscopy using IFEFFIT. *Journal of Synchrotron Radiation* **12,** 537–541 (2005).

35. Cherevko, S. *et al.* Dissolution of Noble Metals during Oxygen Evolution in Acidic Media. *ChemCatChem* **6,** 2219–2223 (2014).

36. Arblaster, J. W. Crystallographic Properties of Platinum. *Platinum Metals Review* **41,** 12–21 (1997).

37. Arblaster, J. W. Crystallographic Properties of Rhodium. *Platinum Metals Review* **41,** 184–189 (1997).

38. Dillamore, I. L. & Roberts, W. T. Preferred Orientation in Wrought in Annealed Metals. *Metallurgical Reviews* **10,** 271–380 (1965).

39. Blackman, J. A. & Binns, C. in *Metallic Nanoparticles* (ed Blackman, J. A.) 1st ed., 1–16 (Elsevier, 2009).

40. Tao, F. *et al.* Evolution of Structure and Chemistry of Bimetallic Nanoparticle Catalysts under Reaction Conditions. *Journal of the American Chemical Society* **132,** 8697–8703 (2010).

8
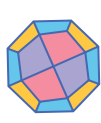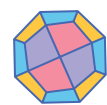
# Summary and Future Outlook

The work in this thesis is centered around cathodic corrosion: a chemical process that severely alters metals, but is significantly less understood than its anodic counterpart. Though cathodic corrosion is still shrouded in unresolved mysteries, this thesis marks an important advance in our understanding of this remarkable chemical phenomenon.

The thesis starts with two chapters that explore the cathodic corrosion behavior of Pt, Rh and Au in 10 $M$ NaOH. In Chapter 2, Pt is shown to start cathodically corroding at much milder potentials than previously assumed. Similar findings are reported for Rh and Au in Chapter 3. Both chapters also support an earlier hypothesis regarding the role of cations in controlling the etching preference of cathodic corrosion.

The role of cations is further investigated for Pt, Rh and Au in Chapter 4. This investigation combines elaborate experimental and theoretical characterization to firmly establish the structure-guiding role of cations. Perhaps surprisingly, Chapter 4 suggests an equally important role for adsorbed hydrogen. Based on these findings, the chapter presents the first concrete hypothesis of the key reaction intermediate during cathodic corrosion: ternary metal hydrides.

Such hydrides are evaluated in Chapter 5, which examines Pt nanoparticles during cathodic corrosion, using *operando* "high-energy resolution fluorescence detection X-ray absorption near edge structure" (HERFD-XANES) experiments. This chapter finds that the ternary metal hydride $Na_2PtH_6$ is a likely candidate for being the enigmatic intermediate. If proven correct in future experimental and theoretical analysis, this would, to our knowledge, be the first detection of this type of hydride in an aqueous environment.

Chapter 2–5 are therefore focused on expanding the available knowledge of cathodic corrosion. Part of this knowledge is applied and elaborated upon in the application-focused Chapters 6 and 7. Chapter 6 illustrates how to optimize catalysts through pretreatment by cathodic corrosion. Chapter 7 then investigates the known use of cathodic corrosion for creating PtRh nanoparticles. In doing so, valuable clues towards the corrosion behavior of alloys are gained and precautions for alloy nanoparticle production are identified.

As such, the presented chapters build upon previous work on cathodic corrosion. They shed light on previously observed cation effects,[1] and indicate the nature of the metallic anion.[2] In addition, they add a modest but relevant contribution to the growing body of literature of cathodic corrosion as a method to produce metal and metal oxide

nanoparticles.[3–6] These contributions facilitate the applications of cathodic corrosion and the relatively unexplored chemistry that drives it.

These advances have nonetheless left many questions unanswered and have generated new questions. A pertinent selection of these questions will be presented below.

First of all, the presence of ternary metal hydrides would imply an importance of a hydrogen donor like $H_2O$. The role of such a donor might be explored by restricting the availability of water. Though the complete exclusion of water is extremely challenging, water-free conditions can be approximated by performing experiments in aprotic solvents or ionic liquids. Mixtures of these solvents with water might also prove useful. The use of non-aqueous solvents will surely generate interesting results regarding the cathodic chemistry of metals and could point towards the reduction of metals towards unexpected species.[7,8]

Additionally, the existence of ternary metal hydrides would need to be studied for metals other than platinum. Such studies would test the generality of proposed reaction intermediate. This would require spectroscopic studies of Rh and Au, but also systematic cathodic corrosion studies of metals like Ir, Cu and Ag. These metals were not studied in the present work due to challenges in electrode preparation, but the use of larger electrodes and an inductive annealing setup could help overcome these challenges.

Furthermore, this thesis largely focuses on qualitatively understanding cathodic corrosion. This qualitative understanding might enable more quantitative future studies on factors like the corrosion kinetics. Exploring these etching kinetics *ex-situ* or even *in-situ* through methods like electrochemical scanning tunneling microscopy could provide a wealth of information on cathodic corrosion.

A final unresolved question is the role of *anodic* corrosion in nanoparticle formation, when it is combined with cathodic corrosion to create nanoparticles. Though Chapter 7 and previous work[2] provide initial results on this matter, further carefully designed experiments would be necessary to unambiguously quantify the role of anodic corrosion. Such experiments would require using a three-electrode setup, instead of the two-electrode setup that is commonly used when making nanoparticles.

Answering these questions could help propel cathodic corrosion from being a niche phenomenon to being a useful component of every electrochemist's toolkit. Doing so would not only explore novel chemistry at the cathodic side of the electrochemical series, but would also inspire new approaches to tackling the electrochemical challenges of the $21^{st}$ century. It is my hope that this thesis has furthered this development of cathodic

corrosion.

# References

1.   Yanson, A., Antonov, P., Rodriguez, P. & Koper, M. Influence of the electrolyte concentration on the size and shape of platinum nanoparticles synthesized by cathodic corrosion. *Electrochimica Acta* **112,** 913–918 (2013).

2.   Yanson, A. I. *et al.* Cathodic Corrosion: A Quick, Clean, and Versatile Method for the Synthesis of Metallic Nanoparticles. *Angewandte Chemie International Edition* **50,** 6346–6350 (2011).

3.   Bennett, E. *et al.* A Synthetic Route for the Effective Preparation of Metal Alloy Nanoparticles and Their Use as Active Electrocatalysts. *ACS Catalysis* **6,** 1533–1539 (2016).

4.   Kromer, M. L. *et al.* High-Throughput Preparation of Metal Oxide Nanocrystals by Cathodic Corrosion and Their Use as Active Photocatalysts. *Langmuir* **33,** 13295–13302 (2017).

5.   Feng, J. *et al.* Cathodic Corrosion of a Bulk Wire to Nonaggregated Functional Nanocrystals and Nanoalloys. *ACS Applied Materials & Interfaces* **10,** 9532–9540 (2018).

6.   Lawrence, M. J. *et al.* Electrochemical Synthesis of Nanostructured Metal-Doped Titanates and Investigation of Their Activity as Oxygen Evolution Photoanodes. *ACS Applied Energy Materials,* acsaem.8b00873 (2018).

7.   Ghilane, J., Guilloux-Viry, M., Lagrost, C., Hapiot, P. & Simonet, J. Cathodic modifications of platinum surfaces in organic solvent: reversibility and cation type effects. *The journal of physical chemistry. B* **109,** 14925–31 (2005).

8.   Ghilane, J. *et al.* Spectroscopic Evidence of Platinum Negative Oxidation States at Electrochemically Reduced Surfaces. *Journal of Physical Chemistry C* **111,** 5701–5707 (2007).

# A   Supplementary Information for Chapter 4

## A.1   Calculated surface structures

This section contains images of the calculated Pt, Rh, and Au structures with adsorbed water (*H$_2$O), in the absence and presence of adsorbed sodium (*Na) (Fig. A.1–A.3). Additional structures were calculated for adsorbed lithium and potassium. Because these structures are similar to those with adsorbed sodium, their visualizations are omitted for brevity.
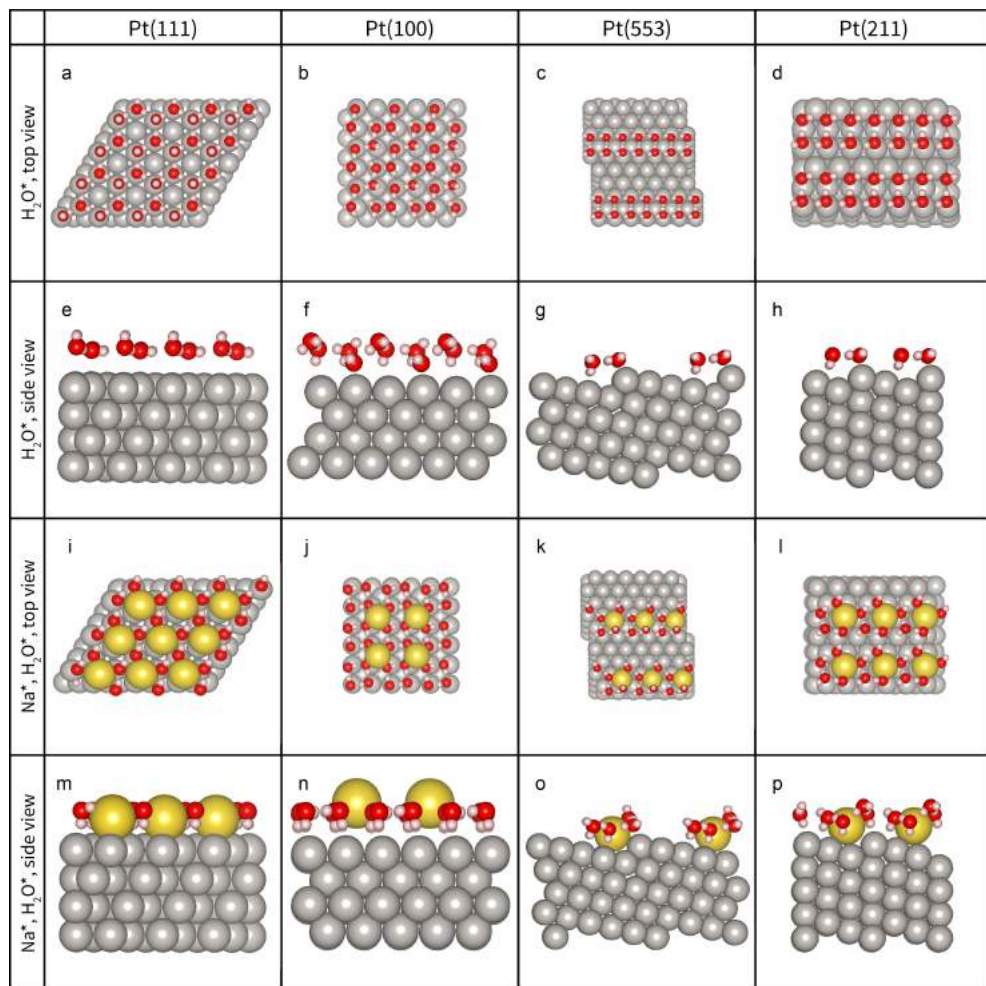
**Fig. A.1 |** Visualizations of the minimum-energy structures for Pt(111) **(a, e, i, m)**, Pt(100) **(b, f, j, n)**, Pt(553) **(c, g, k, o)** & Pt(211) **(d, h, l, p)**. Adsorbed water (*$H_2O$) is displayed in red and white, while sodium (*Na) is displayed in yellow.
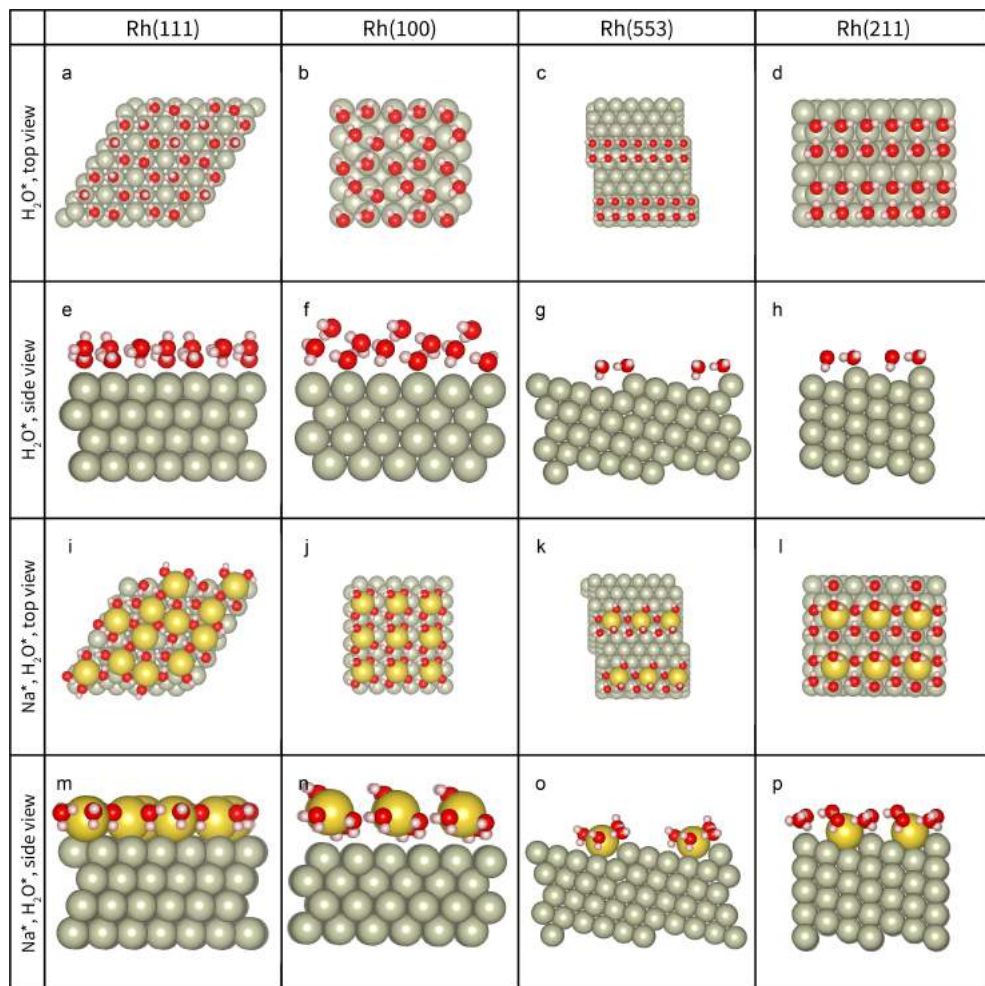
**Fig. A.2 |** Visualizations of the minimum-energy structures for Rh(111) **(a, e, i, m)**, Rh(100) **(b, f, j, n)**, Rh(553) **(c, g, k, o)** & Rh(211) **(d, h, l, p)**. Adsorbed water (*H$_2$O) is displayed in red and white, while sodium (*Na) is displayed in yellow.
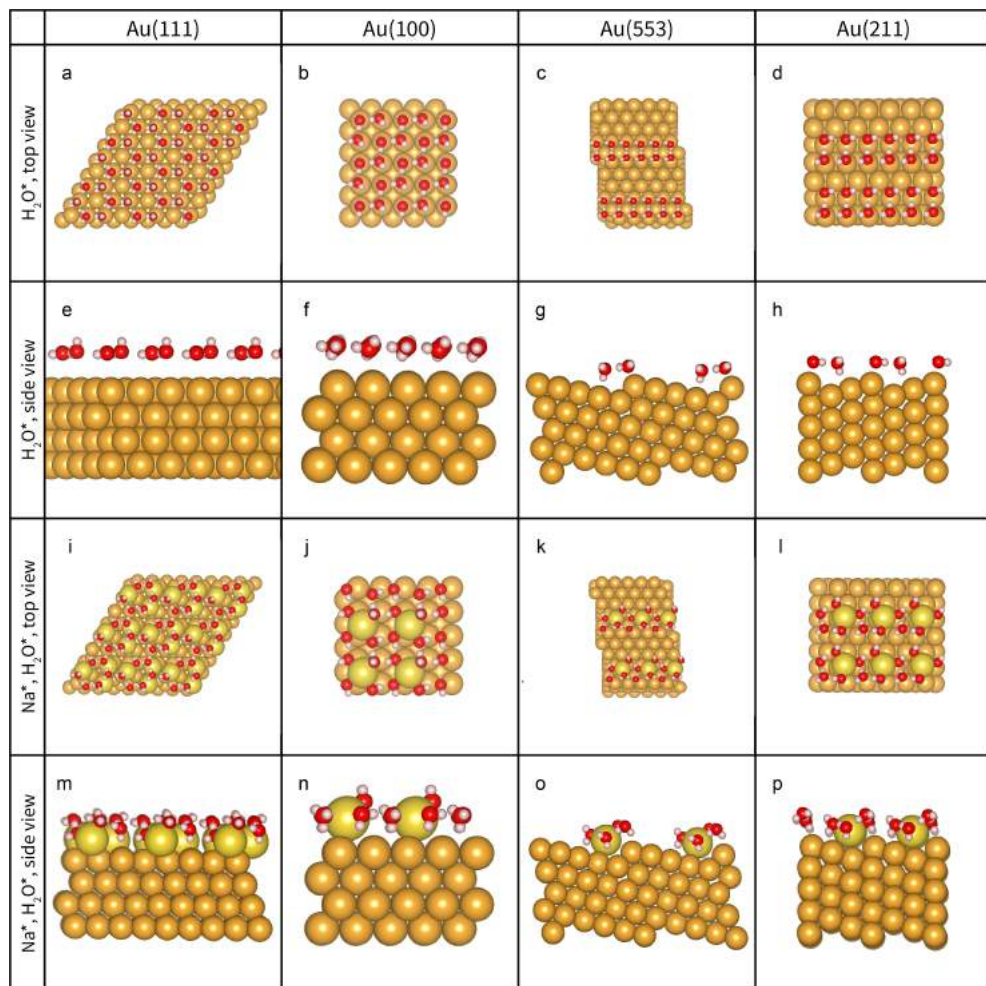
**Fig. A.3 |** Visualizations of the minimum-energy structures for Au(111) **(a, e, i, m)**, Au(100) **(b, f, j, n)**, Au(553) **(c, g, k, o)** & Au(211) **(d, h, l, p)**. Adsorbed water (*$H_2O$) is displayed in red and white, while sodium (*Na) is displayed in yellow.

## A.2   Cathodic corrosion progression: voltammetry

This section presents cyclic voltammograms (CVs) for all studied metals and electrolytes, following the template used in Chapter 2 & 3. The presented plots provide a more elaborate representation of the corrosion behavior of the studied systems. As such, they allow for the concrete determination of the onset potential of Pt corrosion. The onset potential of Rh can be found from Fig. 4.5, while Fig. A.29 allows for the determination of the onset potential of Au. All figures in the current section (Fig. A.4 through Fig. A.15) contain a CV before the onset potential in Panel **a**, a CV at the onset potential in Panel **b** and CVs featuring more advanced corrosion in Panel **c** and **d**. For Pt and Au, brief additional discussion is included to support specific statements in Chapter 4. All CVs shown here in red are the *fourth* characterization cycle after cathodic polarization.

### A.2.1   Platinum voltammograms

The current paragraph will briefly support the statement that an increasing cation concentration causes the formation of increasingly disordered surface sites. Inspection of the CVs in Fig. 4.1 indicates that corrosion in 1 $M$ NaOH leads primarily to the creation of (100) terraces, which are visible in the CV between 0.3 and 0.4 $V$ *vs.* RHE, at the cost of (110) steps. As such, more long-range order terraces are created as less-ordered features such as steps are removed. Similarly, the significant increase in surface area after corrosion in 5 $M$ NaOH is primarily caused by an increase of (100) terrace sites. In contrast, these (100) terrace sites barely increase when corroding in 10 $M$ NaOH. Instead, more steps of both the (100) and (110) orientation are created.
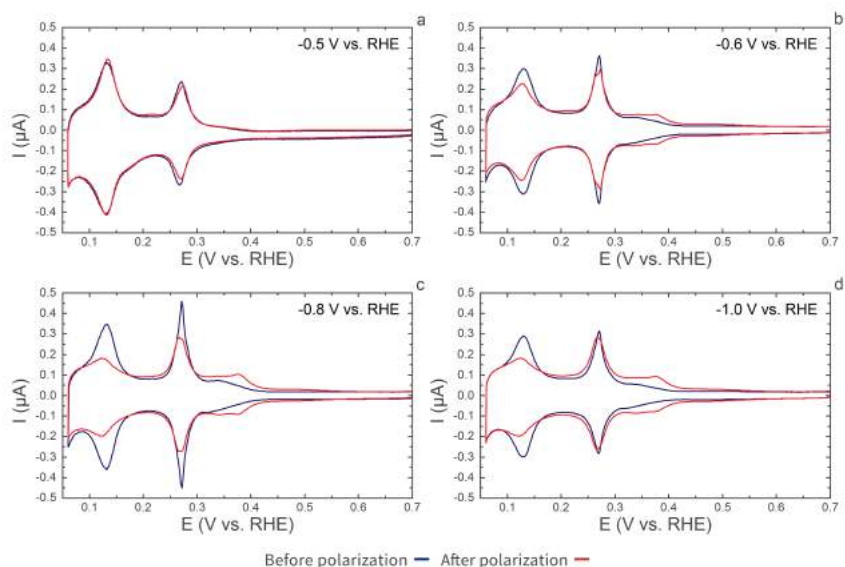
**Fig. A.4** | CVs of Pt before (blue trace) and after (red trace) polarization in 1 *M* LiOH at −0.5 *V* vs. RHE **(a)**, −0.6 *V* vs. RHE **(b)**, −0.8 *V* vs. RHE **(c)** and −1.0 *V* vs. RHE **(d)**. CV electrolyte: 0.5 *M* H$_2$SO$_4$. Scan rate: 50 *mV · s$^{-1}$*.
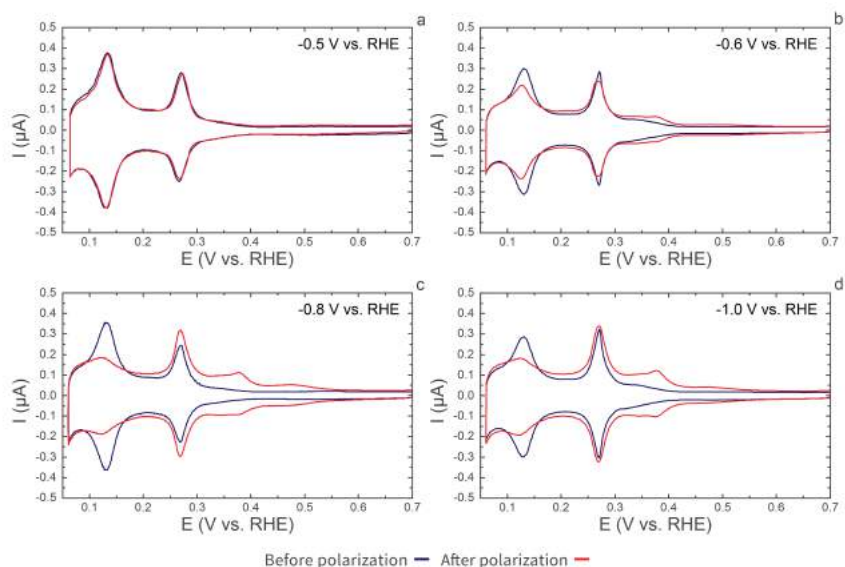


**Fig. A.5** | CVs of Pt before (blue trace) and after (red trace) polarization in 1 *M* NaOH at −0.5 *V* vs. RHE **(a)**, −0.6 *V* vs. RHE **(b)**, −0.8 *V* vs. RHE **(c)** and −1.0 *V* vs. RHE **(d)**. CV electrolyte: 0.5 *M* H$_2$SO$_4$. Scan rate: 50 *mV · s$^{-1}$*.
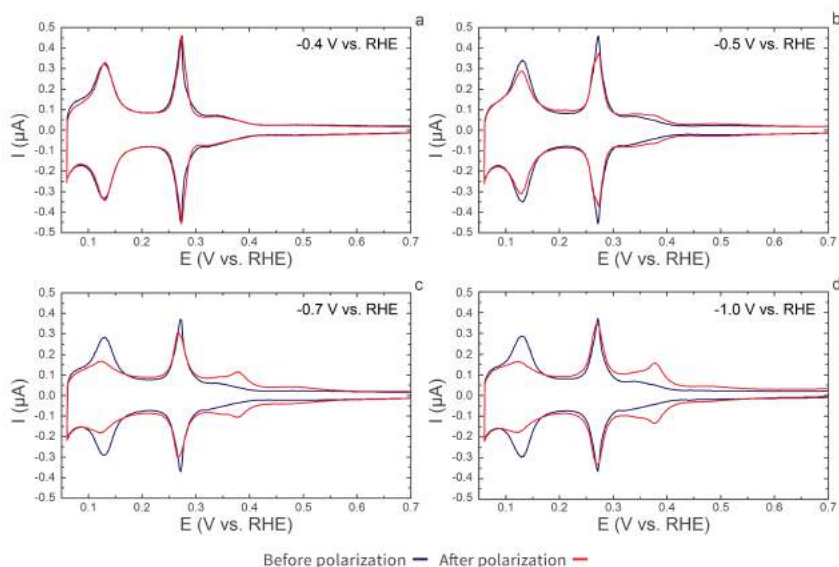
**Fig. A.6 |** CVs of Pt before (blue trace) and after (red trace) polarization in 1 *M* KOH at −0.4 *V vs.* RHE **(a)**, −0.5 *V vs.* RHE **(b)**, −0.7 *V vs.* RHE **(c)** and −1.0 *V vs.* RHE **(d)**. CV electrolyte: 0.5 *M* H₂SO₄. Scan rate: 50 $mV \cdot s^{-1}$.
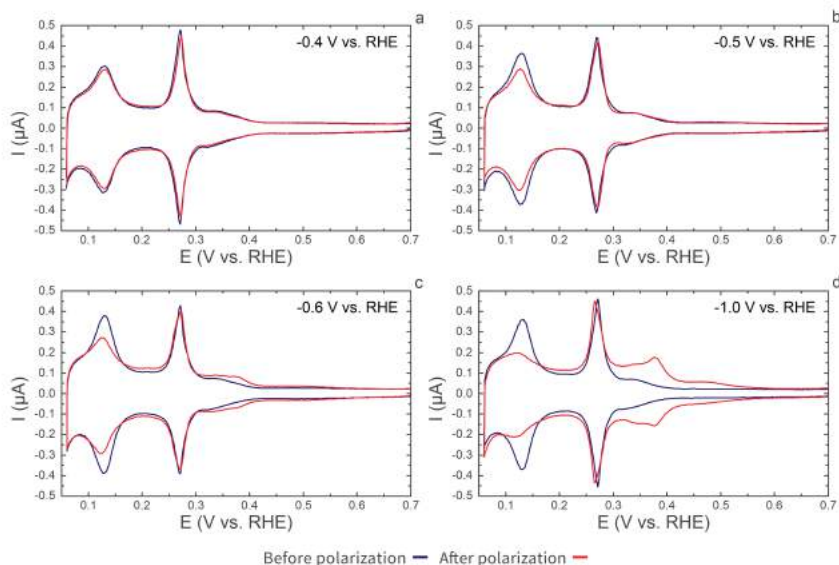


**Fig. A.7 |** CVs of Pt before (blue trace) and after (red trace) polarization in 5 *M* LiOH at −0.4 *V vs.* RHE **(a)**, −0.5 *V vs.* RHE **(b)**, −0.6 *V vs.* RHE **(c)** and −1.0 *V vs.* RHE **(d)**. CV electrolyte: 0.5 *M* H₂SO₄. Scan rate: 50 $mV \cdot s^{-1}$.
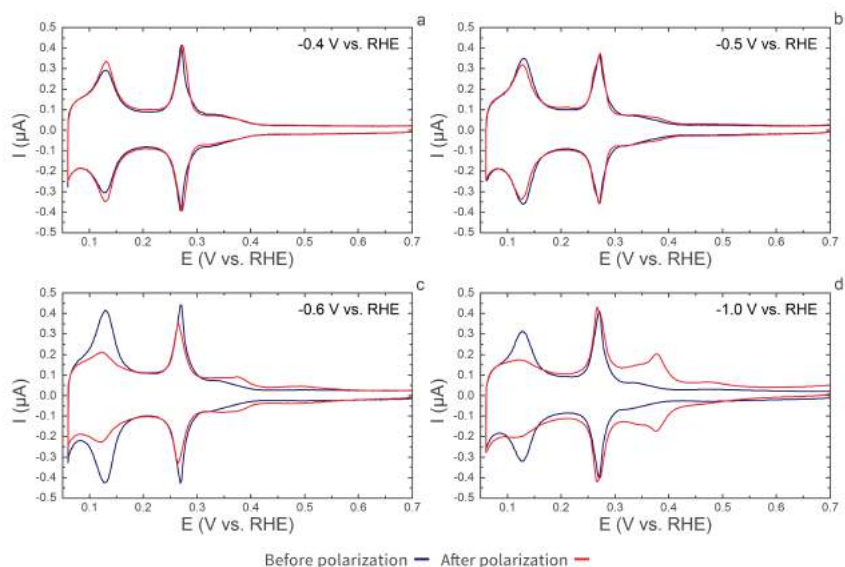
**Fig. A.8 |** CVs of Pt before (blue trace) and after (red trace) polarization in 5 *M* NaOH at $-0.4$ *V* vs. RHE **(a)**, $-0.5$ *V* vs. RHE **(b)**, $-0.6$ *V* vs. RHE **(c)** and $-1.0$ *V* vs. RHE **(d)**. CV electrolyte: 0.5 *M* $H_2SO_4$. Scan rate: 50 $mV \cdot s^{-1}$.
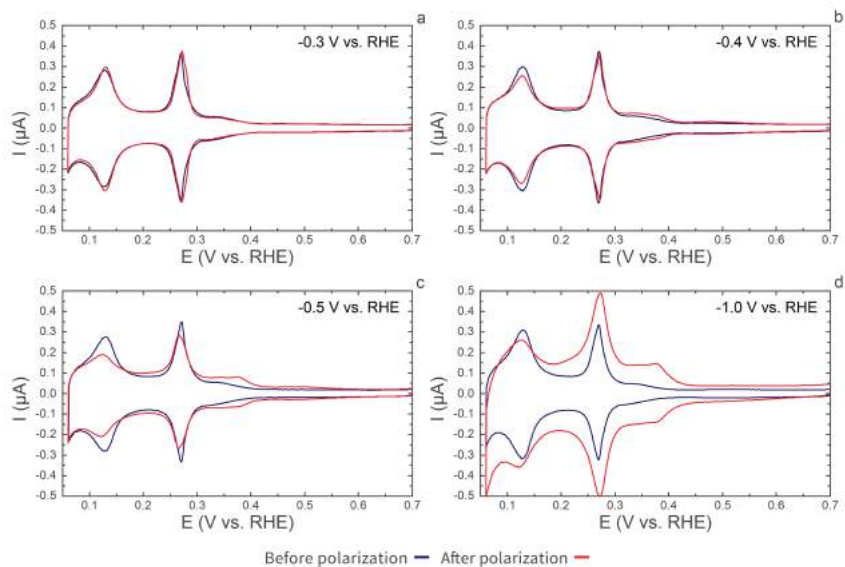


**Fig. A.9 |** CVs of Pt before (blue trace) and after (red trace) polarization in 5 *M* KOH at $-0.3$ *V* vs. RHE **(a)**, $-0.4$ *V* vs. RHE **(b)**, $-0.5$ *V* vs. RHE **(c)** and $-1.0$ *V* vs. RHE **(d)**. CV electrolyte: 0.5 *M* $H_2SO_4$. Scan rate: 50 $mV \cdot s^{-1}$.

## A.2.2 Rhodium voltammograms
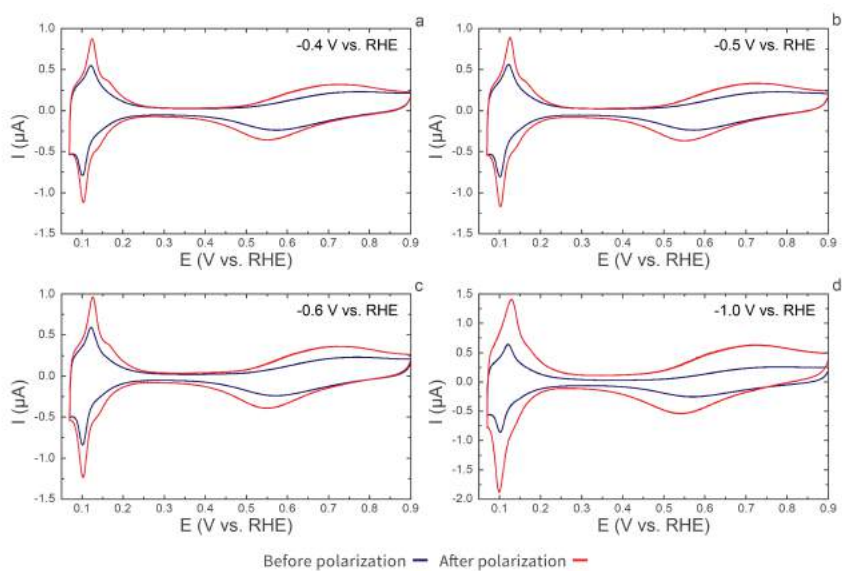


**Fig. A.10 |** CVs of Rh before (blue trace) and after (red trace) polarization in $5\ M$ LiOH at $-0.4\ V$ *vs.* RHE **(a)**, $-0.5\ V$ *vs.* RHE **(b)**, $-0.6\ V$ *vs.* RHE **(c)** and $-1.0\ V$ *vs.* RHE **(d)**. CV electrolyte: $0.1\ M$ $H_2SO_4$. Scan rate: $50\ mV \cdot s^{-1}$.
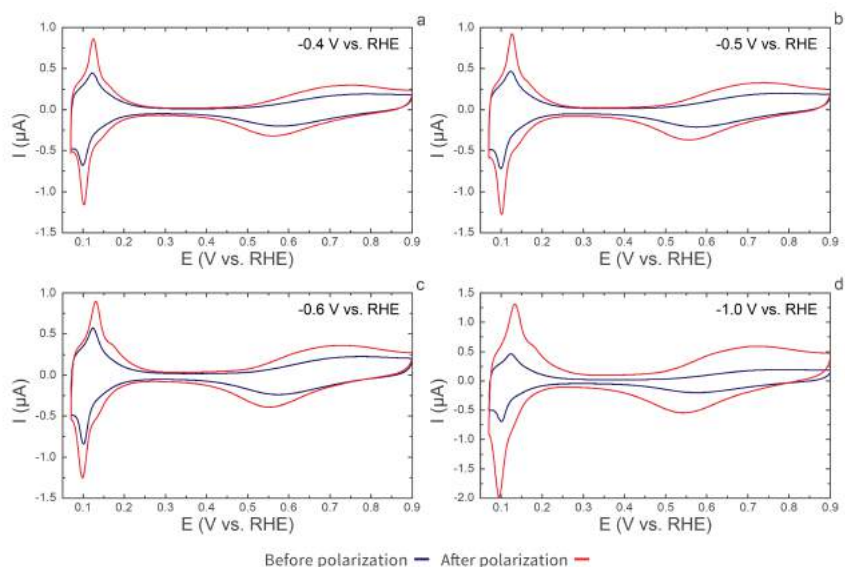
**Fig. A.11 |** CVs of Rh before (blue trace) and after (red trace) polarization in 5 $M$ NaOH at $-0.4$ $V$ *vs.* RHE **(a)**, $-0.5$ $V$ *vs.* RHE **(b)**, $-0.6$ $V$ *vs.* RHE **(c)** and $-1.0$ $V$ *vs.* RHE **(d)**. CV electrolyte: 0.1 $M$ $H_2SO_4$. Scan rate: 50 $mV \cdot s^{-1}$.
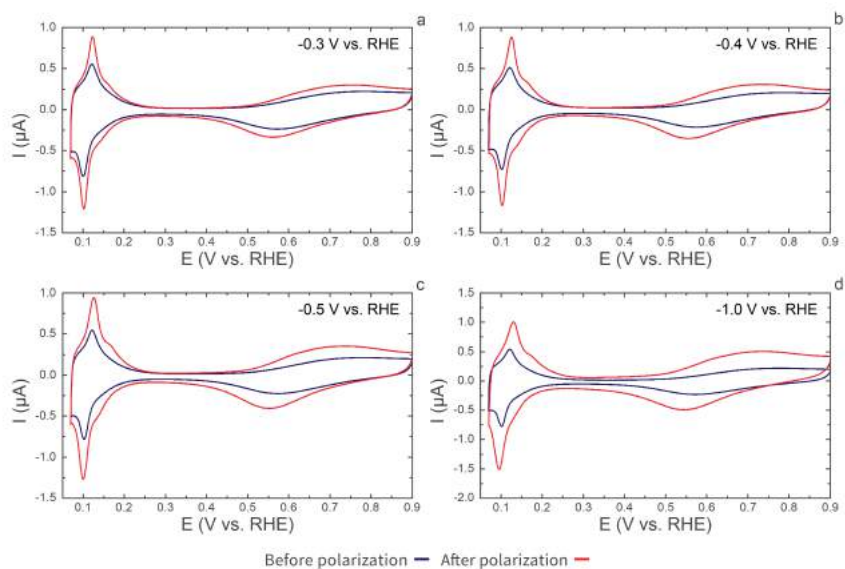


**Fig. A.12 |** CVs of Rh before (blue trace) and after (red trace) polarization in 5 $M$ KOH at $-0.3$ $V$ *vs.* RHE **(a)**, $-0.4$ $V$ *vs.* RHE **(b)**, $-0.5$ $V$ *vs.* RHE **(c)** and $-1.0$ $V$ *vs.* RHE **(d)**. CV electrolyte: 0.1 $M$ $H_2SO_4$. Scan rate: 50 $mV \cdot s^{-1}$.

### A.2.3   Gold voltammograms

The present section will briefly elaborate on the shape of Au voltammograms that are shown here and in Chapter 4. As indicated in Fig. 4.7 and Fig. A.13, corrosion in LiOH induces only small changes in the cyclic voltammogram of Au, whereas more pronounced changes are found for corrosion in NaOH. Beside the differences addressed in Chapter 4, the Au voltammograms after NaOH corrosion (Fig. A.14) also exhibit a pair of peaks at 1.38 and 1.42 *V vs.* RHE. These peaks are sharp and positioned at slightly higher and lower potentials, respectively, compared to the (100) peak on electrodes corroded in LiOH. Thus, the pair of peaks likely corresponds to a small amount of (100) and (111) step sites, of which the CV signal is superimposed on the (100) terrace peak. The presence of this peak pair and of the sharp (111) peak suggest a pronounced difference in corrosion behavior with respect to LiOH.

A similarly pronounced difference is found for corrosion in 5 *M* KOH (Fig. 4.7 & Fig. A.15), which shows a remarkable evolution between the first and fourth CV cycle after corrosion. Though the reason for this evolution is unknown, it does match the dramatic change in facet distribution between the first and fourth cycle. During the first cycle, the electrode appears rather amorphous, resembling a freshly polished electrode that has perhaps undergone several cycles of voltammetry;[1] a sharp peak corresponding to (100) sites is virtually absent in the voltammogram. The shape of this voltammogram changes readily after undergoing several additional cycles to yield an electrode that resembles a sample corroded in 5 *M* LiOH, but with slightly more step sites, (110) terrace sites and (111) sites.
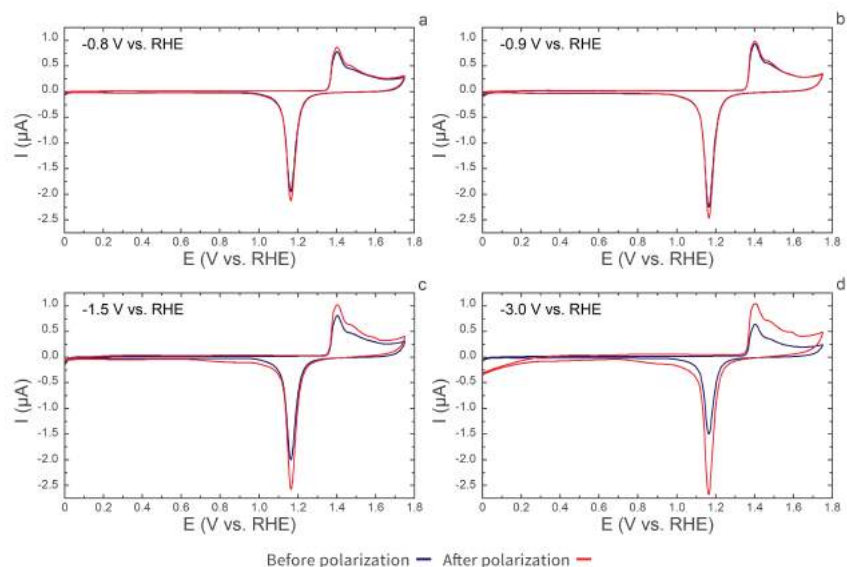
**Fig. A.13 |** CVs of Au before (blue trace) and after (red trace) polarization in 5 $M$ LiOH at $-0.8$ $V$ vs. RHE **(a)**, $-0.9$ $V$ vs. RHE **(b)**, $-1.5$ $V$ vs. RHE **(c)** and $-3.0$ $V$ vs. RHE **(d)**. CV electrolyte: 0.1 $M$ $H_2SO_4$. Scan rate: 50 $mV \cdot s^{-1}$.
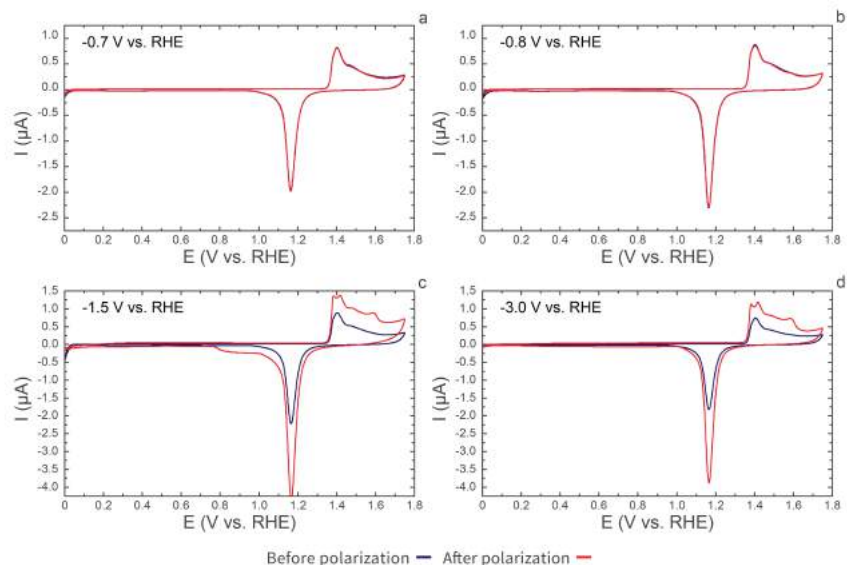


**Fig. A.14 |** CVs of Au before (blue trace) and after (red trace) polarization in 5 $M$ NaOH at $-0.7$ $V$ vs. RHE **(a)**, $-0.8$ $V$ vs. RHE **(b)**, $-1.5$ $V$ vs. RHE **(c)** and $-3.0$ $V$ vs. RHE **(d)**. CV electrolyte: 0.1 $M$ $H_2SO_4$. Scan rate: 50 $mV \cdot s^{-1}$.
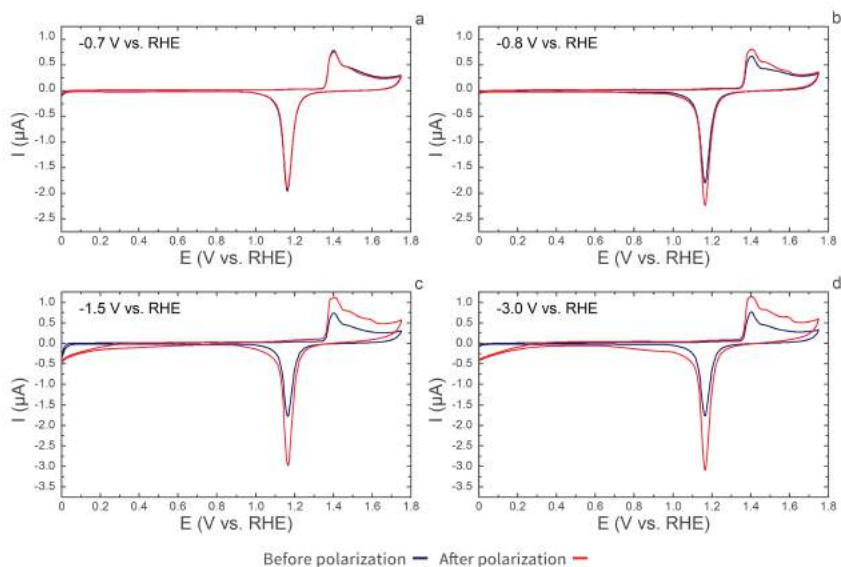
**Fig. A.15 |** CVs of Au before (blue trace) and after (red trace) polarization in $5\ M$ KOH at $-0.7\ V$ *vs.* RHE **(a)**, $-0.8\ V$ *vs.* RHE **(b)**, $-1.5\ V$ *vs.* RHE **(c)** and $-3.0\ V$ *vs.* RHE **(d)**. CV electrolyte: $0.1\ M$ $H_2SO_4$. Scan rate: $50\ mV \cdot s^{-1}$.

## A.3 Cathodic corrosion progression: scanning electron microscopy

This section displays scanning electron micrographs that illustrate the progression of cathodic corrosion as function of the applied electrode potential. These figures are arranged in the same order as the figures in the previous section. Though most figures can be interpreted readily with the information provided in Chapter 4, several electrode features that are not caused by cathodic corrosion are highlighted here for clarity:

- On Pt electrodes, some facets contain roughness that is visible as lines in the micrographs, as can be seen in Fig. A.16 **d, e**, Fig. A.18 **b, d**, Fig. A.19 **a, d**, Fig. A.20 **a, d** and Fig. A.21 **d**. These features were also observed for electrodes that were polarized at less cathodic potentials than the onset of cathodic corrosion and are therefore likely not signs of cathodic corrosion.

- On Rh electrodes, which were not annealed in this study, cracks, pits and ridges such as those in Panel **a** of Fig. A.22 through Fig. A.24 are present. These cracks are also visible on unpolarized electrodes and are therefore not considered signs of

cathodic corrosion (Chapter 3).

– On Au, cracks similar to those observed on rhodium are present. These are similarly observed on untreated electrodes and therefore not thought to be features of cathodic corrosion.

Beside these remarks, several paragraphs of additional discussion are included below for each metal.

### A.3.1 Platinum micrographs

This paragraph will briefly illustrate cathodic corrosion in $1\,M$ electrolytes and motivate the statement that the extent of cathodic corrosion increases with cation size. Starting with LiOH (Fig. A.16), no pronounced roughening is visible at $-1.0\,V$ *vs.* RHE, but triangular etch pits can be observed at more negative potentials. More significant roughening is visible for NaOH (Fig. A.17), which induces the formation of triangular etch pits at less negative potentials than in $1\,M$ LiOH. At more negative potentials, this more extensive corrosion causes the formation of nanoscale corrugation in NaOH. KOH (Fig. A.18) completes this trend, with electrodes appearing slightly more corrugated than in NaOH.

Along with corrosion depending on the cation, it is also sensitive to the applied potential. Interestingly, this dependence appears similar in SEM after corrosion at mild potentials. Specifically, SEM indicates that corrosion starts at triangular (100) etch pits. This is illustrated by electrodes corroded in $5\,M$ NaOH, which contain triangular features within some regions where more severe corrosion occurs (Fig. 4.4 **e** & Fig. A.20 **f**). These features bear resemblance to the well-defined triangular etch pits observed at less negative potentials (Fig. A.20 **b**). It is therefore possible that such well-defined pits serve as starting points of cathodic corrosion: severe corrosion could cause the sides of a triangle to extend into the features in Fig. 4.4 **e**. Selective extension of one triangle side due to curvature of the electrode might even lead to the formation of the etch lines in Fig. 4.2 **b** and Fig. 4.4 **b**. Similar arguments can be based on the corrosion behavior in $1\,M$ NaOH and KOH (Fig. A.17–A.18).
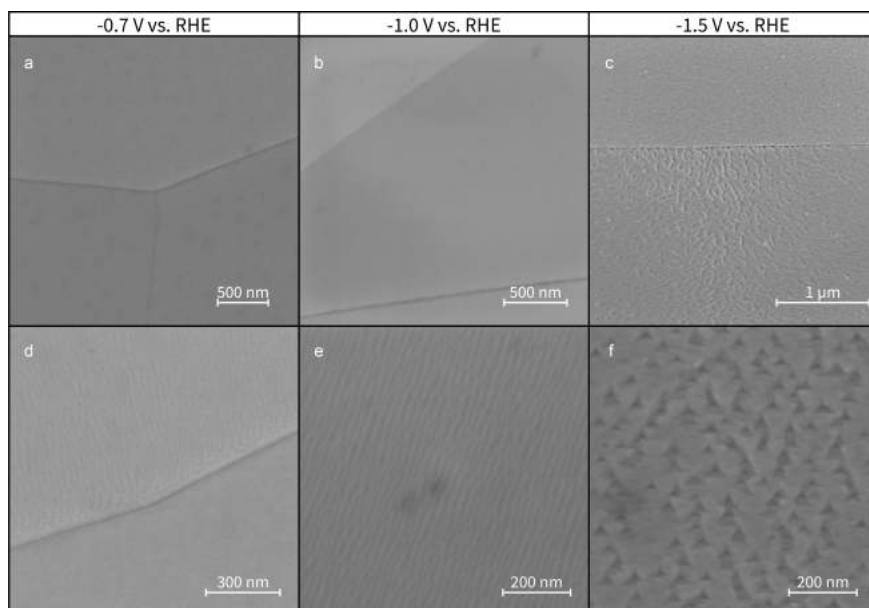
**Fig. A.16 |** Scanning electron micrographs of Pt electrodes corroded at 1 *M* LiOH at −0.7 *V vs.* RHE **(a, d)**, −1.0 *V vs.* RHE **(b, e)** and −1.5 *V vs.* RHE **(c, f)**.
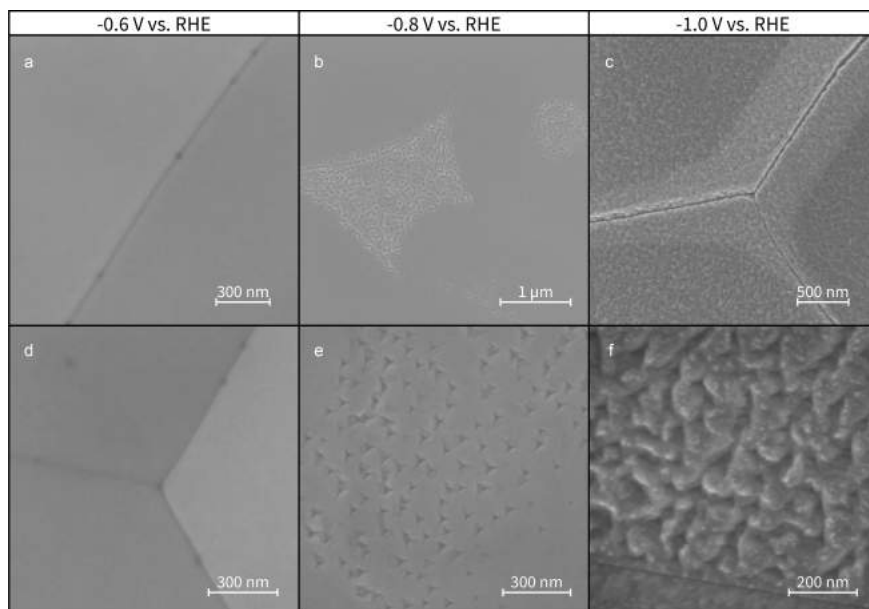


**Fig. A.17 |** Scanning electron micrographs of Pt electrodes corroded at 1 *M* NaOH at −0.6 *V vs.* RHE **(a, d)**, −0.8 *V vs.* RHE **(b, e)** and −1.0 *V vs.* RHE **(c, f)**.
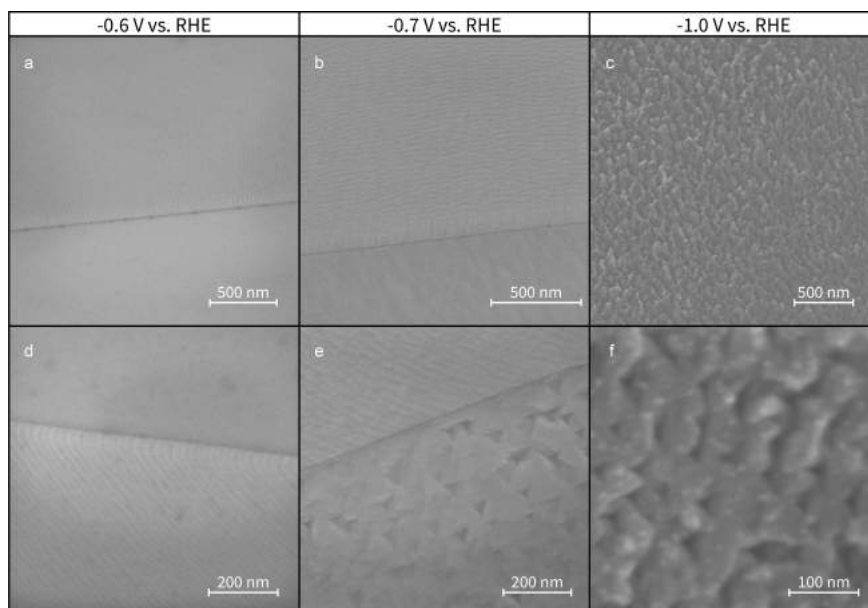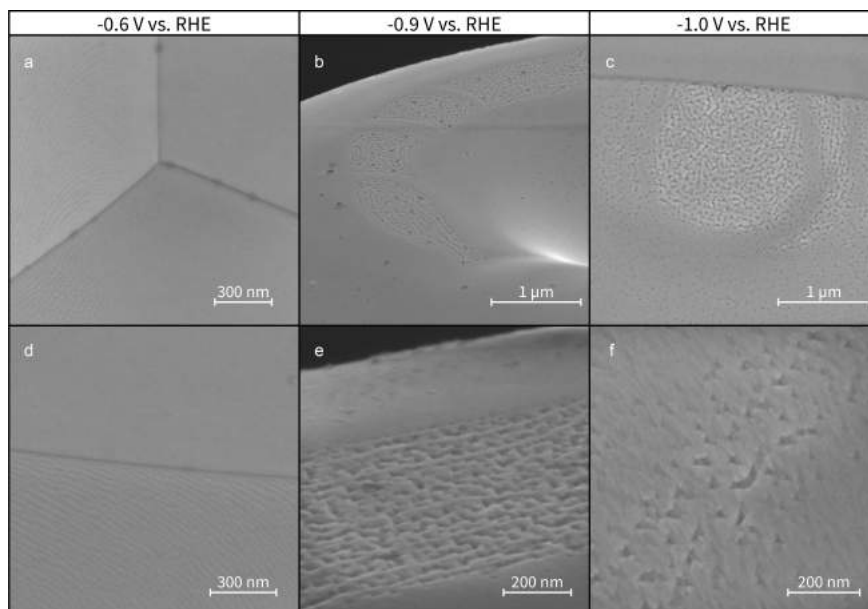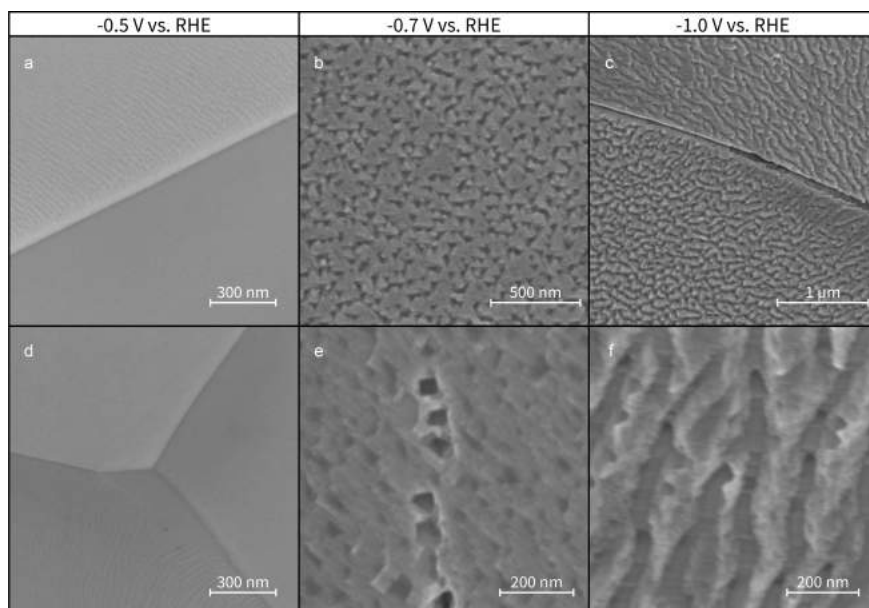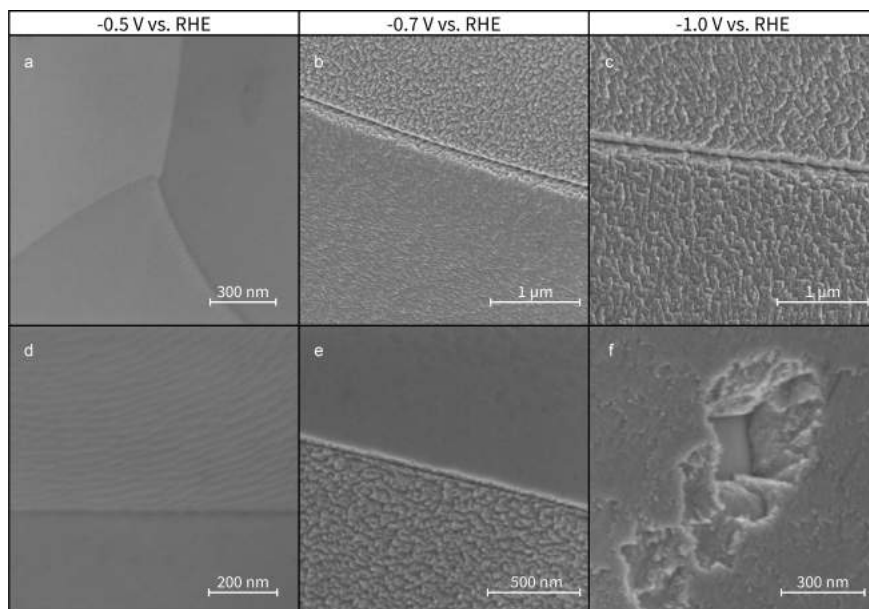
**Fig. A.18 |** Scanning electron micrographs of Pt electrodes corroded at 1 *M* KOH at −0.6 *V vs.* RHE **(a, d)**, −0.7 *V vs.* RHE **(b, e)** and −1.0 *V vs.* RHE **(c, f)**.
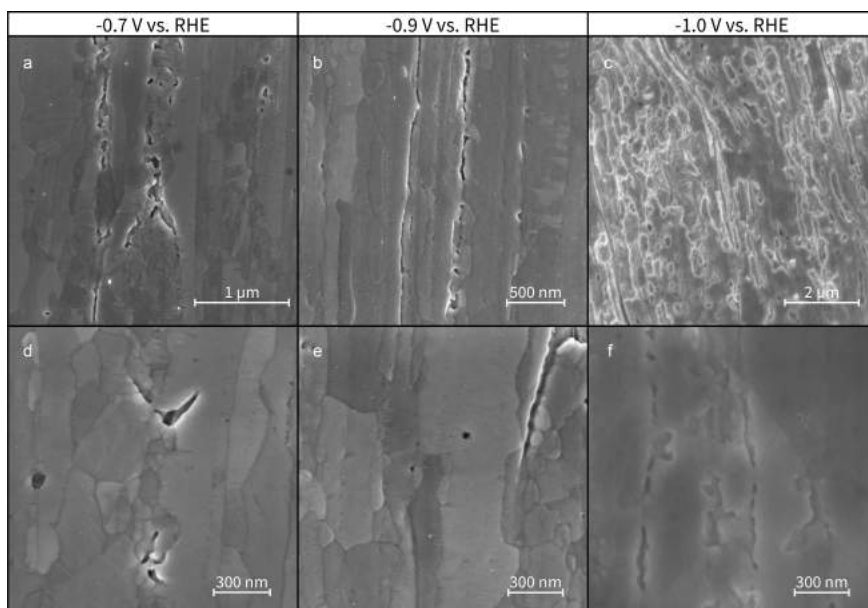


**Fig. A.19 |** Scanning electron micrographs of Pt electrodes corroded at 5 *M* LiOH at −0.6 *V vs.* RHE **(a, d)**, −0.9 *V vs.* RHE **(b, e)** and −1.0 *V vs.* RHE **(c, f)**.

**Fig. A.20 |** Scanning electron micrographs of Pt electrodes corroded at 5 *M* NaOH at −0.5 *V* vs. RHE **(a, d)**, −0.7 *V* vs. RHE **(b, e)** and −1.0 *V* vs. RHE **(c, f)**.
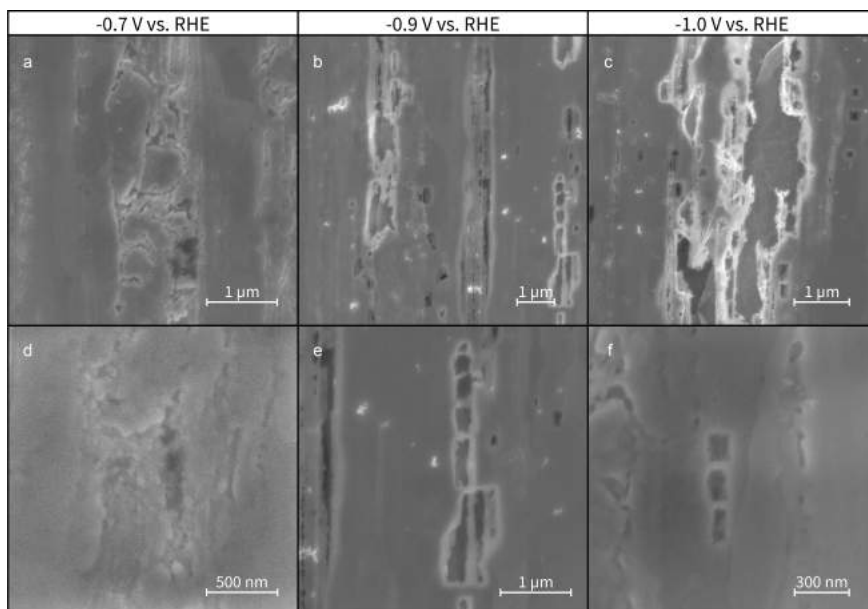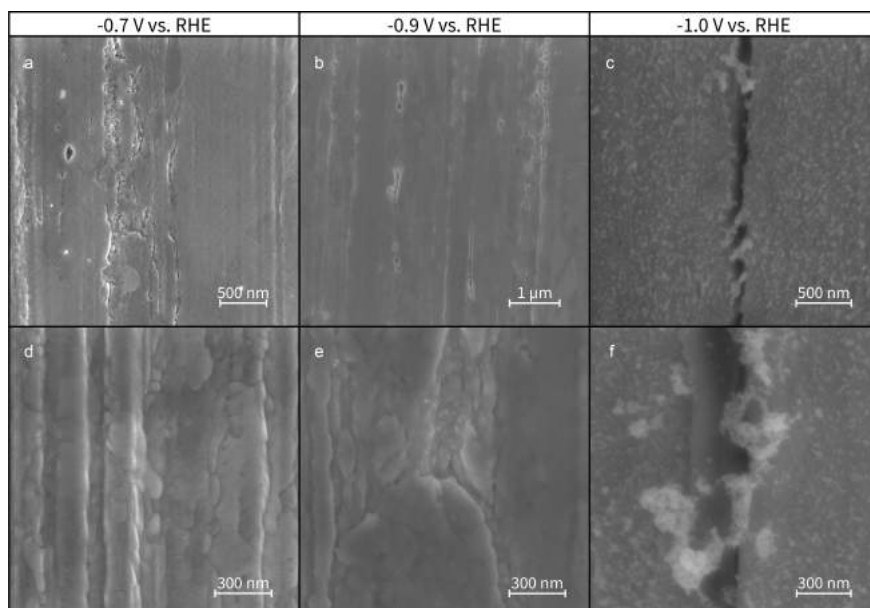


**Fig. A.21 |** Scanning electron micrographs of Pt electrodes corroded at 5 *M* KOH at −0.5 *V* vs. RHE **(a, d)**, −0.7 *V* vs. RHE **(b, e)** and −1.0 *V* vs. RHE **(c, f)**.

### A.3.2 Rhodium micrographs

The current three paragraphs will briefly elaborate on the discussion of the Rh scanning electron micrographs in Chapter 4. As mentioned in this chapter, Rh appears mainly uncorroded after corrosion in $5\ M$ LiOH. One exception to this statement is a single electrode that was treated at $-1.0\ V$ *vs.* RHE. This electrode, which was one of three electrodes that was corroded at this potential and subsequently imaged, contained etching features close to where the electrode was cut from the spool (Fig. A.22 **c**). These etching features resemble those found after treatment in $10\ M$ NaOH and therefore likely correspond to the formation of (100) sites.

More severe corrosion is found for Rh, corroded in $5\ M$ NaOH. After corrosion at $-0.8\ V$ *vs.* RHE, small particles can mainly be found in areas close to where the wire was cut. In contrast, significantly more particles and even etch pits are widespread at $-0.9$ and $-1.0\ V$ *vs.* RHE. The etch pits are several hundreds of nanometers wide and can be up to several micrometers long. They are therefore the largest Rh etch pits found in this study.

Smaller features are found after corrosion in $5\ M$ KOH, in which many small particles are created. These particles are occasionally oriented around a small central etch pit (Fig. 4.6 **c**); such pits are either the source of the particles or instead caused most particles to be displaced around it to form a halo-like arrangement. In any case, a high coverage of particles was observed for all three electrodes imaged after polarization at $-1.0\ V$ *vs.* RHE in $5\ M$ KOH.

**Fig. A.22 |** Scanning electron micrographs of Rh electrodes corroded at $5\ M$ LiOH at $-0.7\ V$ *vs.* RHE **(a, d)**, $-0.9\ V$ *vs.* RHE **(b, e)** and $-1.0\ V$ *vs.* RHE **(c, f)**.



**Fig. A.23 |** Scanning electron micrographs of Rh electrodes corroded at $5\ M$ NaOH at $-0.7\ V$ *vs.* RHE **(a, d)**, $-0.9\ V$ *vs.* RHE **(b, e)** and $-1.0\ V$ *vs.* RHE **(c, f)**.

**Fig. A.24 |** Scanning electron micrographs of Rh electrodes corroded at $5\ M$ KOH at $-0.7\ V$ *vs.* RHE **(a, d)**, $-0.9\ V$ *vs.* RHE **(b, e)** and $-1.0\ V$ *vs.* RHE **(c, f)**.

### A.3.3  Gold micrographs

This paragraph briefly describes the (100)-oriented etch pits on gold after corrosion in $5\ M$ LiOH. The rectangular pits in Fig. 4.8 **d** with 90-degree outlines and pit walls that descend straight into the surface are similar to those observed for platinum and can be taken as signs of (100)-type pits in a (100) surface (Chapter 2). It should be mentioned that these rectangular (100)-type pits and their triangular counterparts in Fig. A.25 **c** were observed on one electrode in an exploratory study for the current work and on only one of the three electrodes that were imaged after corrosion at $-3.0\ V$ *vs.* RHE. The other two electrodes contained more disordered pits, which might be due to these electrode tips having different amounts of stress due to the slightly different cut of the wires. However, all three electrodes exhibited very similar voltammetric profiles. The (100)-type pits therefore seem to be appropriate illustrative examples of the electrochemically detected formation of (100) sites.
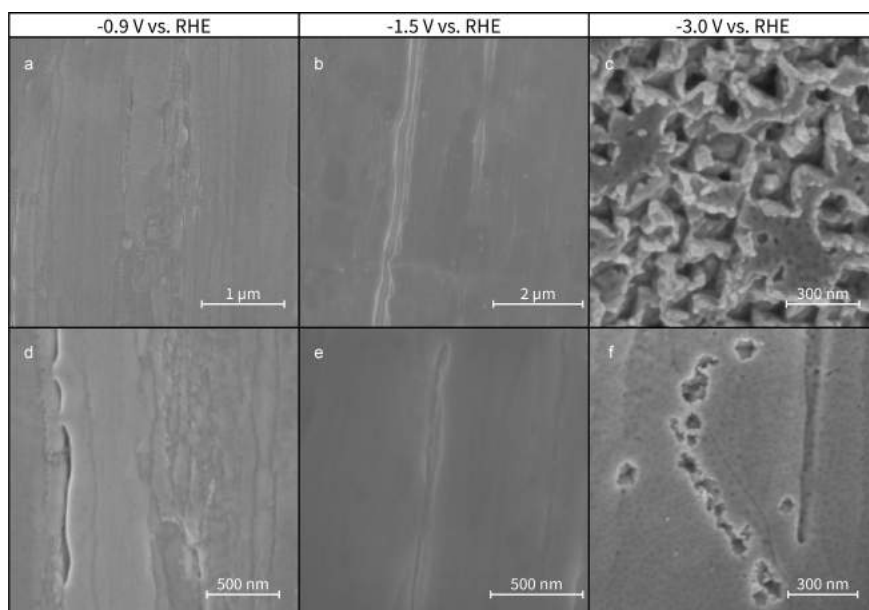


**Fig. A.25 |** Scanning electron micrographs of Au electrodes corroded at $5\ M$ LiOH at $-0.9\ V$ *vs.* RHE **(a, d)**, $-1.5\ V$ *vs.* RHE **(b, e)** and $-3.0\ V$ *vs.* RHE **(c, f)**.
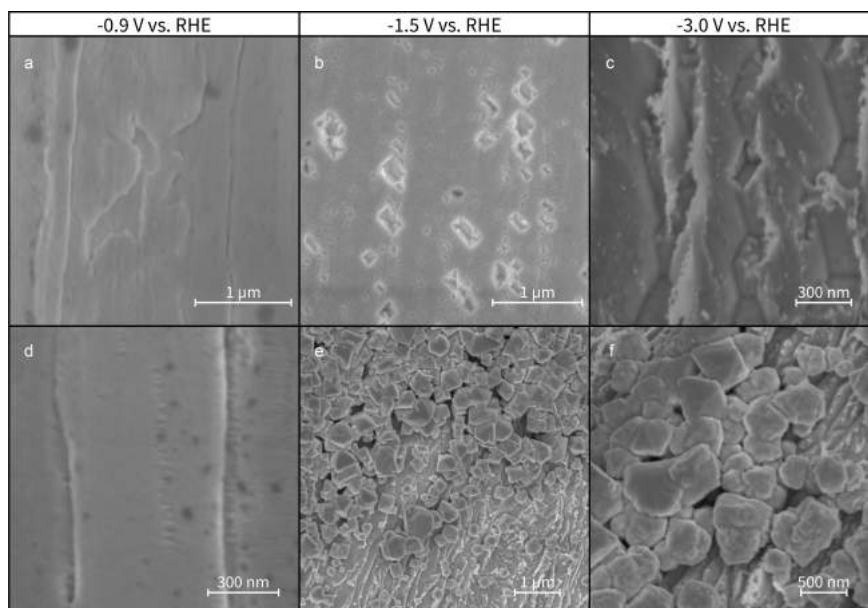
**Fig. A.26 |** Scanning electron micrographs of Pt electrodes corroded at $5\ M$ NaOH at $-0.9\ V$ vs. RHE **(a, d)**, $-1.5\ V$ vs. RHE **(b, e)** and $-3.0\ V$ vs. RHE **(c, f)**.
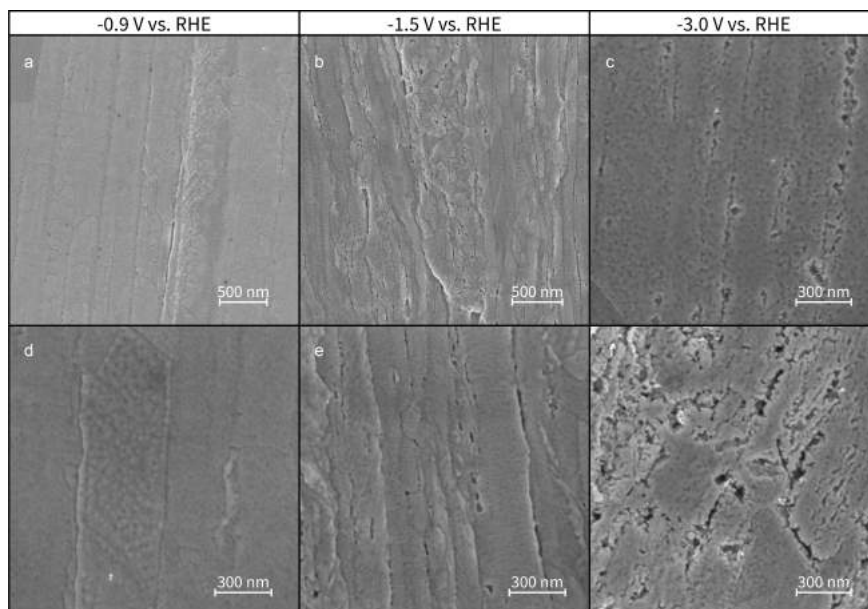


**Fig. A.27 |** Scanning electron micrographs of Pt electrodes corroded at $5\ M$ KOH at $-0.9\ V$ vs. RHE **(a, d)**, $-1.5\ V$ vs. RHE **(b, e)** and $-3.0\ V$ vs. RHE **(c, f)**.

## A.4  The role of cations at different potentials

The presented data in Chapter 4 and in Fig. A.4–A.27 indicate that cations only weakly influence the final surface structure at mild corrosion potentials. In contrast, the influence of cations is much stronger at more negative corrosion potentials. This might be explained by the cation coverage as a function of potential: though Fig. 4.9 indicates cation adsorption during cathodic corrosion, one can reasonably expect the cation coverage to increase as the potential decreases. At these higher coverages, repulsion between cations can amplify differences between the various cations, compared to less negative potentials. At more negative potentials and higher cation coverages, the cations could therefore modulate the facet preference induced by hydrogen, causing more extensive corrosion (visible in Fig. A.16–A.27) and diverging behavior between electrolytes. This hypothesis would explain the experimental data with theoretically established cation adsorption behavior, and could therefore serve as an appropriate mechanistic hypothesis for further studies of electrolyte effects in cathodic corrosion.

## A.5  Model etch pits

This section features three model etch pits, to illustrate how specific features in the scanning electron micrographs correspond to facet distributions seen in cyclic voltammetry. These model pits are displayed in Fig. A.28. The pits are situated in either (111) or (100) surfaces and exclusively have (111) and (100) facets on their pit walls. Pit **a** and **b** match those in Chapter 2, with the exception that the pits shown in the current section do not contain a step edge. For a more elaborate explanation of these etch pits, the reader is referred to Chapter 2 & 3.
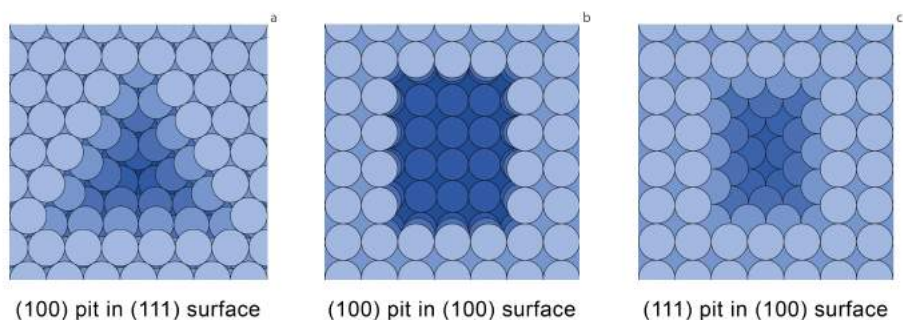
Fig. A.28 | Three model etch pits: a pit with (100)-oriented walls in a (111) surface **(a)**, a pit with (100)-oriented walls in a (100) surface **(b)** and a pit with (111)-oriented walls in a (100) surface **(c)**.

## A.6   Gold onset potential determination

As for gold corrosion in $10\,M$ NaOH (Chapter 3), the first sign of cathodic corrosion is the appearance of a peak corresponding to (111) sites around $1.58\,V$ *vs.* RHE. The formation of these (111) sites is therefore used to determine the corrosion onset potential in $5\,M$ LiOH, $5\,M$ NaOH and $5\,M$ KOH. This is done by comparing cyclic voltammograms of Au electrodes, polarized around the onset potential, presented in Panel **a, c** and **e** of Fig. A.29. In these CVs, the currents are converted to current densities by calculating the electrode surface area through the oxide reduction peak. To do so, the charge of the peak was calculated by integrating it. It was then used to calculate the surface area, by using a specific charge of $390\,\mu A \cdot cm^{-2}$.[2] In order to emphasize the formation of the (111) peak, the derivatives of the current density traces are also presented in Panel **b, d** & **f**.
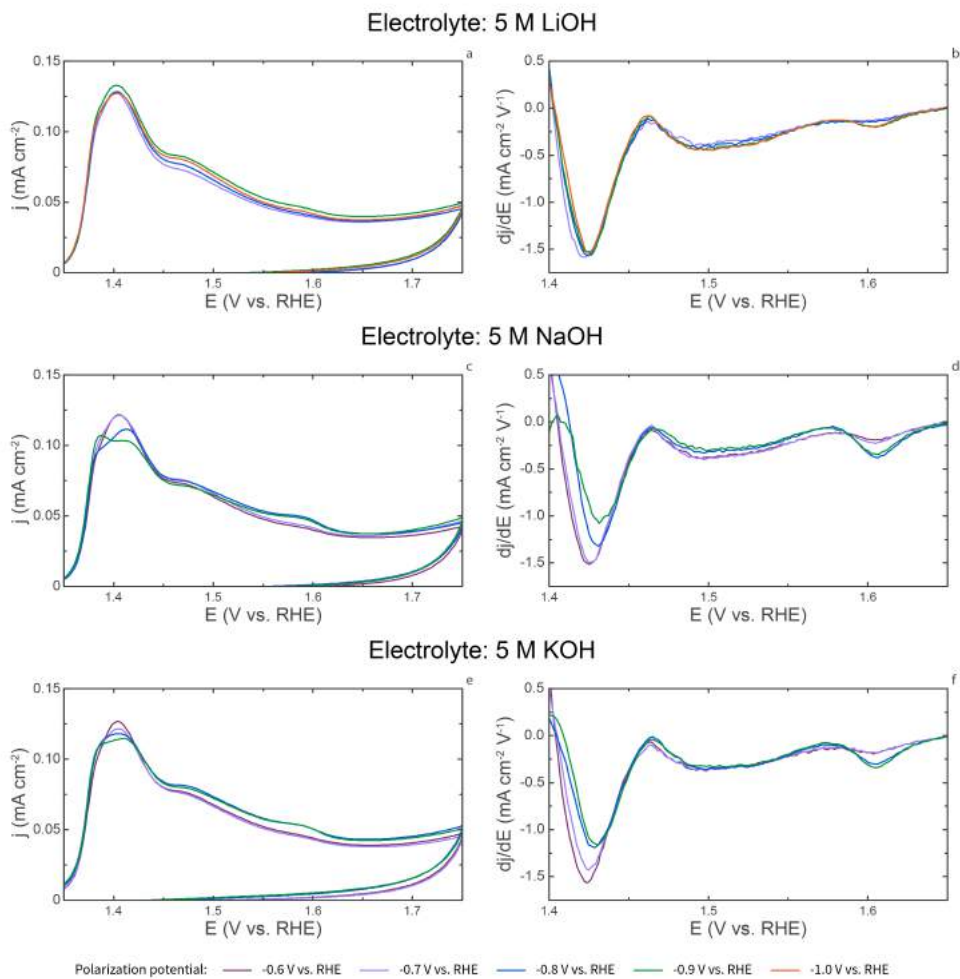
**Fig. A.29 |** Normalized cyclic voltammograms **(a, c, e)** and derivatives of the voltammograms **(b, d, f)** of Au electrodes polarized around the corrosion onset potential in 5 M LiOH **(a, b)**, 5 M NaOH **(c, d)** and 5 M KOH **(e, f)**. CV electrolyte: 0.1 $M$ H$_2$SO$_4$. Scan rate: 50 $mV \cdot s^{-1}$.

## A.7    Computational cation adsorption in vacuum

In addition to calculating cation adsorption while explicitly considering solvation, we also performed calculations for cation adsorption in vacuum. These calculations can directly be compared to those in Chapter 3, which also includes details on the employed computational procedure. The calculated adsorption energies are displayed in Fig. A.30 and indicate that the adsorption of Li is stronger on all of the surfaces than Na or K. This matches the trend we find in Chapter 4 at high cation coverage when including near-surface solvation. As such, the trend in Fig. A.30 is exactly opposite from that found for lower coverage. This indicates that, at lower coverage, solvation may play a significant role in stabilizing the adsorption of the larger cations. The stronger stabilization of these larger cations is supported by the fact that the larger cations retain more of their charge upon adsorption, which would induce more repulsion between neighboring cations and thus a larger interaction with the solvent.

An additional difference between the results in Fig. A.30 and those in Chapter 4 is the calculated facet preference. Though both results generally agree in adsorption being strongest on (100) facets and steps for platinum, the results in Fig. A.30 also suggest this to be the case for the adsorption of Li and Na on Rh, as well as for Li adsorption on Au. In fact, closer examination of the numbers in Fig. A.30 indicates that the preference for adsorption on (100) steps forms a monotonic trend as a function of cation size (Fig. A.31), with Li exhibiting the strongest preference for (211) over (553), followed by Na and K. This trend is not present on the Rh and Au surfaces in the presence of near-surface solvation in Chapter 4, which can be explained in two ways:

– Solvation promotes adsorption in such a way that the binding strength is less dependent on surface structure on Rh and Au than it is on Pt.

– Different solvation structures must be investigated on the Rh and Au surfaces in order to capture solvation more accurately.

For these two reasons, future work should examine the sensitivity of the calculated trends in adsorption to the degree of explicit solvation. In addition, this work should probe the role of the particular water structure examined on each surface.
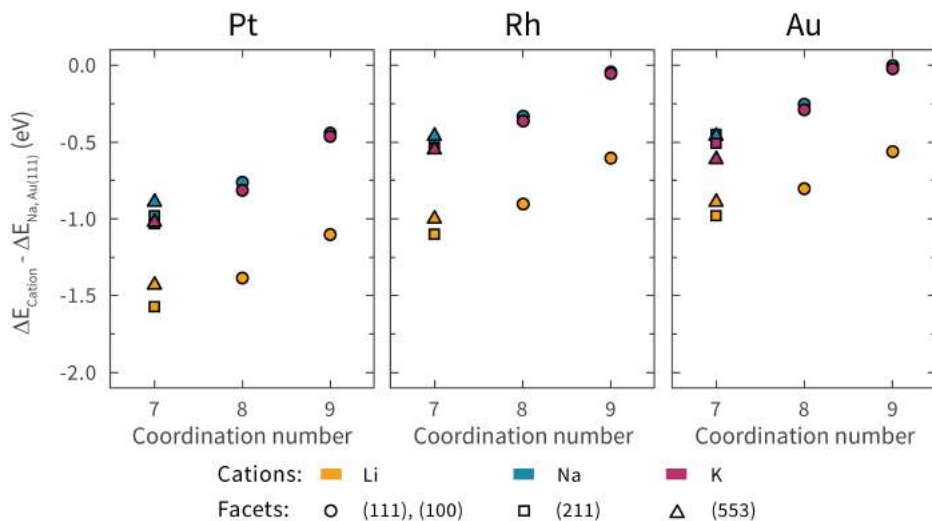
**Fig. A.30 |** Adsorption energies of Li, Na and K on various facets of Pt, Rh and Au, displayed as a function of the coordination number of the adsorption sites. Out of the flat surfaces, (111) has a coordination number of 9 and (100) has a coordination number of 8. Energies are normalized by subtracting the calculated adsorption energy of Na on Au(111), which is $-2\ eV$.
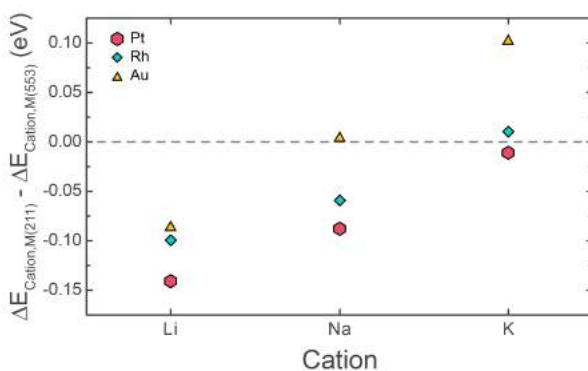


**Fig. A.31 |** Energy difference between adsorption on (211) and (553) facets. Lower values indicate a stronger preference for adsorption on the (211) facet. Positive values indicate a preference for adsorption to the (553) facet.

## A.8 Coverage effects in cation adsorption

As mentioned in Chapter 4, opposite trends are found for cation adsorption on Pt steps and terraces. This is caused by the cation coverage being different for steps and terraces in our calculations. While a high cation coverage is adsorbed along step edges (1/2 mono-layer (ML) per step atom), the stepped surfaces contain relatively wide terraces that lower the coverage per unit area compared to the low-index surfaces (1/3 monolayer on Pt(111) and 1/4 monolayer on Pt(100)). We found this coverage difference to be highly relevant to the trend in adsorption strength in our previous work:[3] the adsorption strength increased alongside cation size for low coverages, but showed the exact opposite behavior at high coverages. This is due to repulsive interactions between the cations being proportional to cation size: bigger cations interact more at high coverage due to their size, and also appear to retain more of their charge upon adsorbing. Large cations therefore experience both stronger steric and coulombic repulsion at high coverages, such that the adsorption trend reverses at coverages above 1/3 to 1/2 ML. The strong coverage dependence may also explain why adsorption appears weaker on some of the stepped surfaces than on the low-index surfaces, while we found the opposite to be true for 1/3 ML coverages on Pt step edges in our previous work.[4]

## A.9    Potentials of zero surface energy

The curves in Fig. 4.10 in Chapter 4 cross zero at various potentials. These potentials are given in Table A.1. As can be seen in the table and Fig. 4.10, the potentials match relatively well with the experimental onset potentials and reproduce the similarity in onset potential between Pt and Rh, as well as Au having a significantly more negative onset potential.

**Table A.1 |** Fit values for spectra at various potentials.

| Metal | Facet | Hydrogen coverage | Potential of zero surface energy ($V$ *vs.* RHE) |
|-------|-------|-------------------|------------------------------------------------|
| Pt | (111) | 1 | $-0.46$ |
| Pt | (100) | 1 | $-0.45$ |
| Pt | (100) | 1.25 | $-0.37$ |
| Rh | (111) | 1 | $-0.53$ |
| Rh | (100) | 1 | $-0.64$ |
| Rh | (100) | 1.25 | $-0.47$ |
| Au | (111) | 1 | $-0.72$ |
| Au | (100) | 1 | $-0.66$ |

## A.10    Corrosion time effect on platinum

Fig. A.32 illustrates the effect of corrosion time on the final state of a platinum electrode. This effect is explored for an applied potential of $-0.5$ and $-1.0$ $V$ *vs.* RHE and corrosion times between 1 and 10 minutes. For -0.5 $V$ *vs.* RHE, a minor decrease in the (110) peak is seen when increasing the corrosion time from 1 to 5 minutes, while the surface remains similar when further extending the corrosion time to 10 minutes. For $-1.0$ $V$ *vs.* RHE, no differences are seen when increasing the corrosion time from 1 to 10 minutes. SEM evaluation of the electrodes (not shown here) corroborates these findings.
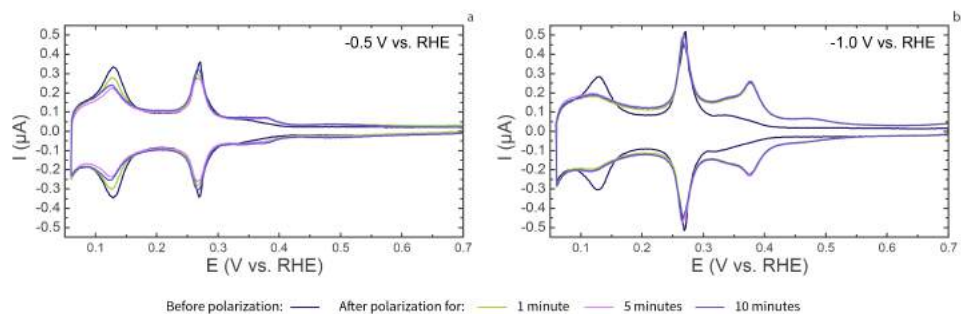
**Fig. A.32 |** CVs of platinum electrodes before (dark blue trace) and after cathodic polarization in 5 *M* NaOH at −0.5 *V vs.* RHE **(a)** and −1.0 *V vs.* RHE **(b)** for 1, 5 and 10 minutes. CV electrolyte: 0.5 *M* H₂SO₄. Scan rate: 50 $mV \cdot s^{-1}$.

# References

1.   Jeyabharathi, C., Ahrens, P., Hasse, U. & Scholz, F. Identification of low-index crystal planes of polycrystalline gold on the basis of electrochemical oxide layer formation. *Journal of Solid State Electrochemistry* **20,** 3025–3031 (2016).

2.   Trasatti, S. & Petrii, O. Real surface area measurements in electrochemistry. *Pure and applied chemistry* **63,** 711–734 (1991).

3.   McCrum, I. T. & Janik, M. J. Unpublished results.

4.   McCrum, I. T. & Janik, M. J. First Principles Simulations of Cyclic Voltammograms on Stepped Pt(553) and Pt(533) Electrode Surfaces. *ChemElectroChem* **3,** 1609–1617 (2016).

# B    Supplementary Information for Chapter 5

## B.1    *Operando* electrochemical flow cell

Fig. B.1 & B.2 display schematic drawings of the flow cell used in this study. The cell was mounted onto its aluminum holder (shown in Fig. 5.1) with two holes that fit around two pins on the holder. The bottom of the cell was covered with a $0.1$ $mm$-thick fluorinated ethylene propylene (FEP) film and thin Kapton foil, which were held in place by an aluminum cover plate. With the FEP film pressed against the polyether ether ketone (PEEK) body of the cell, a thin channel was formed. This channel facilitated the flow of the electrolyte, which was fed in and drained from holes in the side of the cell.

Within the flow cell channel, a Pt strip was used as the counter electrode and placed alongside the working electrode. This strip was made from a $\varnothing = 0.8$ $mm$ Pt wire (Mateck, 99.9%), of which one end was bent and flattened in a rolling press. The bent electrode was sealed into the cell with a custom-made Teflon ferrule and a hollow PEEK connector. The flow channel also contained the HydroFlex working electrode, which was sealed with a Viton O-ring.

Finally, the flow channel contained the $\varnothing = 3$ $mm$ gold disk electrode. This disk was held in place by a Teflon sheath, as can be seen in the Section view in Fig. B.2. Electrical contact with the reference electrode was established by a spring contact, which screwed into the back of the sheath.

## B.2    Additional X-ray absorption spectra

Fig. B.3 presents X-ray absorption spectra in a wider energy range than those in Fig. 5.2. Fig. B.3 shows good overlap between the spectra at higher energies. This indicates consistent normalization for all presented spectra. Additionally, this overlap indicates the overall structure of the nanoparticles to be maintained during the experiments.

Fig. B.4 compares the XANES spectra of Pt nanoparticles, measured at $0$ and $0.4$ $V$ *vs.* RHE. Though the spectra overlap reasonably well, there is a small positive edge shift upon decreasing the electrode potential. This shift is accompanied by a minor whiteline intensity decrease and slight absorption increase at higher absorption energies. These changes were previously assigned to the adsorption of hydrogen on platinum.[1] This is in general agreement with the difference spectrum for $0$ $V$ *vs.* RHE in Fig. 5.3 **a**.
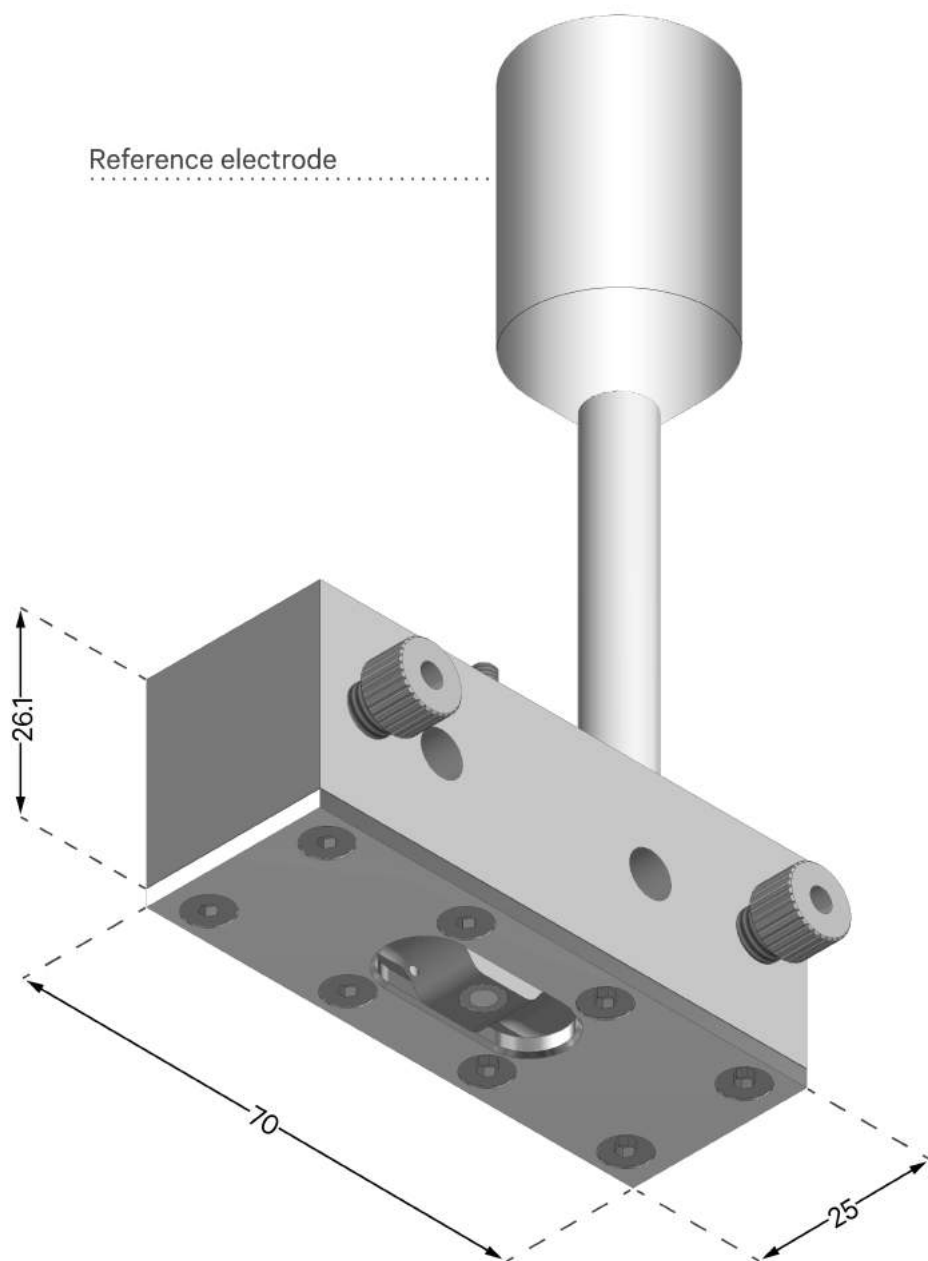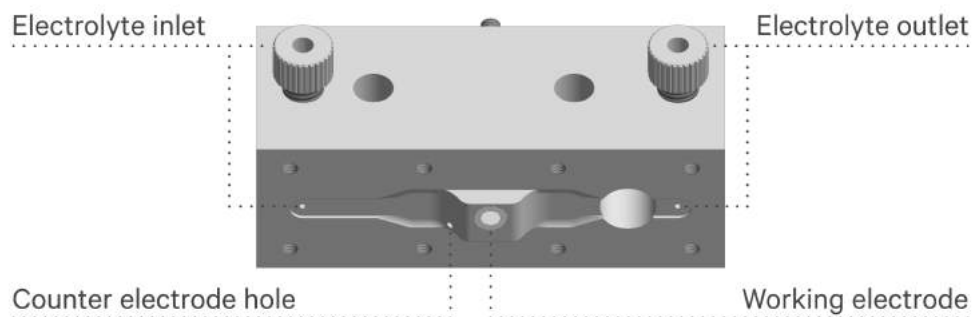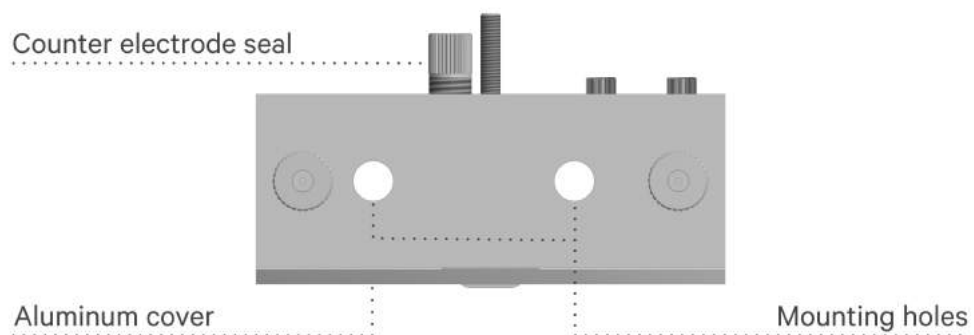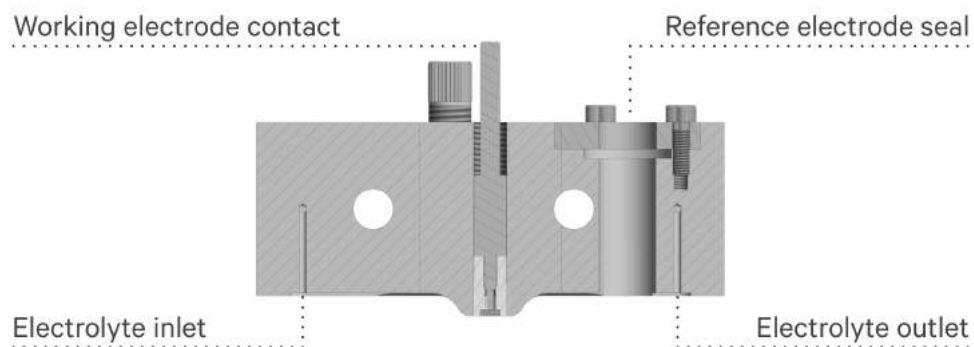
**Fig. B.1 |** Schematic overview of the employed flow cell. Sizes are in millimeters.

Electrolyte inlet

Electrolyte outlet

Counter electrode hole

Working electrode

**PERSPECTIVE**

Counter electrode seal

Aluminum cover

Mounting holes

**SIDE**

Working electrode contact

Reference electrode seal

Electrolyte inlet

Electrolyte outlet

**SIDE SECTION**

**Fig. B.2 |** Various schematic views of the employed flow cell. Aluminum cover plate is not shown in Perspective and Side Section.
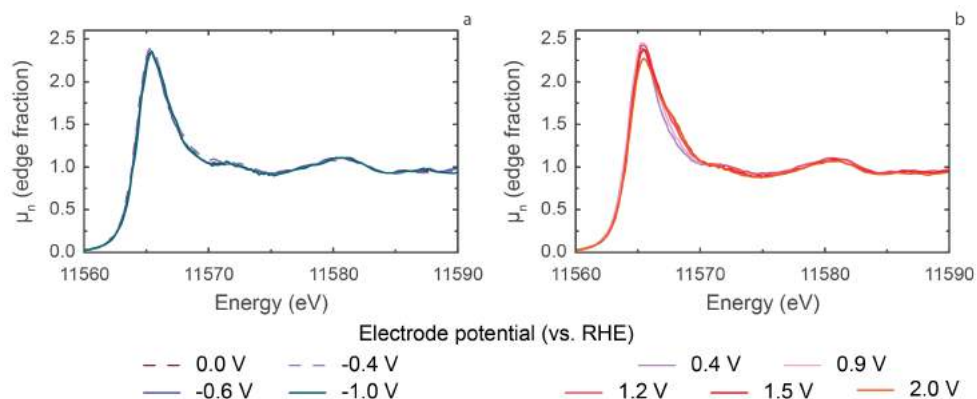
**Fig. B.3 |** Expanded view of the X-ray absorption spectra shown in Chapter 5. Spectra are given for cathodic potentials **(a)** and anodic potentials **(b)**
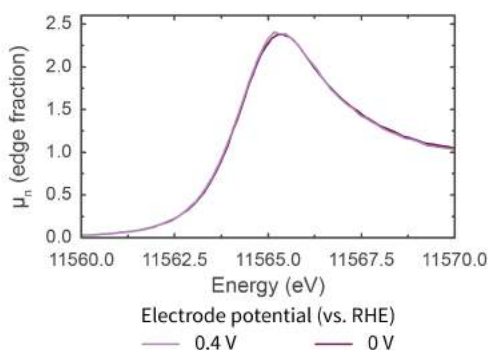


**Fig. B.4 |** Comparison of X-ray absorption spectra of Pt at 0 and 0.4 $V$ vs. RHE.

## B.3  Fit results

The peaks in Fig. 5.4 were fitted to the experimental spectra between $11560$ $eV$ and $11572$ $eV$, using the peak fitting function in ATHENA.[2] To fit the spectra, three functional shapes were used.[1] First of all, an arctangent was used to account for the background. This arctangent was centered at $11564$ $eV$ and had a fixed width of $0.5$ $eV$. Secondly, a pseudo-Voigt peak was used to fit the whiteline. This peak will be referred to as the "low-energy peak". It was centered at $11565.4$ $eV$ and the Gaussian/Lorentzian mixing ratio was fixed to 0.5. The peak width and height were allowed to vary. Thirdly, an additional pseudo-Voigt peak was used to fit the whiteline shoulder. This peak will be referred to

as the "high-energy peak". It was centered at $11567.55\ eV$ and the Gaussian/Lorentzian mixing ratio was fixed to 0.5. The peak width and height were allowed to vary. In ATHENA, the pseudo-Voigt peaks are normalized, such that their height equals their area. Representative fits are given in Fig. B.5, whereas the fit results for all data points are shown in Table B.1.

**Table B.1 |** Fit values for spectra at various potentials. Potentials are given *vs.* RHE

| Applied potential | Background | Low-energy peak | | High-energy peak | | R-factor |
|---|---|---|---|---|---|---|
| | $A_{bg}$ | $A_2$ | $\Delta E_1$ | $A_2$ | $\Delta E_2$ | |
| 2.0 V | 0.97 ± 0.01 | 3.81 ± 0.05 | 2.36 ± 0.03 | 1.83 ± 0.09 | 2.8 ± 0.1 | 0.000646 |
| 1.8 V | 0.97 ± 0.01 | 3.83 ± 0.05 | 2.32 ± 0.03 | 1.9 ± 0.1 | 2.8 ± 0.1 | 0.000668 |
| 1.5 V | 0.98 ± 0.01 | 4.09 ± 0.05 | 2.35 ± 0.03 | 1.8 ± 0.1 | 2.8 ± 0.1 | 0.000611 |
| 1.2 V | 1.00 ± 0.01 | 4.28 ± 0.05 | 2.34 ± 0.03 | 1.42 ± 0.08 | 2.6 ± 0.1 | 0.000593 |
| 0.9 V | 1.018 ± 0.009 | 4.87 ± 0.05 | 2.53 ± 0.03 | 0.67 ± 0.07 | 2.1 ± 0.2 | 0.000647 |
| 0.4 V | 1.023 ± 0.009 | 4.93 ± 0.06 | 2.63 ± 0.04 | 0.27 ± 0.06 | 1.4 ± 0.3 | 0.000953 |
| 0 V | 1.042 ± 0.009 | 4.71 ± 0.06 | 2.58 ± 0.03 | 0.33 ± 0.05 | 1.6 ± 0.2 | 0.000816 |
| -0.2 V | 1.044 ± 0.009 | 4.85 ± 0.06 | 2.58 ± 0.04 | 0.43 ± 0.06 | 1.8 ± 0.2 | 0.000860 |
| -0.4 V | 1.07 ± 0.01 | 4.52 ± 0.06 | 2.51 ± 0.03 | 0.53 ± 0.07 | 2.0 ± 0.2 | 0.000723 |
| -0.6 V | 1.023 ± 0.008 | 4.49 ± 0.05 | 2.51 ± 0.03 | 0.50 ± 0.06 | 2.0 ± 0.2 | 0.000669 |
| -0.7 V | 1.007 ± 0.009 | 4.34 ± 0.05 | 2.49 ± 0.03 | 0.50 ± 0.06 | 1.9 ± 0.2 | 0.000767 |
| -0.8 V | 1.032 ± 0.009 | 4.28 ± 0.05 | 2.38 ± 0.03 | 0.77 ± 0.07 | 2.1 ± 0.2 | 0.000736 |
| -0.9 V | 1.050 0.009 | 4.10 ± 0.05 | 2.37 ± 0.03 | 0.65 ± 0.08 | 2.4 ± 0.3 | 0.000686 |
| -1.0 V | 1.01 ± 0.01 | 4.21 ± 0.06 | 2.43 ± 0.04 | 0.81 ± 0.09 | 2.4 ± 0.2 | 0.000934 |

Table B.1 gives the fit results that were used to make Fig. 5.4. The table contains the following variables: $A_{bg}$ is the step height of the background arctangent; $A_1$ is the height of the low-energy peak; $\Delta E_1$ is the half width at half maximum (HWHM) of the low-energy peak; $A_2$ is the height of the high-energy peak; and $\Delta E_2$ is the HWHM of the high-energy peak. This notation is chosen to be consistent with previous work from literature.[1] Note, however, that this previous work used unnormalized pseudo-Voigt functions.

All fit results in Table B.1 are given with an error. This error equals the standard deviation, as given in the fit results from ATHENA. The only value without an associated error is the R-factor. This factor quantifies the mismatch between the fit and the data and is also taken from the ATHENA fit results. The value for the R-factor is given by equation B.1.[3]

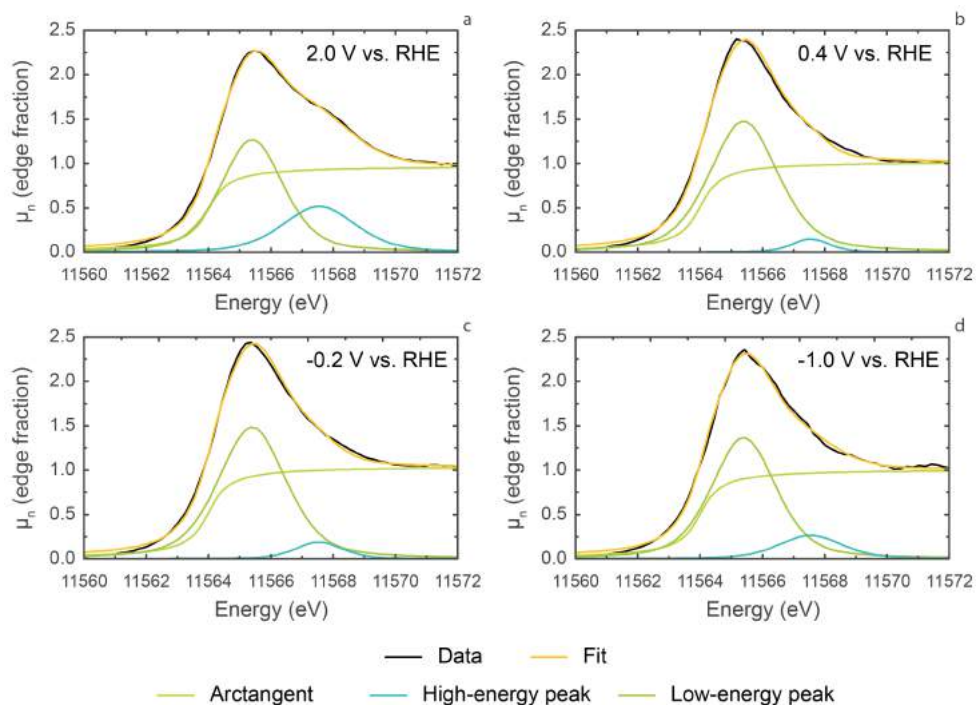$$R = \frac{\sum_{i=1}^{N}(data_i - fit_i)^2}{\sum_{i=1}^{N}(data_i)^2} \qquad \text{(B.1)}$$

**Fig. B.5 |** Representative fits of X-ray absorption spectra of electrodes polarized at 2.0 *V* vs. RHE **(a)**, 0.4 *V* vs. RHE **(b)**, −0.2 *V* vs. RHE **c** and −1.0 *V* vs. RHE.

Here, an R-factor closer to zero equals a better fit.

Representative fits are displayed in Fig. B.5 for four representative potentials. This figure confirms the quality of the fit that is indicated by the low R-factor values in Table B.1.

## B.4    Expanded modeled spectra

Fig. B.6 shows the spectra modeled with OCEAN, over a wider energy range than Fig. 5.5. From Fig. B.6, it appears that the modeled spectra overestimate some of the spectral features. This is most readily seen by comparing the white line intensity around 11565 *eV* with the experimental whiteline intensity; the modeled intensity is approximately 1.5 times higher than in experiments. Similar, though less pronounced, deviations are found for the smaller peaks. However, the location of these peaks and shoulders agrees rather well with those in experimental spectra.
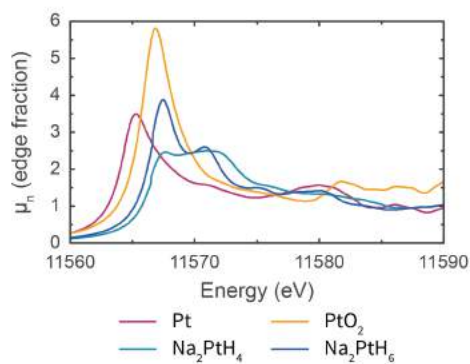
**Fig. B.6 |** Expanded view of the modeled X-ray absorption spectra shown in Chapter 5.

# References

1.  Merte, L. R. *et al.* Electrochemical Oxidation of Size-Selected Pt Nanoparticles Studied Using in Situ High-Energy-Resolution X-ray Absorption Spectroscopy. *ACS Catalysis* **2,** 2371–2376 (2012).
2.  Ravel, B. & Newville, M. ATHENA , ARTEMIS , HEPHAESTUS: data analysis for X-ray absorption spectroscopy using IFEFFIT. *Journal of Synchrotron Radiation* **12,** 537–541 (2005).
3.  Calvin, S. *XAFS for Everyone* 1st ed. **1,** 427 (CRC Press, Boca Raton, FL, 2013).

# C   Supplementary Information for Chapter 6

## C.1   Electrodes employed in this study

Fig. C.1 displays normalized blank cyclic voltammograms (CVs) of the electrodes used in the current study. The shape of these voltammograms is in good agreement with literature voltammograms of corresponding single- and polycrystalline Pt electrodes.[1,2] The voltammograms were normalized using the integrated anodic current densities, without correcting for the double layer.[1,2]

All ORR current densities in this article are reported by normalizing with respect to the *geometric* electrode surface area, as is appropriate when considering reactant mass transport through diffusion or convection.[3] The geometric surface areas of most of the employed electrodes differed by no more than 2% from the electrochemically calculated surface area. The only exception to this statement is Pt(111), for which the electrochemical surface area was 13% smaller than the geometric surface area. Similar deviations were obtained for a different Pt(111) crystal. For Pt(111), normalizing currents by the geometric surface area was therefore critical in calculating limiting current densities that match the Levich equation.
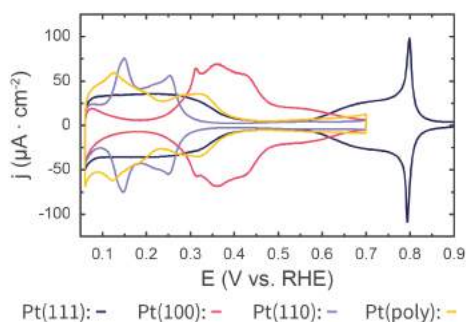


**Fig. C.1 |** Cyclic voltammograms of the employed electrodes: Pt(111), Pt(100), Pt(110) and Pt(poly). Voltammograms were recorded in $0.1\ M$ HClO$_4$, at a scan rate of $50\ mV \cdot s^{-1}$.

## C.2 Comparison of Pt(111) electrodes after cathodic corrosion

Fig. C.2 shows CVs of Pt(111) after cathodic corrosion at various potentials in 1 $M$ NaOH. As can be seen in the figure, there are no significant differences in the post-corrosion voltammograms, as function of the corrosion potential.
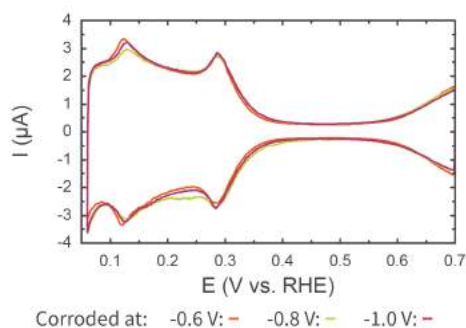


Corroded at:   -0.6 V: —   -0.8 V: —   -1.0 V: —

**Fig. C.2 |** Cyclic voltammograms of Pt(111) after cathodic corrosion at various potentials in 1 $M$ NaOH. Voltammograms were recorded in 0.1 $M$ HClO$_4$, at a scan rate of 50 $mV \cdot s^{-1}$.

## C.3 Validation of the HMRD setup

Fig. C.3 displays cyclic voltammograms for the ORR activity of Pt(111). The CVs contain no pronounced oscillations, which indicates proper concentric alignment of the single crystal. Furthermore, the voltammograms at 0, 200, 400 and 900 $rpm$ contain the characteristic 'butterfly' feature around 0.8 $V$ *vs.* RHE. The presence of the butterfly and the decrease of its intensity with increasing rotation rate is a strong sign of electrolyte cleanliness.[4,5]

Fig. C.4 shows Levich plots for each of the electrodes in this study. The theoretical Levich plots were calculated using the Levich equation:[6]

$$j_L = 0.62 \cdot n \cdot F \cdot D_{O_2}^{\frac{2}{3}} \cdot \omega^{\frac{1}{2}} \cdot v^{-\frac{1}{6}} \cdot C_{O_2}^* \tag{C.1}$$

Here, $n$ equals the amount of transferred electrons; $F$ equals Faraday's constant; $D_{O_2}$ equals the oxygen diffusion constant, $\omega$ equals the radial electrode rotation rate; $v$ equals the kinematic viscosity of the solution; and $C_{O_2}^*$ equals the oxygen concentration. For the studied system, the parameters take the following values: $n = 4$ for the conversion from
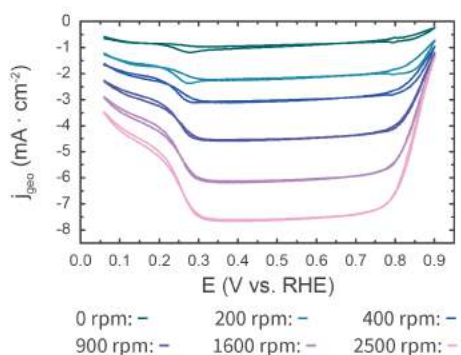
**Fig. C.3 |** Cyclic voltammograms for oxygen reduction on Pt(111), at various rotation rates. Voltammograms were recorded in oxygen-saturated 0.1 $M$ HClO$_4$, at a scan rate of 50 $mV \cdot s^{-1}$.

O$_2$ to H$_2$O; $D_{O_2} = 1.384\ mM$;[7] $v = 8.93 \cdot 10^{-3}\ cm^2 \cdot s^{-1}$;[8] and $C^*_{O_2} = 1.67 \cdot 10^{-5}\ cm^2 \cdot s^{-1}$.[7]
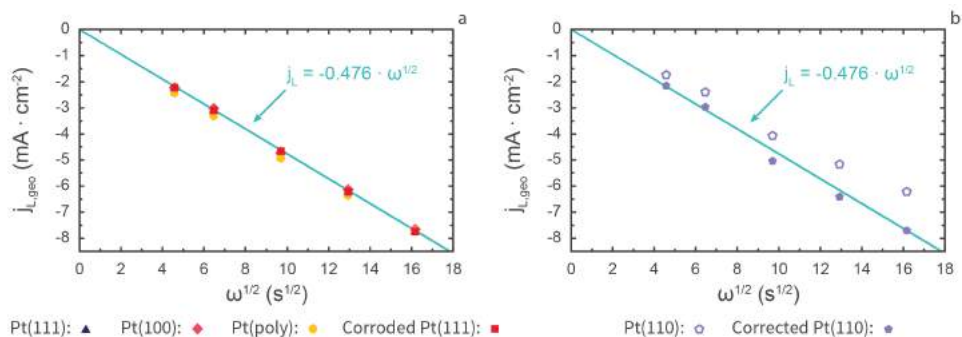


**Fig. C.4 |** Levich plots for the ORR on Pt(111), Pt(100), Pt(poly) and Pt(111) which was corroded at $-1.0\ V$ *vs.* RHE in 1 $M$ NaOH **(a)**. Corrected and uncorrected Levich plots for the ORR on Pt(110) **(b)**. Voltammograms for acquiring the plotted datapoints were recorded in 0.1 $M$ HClO$_4$, at a scan rate of 50 $mV \cdot s^{-1}$.

As can be seen in Fig. C.4 **a**, the Pt(111), Pt(100), Pt(poly) and corroded Pt(111) electrodes are described well by the theoretical Levich plot. However, Fig. C.4 **b** demonstrates that the theoretical behavior is matched less well by Pt(110), for which 20% *lower* Levich slope is obtained. This change in slope is not due to wetting of the side of the electrode, which should increase the magnitude of the slope.[9] The slope change is also not related to dynamic changing of the meniscus shape during rotation, which should cause

a vertical offset in the Levich plot.[9]

Instead, the slope change must be ascribed to a decrease in the apparent electrode area. This is demonstrated by 'correcting' the current densities by dividing them by the relative difference between the obtained current density and the theoretical current density at $2500\ rpm$. This corrected curve is represented by the filled pentagons in Fig. C.4 **b** and matches the theoretical Levich plot well. The deviations from ideal diffusion behavior are therefore compensated for when normalizing the data as done in Fig. 6.3.

## C.4  Kinetic ORR current densities

The ORR activity of the electrodes can also be assessed by calculating kinetic current densities at $0.9\ V$ vs. RHE. These kinetic current densities are calculated by rewriting the Levich equation to:[10]

$$\frac{1}{j} = \frac{1}{j_k} + B \cdot \omega^{-\frac{1}{2}} \tag{C.2}$$

Here, $j_k$ is the kinetic current density and $B$ depends on the various parameters in the Levich equation. $j_k$ is obtained from equation C.2 by plotting the inverse current density *versus* $\omega^{-\frac{1}{2}}$ in a Koutecky-Levich plot. From such a plot, the intercept is obtained through a linear least-squares fit and $j_k$ is then obtained as the inverse of the intercept. The result of this procedure is plotted for all studied electrodes in Fig. C.5.
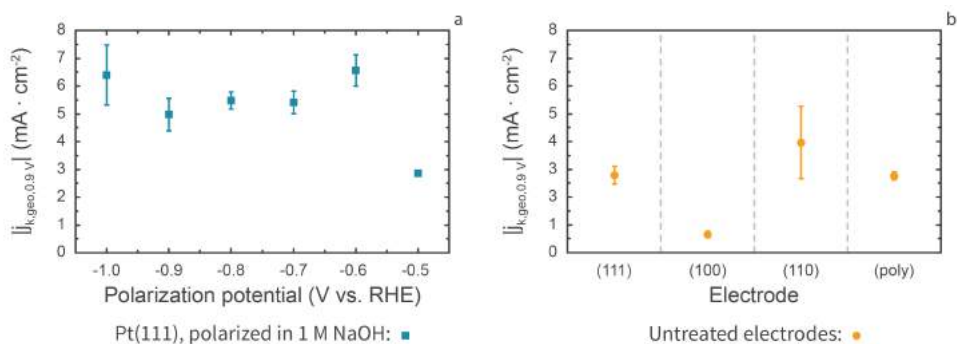


**Fig. C.5 |** Kinetic ORR current densities of corroded Pt(111) (red squares), as function of the polarization potential **(a)** and of uncorroded electrodes (yellow circles) **(b)**. Rotation rate: 1600 $rpm$. Each data point is the average of 3 or more experiments. Error bars represent one standard deviation.

As can be seen, Fig. C.5 is in good qualitative agreement with Fig. 6.3. The slightly larger error bars in Fig. C.5 are related to slight variations in the recorded current densities due to small variations in the meniscus height. Finally, it should be noted that the kinetic current density for Pt(110) in Fig. C.5 is *not corrected* for the aforementioned reduced surface area and is therefore underestimated.

## C.5   Pt(111), corroded in 10 M NaOH

Fig. C.6 displays CVs of Pt(111), corroded at and slightly below the onset potential in $10\,M$ NaOH. These experiments were explorative in nature and were therefore only performed once, with a different Pt(111) electrode.
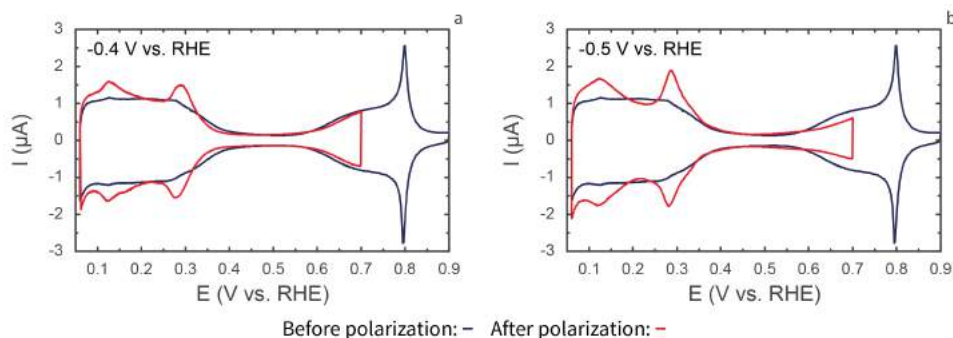


Before polarization: –    After polarization: –

**Fig. C.6 |** Cyclic voltammograms of Pt(111) before (blue trace) and after (red trace) cathodic polarization in $10\,M$ NaOH at $-0.4\,V$ *vs.* RHE **(a)** and $-0.5\,V$ *vs.* RHE **(b)**. Voltammograms were recorded in $0.1\,M$ HClO$_4$, at a scan rate of $50\,mV \cdot s^{-1}$.

The electrode in Fig. C.6 **a** appears similar to those in Fig. 6.1 and Fig. C.2, with an approximately 15% apparent area increase. Indeed, the normalized ORR activity of this electrode at $0.9\,V$ *vs.* RHE and $1600\,rpm$ is similar to those in Chapter 6: 0.32. In contrast, Fig. C.6 **b** indicates significantly more (110) and (100) step sites after corrosion at $-0.5\,V$ *vs.* RHE and a roughly 25% area increase. Interestingly, the electrode has a *lower* normalized ORR activity of 0.27. In fact, the normalized ORR activity in these explorative experiments decreased monotonically with more negative corrosion potentials. The lowest normalized activity of 0.2 was reached at the most negative explored potential of $-0.8\,V$ *vs.* RHE.

# References

1. Gomez, R., Orts, J. M., Alvarez-Ruiz, B. & Feliu, J. M. Effect of Temperature on Hydrogen Adsorption on Pt(111), Pt(110), and Pt(100) Electrodes in 0.1 M HClO4. *The Journal of Physical Chemistry B* **108,** 228–238 (2004).

2. Chen, Q.-S., Solla-Gullón, J., Sun, S.-G. & Feliu, J. M. The potential of zero total charge of Pt nanoparticles and polycrystalline electrodes with different surface structure: The role of anion adsorption in fundamental electrocatalysis. *Electrochimica Acta* **55,** 7982–7994 (2010).

3. Bard, A. J. & Faulkner, L. R. in *Electrochemical Methods: Fundamentals and Applications* 2nd ed. Chap. 5 (Wiley, New York, 2001).

4. Gómez-Marín, A. M., Rizo, R. & Feliu, J. M. Some reflections on the understanding of the oxygen reduction reaction at Pt(111). *Beilstein Journal of Nanotechnology* **4,** 956–967 (2013).

5. Gómez-Marín, A. M., Rizo, R. & Feliu, J. M. Oxygen reduction reaction at Pt single crystals: a critical overview. *Catalysis Science & Technology* **4,** 1685 (2014).

6. Bard, A. J. & Faulkner, L. R. in *Electrochemical Methods: Fundamentals and Applications* 2nd ed. Chap. 9 (Wiley, New York, 2001).

7. Wakabayashi, N., Takeichi, M., Itagaki, M., Uchida, H. & Watanabe, M. Temperature-dependence of oxygen reduction activity at a platinum electrode in an acidic electrolyte solution investigated with a channel flow double electrode. *Journal of Electroanalytical Chemistry* **574,** 339–346 (2005).

8. Wang, W. *et al.* Carbon-supported Pd-Co bimetallic nanoparticles as electrocatalysts for the oxygen reduction reaction. *Journal of Power Sources* **167,** 243–249 (2007).

9. Villullas, H. & Teijelo, M. The hanging-meniscus rotating disk (HMRD) Part 1. Dependence of hydrodynamic behavior on experimental variables. *Journal of Electroanalytical Chemistry* **384,** 25–30 (1995).

10. Schmickler, W. & Santos, E. in *Interfacial Electrochemistry* 2nd ed. Chap. 20 (Springer Berlin, Heidelberg, 2010).

# D    Supplementary Information for Chapter 7

## D.1    EXAFS functions in R-space

Fig. D.1 displays the EXAFS functions in R-space for the alloy particles studied in Chapter 7. Though these graphs display an intensity as function of R, one should note that the graphs are not radial distribution functions.[1]
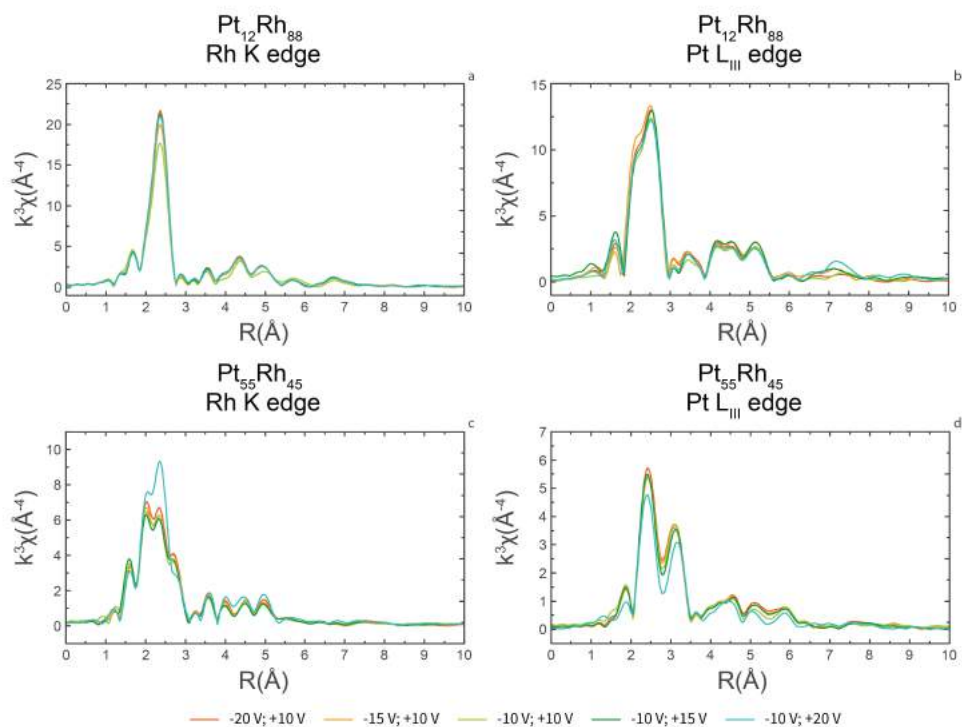


**Fig. D.1 |** EXAFS functions in R-space for the Rh K edge of $Pt_{12}Rh_{88}$ particles **(a)**, the Pt $L_{III}$ edge of $Pt_{12}Rh_{88}$ particles **(b)**, the Rh K edge of $Pt_{55}Rh_{45}$ particles **(c)** and the Pt $L_{III}$ edge of $Pt_{55}Rh_{45}$ particles **(d)**, prepared at various potentials.

## D.2   Nanoparticle X-ray diffraction patterns

Fig. D.2 displays X-ray diffraction patterns of all studied nanoparticles. Several peaks in the diffraction pattern do not correspond to the nanoparticles. Instead, they correspond to reflections of the boron nitride matrix in which the particles were embedded. These peaks are indicated with a blue circle.
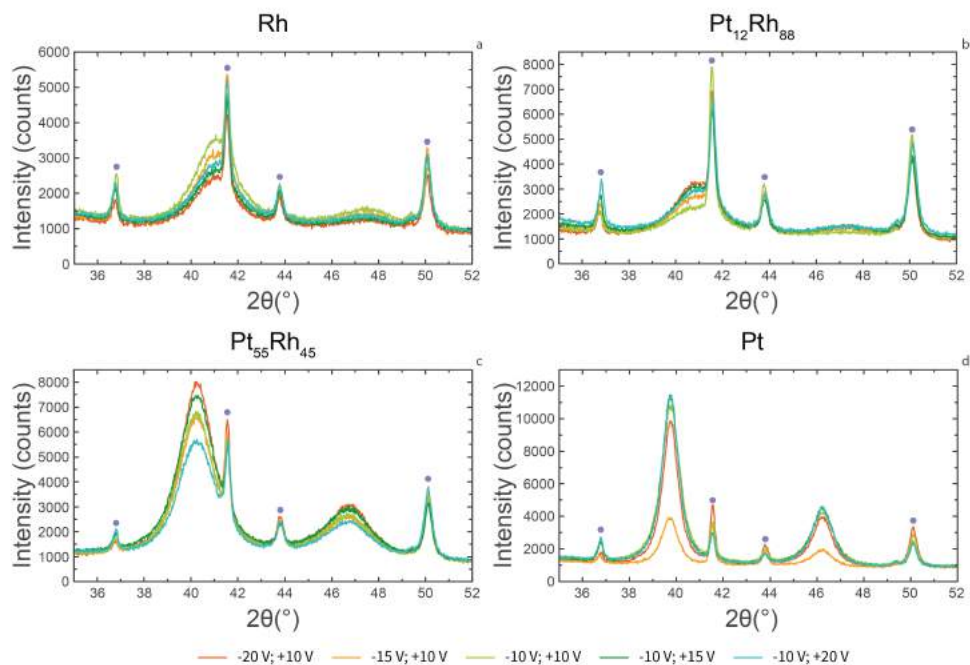


**Fig. D.2 |** X-ray diffraction patterns of Rh **(a)**, $Pt_{12}Rh_{88}$ **(b)**, $Pt_{55}Rh_{45}$ **(c)** and Pt **(d)** particles, prepared at various potentials. Peaks marked with a circle correspond to boron nitride reflections.

## D.3 Particle sizes as determined by transmission electron microscopy

Transmission electron microscopy (TEM) samples were prepared by mixing a droplet of nanoparticle suspension with $1.5\ mL$ of ethanol (Sigma-Aldrich, puriss. p.a.). This mixture was then applied on a TEM grid (Formvar film on copper 300 mesh) and subsequently air-dried. All TEM data were obtained using a JEOL TEM 1010. Average particle sizes and size standard deviations, given in Table D.1, were calculated by analyzing 200 particles per sample. Particle size distributions for Rh, $Pt_{12}Rh_{88}$, $Pt_{55}Rh_{45}$ and Pt were generated by analyzing the same 200 particles per sample. These distributions are displayed in Fig. D.3, Fig. D.4, Fig. D.5, and Fig. D.6, respectively. If agglomerated particles were present, these particles were not treated as one large particle. Rather, the individual primary crystallites were counted as individual particles, in order to facilitate a direct comparison with the X-ray diffraction-based coherent domain sizes.

**Table D.1 |** Average particle sizes and standard deviations for all alloys and potential limits. Particle sizes are given in nanometers

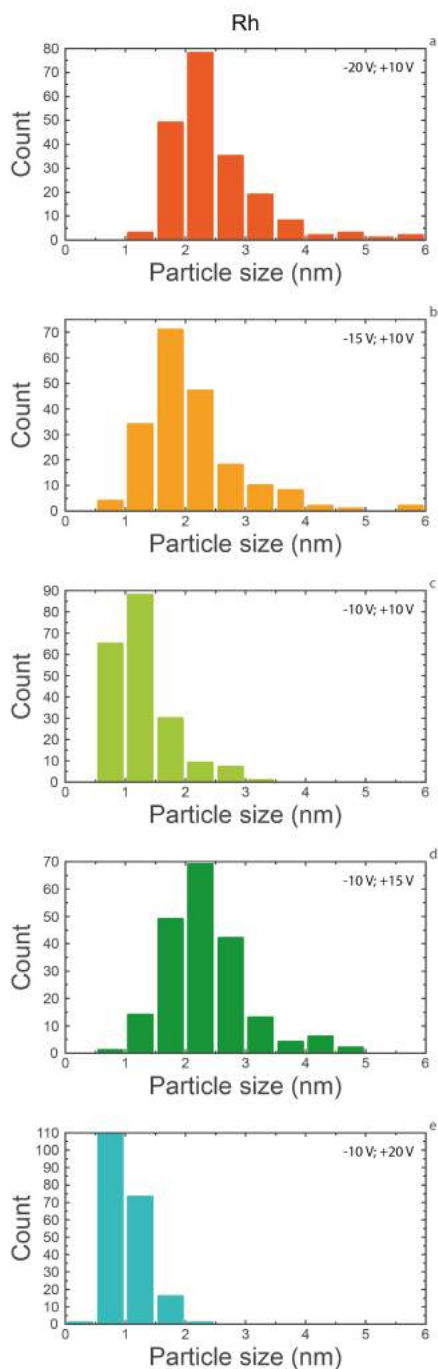| Potential Limits | Rh | $Pt_{12}Rh_{88}$ | $Pt_{55}Rh_{45}$ | Pt |
|---|---|---|---|---|
| -20 V; +10 V | $2.5 \pm 0.7$ | $1.9 \pm 0.4$ | $3.9 \pm 0.8$ | $17 \pm 6$ |
| -15 V; +10 V | $2.2 \pm 1.0$ | $2.2 \pm 0.7$ | $2.8 \pm 1.0$ | $3.4 \pm 2.1$ |
| -10 V; +10 V | $1.3 \pm 0.5$ | $1.8 \pm 0.7$ | $3.0 \pm 0.8$ | $1.7 \pm 0.5$ |
| -10 V; +15 V | $2.3 \pm 0.7$ | $2.3 \pm 0.5$ | $2.7 \pm 1.2$ | $1.8 \pm 0.7$ |
| -10 V; +20 V | $1.0 \pm 0.3$ | $1.6 \pm 0.7$ | $2.3 \pm 0.9$ | $18 \pm 6$ |

**Fig. D.3 |** Particle size distributions for studied Rh nanoparticles.
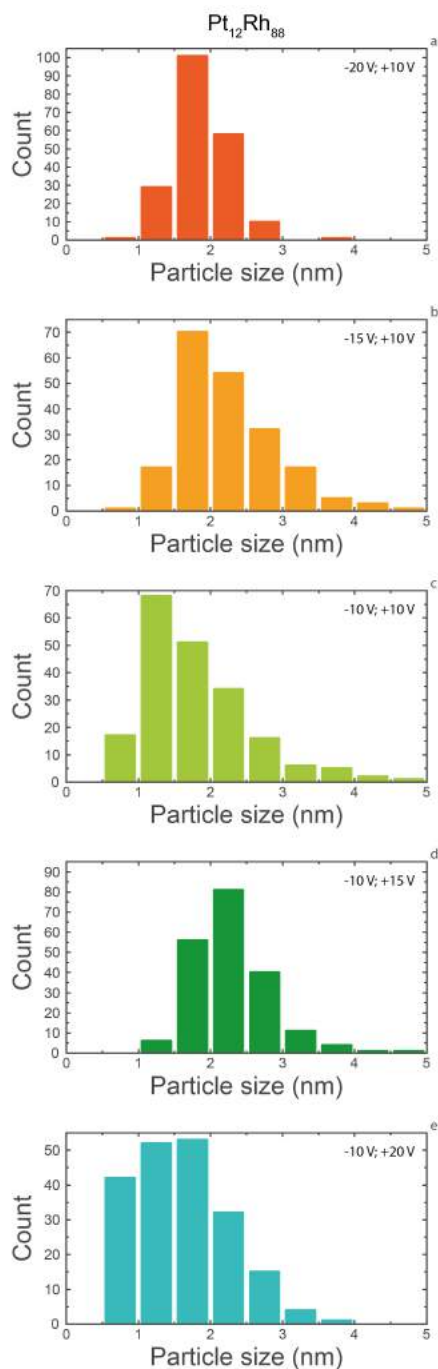
**Fig. D.4 |** Particle size distributions for studied $Pt_{12}Rh_{88}$ nanoparticles.
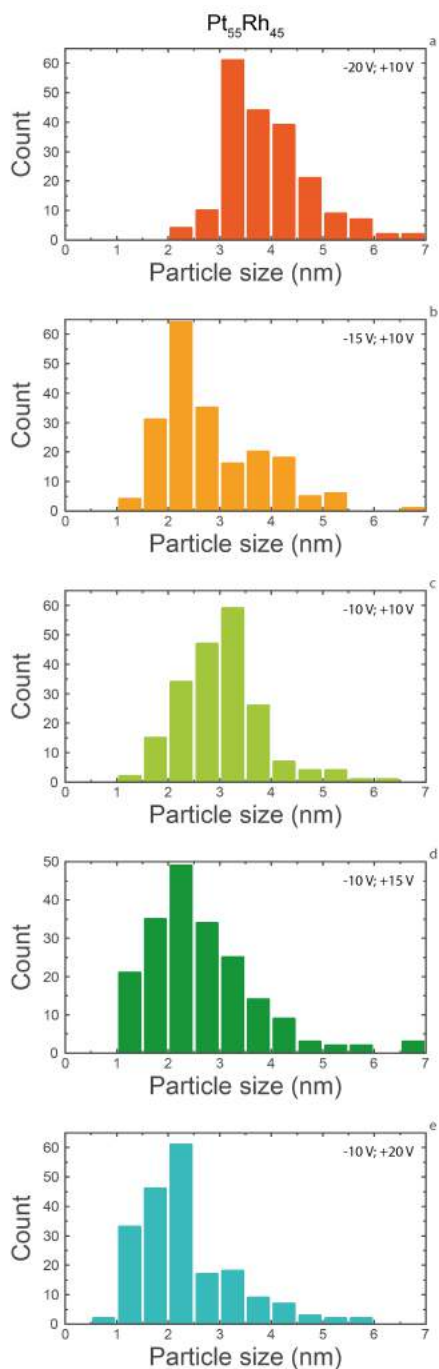
**Fig. D.5 |** Particle size distributions for studied Pt$_{55}$Rh$_{45}$ nanoparticles.
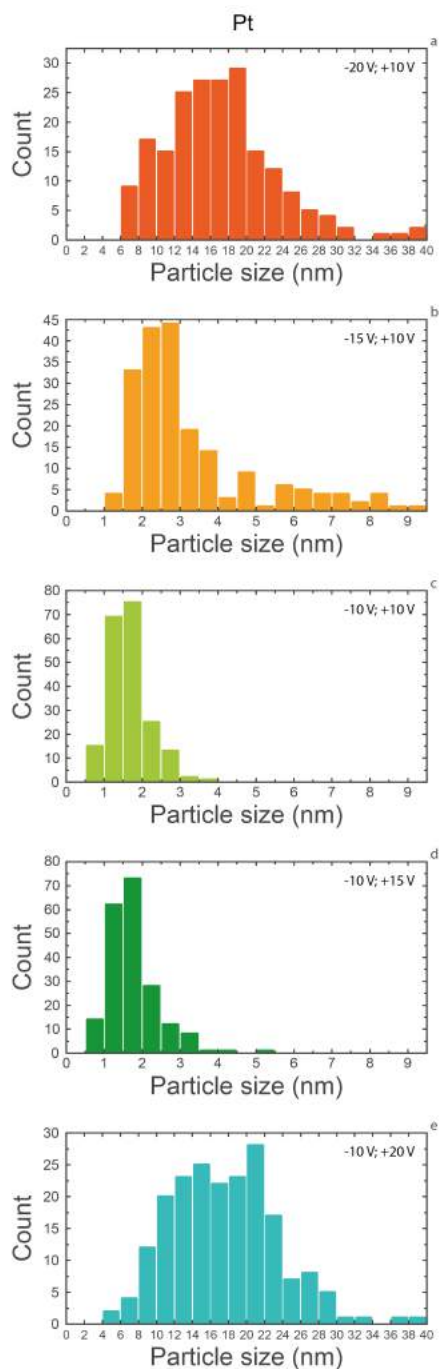


**Fig. D.6 |** Particle size distributions for studied Pt nanoparticles.

## D.4   2D nanoparticle visualizations

This section provides 2D visualizations of the data presented in Fig. 7.4 of Chapter 7. These visualizations, shown in Fig. D.7, consist of one layer of rhodium and platinum atoms. As such, they approximate a 2D cut through a nanoparticle.

For each model, containing 100 atoms, one can estimate the local Pt content that would be observed for these models through Rh K edge and Pt $L_{III}$ edge EXAFS experiments. This is done by counting the number of neighboring platinum atoms ($n_{Pt,i}$) for each atom $i$ in the model and dividing by the total number of neighboring atoms ($n_{t,i}$) for that atom $i$. For each atom, this yields the local relative platinum content ($x_{Pt,i}$):

$$x_{Pt,i} = \frac{n_{Pt,i}}{n_{t,i}} \cdot 100\% \tag{D.1}$$

Averaging this value over either all platinum or all rhodium atoms will lead to an approximation of the Pt edge- and Rh edge-based platinum content, respectively.
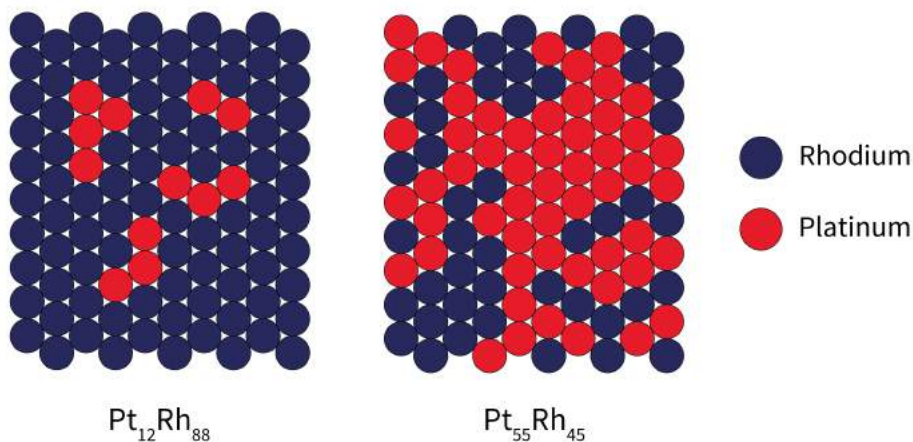


**Fig. D.7 |** 2D visualizations of the studied $Pt_{12}Rh_{88}$ and $Pt_{55}Rh_{45}$ nanoparticles.

The $Pt_{12}Rh_{88}$ surface in Fig. D.7 gives a Pt edge-based platinum content of 25.0% and a Rh edge-based platinum content of 10.2%. In the $Pt_{55}Rh_{45}$ example, the Pt edge-based platinum content is 61.3% and the Rh edge-based platinum content is 51.2%. Though these numbers agree relatively well with the actual data, care should be taken when extrapolating these models as accurate reflections of 3-dimensional nanoparticles. Nonetheless, the two examples can be taken as reasonable first-order approximations of the average elemental distribution of the studied nanoparticles.

## References

1.    Calvin, S. *XAFS for Everyone* 1st ed. **1,** 427 (CRC Press, Boca Raton, FL, 2013).

# Samenvatting

Elektrochemie is het chemische vakgebied dat zich richt op de inherente relatie tussen chemie en elektriciteit. Zodanig is elektrochemie de drijvende kracht achter de opslag en omzetting van energie in batterijen, supercondensatoren en brandstofcellen. Elektrochemie is bovendien ook het veld dat bij zal dragen aan het oplossen van existentiële uitdagingen van de 21$^e$ eeuw, zoals het vinden van $CO_2$-neutrale manieren om de ammonia te produceren die indirect de halve wereldbevolking voedt.

Elektrochemie maakt gebruik van elektriciteit en is dus sterk afhankelijk van elektrisch geleidende materialen. In elektrochemie worden daarom vaak metalen gebruikt, die over het algemeen goed elektrisch geleidend zijn. Deze afhankelijkheid van metalen is de reden dat de elektrochemische eigenschappen van metalen gedurende de afgelopen twee eeuwen uitvoerig bestudeerd zijn. Veel elektrochemische studies van metalen hebben zich vervolgens gericht op corrosie.

Corrosie vindt plaats wanneer een metaal elektronen verliest aan zijn omgeving (oxideert) en wordt omgezet naar verbindingen als metaaloxides. Het bekendste voorbeeld hiervan is roest, dat catastrofale gevolgen kan hebben als bijvoorbeeld bruggen of oliepijpleidingen erdoor worden aangetast. Zulke gevolgen kunnen worden voorkomen door het gebruik van kathodische bescherming.

Kathodische bescherming omvat het verlagen van de elektrochemische potentiaal van een metaal om oxidatie te voorkomen. Dit kan op twee manieren worden gedaan. De eerste manier beschermt een 'nobel' metaal zoals koper door een 'minder nobel' opofferingsmetaal als zink in contact te brengen. De tweede manier beschermt een metaal door een elektrische spanning aan te brengen: het metaal wordt bevestigd aan de negatieve zijde van een spanningsbron en wordt daardoor beschermd tegen corrosie. Op basis van deze tweede beschermingsmethode zou men aan kunnen nemen dat elke voldoende negatieve spanning tegen corrosie beschermt. Dit is echter niet noodzakelijk het geval: een te negatieve spanning kan leiden tot *kathodische* corrosie.

Kathodische corrosie is het centrale onderwerp van dit proefschrift. Hoewel kathodische corrosie al rond het jaar 1900 werd waargenomen door de Duitse chemicus Fritz Haber, is er relatief weinig bekend over dit fenomeen. Een cruciale stap in het begrip van kathodische corrosie is het werk van Yanson *et al.* in 2011. Dit werk sloot expliciet voorgaande hypothesen over het mechanisme van kathodische corrosie uit en formuleerde in plaats daarvan een nieuwe hypothese.

Deze hypothese zal worden toegelicht voor platina, in contact met sterk geconcentreerd natronloog. In een dergelijk systeem corrodeert platina bij negatieve (kathodische) spanningen. Bij deze spanningen ontwikkelt zich een grote hoeveelheid waterstof op metalen als platina. Dit zorgt ervoor dat de oplossing in nabijheid van het platina geen tot weinig 'vrij' water bevat: al het aanwezige water wordt direct omgezet in waterstofgas of is gebonden in de solvatieschil van de aanwezige natrium- en hydroxide-ionen.

In de afwezigheid van vrij water kan platina worden omgezet in een negatief geladen ion (anion). Dit anion lost op in het natronloog en laat een geëtst platina-oppervlak achter. De exacte samenstelling van het anion is vooralsnog onbekend, maar het ion wordt hoogstwaarschijnlijk gestabiliseerd door positief geladen ionen (kationen) zoals natrium-ionen in de oplossing; kathodische corrosie vindt alleen plaats in aanwezigheid van dergelijke kationen.

Nadat het kation-gestabiliseerde anion oplost, verplaatst het zich door de oplossing. Het anion komt snel in aanraking met 'vrij' water en oxideert daardoor tot metallisch platina. Dit platina slaat vervolgens neer op het originele geëtste platina-oppervlak of clustert met andere vrije platina-atomen tot nanodeeltjes.

Momenteel is bovenstaande hypothese het enige gepubliceerde mechanisme dat consistent is met alle gepubliceerde data op het gebied van kathodische corrosie. De hypothese roept echter ook vragen op. Wat is de samenstelling van het mysterieuze gevormde anion? Waarom bevat het geëtste metaaloppervlak vaak geometrische patronen? Hoe gedragen verschillende metalen en hun legeringen zich tijdens kathodische corrosie? En kan kathodische corrosie worden gebruikt voor andere doelen dan de productie van nanodeeltjes?

Dit proefschrift heeft als doel om bovenstaande vragen te beantwoorden. Het richt zich daarom op goed gedefinieerde systemen, waardoor de meeste hoofdstukken geen 'gewone' anodische corrosie bevatten om de gevolgen van kathodische corrosie te versnellen. Daarnaast wordt in de meeste hoofdstukken gebruik gemaakt van referentie-elektrodes om een duidelijk afteltpunt van de elektrochemische potentiaal mogelijk te maken. Dit heeft tot gevolg dat de waargenomen kathodische corrosie relatief subtiel is en niet leidt tot de vorming van praktische hoeveelheden nanodeeltjes. Het proefschrift richt zich daardoor vooral op oppervlakken die geëtst worden door kathodische corrosie. Het proefschrift kan daarnaast worden ingedeeld in vier 'fundamentele' hoofdstukken (Hoofdstuk 2–5) en twee 'toegepaste' hoofdstukken (Hoofdstuk 6–7).

Het eerste fundamentele hoofdstuk is Hoofdstuk 2. Dit hoofdstuk zet het experi-

mentele protocol uiteen dat de basis vormt voor de vier opvolgende hoofdstukken. Met behulp van dit protocol wordt in Hoofdstuk 2 de kathodische corrosie van platina in 10 molair natriumhydroxide bestudeerd. In dit systeem corrodeert platina bij milde spanningen en vormt het geometrische driehoekige en quasi-rechthoekige etsputten in het oppervlak. Deze etsputten komen overeen met de vorming van oppervlak met een (100)-oriëntatie. Deze (100)-voorkeur voor de kathodische corrosie van platina wordt verondersteld te worden veroorzaakt door de adsorptie van natrium-ionen tijdens corrosie.

De voorgaande observaties voor platina worden in Hoofdstuk 3 verkend voor rodium en goud. Hoewel rodium dezelfde aanzetspanning en etsvoorkeur heeft als platina, corrodeert goud bij enigszins negatievere potentialen en wordt bij dit metaal (111)-oppervlak gevormd. Deze verschillen tussen platina en rodium enerzijds en goud anderzijds worden tentatief verklaard door natrium-adsorptie tijdens corrosie. Deze verklaring wordt ondersteund door dichtheidsfunctionaaltheorie-berekeningen van de adsorptie van natrium.

De rol van kationen zoals natrium wordt expliciet bestudeerd in Hoofdstuk 4. In dit hoofdstuk wordt daarom de corrosie van platina, rodium en goud bestudeerd in oplossingen van lithiumhydroxide, natriumhydroxide en kaliumhydroxide. Deze experimenten tonen aan dat kationen inderdaad een sterke invloed hebben op kathodische corrosie. Deze conclusie wordt ook in dit hoofdstuk ondersteund met dichtheidsfunctionaaltheorie. Aanvullende theoretische berekeningen suggereren daarnaast een vergelijkbare rol voor geadsorbeerd waterstof. Op basis van het belang van zowel kationen als waterstof wordt er in Hoofdstuk 4 gesuggereerd dat het gevormde anion tijdens kathodische corrosie een ternair metaalhydride is.

Vervolgens wordt in Hoofdstuk 5 de mogelijkheid van zulke metaalhydrides bestudeerd door middel van Röntgenabsorptiespectroscopie. Deze metingen leggen een kleine verandering in de chemische toestand van platina bloot. Verdere kwantitatieve data-analyse en gesimuleerde absorptiespectra geven aan dat $Na_2PtH_6$ een waarschijnlijke chemische verbinding is die tijdens kathodische corrosie wordt gevormd.

Na deze fundamentele inzichten volgt in Hoofdstuk 6 een voorbeeld van toepassingen van kathodische corrosie. In dit hoofdstuk worden de inzichten uit Hoofdstuk 2 en 4 gebruikt om een platina-eenkristal met een (111)-oriëntatie te optimaliseren voor de omzetting van zuurstof naar water.

Ten slotte biedt Hoofdstuk 7 inzicht in de kathodische corrosie van platina, rodium en hun legeringen. Dit inzicht wordt verkregen door kathodische en anodische corrosie

te combineren voor het maken van nanodeeltjes. Hierdoor wordt inzicht verkregen in het relatieve belang van deze corrosie-mechanismen voor de vorming van nanodeeltjes. De structuur en samenstelling van de gevormde nanodeeltjes worden vervolgens in kaart gebracht door middel van Röntgenabsorptie, Röntgendiffractie en elektronenmicroscopie. Deze analyse geeft aan dat de elementaire samenstelling van gevormde deeltjes enigszins gesegregeerd is.

Hoofdstuk 2 tot en met 7 leiden gezamenlijk tot een completer begrip van kathodische corrosie. De hoofdstukken brengen het corrosie-gedrag van platina, rodium en goud in detail in kaart en leiden vervolgens tot concrete aanwijzingen voor het bestaan van $Na_2PtH_6$ tijdens kathodische corrosie. Deze aanwijzingen zouden, indien bevestigd, de eerste gerapporteerde waarneming zijn van ternaire metaalhydrides in waterige oplossingen.

Het proefschrift biedt niet alleen fundamenteel inzicht, maar vergemakkelijkt bovendien de toepassing van kathodische corrosie: Hoofdstuk 4 geeft richtlijnen voor het vormgeven van metaaloppervlakken door middel van kathodische corrosie. De toepassing van vormgegeven metaaloppervlakken voor katalyse wordt vervolgens geïllustreerd in Hoofdstuk 6. Ten slotte biedt Hoofdstuk 7 aanbevelingen voor de synthese van nanodeeltjes door middel van kathodische corrosie.

Dit proefschrift is daarom een significante stap in zowel het begrip als de toepassing van kathodische corrosie. Mijn hoop is dat deze stap een bijdrage heeft geleverd aan de ontwikkeling van kathodische corrosie als hulpmiddel voor het oplossen van de elektrochemische uitdagingen van de 21$^e$ eeuw.

# List of Publications

## This thesis is based on the following publications

### Chapter 2

Hersbach, T. J. P., Yanson, A. I. & Koper, M. T. M.

Anisotropic Etching of Platinum Electrodes at the Onset of Cathodic Corrosion

*Nature Communications* **7**, 12653 (2016)

### Chapter 3

Hersbach, T. J. P., Mints, V. A., Calle-Vallejo, F., Yanson, A. I. & Koper, M. T. M.

Anisotropic Etching of Rhodium and Gold as the Onset of Nanoparticle Formation by Cathodic Corrosion

*Faraday Discussions* **193**, 207–222 (2016)

### Chapter 4

Hersbach, T. J. P., McCrum, I. T., Anastasiadou, D., Wever, R., Calle-Vallejo, F. & Koper, M. T. M.

Alkali Metal Cation Effects in Structuring Pt, Rh, and Au Surfaces through Cathodic Corrosion

*ACS Applied Materials & Interfaces* **10**, 39363–39379 (2018)

### Chapter 7

Hersbach, T. J. P., Kortlever, R., Lehtimäki, M., Krtil, P. & Koper, M. T. M.

Local Structure and Composition of PtRh Nanoparticles Produced through Cathodic Corrosion

*Physical Chemistry Chemical Physics* **19**, 10301–10308 (2017)

## Other publications

Díaz-Morales, O.,* Hersbach, T. J. P.,* Badan, C., Garcia, A. C. & Koper, M. T. M.
Hydrogen Adsorption on Nano-Structured Platinum Electrodes
*Faraday Discussions* **210**, 301–315 (2018)
*Both authors contributed equally.

Seitz, L. C., Hersbach, T. J. P., Nordlund, D. & Jaramillo, T. F.
Enhancement Effect of Noble Metals on Manganese Oxide for the Oxygen Evolution
Reaction
*The Journal of Physical Chemistry Letters* **6**, 4178–4183 (2015)

Díaz-Morales, O., Hersbach, T. J. P., Hetterscheid, D. G. H., Reek, J. N. H. & Koper, M. T. M.
Electrochemical and Spectroelectrochemical Characterization of an Iridium-Based
Molecular Catalyst for Water Splitting: Turnover Frequencies, Stability, and Electrolyte
Effects
*Journal of the American Chemical Society* **136**, 10432–10439 (2014)

Kwon, Y., Hersbach, T. J. P. & Koper, M. T. M.
Electro-Oxidation of Glycerol on Platinum Modified by Adatoms: Activity and Selectivity
Effects
*Topics in Catalysis* **57**, 1272–1276 (2014)

# Curriculum Vitae

Thom Hersbach was born in 1991 in Purmerend, the Netherlands. Here, he attended high school between 2003 and 2009 at the Da Vinci College, specializing in the "Natuur & Techniek" direction. During high school, Thom participated in the team-based "Extra Talent Project" at the Free University in Amsterdam. His team, supervised by Frank Postma, won the first prize.

After graduating high school *"Cum Laude"*, Thom studied Molecular Science & Technology from 2009 to 2012 at the Technical University of Delft and Leiden University. His BSc degree was obtained *"Cum Laude"* as well. Majoring in Chemistry and minoring in Sustainable Development, Thom wrote his thesis on electrochemical glycerol oxidation in the group of Prof. Dr. Marc Koper at Leiden University, under the supervision of Youngkook Kwon.

Thom remained at Leiden University to pursue his MSc degree in Research in Chemistry (2012–2014), following the "Physical & Theoretical" specialization. Two research projects were carried out during the MSc program. The first project, concerning electrochemical oxygen evolution on an immobilized Ir-based molecular complex, was performed in the group of Prof. Dr. Marc Koper at Leiden University, under the supervision of Oscar Díaz-Morales. The second project, studying the enhancing effects of noble metals on the electrochemical oxygen evolution activity of 3d-metal oxides, was carried out in the group of Prof. Dr. Thomas Jaramillo at Stanford University, under the supervision of Linsey Seitz. During his MSc, Thom additionally won the third prize in the 2013 "Green Brain of the Year" competition of the Middle East Technical University (with Andrei Fedorovski) and was awarded the 2013/2014 title of "Best Chemistry Student" at Leiden University. Thom then obtained his MSc degree *"Cum Laude"* in 2014.

This year also marked the start of Thom's PhD project at Leiden University, guided by Prof. Dr. Marc Koper. The project focused on fundamentally understanding cathodic corrosion. The first year of the project was predominantly spent making nanoparticles and developing a methodology to corrode and carefully characterize metallic electrodes. The produced nanoparticles would lead to Chapter 7, whereas the developed methodology would form the basis for Chapter 2–4 and Chapter 6. Additional experiments at the Stanford Synchrotron Radiation Lightsource would lead to Chapter 5. The PhD project yielded the multifaceted study of cathodic corrosion that is presented in this thesis. Given the multidisciplinary approach of the project, Thom had the great privilege to collaborate

with and learn from many talented scientists.

During the PhD project, Thom assisted in teaching the BSc classes "General and Inorganic Chemistry" & "Physical Chemistry and Kinetics", as well as the BSc practical course "Basic Practical Skills". He was also awarded the honor of designing the cover image of Volume 193 of the Faraday Discussions proceedings in collaboration with Victoria Flores. Thom was additionally awarded the poster prize at the 2016 HRSMC symposium in Leiden, The Netherlands, and the NIOK lecture award at the 2017 NCCC conference in Noordwijkerhout, The Netherlands.

Following the obtainment of his doctorate degree, Thom will continue his academic career as a post-doctoral researcher in the group of Prof. Dr. Richard Crooks at the University of Texas at Austin. In this position, Thom hopes to use dendrimer-encapsulated nanoparticles as models for developing improved nano-sized catalysts. He additionally aims to pursue his interests of running, reading and brewing the tastiest of beers.